

## **INFORMATION TO USERS**

**This manuscript has been reproduced from the microfilm master. UMI films the text directly from the original or copy submitted. Thus, some thesis and dissertation copies are in typewriter face, while others may be from any type of computer printer.**

**The quality of this reproduction is dependent upon the quality of the copy submitted. Broken or indistinct print, colored or poor quality illustrations and photographs, print bleedthrough, substandard margins, and improper alignment can adversely affect reproduction.**

**In the unlikely event that the author did not send UMI a complete manuscript and there are missing pages, these will be noted. Also, if unauthorized copyright material had to be removed, a note will indicate the deletion.**

**Oversize materials (e.g., maps, drawings, charts) are reproduced by sectioning the original, beginning at the upper left-hand corner and continuing from left to right in equal sections with small overlaps. Each original is also photographed in one exposure and is included in reduced form at the back of the book.**

**Photographs included in the original manuscript have been reproduced xerographically in this copy. Higher quality 6" x 9" black and white photographic prints are available for any photographs or illustrations appearing in this copy for an additional charge. Contact UMI directly to order.**

# **UMI**

**A Bell & Howell Information Company  
300 North Zeeb Road, Ann Arbor MI 48106-1346 USA  
313/761-4700 800/521-0600**



VELOCITY ESTIMATION FOR  
CROSSWELL REFLECTION IMAGING USING  
COMBINED DIRECT AND REFLECTED ARRIVAL  
TRAVELTIME TOMOGRAPHY

A DISSERTATION  
SUBMITTED TO THE DEPARTMENT OF GEOPHYSICS  
AND THE COMMITTEE ON GRADUATE STUDIES  
OF STANFORD UNIVERSITY  
IN PARTIAL FULFILLMENT OF THE REQUIREMENTS  
FOR THE DEGREE OF  
DOCTOR OF PHILOSOPHY

Mark Alan Van Schaack

January 1997

**UMI Number: 9723429**

**Copyright 1997 by  
Van Schaack, Mark Alan**

**All rights reserved.**

---

**UMI Microform 9723429  
Copyright 1997, by UMI Company. All rights reserved.**

**This microform edition is protected against unauthorized  
copying under Title 17, United States Code.**

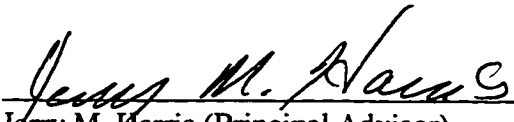
---

**UMI**  
**300 North Zeeb Road**  
**Ann Arbor, MI 48103**

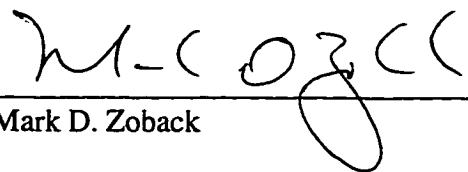


**© Copyright by Mark Alan Van Schaack**  
**All Rights Reserved**

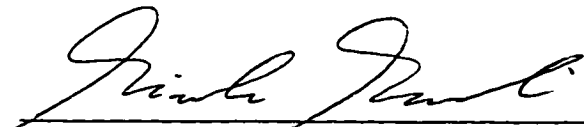
I certify that I have read this dissertation and that in my opinion it is fully adequate, in scope and quality, as a dissertation for the degree of Doctor of Philosophy.

  
Jerry M. Harris (Principal Advisor)

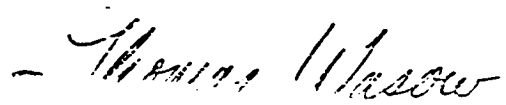
I certify that I have read this dissertation and that in my opinion it is fully adequate, in scope and quality, as a dissertation for the degree of Doctor of Philosophy.

  
Mark D. Zoback

I certify that I have read this dissertation and that in my opinion it is fully adequate, in scope and quality, as a dissertation for the degree of Doctor of Philosophy.

  
Biondo L. Biondi

Approved for the University Committee on Graduate Studies:

  
Thomas Wasson

# Abstract

Data from individual seismic gathers must be accurately imaged to obtain optimal seismic reflection sections. The aspect of this imaging procedure that is of primary importance is the correct positioning of reflection events within the image space. If this is accomplished, multiple images can be added together, by stacking, to extend the coverage of the imaged area and improve the signal-to-noise ratio. Velocity and reflector geometry information play an important role in imaging the seismic data accurately in surface seismic imaging. Crosswell reflection imaging is no exception. In this thesis I present a consistent approach for obtaining the velocity and reflector geometry information needed for crosswell seismic reflection imaging. In addition, I present a wavefront-based mapping transformation method to image the seismic data in a manner consistent with the velocity and reflector geometry solutions.

The approach I used for velocity and reflector geometry estimation is Combined Direct and Reflected Arrival Traveltime Tomography (CDRATT). In the CDRATT inversion, direct arrival traveltimes and reflected arrival traveltimes for selected events are processed to obtain a globally consistent velocity model and the geometries of the selected events. The inversion features a continuation approach for obtaining optimal regularization of the inverse problem. The non-linear tomographic inverse problem is solved in an iterative fashion with fixed regularization weights using the Gauss-Newton method. After the solution achieves certain convergence criteria the regularization weights are relaxed and the tomographic inversion is run again using the solution from the previous continuation step as a starting model. In this way multiple solutions to the inverse problem are obtained starting with smooth models, where the regularization terms dominate the solution, to higher resolution models, where the data dominates the solution.

Seismic reflection images are created from CDRATT velocity and reflector information using the XSP-CDP mapping transformation. I have devised an approach for implementing this transformation which maps the seismic data, without raytracing, in a manner which is consistent with the CDRATT parameterization. This approach uses a wavefront-based technique for calculating mapping trajectories which is simple, efficient, and effective.

The results of applying the CDRATT velocity analysis on field data show that reflection events in separate images are co-located spatially and align well prior to stack when imaged using the CDRATT solution. This results in high quality stacked images. The largest improvements in reflection imaging, compared to stacks created using Direct

Arrival Only (DAO) tomograms, occur near the top and bottom of the surveyed region where the addition of reflection traveltime information has the largest effect. High resolution stacks are also produced using the CDRATT model for field data that have undergone no wavefield processing. This example illustrates the power of stacking when events are aligned well prior to stacking and, thus, the importance of velocity estimation in crosswell seismic imaging.

# Acknowledgments

Many people have contributed to the intellectual and emotional state of mind reflected in this dissertation. Now is the time to identify the culprits. My advisor, Jerry Harris, provided a resource-rich working environment, generous funding, and invaluable professional and personal guidance. His open-door, never too busy to talk, “show me” approach as an advisor had a large impact on my work here at Stanford. It was incredible luck that Jerry and I crossed paths and hooked up as I emerged from my stint in the Middle East. I can’t imagine a better advisor and friend.

I am thankful for the support of my committee members: Mark Zoback, Gary Mavko, Biondo Biondi, and Lynn Orr. Over the years their questions and advice helped me to formulate a map of where I wanted to go with my research. I am also thankful to Bob Langan and Ken Bube for their advice, opinions, helpful discussions, and the use of their inversion codes. Their contributions helped start me off in the right direction, down a path that wouldn’t leave me stranded.

So many of my student colleagues at Stanford have been very good friends. Caroline Lambert, Spyros Lazaratos, Reinaldo Michelena, and Jessé Costa all had a large impact on my thesis work and have been great to work with. Many, many, other friends helped make my time at Stanford unforgettable as well; among them are the Thursday Beer Crowd (Thomas, Christine, Yizhaq, Tony, Liz, Patti, Ian, Martin, Tanja, etc...), the SCANCOR Crowd (Shirin, Maria, Pia, Christian, Christelle, Annelie, Eva, etc...), the STP crowd (Nick, Guan, Le-Wei, Ricardo, Ann, Youli), the Friday Beer Crowd (Ben, Ramón, Phil, Brad, Joe, etc...), and the Married, With Children, But Are Still Fun Crowd (Brian and Dawn).

Finally, I would like to acknowledge my parents and family. Their support, encouragement, heckling, and abuse helped motivate me to finish as fast as I did. It was a special bonus that my studies at Stanford allowed me to spend so much time with them.

# Table of Contents

Abstract ..... iv

Acknowledgments ..... vi

Table of Contents ..... vii

List of Figures ..... xi

1 – VELOCITY ESTIMATION FOR CROSSWELL REFLECTION IMAGING ..... 1

    1.1 Introduction ..... 1

    1.2 Importance of this research ..... 2

    1.3 Imaging problem: reflector misalignment prior to stacking ..... 3

    1.4 Background: velocity analysis approaches ..... 6

    1.5 Solution: Combined Direct and Reflected Arrival Traveltime Tomography ..... 9

        1.5.1 Reflection imaging using CDRATT velocity estimation ..... 9

        1.5.2 Strengths of CDRATT velocity estimation ..... 11

        1.5.3 Shortcomings of CDRATT velocity estimation ..... 12

    1.6 Additional uses of CDRATT velocity estimation ..... 13

    1.7 Thesis organization and overview of results ..... 15

        1.7.1 Chapter 2 – Crosswell seismic reflection imaging ..... 15

        1.7.2 Chapter 3 – A fast approach for calculating XSP-CDP mapping trajectories in a general 2-D media ..... 16

        1.7.3 Chapter 4 – Traveltime tomography using direct and reflected arrivals: theory & implementation ..... 16

        1.7.4 Chapter 5 – Traveltime tomography using direct and reflected arrivals: examples ..... 17

        1.7.5 Chapter 6 – Case study ..... 17

2 – CROSSWELL SEISMIC REFLECTION IMAGING ..... 19

    2.1 Introduction ..... 19

    2.2 Mapping versus migration ..... 20

        2.2.1 The XSP-CDP mapping transformation ..... 21



4.2.1	Direct arrival traveltime tomography .....	70
4.2.2	Combined direct & reflected arrival tomography .....	71
4.2.3	Summary of basic theory .....	73
4.3	Parameterization of the model .....	73
4.3.1	Slowness .....	74
4.3.2	Reflectors .....	74
4.4	Forward modeling — raytracing & traveltimes .....	75
4.4.1	Initial value raytracing .....	76
4.4.2	Calculating reflected raypaths .....	76
4.4.3	The two-point raytracing problem .....	77
4.4.4	Calculating traveltimes and traveltime derivatives .....	77
4.4.5	Calculating reflector depth derivatives .....	78
4.5	Solving the inverse problem .....	78
4.5.1	Regularization — slowness field .....	79
4.5.2	Regularization — reflector geometries .....	79
4.5.3	Problem setup .....	80
4.6	Conclusions .....	81
5 – TRAVELTIME TOMOGRAPHY USING DIRECT AND REFLECTED		
	ARRIVALS: VALIDATION .....	83
5.1	Introduction .....	83
5.2	Forward modeling of synthetic data sets .....	83
5.2.1	Calculating direct arrival traveltimes .....	83
5.2.2	Calculating reflected arrival traveltimes .....	84
5.3	Synthetic Study #1 .....	84
5.3.1	Study #1: acquisition geometry and data specifications .....	86
5.3.2	Synthetic Study #1: inversion and results .....	87
5.4	Synthetic Study #2 .....	90
5.4.1	Study #2: acquisition geometry and data specifications .....	92
5.4.2	Synthetic Study #2: inversion and results .....	93
5.5	Synthetic Study #3 .....	95



5.5.1	Study #3: acquisition geometry and data specifications.....	99
5.5.2	Synthetic Study #3: inversion and results .....	100
5.6	Conclusions .....	102
 6 – THE CDRATT VELOCITY ESTIMATION METHOD:		
	McELROY FIELD STUDY .....	104
6.1	Introduction .....	104
6.2	Field data example: McElroy Survey Mc68-02b .....	105
6.2.1	Site description.....	106
6.2.2	Survey description and data acquisition.....	108
6.2.3	Data description.....	112
6.3	Traveltime picking.....	116
6.3.1	Direct arrivals .....	116
6.3.2	Reflected arrivals .....	117
6.3.3	The Mc68-02b CDRATT traveltime data set .....	125
6.4	Traveltime inversion .....	127
6.4.1	Direct arrival only (DAO) traveltime inversions .....	129
6.4.2	CDRATT inversion — choice of reflector parametrization .....	134
6.4.3	CDRATT inversion — analysis of results .....	138
6.4.4	CDRATT inversion — conclusions.....	140
6.5	Reflection imaging .....	142
6.5.1	Brute stacks .....	143
6.5.2	Limited angle stacking .....	145
6.5.3	Comparison of CDRATT and DAO models.....	149
6.5.4	Reflection imaging without wavefield processing.....	155
6.6	Conclusions .....	159
	References .....	161

# List of Figures

Figure 1.1	Different domains in the mapped data cube.....	4
Figure 1.2	Reflection misalignment in a common reflection point gather.....	5
Figure 1.3	CDRATT velocity estimation flowchart.....	10
Figure 2.1	The XSP-CDP mapping transformation .....	22
Figure 2.2	Crosswell common shot gather simulation .....	23
Figure 2.3	Mapped common shot gather .....	24
Figure 2.4	Resampled mapped common shot gather.....	26
Figure 2.5	XSP-CDP mapping trajectories in a simple model .....	32
Figure 2.6	Source and receiver wavefronts .....	34
Figure 2.7	Reflection point using wavefronts .....	34
Figure 2.8	Creating the combined traveltimes map .....	36
Figure 2.9	XSP-CDP mapping trajectories using wavefronts — simple model ....	37
Figure 2.10	Mapping trajectories using wavefronts — general reflectors .....	38
Figure 2.11	2-D velocity and reflector model .....	39
Figure 2.12	Source traveltimes map in a 2-D model .....	40
Figure 2.13	Creating the combined traveltimes map — 2-D model.....	41
Figure 2.14	Mapping trajectories in a 2-D model .....	42
Figure 2.15	Mapping trajectories from various sort domains .....	45
Figure 3.1	Reflection point for a curved reflector with combined traveltimes map .....	50
Figure 3.2	Reflection point and combined traveltimes isochrons.....	50
Figure 3.3	Calculating mapping trajectories using wavefronts flowchart.....	52
Figure 3.4	Combined traveltimes map with head wave effects #1 .....	54
Figure 3.5	Combined traveltimes map with head wave effects #1 .....	56
Figure 3.6	Combined traveltimes map without head wave effects .....	57
Figure 3.7	Calculating a single mapping trajectory using wavefronts flowchart.....	59
Figure 3.8	Spline reflector with the combined traveltimes map .....	60
Figure 3.9	Interpolated combined traveltimes along a reflector.....	60
Figure 3.10	Calculated mapping trajectories using the wavefront method .....	63
Figure 3.11	Combined traveltimes along downgoing reflection events.....	64
Figure 3.12	Combined traveltimes along upgoing reflection events.....	64
Figure 3.13	Calculated mapping trajectories from various sort domains.....	65

Figure 4.1	Slowness model parameterization using cells.....	70
Figure 5.1	Synthetic model #1.....	85
Figure 5.2	Synthetic model #1 CDRATT inversion results .....	88
Figure 5.3	Synthetic model #2.....	91
Figure 5.4	Synthetic model #2 CDRATT inversion tomogram .....	94
Figure 5.5	Synthetic model #2 CDRATT inversion reflector solutions with model.....	96
Figure 5.6	Synthetic model #2 CDRATT inversion reflector errors.....	97
Figure 5.7	Synthetic model #3.....	98
Figure 5.8	Synthetic model #3 CDRATT inversion tomogram .....	101
Figure 6.1	McElroy Field site map.....	107
Figure 6.2	McElroy Field site geology and logs .....	106
Figure 6.3	McElroy Field CO <sub>2</sub> flood program map .....	109
Figure 6.4	Survey Mc68-02b well deviations — map view.....	110
Figure 6.5	Survey Mc68-02b acquisition geometry .....	111
Figure 6.6	Survey Mc68-02b acquisition geometry subset.....	113
Figure 6.7	Interpreted crosswell seismic gather .....	114
Figure 6.8	Theoretical source radiation and receiver sensitivity patterns .....	115
Figure 6.9	Survey Mc68-02b common shot gather .....	117
Figure 6.10	Common shot gather illustration and direct arrival traveltime pick map.....	118
Figure 6.11	Crosswell wavefield processing flowchart.....	120
Figure 6.12	Combining the processed data sets flowchart .....	121
Figure 6.13	Common mid-depth gather — before and after wavefield processing .....	122
Figure 6.14	Common mid-depth gather illustration and reflected arrival traveltime pick map.....	123
Figure 6.15	Estimated reflection geometries for picked reflection events.....	125
Figure 6.16	Direct and reflected arrival traveltime data set .....	126
Figure 6.17	1-D direct arrival only velocity tomogram.....	130
Figure 6.18	2-D direct arrival only velocity tomogram.....	131
Figure 6.19	2-D direct arrival only slowness tomogram.....	133
Figure 6.20	CDRATT velocity tomograms for various reflector parameterizations .....	135
Figure 6.21	Percent change in velocity tomograms for changing reflector parameterizations .....	137

Figure 6.22	CDRATT velocity tomogram — 11 point reflector parameterization .....	139
Figure 6.23	CDRATT T11 versus 2-D DAO solutions — percent difference.....	141
Figure 6.24	Survey Mc68-02b CDRATT T11 mapped data — brute stack.....	144
Figure 6.25	Angle versus amplitude gather transformation .....	146
Figure 6.26	Mapped processed downgoing reflection data — AVA domain .....	147
Figure 6.27	Mapped processed upgoing reflection data — AVA domain .....	148
Figure 6.28	Limited aperture CDRATT stacks — processed data.....	150
Figure 6.29	Alignment of reflection events in the AVA domain for data mapped with different models .....	151
Figure 6.30	Limited aperture stacks of data mapped with different models .....	153
Figure 6.31	Limited aperture DAO stacks — processed data .....	154
Figure 6.32	Mapped unprocessed downgoing reflection data — AVA domain ....	156
Figure 6.33	Mapped processed upgoing reflection data — AVA domain .....	157
Figure 6.34	Limited aperture CDRATT stacks — unprocessed data.....	158

# **CHAPTER 1**

## **VELOCITY ESTIMATION FOR CROSSWELL REFLECTION IMAGING**

### **1.1 Introduction**

The possibility of imaging the subsurface through the use of crosswell reflection imaging was recognized shortly after the introduction of the Vertical Seismic Profile (VSP). The first published crosswell reflection image was obtained using a version of the VSP-CDP imaging algorithm (Wyatt and Wyatt, 1981) modified for the crosswell acquisition geometry (Baker and Harris, 1984). This image and the images that followed in the next eight years provided various examples of the principles of crosswell reflection imaging. But, while the principles of crosswell reflection imaging are reasonably straightforward, their practical application is not. Early reflection images provided some indication of major features but, in general, suffered from artifacts, distortions, and poor signal-to-noise ratio.

A large step forward in crosswell reflection imaging was work by Lazaratos (1993). As a result of several significant improvements in crosswell data acquisition (Harris et al., 1995) it became feasible to collect finely sampled surveys containing large volumes of data in short periods of time. This broad-coverage densely-sampled data allowed a wide variety of practical processing problems to be addressed in new ways. The final result was a robust approach for creating high-resolution multi-fold crosswell reflection images.

Lazaratos made the observation that a one-step procedure of imaging and stacking (brute stack) failed to produce high-quality images for two reasons: 1) strong coherent noise from a variety of sources was present in the mapped data adversely affecting the signal-to-noise ratio of the final stack, and 2) reflection events were not in-phase prior to stacking reducing the effectiveness of the stacking operation. The first problem was addressed with a variety of post-map filters. The second problem was addressed with operator-guided “residual moveout corrections”.

In this thesis I redefine the problem of the misalignment of reflection events prior to stacking as a velocity estimation issue. In all seismic imaging methods an accurate velocity model is crucial for creating optimal reflection sections. The goal of this thesis is to design and implement a velocity estimation approach suited to the specific demands of crosswell reflection imaging.

## **1.2 Importance of this research**

It is crucial to be able to predict and monitor the flow of fluids within the earth to optimally develop and produce an oil field. Complex reservoirs can be particularly difficult to handle since accurate information at a fine scale is required to adequately describe the flow properties. In this thesis I describe a technique for imaging between wells using a combined direct and reflected arrival traveltime inversion. This technique provides information within the surveyed region with a high degree of resolution and accuracy. Using direct and reflected arrival traveltimes, the locations of selected reflection horizons can be determined with an accuracy of a fraction of the seismic wavelength, only a few feet in the cases shown in the examples in this thesis. This technique provides data necessary for creating accurate crosswell reflection images too. These images provide a more detailed view of earth structure, also with resolution and accuracy on the order of a few feet.

Another element of the information extracted from the traveltime data is a velocity model consistent with both direct and reflected arrivals. Previous crosswell traveltime tomography methods have used only direct arrival traveltimes. The addition of reflected arrival traveltimes leads to several improvements: 1) it reduces the non-uniqueness of the inversion - improving accuracy, 2) improves the angular coverage within the surveyed area - increasing resolution, and 3) provides survey coverage beyond what is possible with conventional tomography. The last point can be particularly significant in field experiments. Many times wells are not drilled much deeper than the reservoir unit. This leads to poor sampling of the reservoir region when only direct arrival traveltimes are used and a corresponding poor quality image of that region. Adding reflection traveltimes eliminates this problem

These improvements are significant because they allow reservoirs to be characterized in a way, and to a degree, not possible with previous methods. Crosswell seismology offers great potential in the areas of reservoir monitoring and characterization. A number of the factors affecting fluid flow can be observed or estimated seismically: structure, lithology, fractures, porosity, and permeability. These observations are potentially the most important oil field application of any seismic imaging technique. The source of crosswell's potential comes primarily from the high frequencies which can be used effectively in the crosswell seismic experiment. High frequencies are possible because source and receiver locations lie beneath the highly attenuating weathered zone, close to the region of interest. These high frequencies, in the kilohertz range, lead to images with resolution on the order of a few feet. High frequencies, however, place strong demands on the accuracy of the velocity model required to create good reflection images. It is this point that is addressed in this thesis.

### 1.3 Imaging problem: reflector misalignment prior to stacking

Lazaratos observed that individual reflection images, each equivalent to a VSP-CDP image, were of higher resolution than the stack of those images. An analysis of the pre-stack data provides the explanation. Figure 1.1 shows two different data domains used in crosswell reflection imaging. His reflection imaging algorithm is an adaptation of the VSP-CDP transform (Wyatt and Wyatt, 1981) which maps seismic trace data on a point-by-point basis from the time-depth domain in which it is acquired to the offset-depth domain of the reflection image. Using this technique, shot and receiver gathers are transformed one by one to the image domain. The individual images resulting from the transformation can be represented as planes in a mapped data cube as shown in Figure 1.1a. To stack the data they are resorted into “Common Reflection Point”, or CRP, gathers. These gathers, shown schematically in Figure 1.1b, are in a sort domain orthogonal to the mapped images. The traces in each CRP gather correspond to a particular offset in the image domain and are stacked to create a single trace, at that offset, in the final reflection image.

An example of the problem causing the degradation in resolution by stacking is illustrated in a CRP gather shown in Figure 1.2. The CRP gather, from Lazaratos (1993), consists of downgoing *P*-wave reflections mapped from Common Receiver Gathers (CRG's) using a direct arrival traveltime tomogram as the velocity model and an assumption of horizontal reflector geometries. The common reflection point, or image offset, is 10 feet away from the source well. The coherent horizontal events in Fig. 1.2 are the downgoing *P*-wave reflections. A final image trace is created by stacking the traces shown. To achieve an optimal stack the reflection events should be lined up in the horizontal direction; this is true independent of the actual shape of the reflector. As can be seen in the CRP gather, particularly between 2700 and 2800 ft, reflection events are not aligned well. The maximum drift of the events is almost 10 ft, nearly half a wavelength. Stacking traces over the full range of receiver depths results in destructive interference and a poor final image as was observed by Lazaratos.

Lazaratos hypothesized a number of possible causes for the misalignment of reflection events in CRP gathers: an inaccurate velocity model, incorrect reflector geometries, weak velocity anisotropy, out-of-plane dips, incorrectly compensated well deviations, and/or acquisition errors. His solution to minimize the moveout of the reflection events in the CRP gathers was “residual moveout corrections”. This procedure is analogous to non-surface consistent statics found in surface seismic imaging. In this approach local statics are calculated to optimize the stacking of selected events and traces are shifted locally, up and

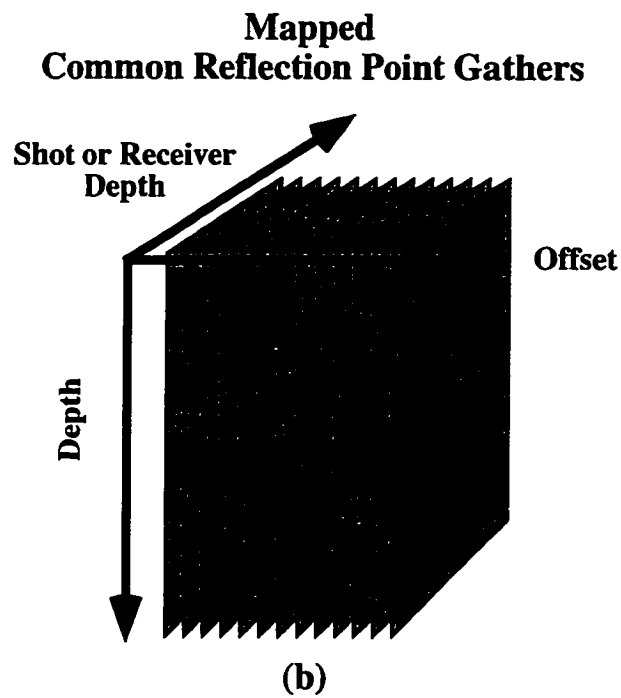
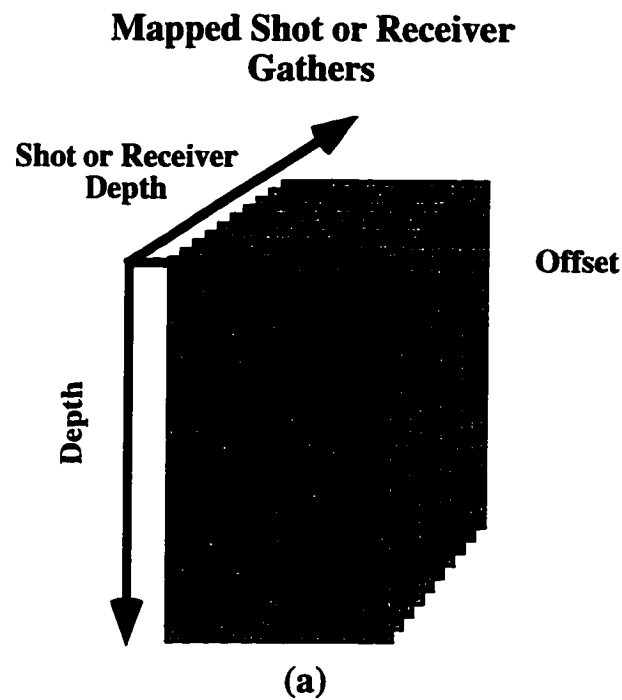


Figure 1.1: Different domains within the mapped data cube. Mapped shot or receiver gathers are represented by the slices shown in (a) above. Following the mapping transformation the mapped data cube can be resorted into Common Reflection Point (CRP) gathers represented by the slices in (b). CRP gathers are stacked to create a trace for each offset of the final image. For optimal stacking events should be aligned horizontally in the CRP domain. (after Lazaratos, 1993)



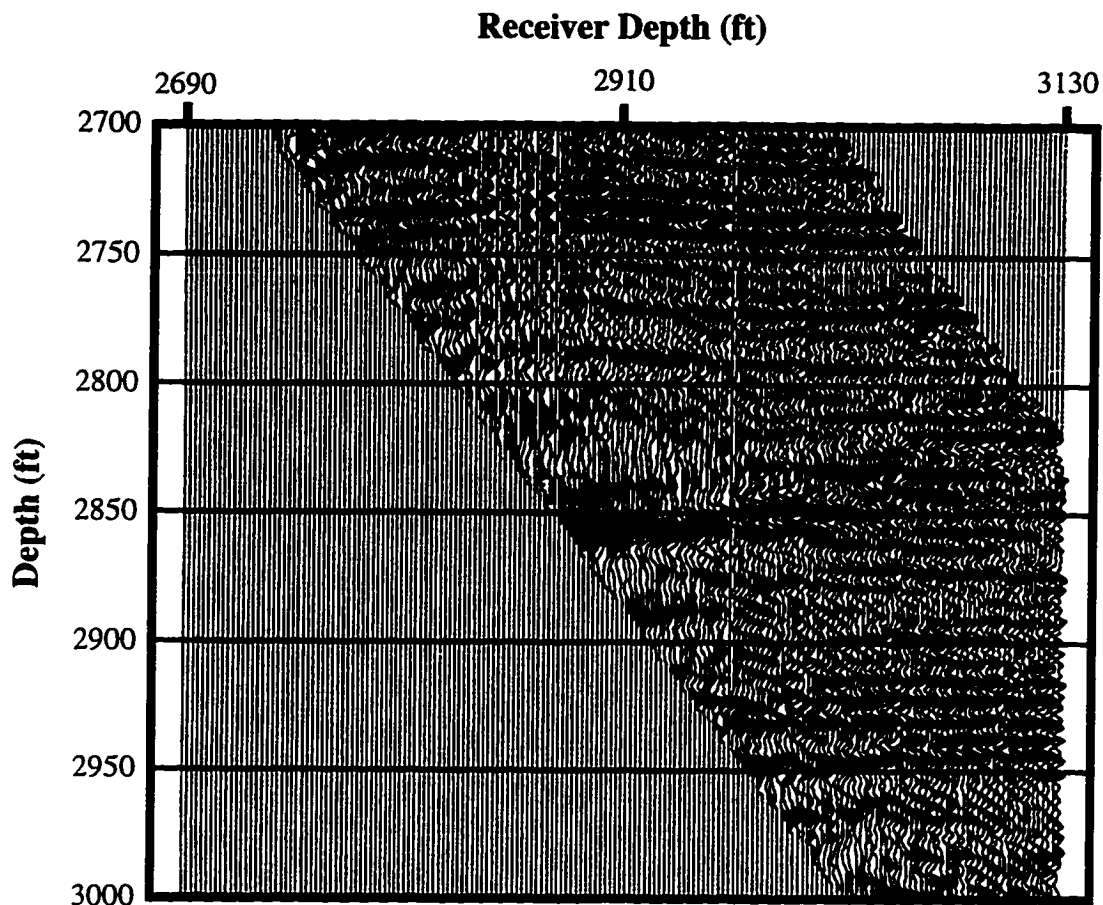


Figure 1.2: A Common Reflection Point (CRP) gather for downgoing *P*-wave reflections. This gather illustrates events with curvature which will degrade the final stacked image. Optimally events in this gather should be flat. These data were collected by Stanford University in west Texas. (after Lazaratos, 1993)

down, using these statics. While residual moveout corrections provide an improvement in the resolution of the final stack the method has a number of shortcomings: 1) it provides only vertical corrections, therefore, it is justified only when the mapping model is accurate enough to make lateral corrections insignificant, 2) the true depths of the events are not accurately preserved, and 3) the process is very labor intensive (Lazaratos, 1993).

A more direct approach for dealing with the residual moveout problem would be to avoid it in the first place by using an appropriate mapping model. In this thesis I define an “appropriate” model as one which locates reflectors accurately and obtains the best quality stack. The equivalent problem in surface seismic imaging is the velocity analysis problem for obtaining “stacking velocities”. The goal of this thesis is to develop a technique to find this model.

## 1.4 Background: velocity analysis approaches

Normal moveout is the basis of most methods for determining stacking velocities in surface seismic imaging. Velocities are chosen such that the application of NMO (normal moveout) corrections aligns the reflections in the Common Mid-Point (CMP) gathers before stacking. Reflections in crosswell data need to be aligned in CRP gathers in a similar manner. Standard surface-seismic velocity-analysis procedures define normal moveout in terms of a hyperbolic relationship between reflection traveltimes and source-receiver offsets. A different relationship is required for the crosswell acquisition geometry. This relationship is more difficult to derive since raypaths corresponding to a single reflection point may not cross the same layers (unlike the surface seismic case).

One approach to crosswell reflection velocity analysis which parallels the surface seismic method is the Common Lateral Point (CLP) method (Smalley, 1993, 1994). The CLP coordinate system allows a moveout equation to be defined for the crosswell geometry. One advantage of this method is that stacking velocities are obtained which are chosen based on the quality of the stack they produce, in the same manner as surface seismic. Yet, while the CLP method has been demonstrated successfully on field data, there are still several drawbacks:

1. a number of stacking velocity analyses may be required *for each reflector*, potentially making this technique very labor intensive,
2. there currently exists no simple relationships to convert from interval velocity to stacking velocity and back, like surface seismic,
3. this technique ignores the large amount of data present in the direct arrivals,
4. CLP imaging assumes flat reflectors which means that data will not be mapped to the correct lateral location in situations where there are dips.

In spite of these drawbacks the CLP method *does* address the problem of optimizing reflector stacking through modifications in the stacking model. The question is whether a more efficient and effective approach might be possible using a wider variety of the information present in the crosswell data set.

Another approach to velocity analysis is that of reflection traveltime tomography. This is actually a velocity *estimation* procedure rather than a velocity *analysis* procedure. The difference in semantics is because stacking velocities are obtained directly from the traveltime data using traveltime tomography. In contrast, velocity analysis methods obtain a velocity model by analyzing the stack quality for a variety of velocities. The criteria for building the velocity model is to then choose the velocities which provide the best quality stack.

Reflection traveltime tomography was originally developed to determine optimal stacking velocities for surface seismic data (Bishop et al., 1985; Stork, 1988, 1992a). Using this approach a velocity model and geometries of selected reflectors are obtained through an inversion of reflection traveltimes. The goal of the inversion is to find a velocity field and reflector depths which best fit the traveltime data in a global sense. The ability of reflection traveltimes to determine reflector depths in surface seismic reflection tomography has been studied extensively and it has been shown (Bishop et al., 1985; Bube et al., 1989; Stork, 1992b; Bube and Langan, 1995) that: 1) in general, reflector geometries are well determined if the ray coverage is sufficient and 2) the average velocity between reflectors is also determined.

Crosswell experiments have long used direct arrival traveltimes for calculating a velocity image between wells. These velocities can be used for a variety of reasons such as determining structural information, rock properties, and time-lapse imaging. Crosswell traveltime tomography and reflection imaging have, however, typically been approached as independent imaging problems. Sometimes a link between the two methods is created by using the direct arrival traveltime tomogram as the reflection imaging model (Khalil et al., 1993; Lazaratos, 1993, 1995). Unfortunately, a major shortcoming of direct arrival traveltime tomography is the non-uniqueness of the solution. Although the calculated velocity field may be consistent with the direct arrivals it is not necessarily consistent with the reflection information. If the velocity and reflector geometries model is not consistent with the reflected arrival information this will lead to the incorrect positioning of reflection events in the image space causing misalignment of those reflections in the CRP gathers, as shown in Fig. 1.2, and consequently a poor stack.

Bube and Langan (1995) have studied the velocity and reflector resolution attainable in the crosswell geometry using both direct and reflected arrival traveltime data. Their work shows that transmission and reflection tomography places reflectors in the right place *even when there are still errors in the velocity field*. This suggests that this method will provide accurate depths, since selected reflectors are located in the right place, and a minimal pre-stack misalignment of events, since the parameter being minimized, traveltime residual, is related to the CRP alignment.

The relationship between traveltime residual and the alignment of reflection events in the pre-stack image domain is relatively straightforward. A reflection event is picked by identifying the traveltime of a constant phase along an event for each trace. If the traveltime residual of a particular reflected arrival's raypath is zero then the modeled time through the inversion model from the source to the reflector and on to the receiver exactly matches the observed traveltime, represented by the time of the phase pick. In this case the phase of the

pick is located, using the imaging algorithm, exactly at the reflection point on the reflector. Traveltime residuals correspond to an event located above or below the true reflection point. So, by accurately positioning the reflector and minimizing the traveltime residuals of all rays reflecting off that reflector the events are aligned in phase.

One important distinction between crosswell reflection tomography and standard surface seismic reflection tomography comes from the availability of direct arrival traveltimes in the crosswell case. A velocity-depth ambiguity arises if ray coverage is insufficient, which often happens in surface seismic tomography for deep reflection events. This has led some surface seismic tomography researchers to advocate iterative approaches for solving the tomography problem which ignore the reflector solutions coming from the inversion. For example, in each iteration reflector locations might be obtained by picking the events from sections migrated using the previous iterations's velocity model. The new reflector geometries are used for ray tracing and redefining the inversion problem. After the solution of the new inversion problem the reflector solutions are discarded and the data are migrated again so that new reflectors locations may be picked (Stork, 1988).

The crosswell geometry and the direct arrival traveltimes available in the crosswell experiment eliminate the need for multiple iterations of picking, inversion, and migration. Each direct arrival traveltime corresponds to a reflection traveltime where the reflection point lies at the source or receiver location. So, adding direct arrival traveltimes is similar to adding reflection events with known depths at the source and receiver wells. In this case there is no velocity-depth ambiguity, which makes their contribution to the inversion one of purely velocity information. This reduces the ambiguity of the reflector depths since there is less ambiguity in the velocity field. Therefore, in the crosswell case, accurate reflector geometries are obtained simultaneously with the velocity model in a single inversion.

Reflector solutions are important in crosswell reflection imaging. The VSP-CDP mapping technique requires knowledge of both the velocity field and reflector geometries to accurately map data. Even if a migration algorithm is used for crosswell imaging, reflector geometries are still needed to evaluate the image quality (Rowbotham and Gouly, 1993). This is because image quality depends on the range of dips sampled around the local structural dip and the distribution of dip angles within that range. So, knowing the local structural dip allows the reflection image to be more accurately interpreted. For these reasons the application of reflection tomography as a velocity estimation tool for crosswell reflection imaging seems promising. It provides a velocity model *and* reflector geometry information which are both needed for reflection imaging.

## 1.5 Solution: Combined Direct and Reflected Arrival Traveltime Tomography

The approach I have developed for crosswell reflection velocity estimation is based on ray-theoretic Combined Direct and Reflected Arrival Traveltime Tomography (CDRATT). My implementation of CDRATT simultaneously inverts direct and reflected arrival traveltimes to solve for an isotropic 2-D velocity field defined by cells, and reflector geometries defined using cubic splines. The inversion results are significant and useful in two ways which are described below.

1. The 2-D velocity model obtained using CDRATT satisfies both direct and reflected arrival information. This model minimizes traveltime residuals which are related to the phase of the reflection events. This allows the reflection events to be aligned in the image domain prior to stacking.
2. CDRATT obtains reflector geometries for selected reflectors. These geometries are needed to create optimal crosswell reflection images using mapping *or* migration algorithms. They can also be used as an interpretational guide in the analysis of the final reflection image.

These features make Combined Direct and Reflected Arrival Traveltime Tomography (CDRATT) a good choice for crosswell reflection velocity estimation.

To effectively utilize the information obtained from the CDRATT inversion for reflection imaging I have developed an XSP-CDP (Crosswell Seismic Profile - Common Depth Point) mapping algorithm with a model definition consistent with the CDRATT parametrization. This allows the model results of the CDRATT inversion to be used directly in the reflection imaging procedure.

### 1.5.1 Reflection imaging using CDRATT velocity estimation

A flowchart providing an overview of the velocity estimation approach I use is shown in Figure 1.3 with the main flow of the CDRATT inversion proceeding down the left-hand-side. In this section I provide an overview of the entire reflection imaging procedure. Details of the important individual steps are presented in Chapters 2–5. An application of crosswell velocity estimation on a field data set is shown in Chapter 6.

The ability to use the CDRATT inversion as a crosswell reflection velocity estimation tool hinges on one's ability to obtain reliable traveltimes from crosswell seismic data. Acquiring these traveltimes constitutes the first steps shown in the Fig. 1.3 flowchart. Direct arrival traveltimes (*P*-waves or *S*-waves) are obtained in the standard fashion used in conventional direct arrival traveltime methods. Reflection traveltimes have required the

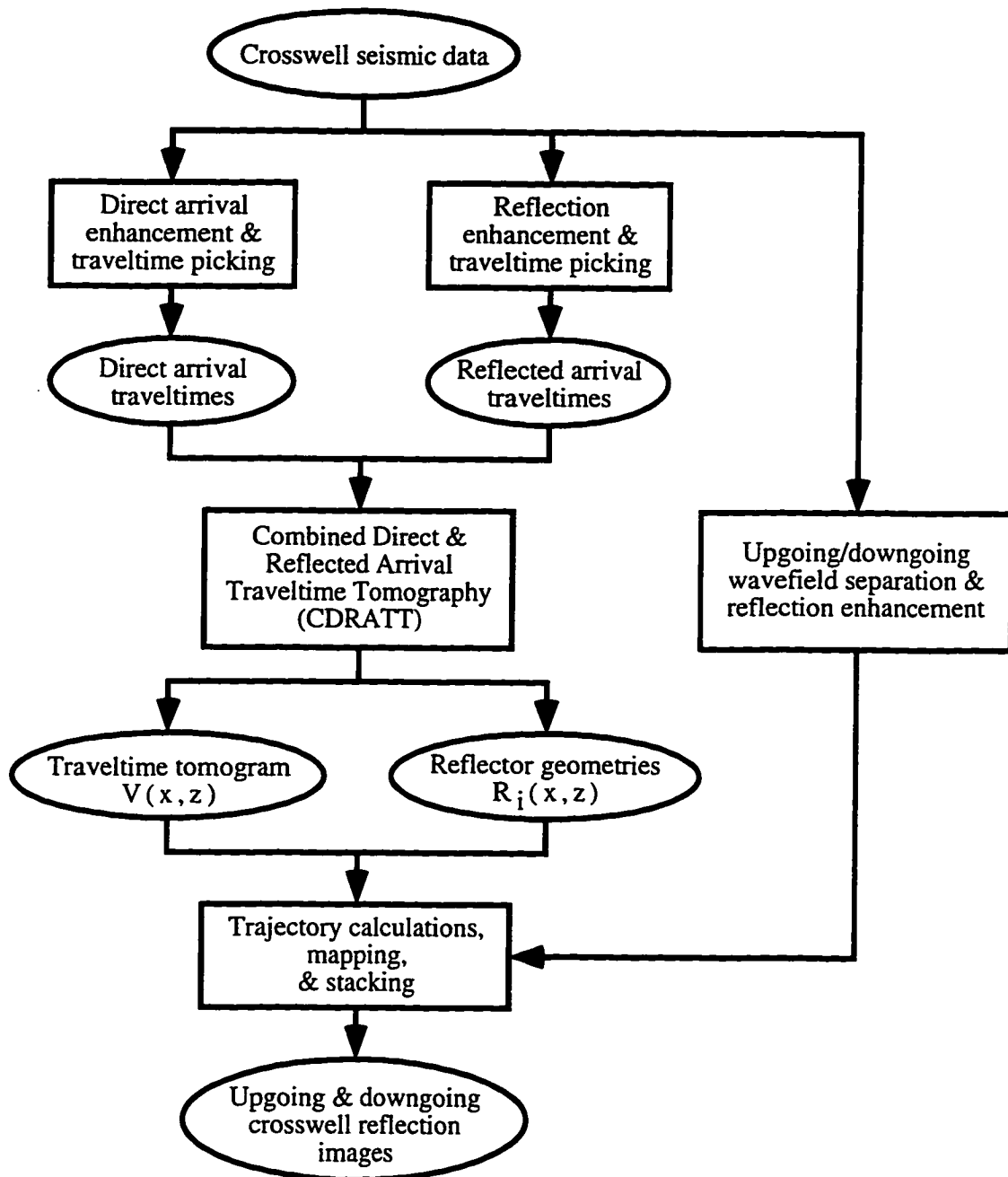


Figure 1.3: This flowchart illustrates the approach used in this thesis for integrating direct and reflected arrival information in a consistent manner. The key to this integration is the ray-theoretic CDRATT inversion. Reflections are imaged using the XSP-CDP mapping transformation. The inputs to the mapping algorithm are the tomography results: a 2-D velocity model and geometries for selected reflectors.

development of a more sophisticated approach to picking. To my knowledge, the reflection traveltimes used in this thesis are the first obtained from crosswell seismic data.

The most important step of reflection traveltime picking is the enhancement of reflection arrivals through wavefield separations and filtering. Once the crosswell data have been processed to enhance reflections individual reflection events are identified and picked. Upgoing and downgoing reflections are picked as separate events to avoid having to identify which upgoing reflections correspond to which downgoing reflections. The minimum number of reflectors processed is determined by the interpreter's ability to locate and pick them. The maximum number is limited by the size of the inversion problem which can be handled by the available hardware resources.

Once the set of direct and reflected arrival traveltimes is obtained the next step, shown in Fig. 1.3, is the CDRATT inversion. The CDRATT inversion calculates a 2-D velocity model and the geometry of each of the picked reflectors. While the inversion problem itself is non-linear and requires a number of iterations to converge on an optimal model the velocity estimation is completed in a single run of the CDRATT inversion.

Once the CDRATT inversion is completed the reflection mapping is entirely determined by the calculated velocity and reflector geometry model. The final step shown in Fig. 1.3 is reflection imaging using the CDRATT model. Upgoing and downgoing images are created separately in this step although both images are created using the same velocity model and reflector geometries. The final reflection images can be obtained by brute stacks of the mapped data. Improvements to these brute stacks can be made using procedures outlined by Lazaratos (1993) to control the range of angles used in the final stack. Crosswell data vary significantly in terms of signal-to-noise ratio and poor quality data can be effectively eliminated using filters based on incidence angle.

### 1.5.2 Strengths of CDRATT velocity estimation

CDRATT crosswell velocity estimation combines two popular ray-theoretic inversion techniques, crosswell direct arrival traveltime tomography and surface seismic reflection tomography, in a single consistent approach. Both of these techniques have been shown to be robust in field data applications. CDRATT velocity Estimation provides reflector geometry information for picked reflectors which has been obtained through an explicit calculation of reflector depths. Theoretical studies of this combined inversion (Bube and Langan, 1995) show that the calculated reflector depths are well resolved. This is the first crosswell reflection imaging method to provide reflector geometry information directly. This is important because reflector geometries are needed for optimal reflection imaging in both mapping and migration approaches (Lazaratos, 1993; Rowbotham and Goulty, 1993).

Another advantage of CDRATT velocity estimation is that the only interpretive part of the technique is the initial traveltimes picking step. Once traveltimes are picked there is no further need to repick reflection events or iterate towards reflector geometry solutions. This eliminates much of the labor-intensive event identification and picking required by the “residual statics method” (Lazaratos, 1993) and the CLP method (Smalley, 1993, 1994). The residual statics method requires that individual reflection events be picked from the stacked data for a variety of CRP gathers to calculate static corrections. In poor signal-to-noise conditions reflection events may be ambiguous making the picking difficult and inaccurate. In the CLP method, reflection events must also be aligned one by one for different image offsets through the application of NMO-like velocity corrections. This method is also sensitive to the interpreter’s ability to distinguish between noise and signal in the image domain.

Finally, while this implementation of crosswell reflection velocity estimation uses a 2-D isotropic model parameterization, the approach itself is general and can be extended to include anisotropic models. For reasons outlined in Chapter 2 I use an XSP-CDP mapping technique instead of a migration technique. This too can be modified if necessary without altering the overall velocity estimation approach.

### 1.5.3 Shortcomings of CDRATT velocity estimation

The disadvantages of the CDRATT velocity estimation approach lie primarily in the individual shortcomings of traveltimes tomography and XSP-CDP mapping. One important shortcoming is the need to pick direct and reflected arrival traveltimes. Direct arrival traveltimes picking is normally straightforward but picking reflected arrival traveltimes can be particularly difficult. The reflection traveltimes used in this thesis could be picked only after significant preprocessing of the seismic data. Preprocessing was required to improve the signal-to-noise ratio of the reflection events and make them possible to pick. While this is an important shortcoming, it exists primarily due to the current state of crosswell hardware, processing, and acquisition technology. As these evolve, obtaining reflection picks should be less difficult. In addition, the use of sophisticated seismic interpretation stations, which allow the semi-automated picking of event horizons, should ease the burden on the interpreter.

The other significant shortcomings are related to the ray-theoretic assumption inherent in CDRATT and XSP-CDP mapping. A basic limitation of ray theory is that it does not appropriately describe the actual wave propagation if heterogeneities exist in the media close to the wavelength of the experiment’s sampling frequencies. The effect this has on crosswell traveltimes tomography is that it limits the maximum resolution of the tomogram



to approximately that of the Fresnel zone width (Williamson and Worthington, 1993). For XSP-CDP mapping the ray-theoretic assumption provides a limit to lateral resolution which is also about a Fresnel zone width, although vertical resolution can still be a fraction of the effective vertical wavelength (Lazaratos, 1993).

Wave-theoretic approaches offer one means of overcoming the inadequacies of ray theory (Zhou et al., 1995). They also can reduce the non-uniqueness of the inversion problem since they use virtually the entire wavefield as data. While these theoretical advantages are substantial they are difficult to achieve in the crosswell experiment. This is due primarily to the complexity of the crosswell wavefield. Since the fundamental direction of wave propagation is parallel to formation layers, elastic effects, such as conversions, play a dominant role (Van Schaack et al., 1995). Borehole modes, such as tube waves, also can be substantial in the crosswell wavefield. Another complicating factor is that borehole coupling effects can lead to strong variations in amplitude between traces. These factors, and others, have contributed to a significant gap between theory and practical applications of wave-theoretic approaches. Further research is required to close this gap.

While the combined integration approach described in this paper is limited by the effectiveness of the ray-theoretic CDRATT and XSP-CDP transformation, the limitations of these approaches have become reasonably well understood and their effective use in field experiments has shown them to be reliable and robust when correctly applied. In the future, as wave-theoretic approaches develop into an effective way to process field data, CDRATT velocity estimation should be a useful tool for providing the accurate starting model which these techniques typically require.

## 1.6 Additional uses of CDRATT velocity estimation

In surface seismic imaging the NMO stacking velocity at a particular depth is equal to the rms (root-mean-square) velocity at that same depth (Taner and Koehler, 1969). In crosswell imaging stacking velocities can have a more fundamental meaning. Under the appropriate conditions the crosswell velocities will be equal to the interval velocities. For a model parametrization such as the one I use in the CDRATT inversion some of these conditions are:

1. the data must be adequately described by ray theory,
2. the velocity field must be isotropic,
3. the dip of any reflection events must be in the plane of the image.

If these conditions are met the stacking velocity model obtained using the CDRATT

inversion should provide an accurate map of the interval velocities within the surveyed area. This map, or velocity tomogram, is important since rock properties can often be inferred from the velocity information.

Direct arrival traveltimes tomography has been used successfully in the field for monitoring EOR steam floods (Justice et al., 1989; Paulsson et al., 1994; Mathisen et al., 1995), seismic characterization of crystalline rocks (Wong et al., 1983; Paulsson et al., 1985), and reservoir characterization (Lines et al., 1995; Langan et al., 1995). While traveltimes tomography has shown its usefulness it still has some serious limitations which result from the source-receiver coverage of the crosswell experiment.

The typical crosswell experiment has two types of coverage problems. The first coverage problem is the well studied effect of limited angular coverage (Menke, 1984; Bregman et al., 1989). The inverse Radon transform (Radon, 1917), on which traveltimes inversions are generally based, requires complete angular coverage to exactly reconstruct an object from its projections. The incomplete coverage found in the typical direct arrival traveltimes inversion results in a loss of resolution and non-uniqueness, e.g. more than one answer exists that is consistent with the direct arrival traveltimes.

The second problem results from effects of projection truncation (Rector and Washbourne, 1994). Projection truncation describes the variation of angular coverage within the surveyed area due to the limited extent of source and receivers. For example the angular coverage at the top and bottom of the surveyed area in a typical survey is restricted to nearly horizontal rays while in the middle of the survey the broadest range of angles are available. The result of this changing coverage is that the resolution of the tomogram varies spatially within the image and will tend to be poorest at the top and bottom of the surveys. This effect can restrict the usefulness of direct arrival traveltimes tomography because often the zone of interest, the reservoir, is located at the bottom of the survey (many wells are not drilled much deeper than the reservoir).

The theoretical advantages of using more of the data present in the crosswell wavefield to improve resolution and reduce non-uniqueness in the traveltimes inversion are generally agreed upon. The difficulty lies in designing a robust approach to accomplish this. One of the possible methods is adding the data available from reflection events. Part of the work of Bube and Langan (1995) included an analysis of improvements in the slowness resolution resulting from the addition of reflection arrivals to the traveltimes inversion. Their main observation was that only the depth of the reflection events was well resolved. They did find improvements in velocity resolution in the vicinity of picked reflectors though. Their speculation was that including traveltimes from a number of reflectors should provide further improvements to the slowness resolution. This increase in resolution can be

particularly important at the top and bottom edges of the image which typically suffer from artifacts due to the problem of projection truncation. So, while the main purpose of CDRATT velocity estimation is to calculate information required for reflection imaging, it can also be viewed as a method for increasing the accuracy and resolution of traveltime tomography by adding reflection traveltimes.

## **1.7 Thesis organization and overview of results**

In this chapter I have described a method for the velocity estimation of crosswell reflection data using Combined Direct and Reflected Arrival Traveltime Tomography. In Chapters 2–5, I present the theory and implementation of the CDRATT inversion and XSP-CDP mapping algorithm used in the CDRATT velocity estimation method. Finally, in Chapter 6, I provide a validation of the method by applying it to a field data set collected by Stanford University in west Texas.

### **1.7.1 Chapter 2 – Crosswell seismic reflection imaging**

In the first part of Chapter 2 I discuss the concepts of crosswell reflection imaging and provide a review of the two basic approaches, mapping and migration. I have chosen to use the XSP-CDP mapping technique in this thesis. The XSP-CDP mapping technique has been shown to be an efficient, accurate, and robust technique for processing field data. While, in general, migration offers a number of theoretical advantages, in practice these advantages prove to be less significant in the crosswell experiment. This is due primarily to the limited angular coverage resulting from the crosswell geometry and the sensitivity of migration to noisy data.

I describe a general approach for determining mapping trajectories over a range of model complexities: from homogeneous velocities with flat reflectors, to general 2-D velocity distributions with dipping/curved reflectors. This approach is based on wavefronts and combined traveltime maps. The importance of this approach is that it is the basis of a fast and efficient technique of calculating mapping trajectories in general models. This technique is described in detail in Chapter 3.

Finally, I discuss the advantages and disadvantages of mapping data in the various domains which are available in the typical crosswell data set. Common Mid-Depth Gathers (CMG's) offer advantages over the frequently used Common Receiver Gathers and Common Shot Gathers (CRG's and CSG's). This is primarily because the density and distribution of mapping trajectories of a CMG in the image domain is the most uniform. This allows events in each mapped gather to be imaged with less chance of spatial aliasing.

### **1.7.2 Chapter 3 – A fast approach for calculating XSP-CDP mapping trajectories in a general 2-D media**

In Chapter 3 I describe a new approach for calculating XSP-CDP mapping trajectories in general 2-D media based on wavefronts and combined traveltime maps. One important feature of this wavefront approach is that the reflection point for a source-receiver-reflector combination is defined by the point along the reflector interface where the combined traveltime is stationary, e.g. a minimum or maximum value. This simple definition is allowed as a result of a fundamental assumption made in XSP-CDP mapping that states that there is at most one reflection point for each source-receiver-reflector combination. This assumption is fairly realistic in crosswell surveys acquired in oil fields since most reflector geometries are relatively simple at the scale of 200–600 ft.

I have implemented the combined traveltime XSP-CDP mapping approach in a way which is consistent with the parameterization used in the CDRATT inversion described in Chapter 4. While I use an isotropic velocity model for all work done in this thesis the combined traveltime map trajectory calculation can be extended in a straightforward manner to more complex anisotropic velocity models. The majority of the implementation itself is unaffected by this modification. Only the algorithm used to generate traveltime maps need be modified to incorporate the new model definition.

### **1.7.3 Chapter 4 – Traveltime tomography using direct and reflected arrivals: theory & implementation**

In Chapter 4 I provide a description of the theory and my implementation of Combined Direct and Reflected Arrival Traveltime Tomography (CDRATT). The choice of CDRATT as the computational tool is based, in part, on the success of ray-theoretic direct arrival traveltime tomography. Skeletonizing the data to a set of direct and reflected arrival picks allows an inversion to be designed which focuses on the desired events. In addition, the use of traveltime data significantly reduces the size of the data set to be considered when compared to full waveform methods.

I parameterize the 2-D isotropic velocity model using cells. The reflectors are defined using cubic splines. The solution of the parameters is obtained through a series of linearized steps which solve the non-linear traveltime inversion problem. This is accomplished using the Gauss-Newton approach. Regularization is added to the inverse problem in the form of smoothing penalty terms: first derivative penalty terms are used to regularize the vertical and horizontal slowness while a second derivative penalty term is used for the reflector parameters. The optimal penalty term weights are obtained by solving the inverse problem

repeatedly in a series of continuation steps. Penalty weights are initialized with a strong weight compared to the data in the first iteration and the inverse problem is solved. In each subsequent continuation step the weights of the penalty terms are decreased and the inverse problem is solved again using the result of the previous continuation step as the starting model. In this way the solutions evolve from smooth results dominated by the penalty terms to higher resolution results dominated by the data.

#### **1.7.4 Chapter 5 – Traveltime tomography using direct and reflected arrivals: examples**

In Chapter 5 I present the results of several CDRATT inversions of synthetic ray-theoretic traveltime data to provide a validation of the CDRATT algorithm. Two of the synthetic examples test the ability of the CDRATT inversion to accurately recover reflector geometries, in particular, curved reflectors and discontinuous reflectors. The third study is based on an actual field data set's acquisition parameters. Synthetic traveltimes are calculated through a model based on the field geology. The purpose of this example is to provide a guide for the processing and interpretation of the field data set which is presented in Chapter 6.

The Chapter 5 data sets were created using a ray-theoretic eikonal code. The examples were designed in part to test the theoretical predictions of the accuracy of the calculated reflector depths. The predictions, based on the acquisition geometries of the 1991 and 1993 McElroy Reservoir Geosciences Project (MRGP) surveys, were that reflector depths could be recovered with an accuracy of about 0.5 ft for the ~180 ft offset survey and about 2.5 ft for the ~600 ft offset. These predictions were confirmed in the synthetic surveys. A second prediction was that good resolution of reflector depths could be expected in spite of mediocre velocity resolution. This prediction was also supported by the results of these inversions.

#### **1.7.5 Chapter 6 – Case study**

In Chapter 6 I test the effectiveness of CDRATT velocity estimation using a field data set collected by Stanford University from an experiment site in west Texas. The data are high quality which allow accurate wavefield separation and reflection processing. This processing is necessary to obtain accurate reflection traveltimes picks that are required in the CDRATT inversion. Direct arrival traveltime picks are obtained in a traditional manner. In the Chapter 6 example, *S*-wave direct and reflected arrivals are used for inversion and mapping. *S*-waves were chosen for this study primarily due to the higher signal-to-noise

ratio of these events in the crosswell data set.

A variety of traveltimes inversions are performed on the Mc68-02b data set. The first two inversions are 1-D and 2-D direct arrival only (DAO) inversions used as a reference against which to compare the CDRATT results. Next, a study is performed to determine the optimal parametrization of the reflectors in the CDRATT inversion. For the Mc68-02b data set defining each reflector with 11 nodes is judged to be an optimal balance between allowing complexity and maintaining a stable inversion. From the inversions results the CDRATT model provides the best representation of the average well log velocities and substantially less edge artifacts than the 2-D DAO velocity model.

Following the study of the CDRATT results the effectiveness of the CDRATT model for reflection imaging is confirmed. The quality of the “brute” stacks is quite high with reflector wavelengths of 5-10 ft. These stacks are improved by filtering in the Amplitude Versus Angle domain (Lazaratos, 1993) to remove noise, wavelet stretch, and provide a more stationary wavelet. Following this the CDRATT, 1-D and 2-D DAO models are used to image the reflection data providing a comparison of the relative effectiveness of each as a reflection imaging model. The moveout of the reflection events in the AVA domain is minimal using the CDRATT model. This provides a better quality stack those obtained from the other models where the moveout of events in the AVA domain is greater.

The maximum difference in the reflection images obtained using the CDRATT and DAO models is seen near the top edge of the downgoing stacks. Using the DAO models “residual moveouts” of up to 5 ft are present which are shown to have a deleterious effect on the final stack. Finally, the importance of the mapping model is emphasized by mapping and stacking completely unprocessed data to obtain a good quality stack. The unprocessed-data limited-angle stacks actually contain higher frequency information (spatially) than the stacks produced using the processed data. This suggests that improvements need to be made in wavefield separation and reflection enhancement routines.

Overall this thesis shows that CDRATT velocity estimation is effective at obtaining imaging models, consisting of a velocity image and reflector geometries, suitable for high-resolution crosswell reflection imaging. In addition, under the conditions of the west Texas field experiment, CDRATT produced a superior velocity tomogram with less artifacts and a better correlation with well logs.

## **CHAPTER 2**

# **CROSSWELL SEISMIC REFLECTION IMAGING**

## **2.1 Introduction**

Crosswell seismic reflection imaging followed very quickly in the footsteps of VSP (vertical seismic profile) imaging technology. Wyatt and Wyatt (1981) provided the first description of how reflecting horizons could be imaged with offset VSP data. Their observation, simplified using horizontal reflectors and a 1-D velocity field, was that reflections occur from points intermediate (in offset) to the source and receiver locations. Using this simplification they described an imaging procedure, the “VSP-CDP stack”, which could be used to convert time-depth seismic data to an offset-depth reflection image similar to depth migrated surface seismic sections. Soon after, Dillon and Thomson (1984) published a comprehensive study of the ways the subsurface could be illuminated for a wide variety of VSP acquisitions geometries including: offset source, walkaway, and deviated well. They also used the VSP-CDP imaging approach. Almost simultaneously, Baker and Harris (1984) extended the concept of VSP-CDP imaging to include the crosswell acquisition geometry and created one of the first crosswell reflection images.

Although crosswell reflection imaging was introduced and demonstrated soon after crosswell data acquisition became feasible, the majority of crosswell imaging research has been directed towards traveltime tomography. Standard traveltime tomography uses the traveltimes of the direct arrival seismic energy and inverts these data using mathematical algorithms similar to those used to process medical CAT scans. The attraction of traveltime tomography is that identifying and collecting direct arrival traveltimes is relatively straightforward which allows imaging research to focus on the inversion problem itself. While crosswell traveltime inversion is far from trivial it is fundamentally a mathematical problem which can be attacked using well known inversion concepts.

Even though much of the early research in crosswell imaging focused on traveltime tomography, progress was still made in the area of crosswell reflection imaging. Two early papers provided a second direction to crosswell reflection imaging by introducing crosswell migration. Zhu and McMechan (1988) and Hu, McMechan, and Harris (1988) demonstrated the use of acoustic prestack finite-difference reverse-time migration on both synthetic and scale-model examples. Following these papers, research in reflection imaging has been relatively evenly divided between work which advocates a mapping-based approach: Delvaux et al. (1987), Iverson (1988), Abdalla et al. (1990), Goultly et al.

(1990), Smalley and Harris (1992), Lazaratos et al. (1993), and Lazaratos et al. (1995), and work performed which advocates a migration-based approach: Beydoun et al., (1989), Findlay et al. (1991), Rowbotham and Goult (1993), Mo and Harris (1993), Qin and Schuster (1993), and Tura et al. (1994)

I have chosen to use a variation of the VSP-CDP imaging method for my integrated approach to crosswell velocity and reflection imaging. At the beginning of this chapter I discuss the reasons behind this choice. First I provide reviews of the VSP-CDP transformation and the migration technique as applied to the imaging of crosswell seismic data. Following these reviews I discuss the pros and cons of each of the techniques in the imaging of crosswell reflection data and justify my choice of the mapping approach. Next, I introduce a conceptual approach for defining mapping trajectories. I use this approach to describe how mapping trajectories are calculated in increasingly complex models. The description of this conceptual approach is important because it is used as the basis of a fast and general mapping algorithm which I introduce in Chapter 3. Finally, I discuss issues of imaging crosswell seismic data from the different sort domains: common shot, common receiver, common mid-depth and common offset.

## 2.2 Mapping versus migration

The goal of crosswell reflection imaging algorithms is to convert crosswell seismic reflection data from the time-depth domain in which it is acquired to an offset-depth domain in which the structural information present in the data can be more easily interpreted. Two methods of accomplishing this are mapping transformations, such as the VSP-CDP transformation (Wyatt and Wyatt, 1981), and migration, such as prestack finite-differences reverse-time migration (Hu, McMechan, and Harris, 1988). Both of these approaches have been successfully applied to field data.

In a full aperture migration time-data values are spread around the entire migration ellipse. In a process known as limited aperture migration time-data values are spread only over the portions of the migration ellipse which correspond to a defined range of reflector dips. Taking this to its limit mapping can be viewed as a form of limited aperture migration where the aperture corresponds to just a single dip, this is sometimes referred to as “zero aperture migration”. Mapped and migrated images are almost identical when the aperture of the migration operator is limited to the dips used in a VSP-CDP transformation (Wiggins et al., 1986).

In my work I have adopted the approach of the VSP-CDP transformation for imaging crosswell reflection data. This is done for reasons that are related to the particulars of the



acquisition and geometry of the crosswell experiment. To understand these reasons I review the basics of mapping and migration in the next section. Following this, I compare their strengths and weaknesses when applied to crosswell reflection imaging and justify my choice of XSP-CDP mapping for the examples shown in this thesis.

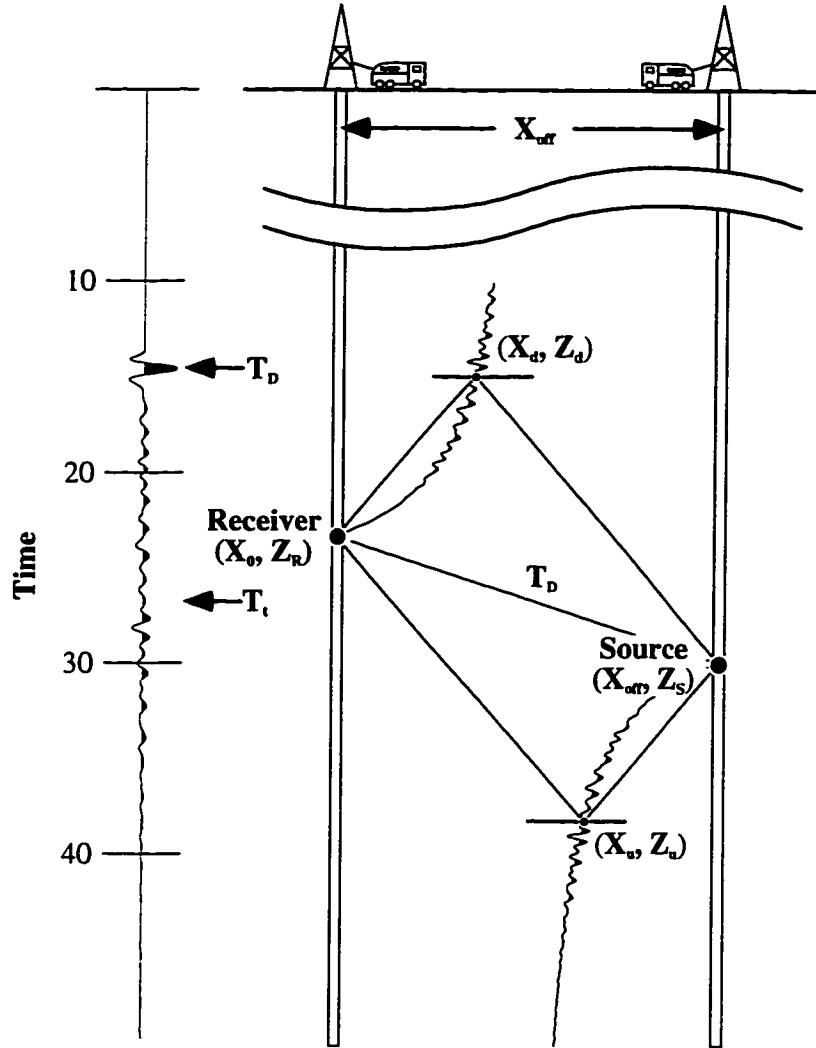
### 2.2.1 The XSP-CDP mapping transformation

The VSP-CDP mapping algorithm, introduced by Wyatt and Wyatt (1981), is an approach which allows Offset Vertical Seismic Profile data recorded in the time-depth domain to be transformed to the offset-depth image domain. The basics of VSP-CDP mapping are applicable to the crosswell case with one important difference. One of the fundamental assumptions in VSP-CDP mapping is that each datum value in the seismic trace maps to a unique point in the offset-depth image domain. The crosswell experiment allows the possibility of imaging both upgoing reflections *and* downgoing reflections so each datum value in the seismic trace maps to *two* points in the image domain. This important difference between the methods has prompted researchers to use the designation of XSP-CDP (Crosswell Seismic Profile - Common Depth Point) mapping for the VSP-CDP mapping approach modified for the crosswell case. I will use this nomenclature in my discussion of crosswell imaging although typically upgoing and downgoing reflections are imaged in two separate steps, each similar to the VSP-CDP method.

Figure 2.1 provides an illustration of the XSP-CDP transformation concept. The fundamental principle of the XSP-CDP mapping technique is that each time element of a seismic trace, beginning with the direct arrival, is mapped to two potential reflection points, one pertaining to a downgoing reflection and the other to an upgoing reflection. In essence, each seismic trace is spread along the upgoing and downgoing trajectories of the corresponding source-receiver pair. A crosswell reflection image is created by mapping traces from an entire gather and imaging them simultaneously. From the mapped image reflection interfaces can be identified as coherent events.

To illustrate the XSP-CDP mapping procedure I have computed a synthetic shot gather using a simple velocity model and reflector geometries. Figures 2.2 shows seismic trace data from a single source location produced in a computer simulation with a typical crosswell experiment geometry. In this simulation wells are 200 ft apart and receivers range over a 500 ft interval, 2650–3150, every 2.5 ft. The source depth is 2800 ft. For simplicity the data were calculated using an acoustic algorithm with a constant velocity model of 17,850 ft/s and horizontal reflectors defined by changes in density.

Figure 2.3 shows the XSP-CDP transformed seismic trace data. In this case the trace amplitude data have been spread along the mapping trajectories in the same manner as in



$$C = \sqrt{(T_t V)^2 - X_{\text{off}}^2}$$

$$X_u = \frac{X_{\text{off}}}{2} \left( \frac{C - Z_{\text{off}}}{C} \right)$$

$$X_d = \frac{X_{\text{off}}}{2} \left( \frac{C + Z_{\text{off}}}{C} \right)$$

$$Z_{\text{off}} = Z_R - Z_S$$

$$Z_u = \frac{1}{2}(Z_R + Z_S + C)$$

$$Z_d = \frac{1}{2}(Z_R + Z_S - C)$$

Figure 2.1: Basics of the XSP-CDP mapping transformation. As seen in this figure, points from the crosswell seismic trace (following the direct arrival) are mapped to two locations, one a downgoing reflection point and the other an upgoing reflection point. Knowledge of the velocity field and reflector orientations is required to determine these points.

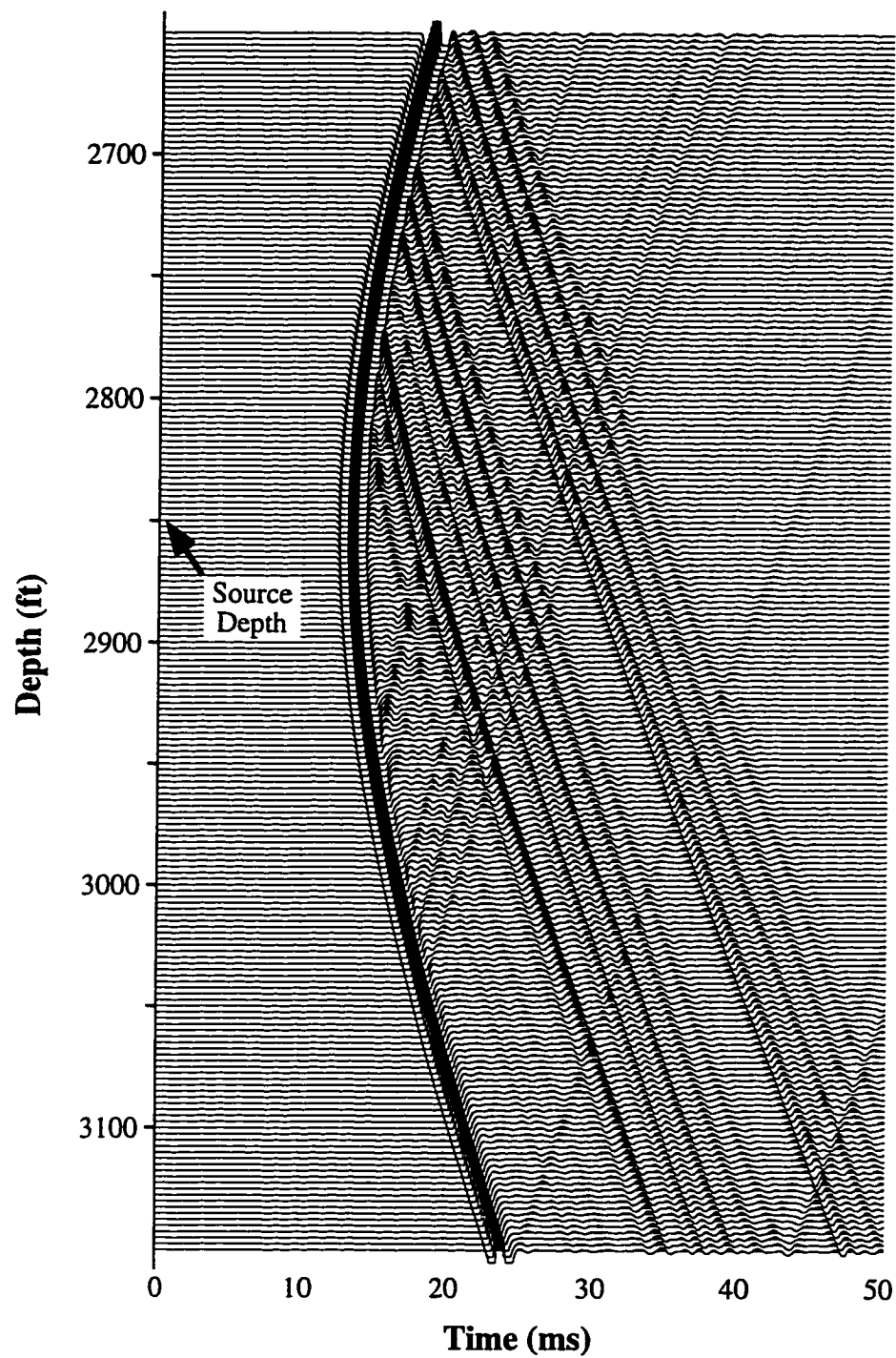


Figure 2.2: A crosswell shot gather simulation. The model is constant velocity, 15000 ft/s, with horizontal reflectors defined by density contrasts. The data were calculated using an acoustic finite-differences algorithm. Receiver locations range in depth from 2650–3150 ft, every 2.5 ft. The source, 200 ft offset from the receiver “well” is located at 2800 ft.

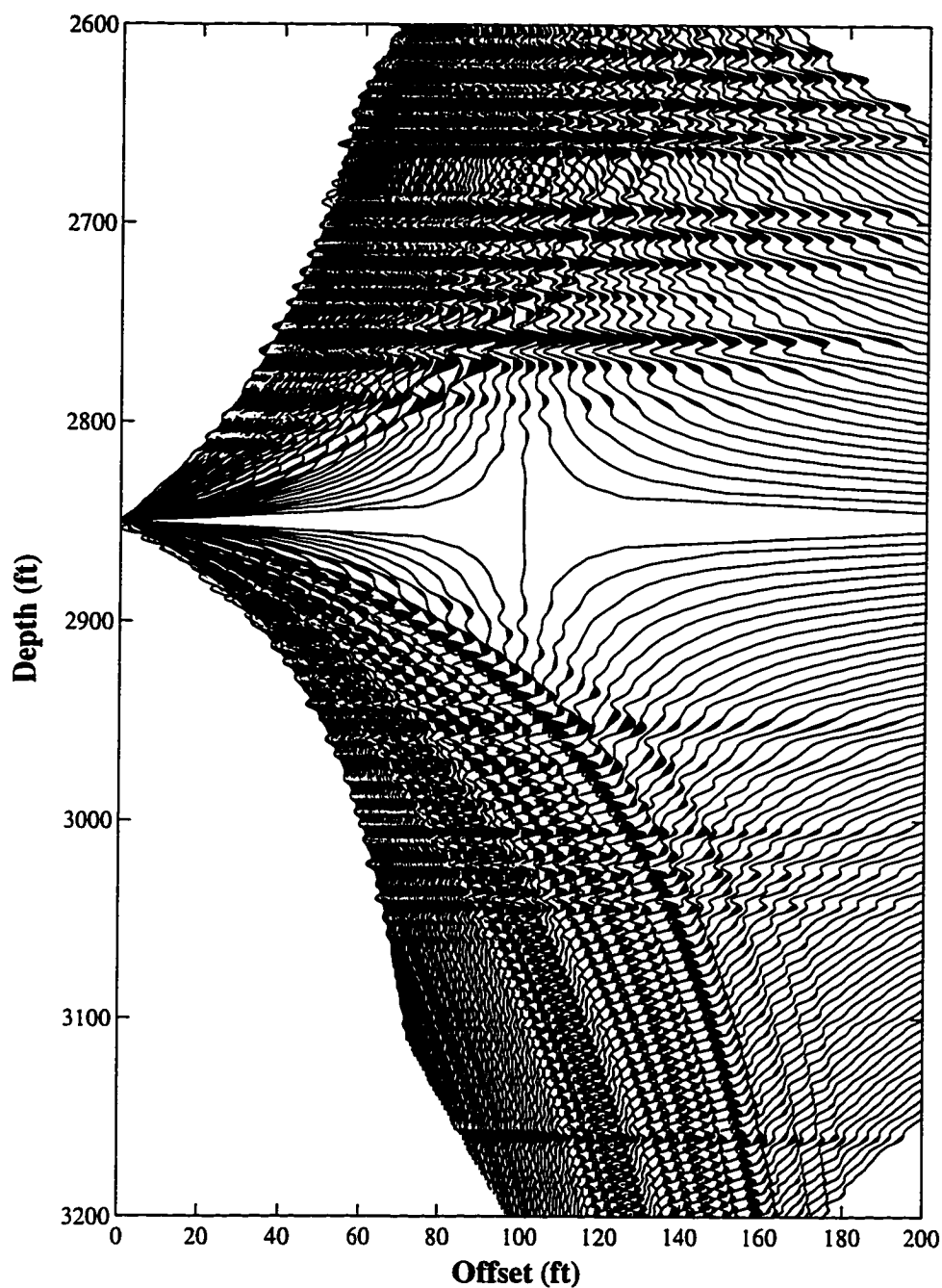


Figure 2.3: This is one method of displaying data mapped using the XSP-CDP transformation. The mapped data come from the shot gather simulation shown in Fig. 2.2. The events moving out steeply away from the source are a consequence of the XSP-CDP transformation mapping each seismic datum value to two spatial locations. The dipping events above the source are upgoing reflections imaged with the downgoing trajectories and vice versa. This illustrates the importance of upgoing/downgoing wavefield separation for optimal imaging.

Fig. 2.1. The data were transformed using the correct velocity and reflector information so the XSP-CDP transformation maps events to their correct spatial locations. While the imaging method shown in Fig. 2.3 is useful for illustrating the concept of the XSP-CDP transformation it is not very useful for crosswell imaging. The primary drawbacks are that images from different gathers can not be stacked to create multi-fold images and the mapped data cannot be post-processed in the image domain. Multi-fold imaging and post transformation filtering are crucial for optimizing signal-to-noise ratio in crosswell images (Lazaratos, 1993).

The most common method used to image the transformed data is with traces evenly sampled in offset and depth. This allows images from different gathers to be stacked together. Resampling is typically accomplished by binning the transformed trace data during the mapping procedure and interpolating between the bins in the horizontal and vertical dimensions. Following this, the interpolated data are sampled evenly to create the final seismic image (Lazaratos, 1993). An example of this procedure applied to the gather shown in Fig. 2.2 is illustrated in Figure 2.4. I have included an upgoing and downgoing imaged trace from Fig. 2.3 to aid in the comparison of the two imaging techniques. Additional details of the interpolation scheme are discussed in Section 2.4.

The mapped gather shown in Figure 2.4 highlights several important points about XSP-CDP imaging. 1) Unlike traditional VSP-CDP imaging the XSP-CDP transformation images reflectors below and *above* the source point. 2) Reflections outside the acquisition geometry, e.g. above 2650 ft and below 3150 ft, can be imaged. 3) Horizontal reflectors are readily apparent in Fig. 2.4 but so are other events curving upwards and downwards from the source location. Events curving up above the source depth are upgoing reflections and events curving down below the source depth are downgoing reflections. Since data in each trace are mapped to two points in the XSP-CDP transformation, events that map correctly in one part of the image, a downgoing event for example, will show up as coherent noise when mapped along the trajectories calculated to map upgoing events. In other words, when imaging reflections from one direction, the reflections coming from the other direction map as noise. This illustrates one reason why wavefield separation is needed in creating reflection images with the highest possible signal-to-noise ratio.

As will be shown later, the model used in the XSP-CDP mapping is of primary importance in obtaining optimal crosswell reflection images. Models consisting of a homogeneous velocity and flat reflectors are often too simple to obtain adequate imaging results in field data applications. In simple layered geologies the mapping trajectories can be calculated using a 1-D velocity model with the assumption of horizontal interfaces (Dillon and Thomson, 1984). If 2-D velocity and/or reflector geometries are present a 1-D

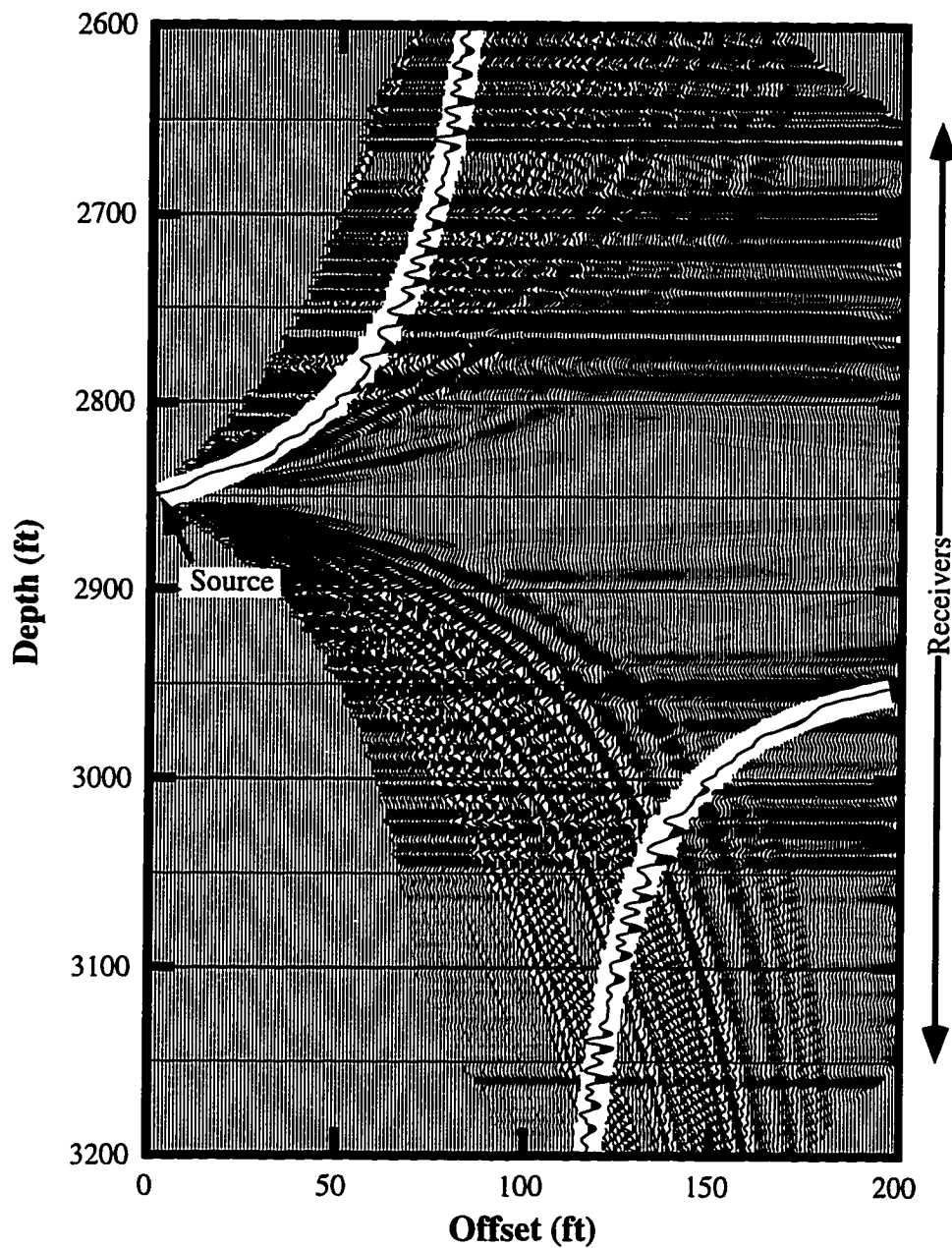


Figure 2.4: A crosswell shot gather simulation, from Fig. 2.2, mapped using a conventional imaging technique. Compare this display with that shown in Fig. 2.3. A trace from that display is included to aid this comparison. The primary advantage of this format is that the mapped data can be further processed before and after stacking with other mapped gathers to improve the signal-to-noise level.

assumption will map reflections to the incorrect offset-depth location. To avoid this problem in VSP-CDP imaging, mapping algorithms have been developed which calculate mapping trajectories using a 2-D model of velocity and reflector geometries (Cassell et al., 1984).

### **2.2.2 Crosswell seismic migration**

The primary difference between mapping transformations and migration is that mapping transformations assume that each time-data value of the seismic trace results from a reflection at a unique offset-depth location while migration algorithms allow that each time-data value can come from an infinite number of offset-depth locations. In the migration approach each time-data value is, in essence, positioned at all these locations simultaneously. While there are an infinite number of possible reflection points all these points lie on an isochron, sometimes referred to as the “migration ellipse” or “migration operator”, which is defined by the source and receiver locations and a velocity model. The offset-depth reflection image is created by adding, or “stacking”, the migrated images for a number of source-receiver combinations. At points where a reflection actually occurs the time-data values of that reflection add constructively. The time-data values destructively interfere in locations where no reflection is present. In this manner migration is capable of imaging more than one dip at each offset-depth location.

### **2.2.3 Mapping versus migration in crosswell reflection imaging**

The main advantage of migration imaging in the general case is that previous knowledge of reflector dips is not required and more than one dip can be imaged at an offset-depth location. There are, however, several aspects of the crosswell experiment which suggest that mapping techniques may be more robust in creating crosswell reflection images. To justify my decision to use mapping instead of migration to image reflections the performance of each approach will be discussed in the context of the crosswell experiment. Important points about several discriminating factors must be addressed:

1. migration can correctly image reflectors when dip information is not known,
2. incorrect reflector geometries may lead to mispositioned reflectors in mapping approaches,
3. migration can handle more than one dip at each location while mapping can image only one dip at each image location,

4. migration algorithms spread noise in the offset-depth image domain while in mapping approaches noise which is coherent in the time-depth domain will remain coherent after transformation to the offset-depth domain,
5. computational requirements of migration techniques are higher than mapping techniques.

**Point 1: Migration can correctly image reflectors without dip information.**

In the general case both migration and mapping require an accurate velocity model to correctly image reflections but migration does not need the information on reflector geometries that mapping algorithms require. Unfortunately the limited illumination of reflection events which results from the crosswell acquisition geometry affects the ability of migration to create satisfactory images without some reflector information. The quality of the migrated seismic reflection image depends on the distribution of dips sampled at each point. Optimally focused migrated images should include dips of  $\pm 15^\circ$  relative to the local structural dip (Rowbotham and Goult, 1993). If the local structural dip does not lie within the sample range then the image is smeared into the familiar, characteristic migration “smiles” (Carrion, Sato, and Buono, 1991).

Migration *can* be adapted to use whatever dip information is available in a limited aperture migration. This will reduce the artifacts which arise from limited illumination but if the dip of the event lies outside of the defined range it will not appear correctly located in the migrated image (Wiggins et al., 1986). The important point is that in order to obtain satisfactory migrated images in crosswell reflection imaging the reflector geometries *do* need to be known even if a  $\pm 15^\circ$  aperture is available. This means that the requirements and performance of mapping and migration are more similar in the crosswell experiment than in surface seismic imaging.

**Point 2: Incorrect reflector geometries misposition reflectors in mapping approaches.**

Although crosswell reflection imaging using migration requires some reflector dip information to produce optimal images the reflectors can still be correctly located even if this information is not exact. Mapping, however, will misposition reflectors if the reflector dip information is not correct. Lazaratos (1993) studied the magnitude and nature of this error for the crosswell experiment. Although Lazaratos used horizontal reflectors in his study of the magnitude of the horizontal and vertical mispositioning caused by dipping reflectors his findings provide an indication of the magnitude of the errors when the dip of a dipping reflector is estimated incorrectly. He also used a homogeneous velocity function (and hence straight raypaths) in his study. His findings for reflections dipping in the plane of the crosswell experiment are summarized in the following list.



1. The mispositioning of dipping events (when the reflector is assumed horizontal) is proportional to the interwell distance.
2. For a given dip the mispositioning depends on the apparent angle of incidence (with respect to the assumed horizontal reflector). In general the errors increase with increasing angle of incidence.
3. When the velocity field correctly predicts the first arrivals of the seismic energy there is no error in the vertical and horizontal position of the imaged reflector at the wells. This is because a reflection and direct arrival traveltimes are identical where the reflector intersects the well.
4. For a dip error of  $\pm 10^\circ$  the maximum vertical mispositioning is on the order of 2 percent of the interwell distance while the maximum horizontal mispositioning is on the order of 20 percent of the interwell distance.

Mapping will correctly position events when the reflector geometry is known for the events. Since reflection events will always be correctly positioned at the wells (given the correct velocity model), and the vertical and lateral mispositioning is a function of interwell offset, the mispositioning of events between the wells manifests itself as a distortion in the reflector geometry. This distortion will act to make linear reflection events slightly curved. The amount of distortion is relatively small for dip errors of less than approximately  $\pm 10^\circ$  (Lazaratos, 1993). So, if the dip of the reflection events is known to the accuracy required to produce optimal images using the migration technique ( $\pm 15^\circ$ ) a reflection image obtained using a mapping technique should also be relatively accurate.

**Point 3: Migration can simultaneously image multiple dips.**

Migration can handle more than one dip at each location while, in typical applications, mapping can image only one dip at a time. Conceptually mapping *can* be used to image multiple dips at a single location if necessary. This can be accomplished using multiple passes of the mapping program with different reflector geometries to account for each of the dips to be considered. These images would then be added to create a single image of the complex interwell structure. This technique, however, is seldom used in practical applications of the mapping approach.

In surface seismic imaging the ability to image multiple dips at a single location can be significant where, for instance, fault plane reflections or salt dome contacts may exist at dip angles significantly different than the dips of local formations. In typical applications of crosswell reflection imaging to oilfield reservoirs the capability of migration to image simultaneously more than one dip at each location has less consequence. This is true for several reasons. The first reason is related to the observation, stated above, that a knowledge of the local reflector geometries should be known to about  $\pm 15^\circ$  to produce an optimally focused migrated image. Therefore the ability of migration to image more than

one dip at a single location is limited to instances where the dips fall within the 30° degree range of this estimate. If the dips of the reflections vary by much more than this migration will not be any more effective than mapping in imaging the multiple dips.

The second reason that makes using mapping techniques less of a problem is that the ability to image several dipping events at a single location is not always necessary in the geologic structures where crosswell imaging is used. Common applications of crosswell imaging are oilfield reservoir characterization and reservoir monitoring. In many large oilfields where crosswell imaging is used, complex structural variations are not present. It is precisely this lack of significant structural complexity that produces the large field in the first place. Although geologic structures may not be complex the information provided by crosswell reflection images can still be important. The crosswell reflection images can provide stratigraphic information at a scale that can not be seen in surface seismic or VSP imaging. Also, crosswell reflection images can provide information to correlate the tops and bottoms of formations between wells. These correlations are often ambiguous when the only information present is well log data.

In conclusion, the ability of migration to image more than one dip in space at a time is restricted in the crosswell experiment. This is a result of the narrow aperture of illumination of reflection events which necessitates the use of limited aperture migration to create optimally focused images. In addition, in many crosswell applications the ability to image more than one dip simultaneously is not needed. This is another area where the performance of mapping and migration is more similar than in the surface seismic case due to limitations imposed by the crosswell geometry.

#### **Point 4: Migration spreads noise in the image domain.**

Migration is sensitive to noise in the data. This noise can take many forms in crosswell seismic data, being either random or coherent. Coherent noise may result from wave modes not accounted for by the migration scheme used, such as elastic modes in an acoustic migration, or tube waves. Wavefield separation techniques can be used to minimize coherent noise prior to migration by separating the desired reflections from the total wavefield (Rector et al., 1994; Rowbotham and Goult, 1994). Still, migration routines spread remnant noise over the aperture of the migration operator. A single noise spike can be spread over three quarters of a migrated image when attempting to image reflections with a dip as mild as 15° making noise identification ambiguous in the image domain. Since mapping is a point to point transformation noise is not spread over the image as it is in migration. This better preserves the appearance of the data and makes misinterpretation

of smeared noise events as reflections less likely (Lazaratos, 1993). Also, noise which is coherent after mapping, can still be removed, potentially, using post-map filters.

**Point 5: Migration is more costly than mapping.**

Most of the points presented above show that migration still provides advantages over mapping although these advantages are not as significant in the crosswell reflection imaging as in surface seismic imaging. One area where mapping shows a clear advantage over migration is in cost, e.g. computer time. Since mapping is simply a point to point transformation it is relatively inexpensive in computational costs. Migration algorithms vary greatly in their complexity but a simple Kirchhoff migration of crosswell seismic data may take an order of magnitude more time to perform than mapping.

## **2.2.4 Summary of the mapping and migration comparison**

In this section, Section 2.2, I have compared and contrasted the use of migration and mapping techniques for crosswell seismic imaging. While migration techniques provide advantages over mapping in a number of areas these advantages are less significant in the crosswell experiment. In addition, mapping techniques are superior for imaging noisy data and are computationally less expensive. For these reasons I have chosen to use mapping, specifically the XSP-CDP mapping method, in my imaging method following CDRATT velocity estimation. There will certainly be situations where migration, due to its advantages, will be necessary to successfully image complex geologic structure in the crosswell experiment. In these cases the CDRATT velocity estimation approach is still valid for obtaining structural and velocity information required for the migration of the data. Wiggins et al. (1986) described a two step approach of VSP-CDP imaging followed by migration for cases where the benefits of migration are needed.

## **2.3 XSP-CDP mapping in complex media**

In the next few sections I will review the concepts behind calculating individual mapping trajectories for increasingly complex models: 1-D velocity and reflectors, 1-D velocity and 2-D reflectors, and finally 2-D velocity and reflectors. Following this I will show how these trajectories are used to create the offset-depth seismic reflection image. The purpose of this review is to provide a background for the introduction of a new mapping approach, described in Chapter 3, which can map crosswell data quickly, without raytracing, using CDRATT models consisting of a general 2-D velocity medium and 2-D reflector interfaces.

### 2.3.1 XSP-CDP mapping trajectories in a 1-D media

The basic method behind XSP-CDP mapping is illustrated in Figure 2.5. To simplify the explanation the example shown in Fig. 2.5 consists of a homogeneous velocity model (and therefore straight rays) and six horizontal reflectors. I will focus on the upgoing reflections and the resulting upgoing reflection mapping trajectory, the calculation of the downgoing mapping trajectory is similar. Three reflecting interfaces are responsible for upgoing reflections in Fig. 2.5: Horizons C, D, and E. These three horizons result in reflections from points  $R_C$ ,  $R_D$ , and  $R_E$ . Horizon C lies at the same depth as the receiver so the reflection point,  $R_C$ , is located at the receiver position. Reflection points  $R_C$  and  $R_D$  lie intermediate to the two wells and are obtained using the Law of Reflections, the angle of incidence equals the angle of reflection. Reflection points  $R_C$ ,  $R_D$ , and  $R_E$  define the mapping trajectory at their corresponding depths. The complete upgoing reflection mapping trajectory is defined by the reflection points for upgoing reflections at all possible depths.

Mapping data from the seismic trace to points along the mapping trajectory requires that the traveltime from source, to each reflecting point, and on to the receiver be calculated

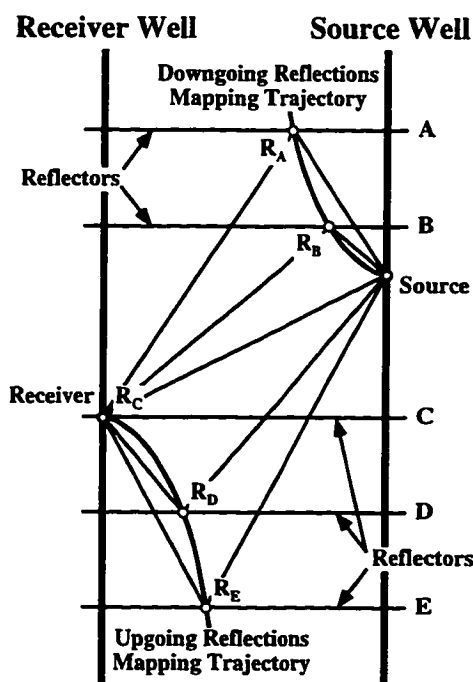


Figure 2.5: XSP-CDP transformation upgoing and downgoing mapping trajectories in a simple homogeneous model with flat reflectors.

for all points on the trajectory. This is commonly done during the calculation of the mapping trajectory. Once all this information is available the transformation is accomplished by “mapping” the amplitude values from each time step of the seismic trace to the  $x$ - $z$  image coordinates corresponding to the equivalent time value on the mapping trajectory. One point to be noted in this constant velocity example is that the velocity of the model does not affect the shape of the mapping trajectory at all. The velocity of the medium changes only the traveltime values associated with the  $x$ - $z$  points on the trajectory and where along the trajectory the trace data values are placed.

### 2.3.2 Determining reflection points using wavefronts and combined traveltimes maps

To more clearly show how the XSP-CDP mapping algorithm is extended to 2-D velocity models, dipping reflectors, and curved reflectors, I will first describe a general approach for obtaining reflection points using the concepts of reciprocity, traveltimes maps, and wavefronts. These concepts will be used in Chapter 3 where I introduce a method for calculating mapping trajectories without raytracing.

Figure 2.6 illustrates a simple source and receiver geometry with wavefronts corresponding to a constant velocity model. A source wavefront is defined by the trajectory of points which all have the property that the traveltime from the source location to any of these points is constant. Defining the receiver wavefront requires the use of reciprocity. The principle of reciprocity assures that the traveltime along a path between two points is independent of the direction of travel. Using reciprocity the receiver wavefront can be defined in the same way as the source wavefront. The receiver wavefront consists of the trajectory of points which have the property that the traveltime from the receiver location to any of these points is constant.

Figure 2.7 shows the reflection point of Fig. 2.6 at the limit of small scale where the source and receiver wavefronts can be approximated by lines. The incident angle of the source wavefront can be defined using the normal to the wavefront at the reflection point. Reciprocity allows the direction of travel of the reflected wave to be reversed so that the normal to the receiver wavefront at the reflection point is equivalent to the direction of travel of the reflected wave. In Fig. 2.7 it can be observed that a consequence of the Law of Reflection in terms of wavefronts is that the source wavefront, the receiver wavefront, and the reflecting horizon make up an isosceles triangle at the reflection point. From this observation the Law of Reflection can be restated using wavefronts as: *the angle between*

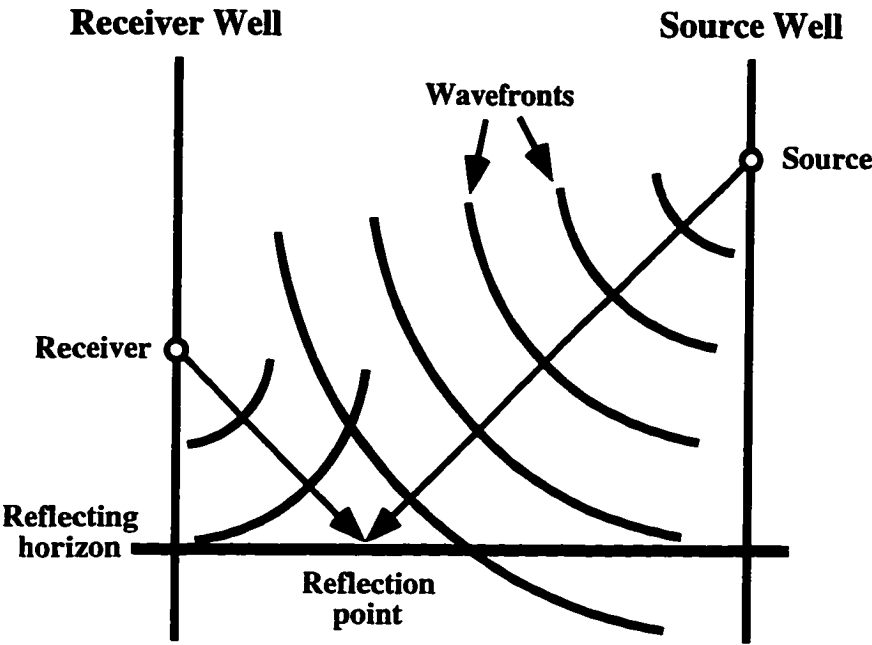


Figure 2.6: Source and receiver wavefronts for a simple homogeneous model. The wavefronts represent isochrons of the source and receiver traveltim maps. The raypaths, such as those shown, will always be orthogonal to the wavefronts.

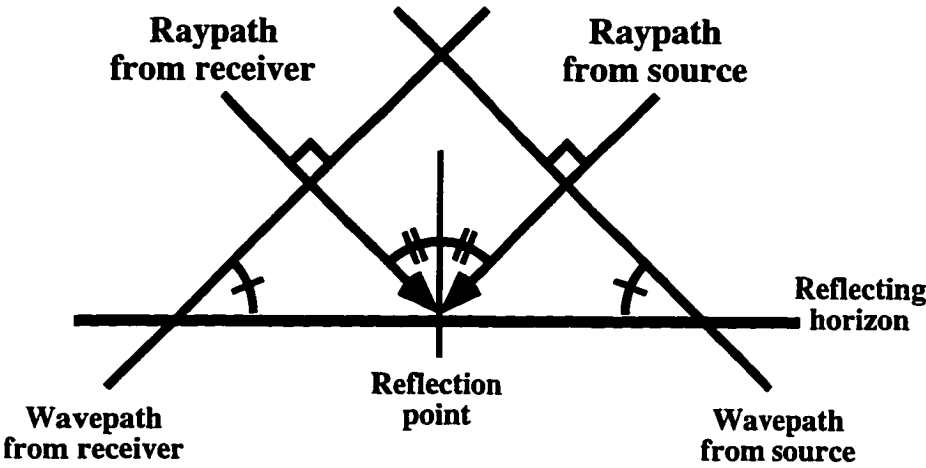


Figure 2.7: The reflection point of Fig. 2.6 shown at the limit of small scale. At this scale the source and receiver wavefronts can be approximated by lines. A consequence of the Law of Reflection in terms of wavefronts is that the source and receiver wavefronts, along with the reflecting horizon, make up the sides of an isosceles triangle at the reflection point.

*a wavefront from a source point and a reflection surface is equal to the angle between a wavefront from the receiver point and the reflection surface (Matsuoka and Ezaka, 1992).*

The next step in describing this general approach for determining reflection points is to define the combined traveltime map and the properties of its isochrons. First, it is necessary to describe source and receiver traveltime maps and their wavefronts. A source traveltime map is an image where the value of each  $x$ - $z$  point on the map equals the traveltime from the source location to that point. Based on this definition the source wavefronts are defined by isochrons on the source traveltime map. A receiver traveltime map is equivalent to the source traveltime map except the values of the map equal the traveltimes from the receiver location to every point on the map.

The combined traveltime map is simply the sum of the source and receiver traveltime maps. Figure 2.8 shows a schematic illustrating the addition of source and receiver traveltime maps to create the combined traveltime map. A constant velocity model is used in this example which results in circular wavefronts/isochrons in the source and receiver maps and elliptical isochrons on the combined traveltime map. One important feature of the isochrons of the combined traveltime map is that at any point on the isochron the angle between the source wavefront and the tangent to the isochron equals the angle between the receiver wavefront and tangent to the isochron. This feature, combined with the Law of Reflection for wavefronts, means that *a reflection point on an arbitrarily defined reflecting horizon is located where the tangent of the combined traveltime isochron equals the tangent of the reflecting horizon.*

An approach for calculating reflection points for source-receiver and reflecting horizon pairs using wavefronts is to first calculate isochron ellipses on the combined traveltime map for all traveltimes. The next step is to find points where the tangent of an isochron equals the tangent of the reflecting horizon under consideration. The  $x$ - $z$  point of tangency is the reflection point and constitutes a point on the mapping trajectory. One potential source of ambiguity is where there is more than one point of tangency between the reflecting horizon and the isochron ellipse. This, however, violates the assumption made in XSP-CDP mapping inherited from the VSP-CDP mapping method that states that there is at most one reflection point for each source-receiver-reflector combination. This assumption implies that the reflector geometries should be relatively simple for mapping techniques to be used correctly. But, as mentioned before in Point 3 of Section 2.2.3, reflector geometries are not normally excessively complex in oilfield applications of crosswell seismology at the offset distances of 100–600 ft commonly used. So, the “single reflection point” assumption of XSP-CDP mapping is typically valid.

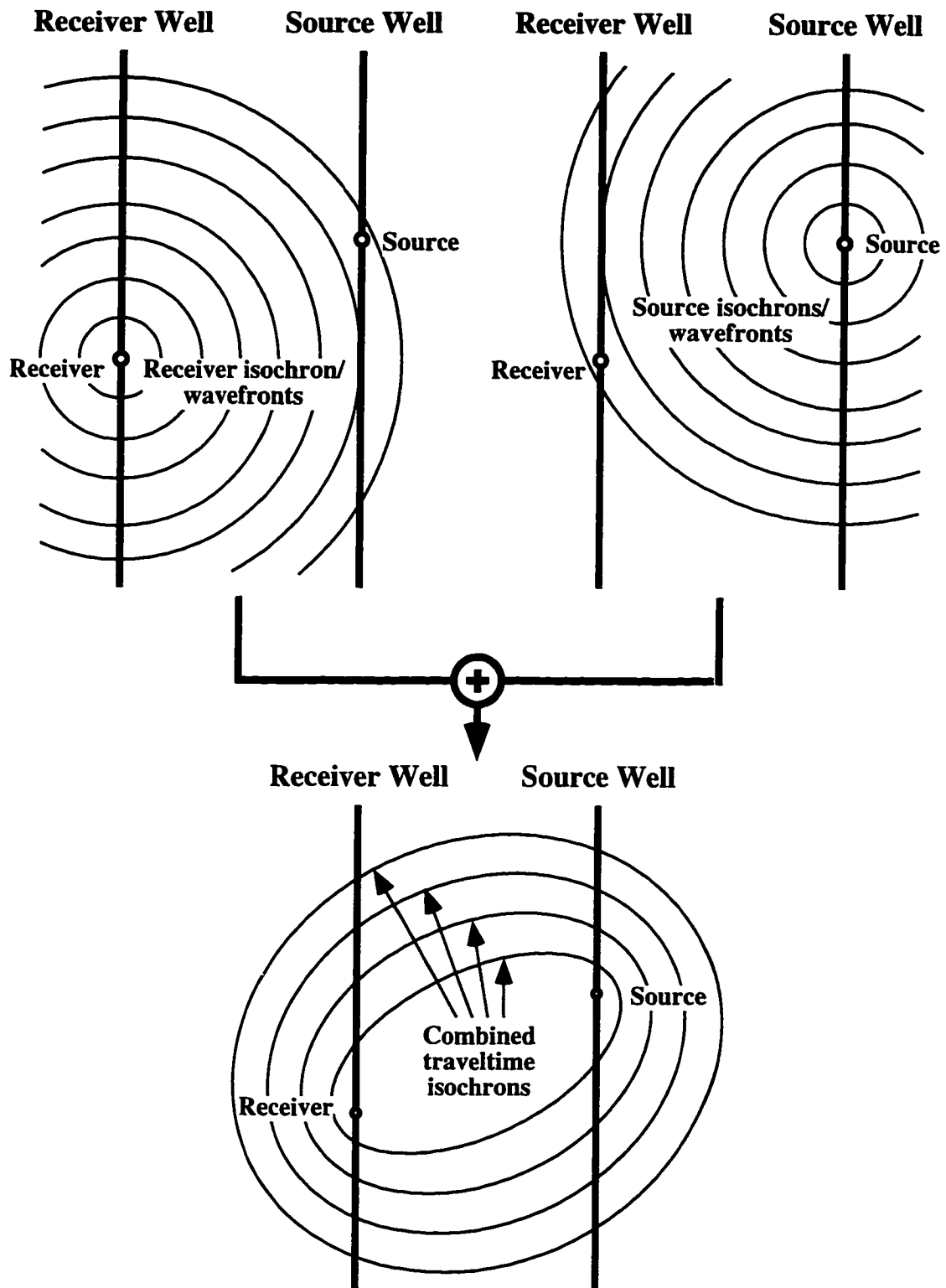


Figure 2.8: A schematic illustrating the source and receiver traveltime maps being added to create the combined traveltimes map.



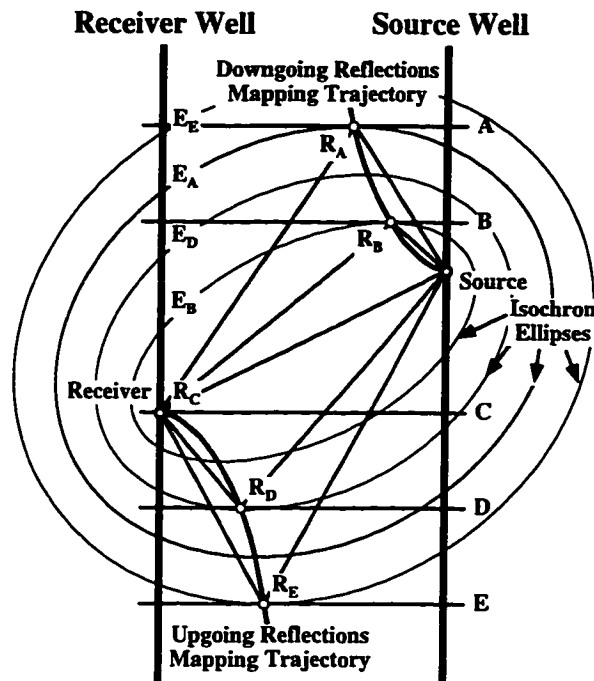


Figure 2.9: The mapping trajectories shown in Fig. 2.5 formulated in terms of shared points of tangency between the reflecting horizons and isochrons of the combined traveltime map.

Figure 2.9 shows the model presented in Fig. 2.5 with the addition of combined traveltime isochrons. Only isochrons which share points of tangency with the reflecting horizons have been plotted. Since the model is homogeneous these isochrons are ellipses. In this figure it can be seen how the reflection points  $R_A$ ,  $R_B$ ,  $R_D$ , and  $R_E$  are defined by shared points of tangency between the reflecting horizons and the combined traveltime ellipses. The combined traveltime isochron corresponding to reflection point  $R_C$  has collapsed to the line connecting the source and receiver. In the limit of this collapse the shared point of tangency lies at the receiver location.

### 2.3.3 XSP-CDP mapping trajectories with dipping reflectors

XSP-CDP mapping trajectories are easily defined for dipping and/or curved reflectors using the approach of wavefronts and combined traveltime maps to determine reflection points. In Figure 2.10 I've modified the previous model by replacing reflectors A, B, C, D, and E with curved or dipping reflectors  $A'$ ,  $B'$ ,  $C'$ ,  $D'$ , and  $E'$  and by updating the mapping trajectories to honor the new reflection points  $R_A'$ ,  $R_B'$ ,  $R_C'$ ,  $R_D'$ , and  $R_E'$ . In the XSP-CDP transformation each time data value from the seismic trace is mapped to one offset-depth point for downgoing reflections and one offset-depth point for upgoing reflections. While the combined traveltime isochrons are the same as those used in the previous example the

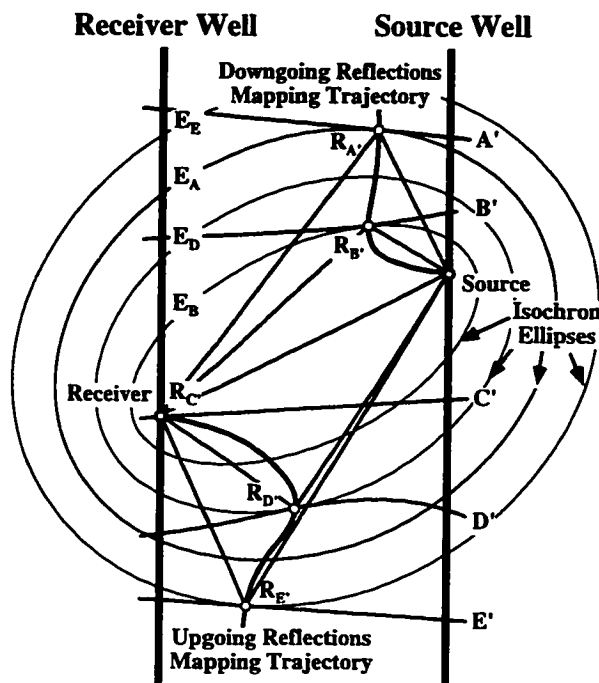


Figure 2.10: The wavefront method used to obtain mapping trajectories in a homogeneous model with dipping and curved reflectors. The reflection points are still defined by shared points of tangency.

new reflectors result in new spatial coordinates for each time data value (except for reflection point  $R_C$ ). The difference in reflection locations illustrates the kind of positioning errors which can result if XSP-CDP mapping is performed with incorrect reflector geometry information. Also, in this example I've interpolated the mapping trajectory between known reflection points in a smooth fashion. The exact trajectory, however, will depend on the reflector geometries between the reflecting horizons shown.

### 2.3.4 XSP-CDP mapping trajectories in a 2-D velocity model

The extension of the XSP-CDP mapping to accommodate 2-D variations in the velocity field is also simple in concept using wavefronts and combined traveltimes maps. The approach of finding reflection points by locating common points of tangency between the isochrons of the combined traveltimes map and the reflecting horizons remains valid even though the combined traveltimes isochrons are distorted by the 2-D velocity field and the raypaths are no longer straight. The ability to calculate mapping trajectories in a 2-D velocity field with 2-D reflector geometries is required to make use of the model obtained using CDRATT velocity estimation. Therefore, to provide an early introduction to the kind of data used later in the field examples, I have used field data to illustrate this example. The

XSP-CDP input parameters are a 2-D velocity field calculated using traveltime tomography and reflector geometries estimated from well log correlations.

Figure 2.11 shows a velocity model and reflector geometries. The velocity model, Figure 2.11a, has a velocity distribution which is primarily 1-D in nature although there are some small lateral variations. The reflector geometry model, Figure 2.11b, contains linear reflectors dipping shallowly to the right above 3050 ft, and more steeply to the left below 3050 ft.

Source and receiver traveltimes are calculated using a finite-differences eikonal code (Mo, 1994). Isochrons of these traveltimes are visualized using a random colortable. As I use this display technique often I will show a specific example. Figure 2.12a shows a source traveltimes map displayed with a conventional colortable. This map was calculated with the velocity field shown in Fig. 2.12. In Figure 2.12b I show the same traveltimes map redisplayed with a random colortable. The randomized colortable enhances the visualization of the wavefronts of the traveltimes map by making adjacent isochrons distinctly different colors.

The first step in calculating the combined traveltimes map for a particular source-receiver pair is to calculate two traveltimes maps, one for the source and one for the receiver. These two traveltimes maps are then added together, as in Fig. 2.8, to create the combined traveltimes map. Figure 2.13 illustrates this process for source and receiver traveltimes maps

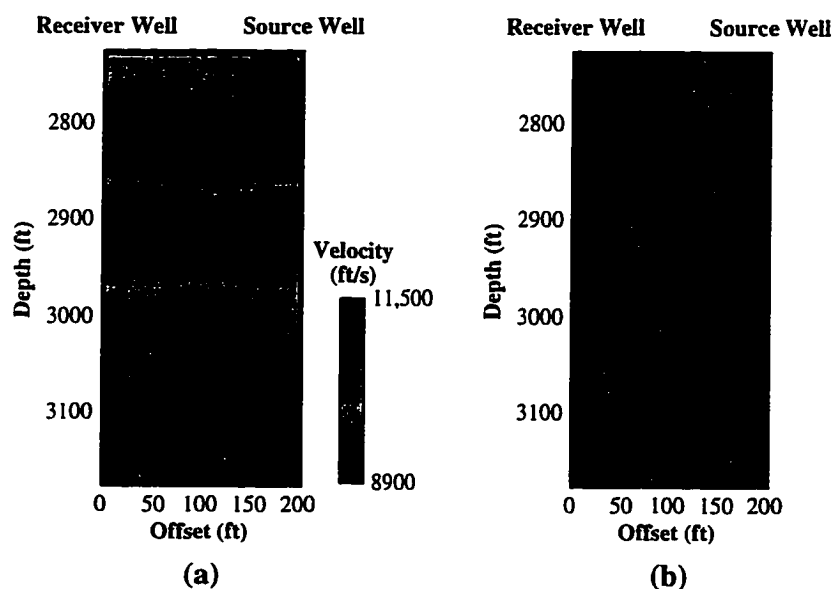


Figure 2.11: A 2-D velocity model (a), and reflector geometries (b), obtained from a field data experiment. These are used to illustrate the wavefront method's use for calculating mapping trajectories in general 2-D models.

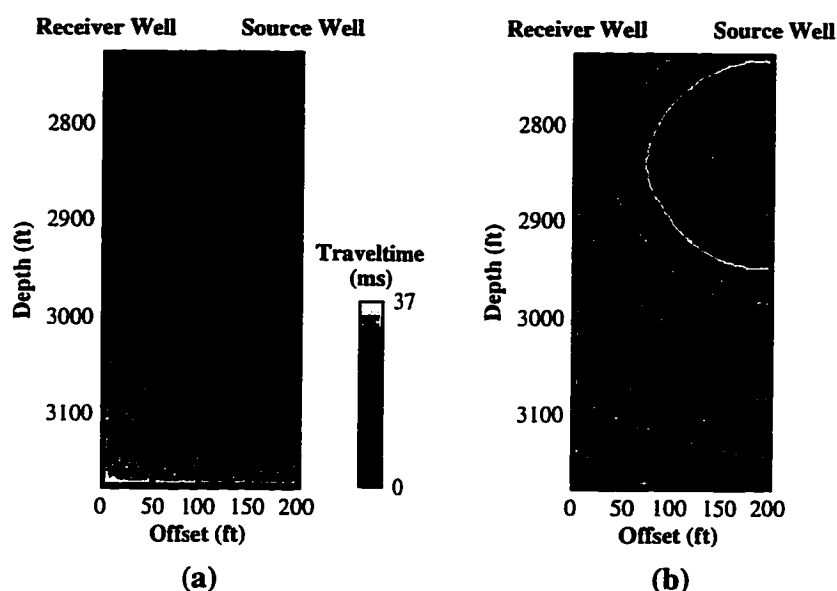


Figure 2.12: A source traveltimes map (a) calculated from the model shown in Fig. 2.11 using a finite-differences eikonal code. The map is redisplayed using a random colortable in (b) to enhance the isochrons. The 2-D nature of the velocity model can be seen in the deviations of each isochron from a circular trajectory.

calculated using the tomogram velocity field in Fig. 2.11. Note that the combined traveltimes isochrons shapes are still relatively elliptical.

Now that I have a qualitative display of the isochron ellipsoids I can use it, along with the reflector geometries shown in Fig. 2.11b, to determine the mapping trajectories. Figure 2.14 shows the combined traveltimes isochron map, the reflector geometries, and the mapping trajectories in one display. The reflection points, seen at the intersections of the mapping trajectory and the reflecting horizons, are defined by points of tangency between the isochron ellipsoids and the reflecting horizons. In this example the points of tangency have been estimated visually. A procedure for calculating these points quantitatively is described in Chapter 3.

## 2.4 From trajectories to images

The calculation of a single XSP-CDP mapping trajectory is the starting point of the XSP-CDP imaging procedure. In Section 2.3 I discussed how mapping trajectories for a single source-receiver combination are determined for models of various complexity. In this section I discuss how mapping from different domains can affect the final image. These

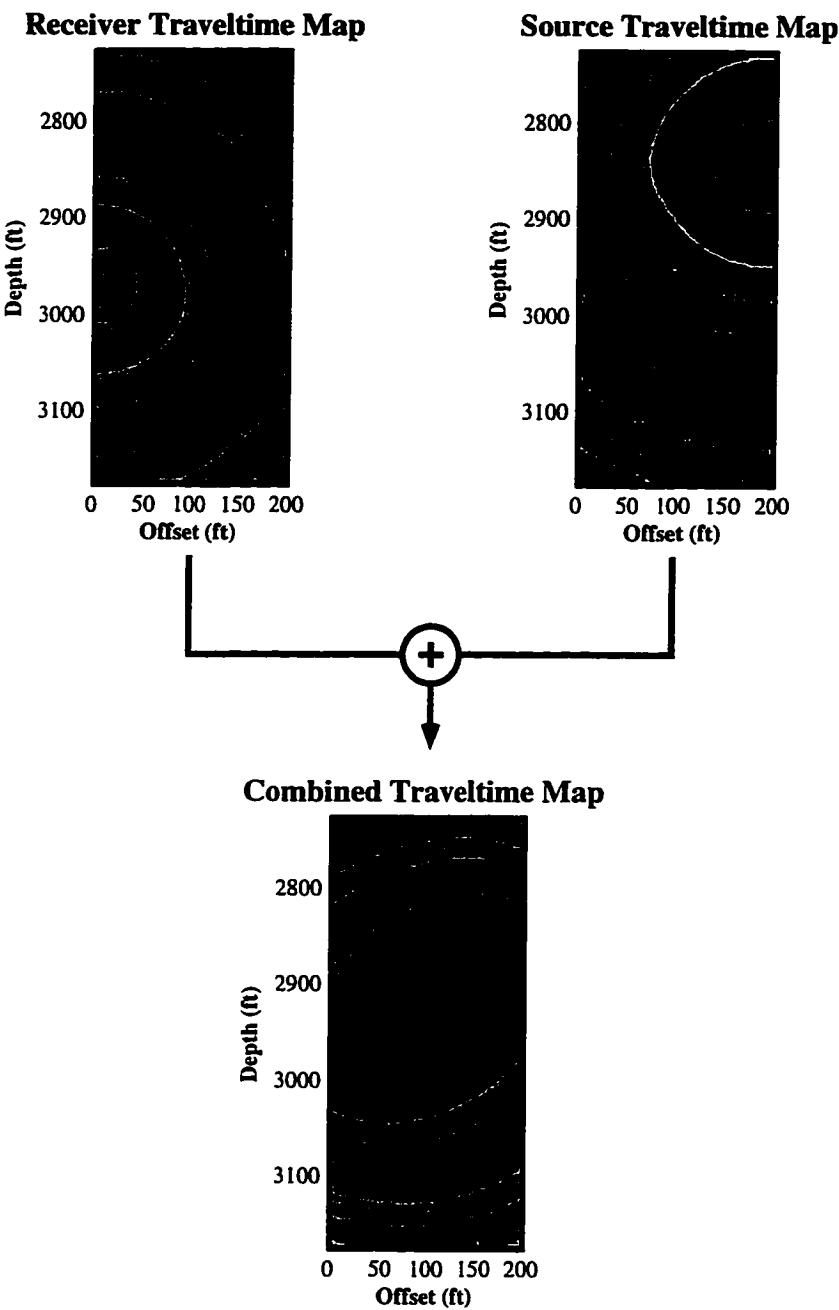


Figure 2.13: This figure illustrates the addition of source and receiver traveltime maps to create a combined traveltime map. The source and receiver maps were calculated using the 2-D velocity model shown in Fig. 2.11.

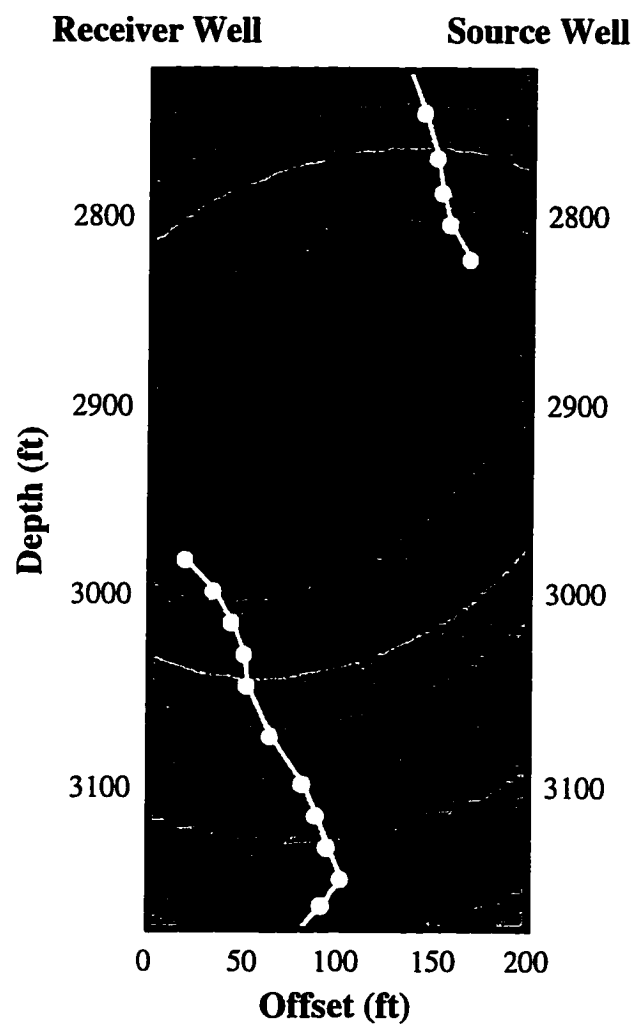


Figure 2.14: This figure illustrates how the reflector geometries shown in Fig. 2.11 are used with the combined traveltimes map from Fig. 2.13 to obtain mapping trajectories in a general 2-D model. The reflection points are defined by shared points of tangency between the reflecting horizons and the combined traveltimes map isochrons.

effects are primarily due to details in the implementation of the imaging step. To aid the discussion I will provide a short description of how the mapping is implemented first.

### 2.4.1 XSP-CDP data transformation

The discussion in Section 2.3 focused primarily on defining the  $x$ - $z$  points of the mapping trajectory with less emphasis on the corresponding temporal information required to transform the data. The  $x$ - $z$  coordinates of the mapping trajectory are only half the data needed for the transformation; the corresponding relationship between the  $x$ - $z$  trajectory points and the temporal data points of the seismic trace is also required. These data are then used to transform a gather from the time-depth seismic trace domain to the offset-depth image domain. The algorithm I use for doing this was developed by Lazaratos (1993).

As discussed briefly in Section 2.2.1, the most common way to image the transformed data is with traces evenly sampled in offset and depth. This allows images from different gathers to be stacked together directly. Resampling is typically accomplished by binning the transformed data and interpolating in the horizontal and vertical dimensions. The result of this imaging procedure applied to the data in Fig. 2.2 is shown in Figure 2.4.

The evenly sampled image data provided by the technique shown in Fig. 2.4 allow stacking and processing following the mapping transformation. Another advantage of this technique is that the reflectors appear more continuous from well to well, especially close to the receiver well. In the image shown in Fig. 2.3 the trace spacing close to the receiver well is relatively sparse making it difficult to follow the reflectors. Unfortunately the results of this technique may suffer if the reflectors are not horizontal. If reflectors are dipping they may become aliased in the image domain resulting in image artifacts due to errors in the interpolation. This aliasing can be minimized by transforming the data from domains which, after transformation, provide more even sampling in the offset ( $x$  coordinate) dimension of the image domain. This is discussed in more detail in the next section.

### 2.4.2 XSP-CDP mapping in different domains

The effectiveness of the interpolation algorithm used in the image resampling scheme depends on the sparseness of the data being sampled. If reflection events are dipping too steeply in the image domain they may be spatially aliased along the interpolation direction resulting in incorrect interpolation. This problem can be minimized by choosing among the various data domains from which crosswell seismic data can be sorted. The average density of mapping trajectories in the offset dimension of the image space varies among the different domains. This makes the choice of pre-mapping sort domain important. In this

section I review some of the common data domains and discuss the advantages and disadvantages of each in the crosswell data transformation.

Figure 2.15 shows mapping trajectories displayed in several of the most commonly used data domains. The model used to calculate the trajectories consists of a constant velocity with horizontal reflectors. The four data domains shown in Fig. 2.15 are Common Shot Gather (CSG), Common Receiver Gather (CRG), Common Mid-Depth Gather (CMG), and the Common Offset Gather (COG). These gathers are equivalent to their surface seismic counterparts except the variable dimension is vertical, not horizontal. For example, in a CMG the average of the source and receiver *depths* is constant.

Ray shooting methods are typically most efficient at linking rays in either the CSG or CRG domains. This is because a single reference fan can be calculated initially and used to guide the process for linking a number of rays in each gather. In both the CMG and COG domains a new reference fan is required to calculate each ray since all source and receiver locations are unique in these gathers. This makes the CMG and COG data domains very inefficient for calculating trajectories using ray shooting methods, so mapping trajectories are most commonly calculated in the CSG or CRG domains.

While the CSG and CRG domains may be more efficient for calculating the mapping trajectories there may be advantages to mapping in a less commonly used domain, the CMG domain. In spite of the fact that the sort type does not affect the mapping trajectories, or the total number of traces mapped, the different domains *can* have an effect on the accuracy of the interpolation used in the transformation step. This is true because, after mapping, the different domains provide information in the image domain at different spatial densities, as seen in Fig. 2.15. Interpolation of the mapped data, in both the vertical and horizontal directions, is required to obtain the evenly sampled data in the offset-depth image domain needed for stacking. If the spatial density of information prior to interpolation is insufficient to prevent aliasing, the data will not be correctly interpolated.

One advantage of the CMG is that the moveout of horizontal reflectors is minimized in the time-depth data domain making the transformed wavelet nearly stationary in depth in the offset-depth image domain (Lazaratos, 1993). This suggests that horizontal interpolation will be more accurate in the CMG because the stretching of the wavelet is almost constant at each depth. Also, as can be seen in Fig. 2.15, the CMG provides the most uniform spacing of mapping trajectories at each depth. This minimizes the aliasing of steeply dipping events. And, while steeply dipping events can still be aliased in the CMG domain, the dip at which events become aliased is constant across the image for each depth making it easier to protect against it.



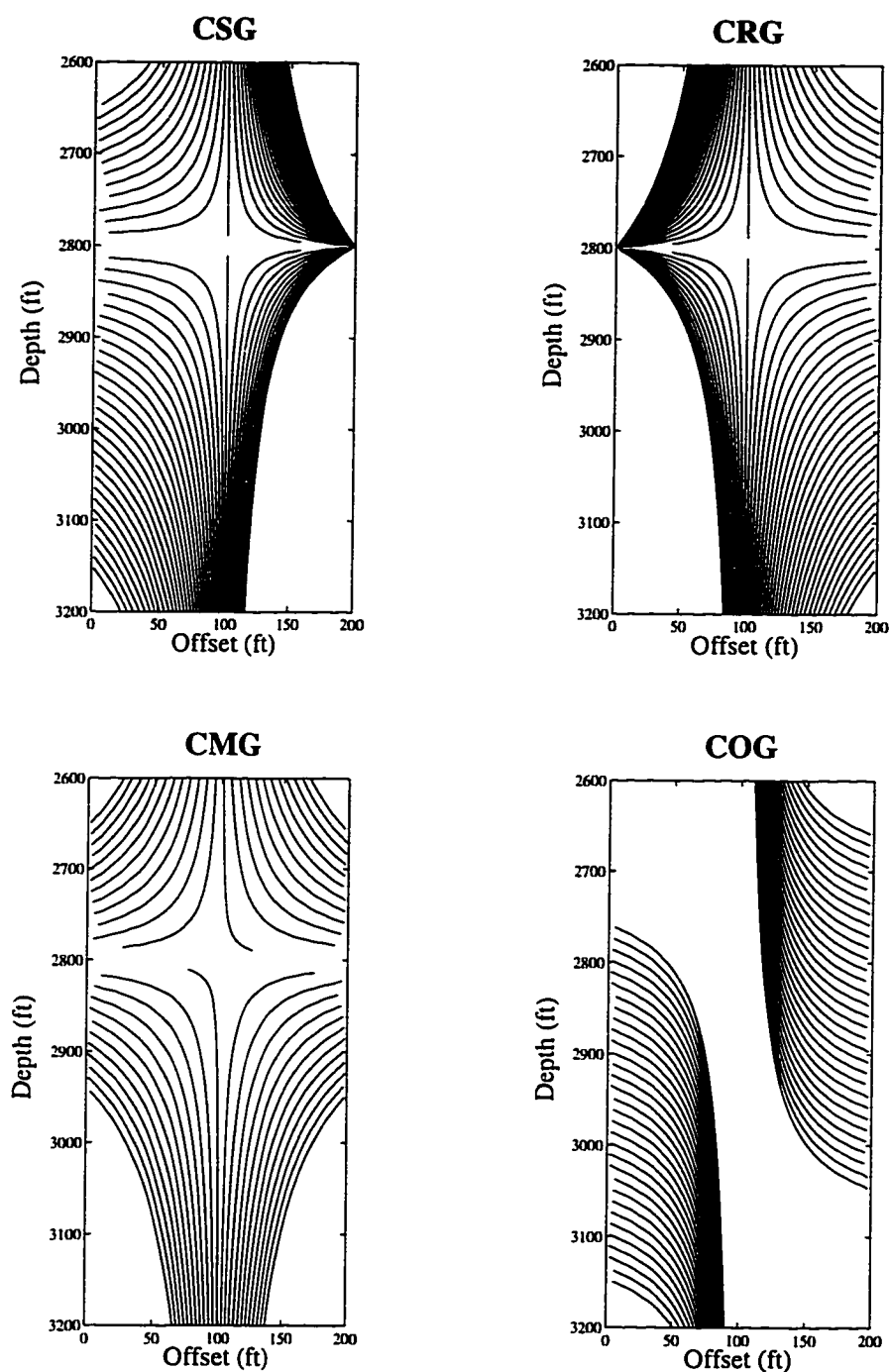


Figure 2.15: Mapping trajectories for crosswell seismic traces in 4 sort domains: common shot, common receiver, common mid-depth, and common offset. As can be seen in this display, the CMG provides the most uniform coverage in the image space and the COG the least uniform. In a homogeneous model with flat reflectors, reflections at each depth would have the same angle of incidence for all trajectories in a mapped CMG. This results in a uniform wavelet at each depth

The orthogonal sort to the CMG, the COG, appears to have fewer benefits with respect to mapping. As can be seen in Fig. 2.15, the COG mapping trajectories are unevenly spaced along the  $x$  axis (offset) at each depth. This can lead to aliasing of dipping events, which occurs as a function of offset within the image. In addition, the wavelet is not stationary at each depth which can reduce the potential accuracy of the interpolation step. Finally, the upgoing and downgoing images overlap in depth. While upgoing and downgoing data are typically separated before mapping, a single mapped gather covers a much more restricted portion of the image domain as compared to the other domains.

In summary, different data domains have their own advantages and disadvantages with respect to XSP-CDP reflection imaging. CSG's and CRG's are commonly used in data acquisition and are efficient for calculating mapping trajectories using ray shooting techniques. On the other hand, they tend to image primarily near one well or the other, the trajectories are not so evenly spaced at each depth, and the transformed wavelet is not stationary at each depth. The CMG avoids these deficiencies. It is more suitable for optimal imaging but is a less efficient domain for calculating mapping trajectories.

## 2.5 Conclusions

In this chapter I have provided a background of the XSP-CDP mapping technique. I have also provided a short comparison of mapping techniques and migration techniques as applied to the crosswell imaging problem. While migration has many theoretical advantages over mapping, the high levels of noise and the limited angular coverage commonly found in the crosswell experiment make the XSP-CDP mapping preferable for many imaging problems. In addition, migration is much more computationally expensive than mapping. For these reasons I use XSP-CDP mapping as the imaging tool in this CDRATT velocity estimation study. Migration, however, can be substituted for mapping in this thesis without any changes in the philosophy of the velocity estimation approach.

The XSP-CDP approach of crosswell reflection imaging consists of two basic parts: 1) calculating mapping trajectories based on a velocity and reflector model, and 2) using these trajectories to transform the seismic data to the offset-depth image domain. I have reviewed the calculation of the mapping trajectories for models of various complexity using the concept of combined traveltimes maps. Using this concept, mapping trajectories are determined for each source-receiver combination by first calculating traveltimes maps for both the source and receiver and combining them. Next, a reflection point is found for each reflecting horizon by identifying the shared point of tangency between the reflecting horizon and the combined traveltimes isochrons. The location of the point of shared

tangency corresponds to the reflection point and defines one point of the upgoing or downgoing mapping trajectory for that source-receiver pair. The entire upgoing and downgoing mapping trajectories are determined by finding the reflection points for a number of reflecting horizons. One important advantage of the combined traveltimes approach to calculating mapping trajectories is that it is general and can be used in complex models, including those incorporating anisotropy.

After mapping trajectories have been calculated the seismic data are transformed into the offset-depth image domain. This is done by interpolating the mapped data and extracting traces that evenly sample the data in offset and depth. Using this technique mapped data can be later processed and stacked. Crosswell seismic data may be mapped from different domains. CSG's and CRG's are efficient domains to calculate mapping trajectories using ray-shooting approaches. The CMG maps the data in such a way that for a simple model the transformed wavelet is stationary at each depth and the trajectories are evenly spaced in offset at each depth. This makes the CMG gather optimal for mapping crosswell seismic data with the minimum amount of aliasing and distortion.

## **CHAPTER 3**

# **A FAST APPROACH TO CALCULATING XSP-CDP MAPPING TRAJECTORIES IN A GENERAL 2-D MEDIA**

### **3.1 Introduction**

In Chapter 2 I reviewed the basics of the XSP-CDP mapping transformation and described an approach for determining reflection points using the concepts of wavefronts and the combined traveltimes map. As mentioned previously, the XSP-CDP transformation consists of two basic steps: 1) calculating the mapping trajectories defined by the mapping model, e.g. the velocity image and reflector geometries, and 2) using these trajectories to transform the seismic data from the depth-time domain to the offset-depth image domain. While the concepts behind calculating mapping trajectories are straightforward the implementation of these concepts can be complicated. The main difficulty in XSP-CDP mapping lies in calculating mapping trajectories when the mapping model is complex.

Typically each point on the mapping trajectory is determined separately using a ray-shooting method. This is done by linking a source and receiver pair through a reflection off a horizon. The process of linking the source and receiver requires that rays be shot one after the other with the launch angle modified slightly each time until the raypath intersects the receiver borehole closely enough to be considered “captured”. When the mapping model is complex a large number of rays may be shot before the one ray needed to determine the reflection point is found. It sometimes occurs that the modifications to the launch angle may become so small that the machine precision may be insufficient to obtain a satisfactory raypath. Calculating mapping trajectories in complex models can be so costly in terms of computation time as to be unfeasible. Simplifying the model can reduce computation time but usually at the expense of image accuracy and quality.

In this section I introduce a ray-theoretic technique for calculating XSP-CDP mapping trajectories without raytracing. Mapping trajectories can be calculated quickly with this technique in 2-D velocity models with dipping and/or curved reflecting horizons. The implementation of the technique described here is designed for isotropic media but the concept can be extended easily to complex anisotropic models, including monoclinic. This algorithm reduces computation time by several orders of magnitude compared to traditional methods of trajectory calculation.

## 3.2 Calculating XSP-CDP trajectories without raytracing

An approach for calculating XSP-CDP mapping trajectories without raytracing can be formulated as an extension of work done by Matsuoka and Ezaka (1992). Their work describes a method for calculating direct and once-reflected raypaths using the concepts of reciprocity and wavefronts. As described in Chapter 2, reflection points occur where the tangent of an isochron of the combined traveltime map equals the tangent of the reflecting horizon. The difficulty of implementing this concept lies in determining these points. One criteria for identifying reflection points using isochrons of the combined traveltime map is that the reflection points correspond to stationary points of total traveltime along the reflecting interface. The validity of this can be proven using a geometrical argument or the weak formulation of Fermat's principle (Born and Wolf, 1980). I will do this using both approaches.

### 3.2.1 Reflection points are stationary points of traveltime

To show that reflection points correspond to stationary points of total traveltime along the reflecting interface using a geometrical argument I have modified Figure 2.9 from Chapter 2 to include only one reflector. This new model is shown in Figure 3.1. Figure 3.2 shows a close-up of the reflection point  $R_D$ . A fundamental assumption of the XSP-CDP transformation is that for any source-receiver combination there is at most one reflection point for each reflecting horizon. Under this assumption it can be seen that a reflecting horizon can be related to a combined traveltime isochron in only one of three ways: the reflecting horizon does not touch the isochron, the reflecting horizon crosses the isochron one or more times, or the reflecting horizon shares only one point, a point of tangency, with the isochron.

The gradient of a combined traveltime isochron is normal to its tangent in isotropic media. For a point to satisfy the conditions for being a reflection point under the Law of Reflections for wavefronts the tangent of the reflecting horizon and the tangent of the isochron must be equal at that point. Since the tangent of the combined traveltime isochron is normal to the gradient, the derivative of traveltime along the tangent must be zero. As the tangent of the reflecting horizon is equal to the tangent of the isochron at the reflection point the derivative of traveltime at the reflecting horizon must also be zero. Therefore the reflection point is a stationary point of traveltime on the reflecting horizon.

A reflection point can also be shown to be a stationary point using the weak formulation of Fermat's principle (Born and Wolf, 1980). A reflection point on a reflecting horizon lies

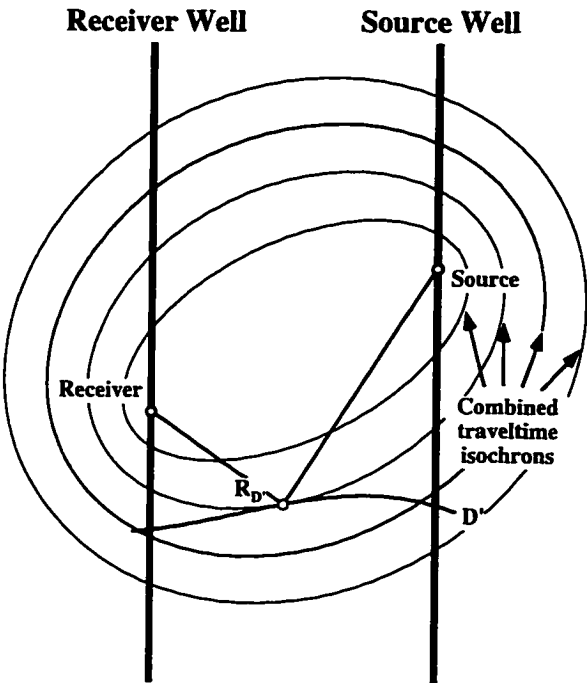


Figure 3.1: In this illustration the example shown previously in Fig. 2.9 has been simplified to include a single reflector,  $D'$ , and the reflected raypath from a single source-receiver pair.

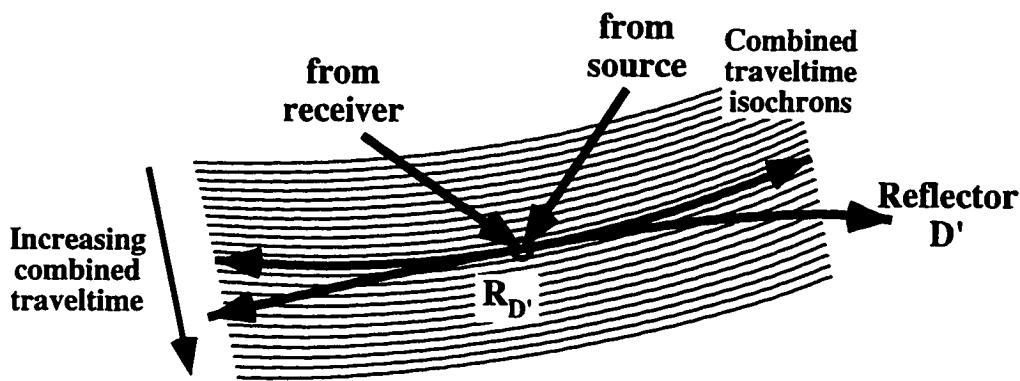


Figure 3.2: A close-up of the reflection point in Fig. 3.1. This figure illustrates graphically how the reflection point corresponds to a point where the combined travelttime along the reflecting horizon is stationary. In this case the stationary point is a travelttime minimum.

along a path which connects the source and the receiver through the reflection point. Under the weak formulation of Fermat's principle small perturbations of the location of the reflection point along the reflecting horizon *must*, to first order, result in *no* change to the total traveltime. This is a more fundamental proof of the stationarity of the traveltime at the reflection point since the reflection point is *defined* by the property of stationarity. More importantly, this proof also applies to anisotropic media whereas the geometrical proof is true only for isotropic media.

### 3.2.2 An efficient approach for calculating mapping trajectories

The property of stationarity of combined traveltime along the reflecting horizon allows a simple and straightforward approach for calculating mapping trajectories to be formulated. The flowchart for this procedure is shown in Figure 3.3. First, traveltime maps for all sources and receivers are precalculated using a model consisting of reflector geometries and a velocity model. Second, traveltime maps for the source and receiver of interest are added together to create the combined traveltime map. Third, the total traveltime for each point along a reflecting horizon is obtained from the combined traveltime map. Fourth, the point on the reflecting map where the traveltime is stationary is determined. This point corresponds to the reflection point and is one point on the mapping trajectory for that source-receiver combination. Reflection points for the remaining reflectors are determined sequentially until both the upgoing and downgoing mapping trajectories for the current source-receiver combination are defined. Finally, mapping trajectories for all source-receivers are determined sequentially resulting in mapping trajectories for the entire gather.

The efficiency of this approach results from the precalculation of all the source and receiver traveltime maps. When all source and receiver maps are precalculated the combined traveltime map for any source-receiver combination can be created quickly by simply reading and adding their precalculated maps. In this way the total number of maps required to determine all mapping trajectories is equal to the sum of the different source and receiver locations. After all traveltime maps are calculated the number of subsequent calculations is determined by the product of the number of source-receiver combinations and the number of reflecting horizons.

## 3.3 Implementation

In the seismic reflection method the imaging procedure and the velocity analysis procedure should be consistent to obtain optimal results. Prerequisites for attaining this

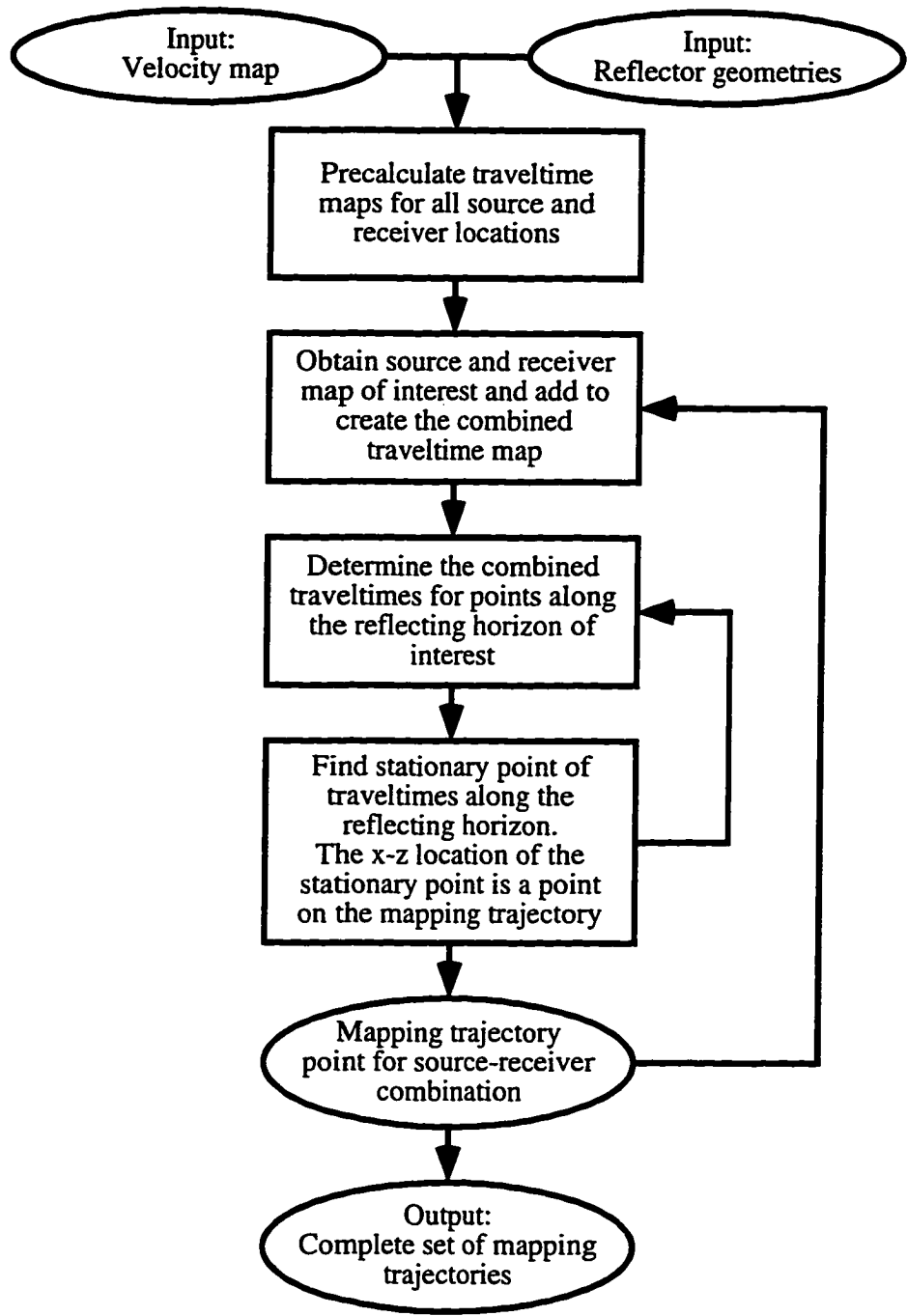


Figure 3.3: This flowchart illustrates the procedure for calculating mapping trajectories using the wavefront method of obtaining reflection points. The efficiency of this approach is obtained primarily through the precalculation of all the necessary source and receiver traveltimes maps. This also allows trajectories to be calculated efficiently in any sort order, such as the Common Mid-Depth domain.



consistency are that the assumptions and parameterization of the model used in the velocity analysis and reflection imaging be the same. The determining factors which lead to the choice of one model parameterization over another in this thesis are encountered primarily in the CDRATT inversion. These factors are discussed at length in Chapter 4. For now, the basic assumption is of a ray-theoretic model. The parameterization of the model is one where a 2-D isotropic velocity field is defined by cells in offset-depth Cartesian coordinates. Reflectors are defined at points spaced equally across the image. Reflector locations intermediate to the defined points are calculated using cubic splines, resulting in a smooth function in offset and depth. Well deviations are included by projecting the wells to a 2-D image space.

### 3.3.1 Calculating traveltimes maps

The choice of a method for the calculation of the traveltimes maps is an important decision in the implementation of the XSP-CDP mapping algorithm. Errors in the traveltimes maps will propagate through the imaging steps resulting in a mispositioning of the mapped data. Fortunately many accurate algorithms have been developed in recent years using a variety of different approaches. Two commonly used approaches are: finite-difference solutions of the eikonal equation (Vidale, 1988; Van Trier and Symes, 1991; Zhang, 1993) and methods based on Huygen's principle or graph theory (Saito, 1989; Moser, 1989).

Matsuoka and Ezaka (1992) described one advantage of using combined traveltimes maps to calculate direct and reflected arrival raypaths as the ability of this approach to include head waves. Many methods of traveltimes inversion use first breaks which may result from head waves. In the shooting method the paths of head waves cannot be calculated since an infinite number of possible head wave paths exist for any given shooting angle. Figure 3.4 illustrates source and receiver maps computed using a model with a strong velocity contrast added to create the combined traveltimes map. The head wave can be seen as an upward traveling linear event in both the source and receiver traveltimes maps. In the combined traveltimes map the first arrival raypath is defined by the minimum traveltimes, which in Fig. 3.4 result from a refracted head wave.

Unfortunately the presence of head waves in the traveltimes maps leads to errors in calculating the mapping trajectories. One problem is that in the combined traveltimes map approach reflection points are defined by stationary points along reflecting horizons. The traveltimes along the segment of the head wave raypath lying along the interface are all equal. Since reflection points are defined as stationary points this contradicts the XSP-CDP mapping assumption that there is at most one unique reflection point on each reflector for

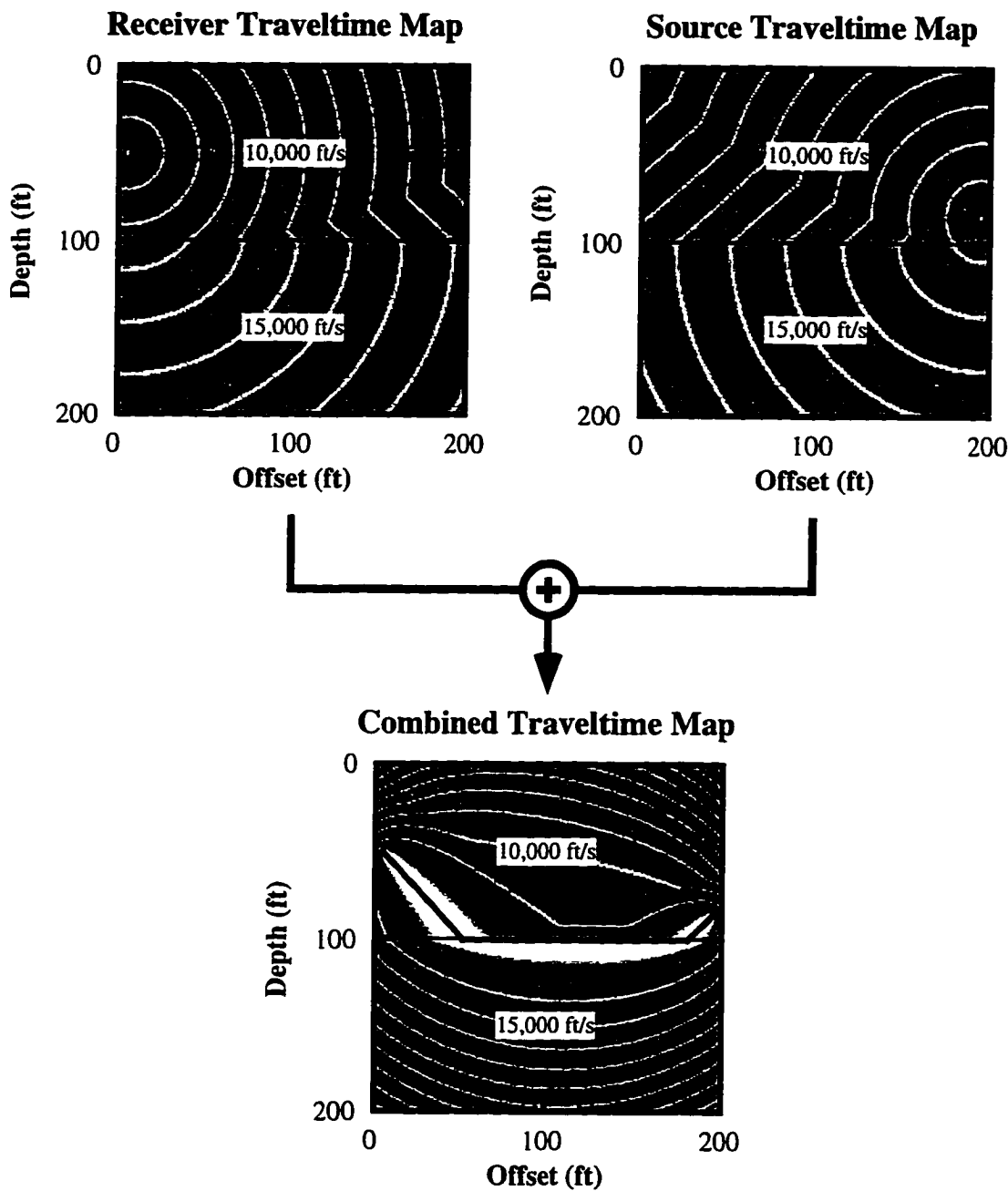


Figure 3.4: A combined traveltime map with dominant head waves. The source and receiver traveltime maps shown here were calculated using a Vidale-type finite-differences eikonal code (1988) which obtains first arrival traveltimes. The head wave in each traveltime map can be seen as an upward-traveling linear event. In this example the first, or fastest, arrival is a refracted head wave. The raypath for this event is defined by the minimum combined traveltime values.

each source-receiver pair. In essence the reflection point cannot be correctly determined using the notion of stationarity of traveltimes in the presence of head waves. The second problem is that even if the location of the reflection point can be identified the traveltimes of the combined traveltime map corresponding to that location will be incorrect. The traveltimes will be that of the head wave first arrival.

In practice, head waves are not a large problem in models calculated using the CDRATT velocity estimation method. The velocity models used for reflection imaging are the result of a combined direct and reflected arrival traveltime inversion. The parameterization of the model and the smoothing constraints used in the CDRATT inversion preclude the possibility of the large velocity contrasts required to create head waves. For this reason, virtually any accurate method for calculating traveltime maps will provide good results for many of the cases encountered. Nevertheless, it may be desirable to map data with a model which has sharp velocity contrasts between layers. For this reason I have chosen to use a finite-differences eikonal code which calculates energetic arrivals.

The scheme I use to calculate traveltime maps is a derivative of an approach formulated by Mo (1994). Mo's approach is based on Vidale's (1988) finite-difference solution of the eikonal equation. The fundamental difference between the two codes is that Mo's approach allows wavefronts to be discontinuous across boundaries. This occurs at post-critical incidence. Figure 3.5 shows an example of Vidale's approach applied to the calculation of source, receiver, and combined traveltime maps. This example is similar to that shown in Fig. 3.4 except that both upgoing and downgoing head waves are present. Figure 3.6 shows the same traveltime maps calculated using Mo's method.

A comparison of Figs. 3.5 and 3.6 yields several observations. In Fig. 3.5 the first arrival is a downgoing head wave from the interface at 100 ft. The first arrival in Fig. 3.6 is a direct arrival along the straight raypath connecting the source and receiver. Wavefronts created using Vidale's method are continuous while those resulting from Mo's method can be discontinuous across the interfaces. Finally, differences in the combined traveltime maps are confined to be within the slow layer; outside the slow zone the wavefronts are identical in Vidale's and Mo's method. Using Mo's energetic-arrival eikonal scheme allows mapping trajectories to be calculated correctly in zones where head waves are present. Outside of these zones the results are identical to those that would be obtained using Vidale's finite-difference eikonal scheme.

In summary, there are a wide variety of methods to calculate traveltime maps. Much of the research in the area of developing these techniques has been directed toward increasing their efficiency and accuracy in complex velocity models. While all of these techniques

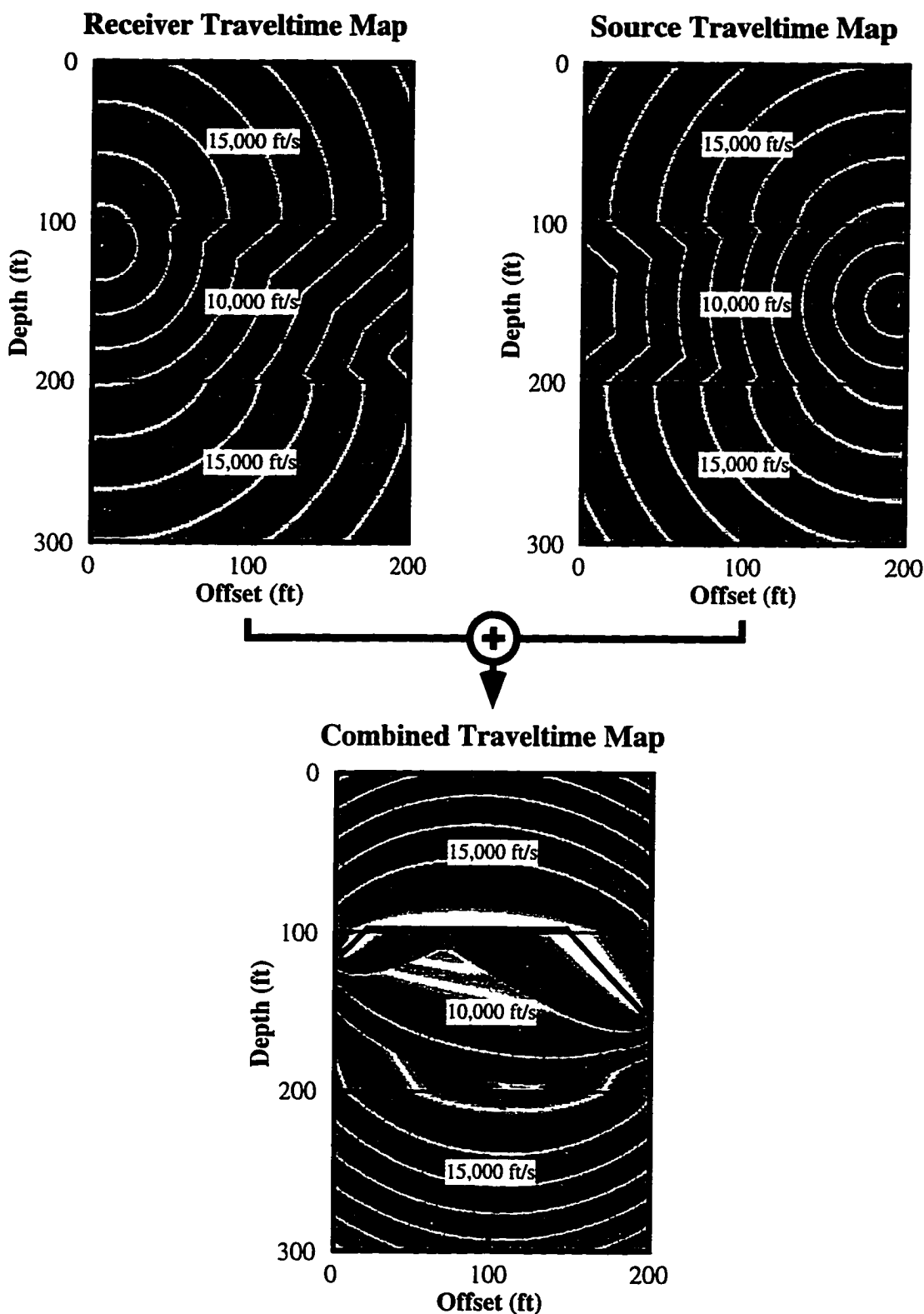


Figure 3.5: A second example of a combined traveltime map calculated from source and receiver maps which have strong head-wave events. In this case the head waves occur from velocity contrasts above and below the source and receiver positions.

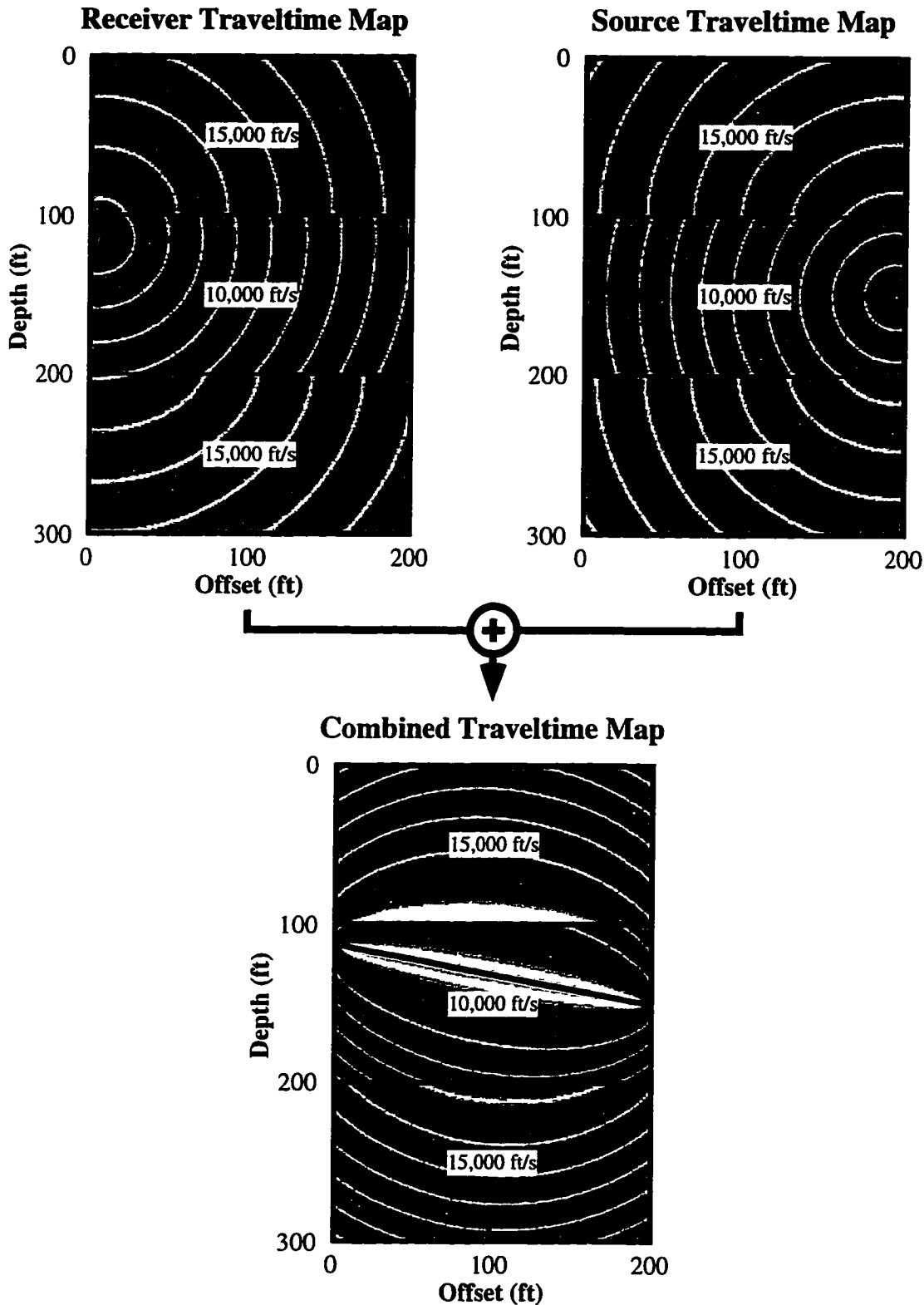


Figure 3.6: A combined traveltime map obtained through the use of an energetic-arrival finite-differences eikonal code (Mo, 1994). In this example head waves are removed effectively, which will allow accurate mapping trajectories to be calculated.

offer their own advantages and disadvantages I have chosen to use Mo's energetic-arrival approach to calculate traveltimes for the following reasons:

- it incorporates the simplicity, efficiency, and accuracy of Vidale's finite-differences eikonal code,
- it uses a model which is consistent with the CDRATT model parametrization,
- the effects of head waves are minimized.

With respect to future development, the ability to calculate mapping trajectories using the combined traveltimes map approach is independent of the technique used to calculate the traveltimes maps. Newer, faster, and more accurate techniques can therefore be incorporated easily. As the model parameterization is modified to incorporate increasing complexity, anisotropy for example, XSP-CDP mapping can be accomplished in the same fashion with only the calculation of the traveltimes maps requiring modification.

### 3.3.2 Determining stationary points along the reflecting horizon

Once a combined traveltimes map has been calculated for a source-receiver pair the final step in defining the mapping trajectories is to determine the reflection points for the reflecting horizons. As previously described, the reflection point on a reflecting interface is defined by the stationary point of combined traveltimes. By locating the stationary point on each horizon we locate the reflection point. All reflection points for a source-receiver pair define the upgoing and downgoing mapping trajectories.

A schematic for the flow used to calculate the mapping trajectories for a single source-receiver pair is shown in Figure 3.7. The input data for this procedure are the combined traveltimes map for the source and receiver of interest and a set of reflector geometries defining the reflector orientations over the zone covered by the combined traveltimes map. In the integrated approach to crosswell imaging described in this thesis the reflector geometries and the velocity model used to calculate the traveltimes maps are obtained using the combined direct and reflected arrival traveltimes tomography described in Chapters 3 and 4.

Reflectors are parameterized using a cubic spline representation which forces the reflectors to vary smoothly. This is helpful for solving the 2-point raytracing problem for reflected raypaths. Each reflector is defined by a set of depth values which are evenly spaced across the imaged area. Figure 3.8 shows an example of an imaged area defined by the combined traveltimes map and a single reflector. The combined traveltimes map is represented by the grid of evenly spaced vertical and horizontal grey lines. A combined traveltimes value is defined at each intersection point of the grey grid lines. The wells fall

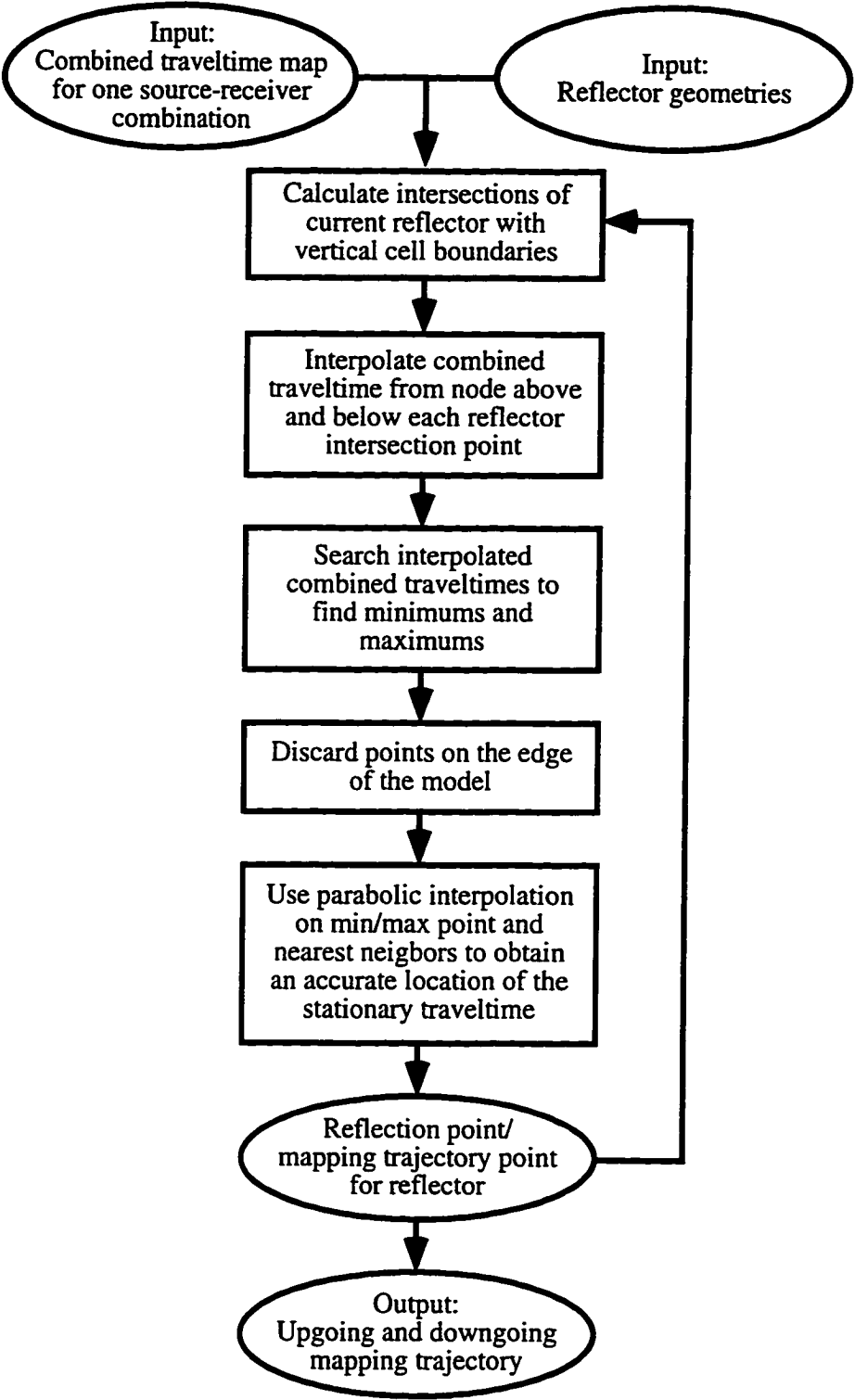


Figure 3.7: A flowchart describing the procedure for calculating the upgoing and downgoing mapping trajectories for a single source-receiver pair using the wavefront method.

within the imaged area and are defined by the source and receiver locations within the imaged area. The reflector is defined by a set of depth values equally spaced across the model. The location of the reflector in between these points is determined using a cubic spline algorithm.

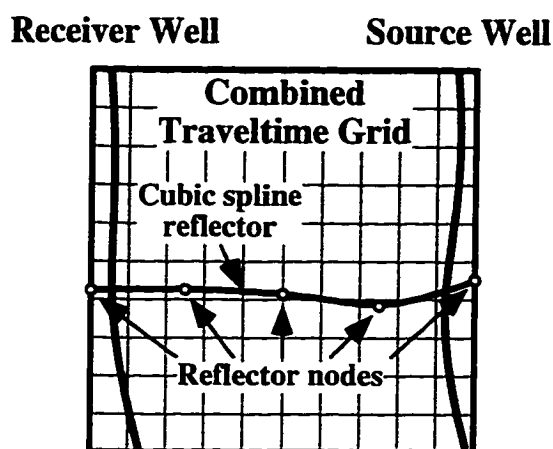


Figure 3.8: Reflectors are defined at points equally spaced across the image area. The reflector is interpolated between these point using cubic splines.

The next step in determining the reflection point is to obtain traveltimes along the extent of the reflecting horizon. The procedure used to accomplish this is to calculate the intersection of the reflector with the vertical node lines. The result of this calculation is illustrated in Figure 3.9. Once the intersection of the reflector with the vertical node lines

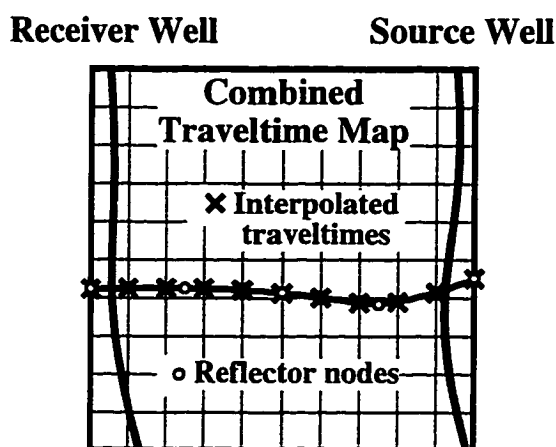


Figure 3.9: The reflector depth is determined for each vertical node using cubic splines. Combined traveltimes along the reflector can be defined through linear interpolation of the traveltime values above and below each interpolated reflector point.



is computed traveltimes values at the nearest nodes, above and below the intersection point, can be used to obtain an interpolated traveltimes at the reflector. This procedure is used to define the combined traveltimes along the entire reflecting horizon. The problem of identifying the stationary point from these interpolated combined traveltimes is an exercise in locating the minimum and maximum values and determining which of these is the stationary point. One important note: if the XSP-CDP mapping assumption is valid, that there is at most one reflection point per reflecting interface, there should no more than one stationary point along the reflecting horizon. This requires that there be no local minima or maxima combined traveltimes values along the reflecting horizon. It also requires that only one of the two points be valid as a true stationary point. A second note: for the reflection point to be a combined traveltimes maximum the curvature of the reflector must exceed the curvature of the combined traveltimes isochron at the reflection point. I have never found this to occur in the reflection geometries I have observed in crosswell images, although it is possible. So, realistically, the search criteria for the stationary point of combined traveltimes could be simplified to be that of traveltimes minimum. But, to keep the algorithm general, I discuss the search procedure in terms of the general case. This is where the stationary point of combined traveltimes can be a traveltimes minimum or maximum.

Traveltimes values at the left or right edge of the image may be minimum or maximum values of traveltimes but they must be discarded since knowledge of the traveltimes past the edge must be used to determine whether they are actually stationary points. After the edge points have been discarded there should be, at most, one minimum or maximum point left. Since the location of this point is discretized by the vertical node line spacing it represents an estimate of the true location of the stationary point. If the spacing of nodes is fine this estimate may be adequate for mapping. I obtain a more precise estimate of the location of each stationary point using a parabolic interpolation scheme. The minimum/maximum traveltimes and the adjacent traveltimes values are used to define a parabola from which a more accurate estimate of the stationary point can be calculated. The final estimate of the stationary point represents the reflection point on the reflector which defines one point along either the upgoing or downgoing mapping trajectory.

### 3.4 Examples and applications

The combined traveltimes map approach for calculating mapping trajectories has been shown to be relatively straightforward in spite of the fact that it can be used to map 1-D through 2-D crosswell data with equal efficiency. In this section I provide an example of

how all the previously described steps of the implementation are used to calculate a mapping trajectory.

### 3.4.1 Calculating a mapping trajectory for a single source-receiver pair

I will now illustrate the computation of the upgoing and downgoing mapping trajectories for the single source-receiver pair used in Fig. 2.14 from Chapter 2. Figure 2.14 is redisplayed in Figure 3.10 with the reflecting horizons labeled from top to bottom. Reflectors  $R_1$  and  $R_{25}$  are at the top and bottom of the image area defined by the combined traveltime map. The traveltimes on the combined traveltime map are defined every 5.0 ft in both the vertical and horizontal directions: 41 in the horizontal direction and 91 in the vertical direction. In this example the reflecting horizons are linear, defined by the intersection depths with the sides of the image.

The flow diagram shown in Fig. 3.7 is used as a guide for the process of determining the mapping trajectories. For each reflector in turn, the intersection of the reflector with the vertical nodes is found, or in other words, the depth of the reflector every 5.0 ft across the image is determined. The depth of intersection of the reflector with the vertical nodes is used to interpolate between nearest vertical neighbors to find the combined traveltime at the reflector. The traveltimes are then searched to find the minimum and maximum traveltime values along the interface and the edge points are discarded. The stationary point is estimated from the remaining minimum or maximum traveltime using parabolic interpolation so that a lateral resolution of better than 5.0 ft can be achieved. The reflection point is recorded and the next reflecting horizon is considered.

Figures 3.11 and 3.12 show data used in the determination of the downgoing and upgoing mapping trajectories seen in Fig. 3.10. Combined traveltimes along each reflector are shown including the final interpolated value. Several points can be observed in Figs. 3.11 and 3.12. First, a number of reflectors are omitted, specifically Reflectors 7–13. These reflectors lie vertically between the source and receiver locations so no reflections are possible. In spite of this, stationary points of combined traveltime may exist so they are excluded prior to the search for reflection points. The second point is that the stationary points are all traveltime minima for both upgoing and downgoing reflections. This is not true in general. If the curvature of the reflector exceeds the curvature of the combined traveltime isochron the stationary point of traveltime may be a traveltime maximum.

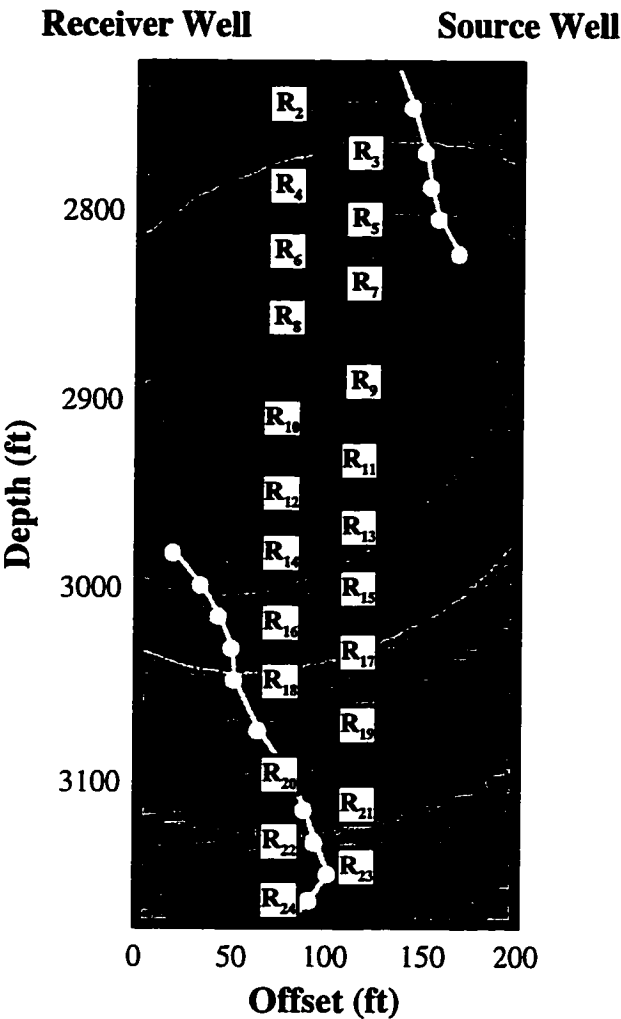


Figure 3.10: This figure illustrates how upgoing and downgoing mapping trajectories are calculated using the wavefront method for the single source-receiver combination previously shown in Fig. 2.13. Reflection points are defined for each reflecting horizon from top to bottom by locating the point of stationarity of combined traveltime along the individual reflector. These reflection points constitute points on the mapping trajectory. Mapping trajectory points intermediate to these are obtained by interpolation.

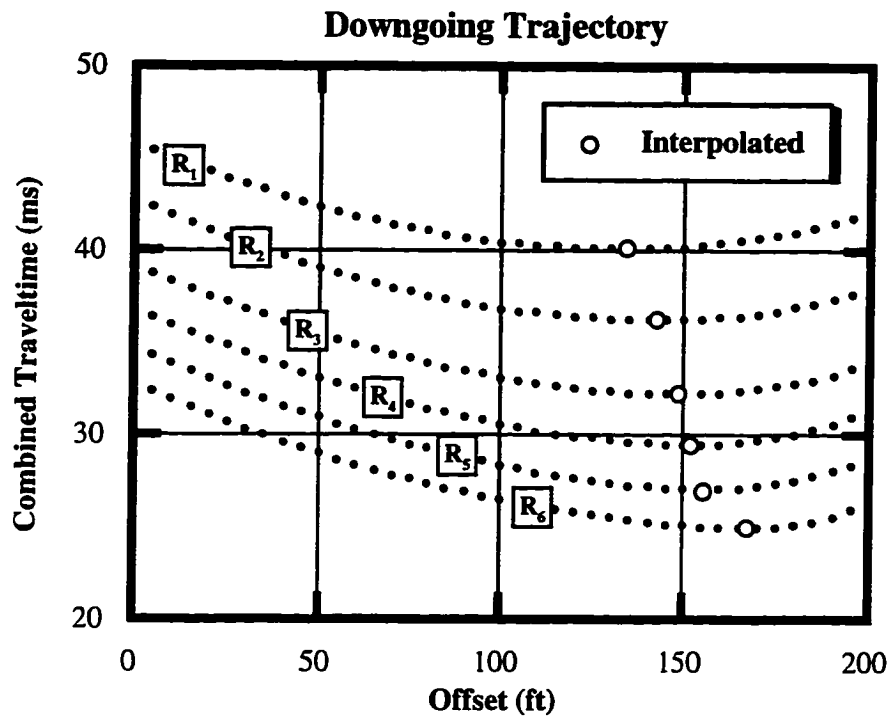


Figure 3.11: Combined traveltimes along each of the reflecting horizons leading to downgoing reflections. An accurate estimate of the stationary point of combined traveltime for each reflector is obtained using a parabolic interpolation routine.

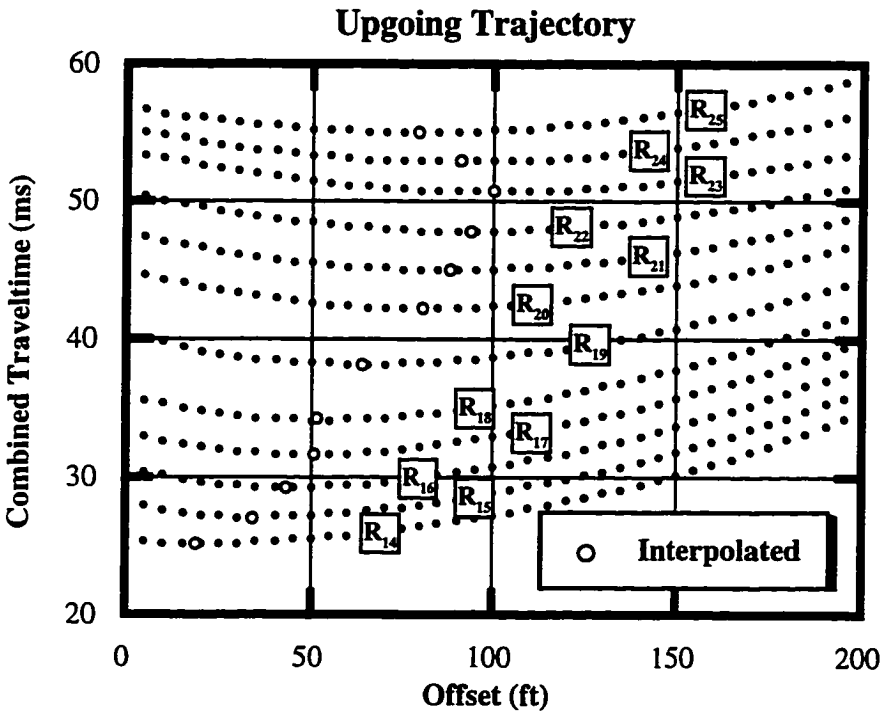


Figure 3.12: Combined traveltimes along each of the reflecting horizons leading to upgoing reflections and interpolated stationary points.

### 3.4.2 Mapping trajectories in different domains

In Chapter 2 the potential advantages and disadvantages of mapping from the different data domains (CRG, CSG, CMG, and COG) were discussed. Figure 2.15 provided an illustration of mapping trajectories in these different domains using a constant velocity medium with horizontal reflectors as the model. Figure 3.13 shows mapping trajectories in these same domains calculated using the 2-D model shown in Fig. 2.10. These trajectories were calculated using the combined traveltimes approach.

The mapping trajectories shown in Fig. 3.13 have the same basic characteristics as those shown in Fig. 2.15. The effect of the 2-D velocity model and dipping interfaces is reflected in the distortion of the mapping trajectories in all of the domains. The COG trajectories show the undesirable trait of overlapping each other in the bottom right-hand portion of the image area. Overlapping results in partial stacking of the data during the transformation. This precludes the possibility of processing prior to stacking since the data would be stacked in the mapping procedure. The CMG data domain still exhibits the desirable property of spacing the trajectories in the most uniform manner throughout the image area.

## 3.5 Conclusions

In this chapter I have introduced a new method for calculating XSP-CDP mapping trajectories without the use of raytracing. This method is designed to use an input model that is consistent with the CDRATT velocity estimation parameterization: a 2-D isotropic velocity field defined using cells and reflectors defined using cubic splines. The approach for calculating mapping trajectories is based on wavefronts and combined traveltimes maps

Calculating mapping trajectories using wavefronts and combined traveltimes maps is efficient. Upgoing and downgoing mapping trajectories are obtained in two steps. First traveltimes maps are calculated for all source and receiver locations. In the second step mapping trajectories are determined by adding the appropriate source and receiver traveltimes maps and then locating reflecting points on each interface. The reflecting point on each interface coincides with the stationary point of total traveltimes along the interface. Since the traveltimes maps are precalculated, mapping trajectories can be determined for source and receiver combinations in any order without any loss of efficiency.

Traveltimes maps are calculated in the implementation described in this chapter using an energetic-arrival finite-difference eikonal code. This minimizes the distortion of the mapping trajectories due to head waves in models which have strong velocity contrasts. One feature of the combined traveltimes approach for calculating mapping trajectories is

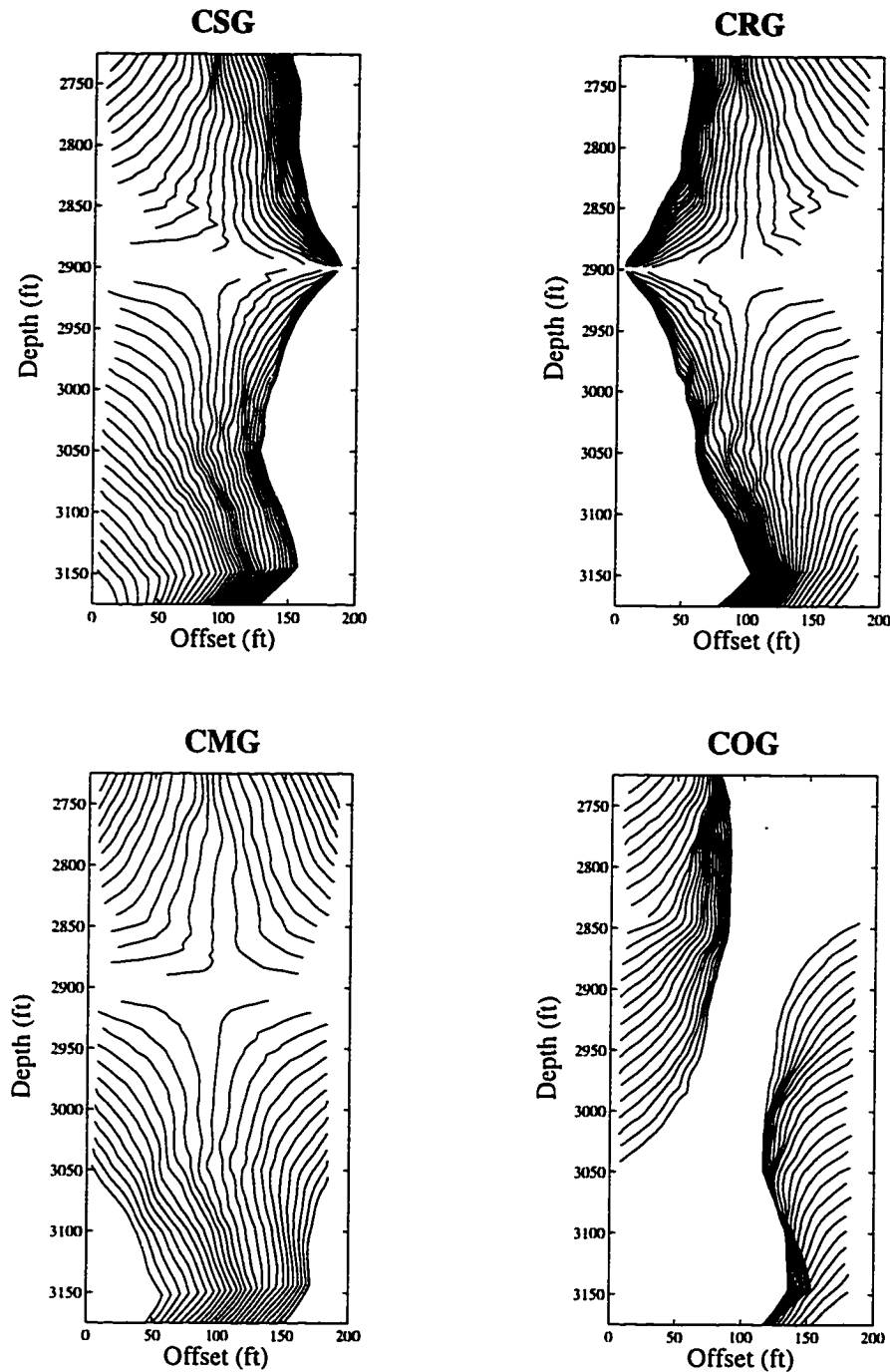


Figure 3.13: Mapping trajectories in different domains obtained using the wavefront method. These trajectories were calculated using the 2-D velocity model and reflector geometries shown previously in Fig. 2.10. Compare these trajectories to the equivalent trajectories for a homogeneous model and flat reflectors shown in Fig. 2.15.

that the method can be extended to more complex models such as those incorporating anisotropy. The only aspect of the method that needs to be modified to handle more complex models is the algorithm for calculating traveltime maps. The calculation of the mapping trajectories and the data transformation are independent of the traveltime map calculations. Extending the wavefront mapping technique to include anisotropic models will be important in future work for imaging reflections in media where velocity anisotropy is significant.

## CHAPTER 4

# TRAVELTIME TOMOGRAPHY USING DIRECT AND REFLECTED ARRIVALS: THEORY AND IMPLEMENTATION

### 4.1 Introduction

The potential of surface seismic reflection tomography as a velocity estimation tool has been a focus of study in the recent past (Bishop et al., 1985; Ivansson, 1986; Stork, 1988; Bube et al., 1989). Little work, however, has been done in the area of crosswell reflection tomography. Partly this is because reflections have been effectively extracted from crosswell data only recently (Lazaratos, 1993; Lazaratos et al., 1995). Calnan and Schuster (1989) compared direct arrival and combined direct and reflected arrival tomography in a theoretical study. This study was performed using straight rays, fixed horizontal reflectors, and vertical boreholes. Their conclusion was that the primary benefit of direct and reflected arrival tomography was that it could yield a finer velocity resolution than allowed by direct arrival tomography.

More recently, resolution analyses were performed by Bube and Langan (1995) using acquisition parameters based on the 1991 and 1993 McElroy Reservoir Geosciences Project (MRGP) experiments (Harris et al., 1995). The motivation of these analyses was to obtain information on how well reflector depths and velocity might be resolved in a combined direct and reflected arrival inversion. Two synthetic problems were formulated: one based on the ~180 ft McElroy profile, and the other based on the ~600 ft profile. These studies estimated errors in reflector depths of a *few inches* for the 180 ft survey and 0.5–2.5 ft for the 600 ft survey. Another observation, consistent with those made in surface seismic tomography, was that good resolution of reflector depths could be expected in spite of mediocre velocity resolution. These results suggest that CDRATT can be an effective velocity estimation tool for crosswell reflection imaging.

In this chapter I describe the theory and implementation of CDRATT. First I review the basic setup of the linearized system of equations defining the inverse problem. This is done in a systematic fashion extending direct arrival traveltime tomography to CDRATT. Then I discuss the details of the CDRATT implementation including model parameterization, raytracing, and calculating traveltime and depth derivatives. Finally, I discuss the solution of the inverse problem including the problem set-up, regularization, and continuation approach. Numerical tests and validations are provided in Chapter 5.



## 4.2 Crosswell traveltimes tomography: basic theory

Ray-theoretic seismic traveltimes tomography is typically a non-linear problem due to large variations of velocity within the Earth. Traveltimes tomography is non-linear in the sense that the velocity field is required to calculate the raypaths which are required to solve for the velocity field. One procedure used to solve the non-linear tomography problem is the Gauss-Newton method (Marquardt, 1963). In the Gauss-Newton method the non-linear problem is linearized by using an initial estimate of the model parameters. The solution of the linearized problem is an updated estimate of the model parameters. This procedure is performed in an iterative fashion until some convergence criteria is finally reached; usually convergence is assumed when the difference between the updated solution and the initial estimate becomes negligible.

To describe how reflection traveltimes and reflector depths are added to the tomography problem I will focus on a single linearized step:

$$\mathbf{A} \mathbf{x} = \mathbf{t} \quad \text{Eqn. 4.1}$$

where  $\mathbf{A}$  is the traveltimes derivative matrix,  $\mathbf{x}$  is the model parameters vector, and  $\mathbf{t}$  is the observed traveltimes vector. The dimensions of  $\mathbf{A}$  are  $m \times n$ , where  $m$  is the number of traveltimes observations and  $n$  is the number of parameters being calculated. Usually the matrix  $\mathbf{A}$  is overdetermined so the problem is solved using least squares or some other norm. Also, since an estimate of  $\mathbf{x}$  is used to define  $\mathbf{A}$ , the problem typically is defined in terms of residual traveltimes ( $\Delta t$ ) and perturbations to the parameters ( $\Delta \mathbf{x}$ ). To keep the explanations simple I limit the discussion in this section to the setup of Eqn. 4.1. Later in this chapter I describe the solution of the actual inverse problem.

The exact form of  $\mathbf{A}$  and  $\mathbf{x}$  are related to how the model is parameterized. In order to be more specific about the setup of matrix  $\mathbf{A}$  I use a simple model parameterization. One of the simplest ways to parameterize the slowness model is as orthogonal, constant slowness (1/velocity) cells. Figure 4.1 shows a simple numbering scheme for this constant slowness parameterization and how the values are stored in vector  $\mathbf{x}$ . The values of matrix  $\mathbf{A}$  are the derivatives of traveltimes with respect to the model parameters, in this case slowness only. Each row of  $\mathbf{A}$  corresponds to an individual raypath of a source-receiver pair. Each column in that row contains the contribution of a particular cell to the traveltimes of that raypath. Only cells crossed by a ray have non-zero traveltimes derivatives in the constant slowness cell parameterization and the value of the traveltimes derivative is the length of the ray in that cell.

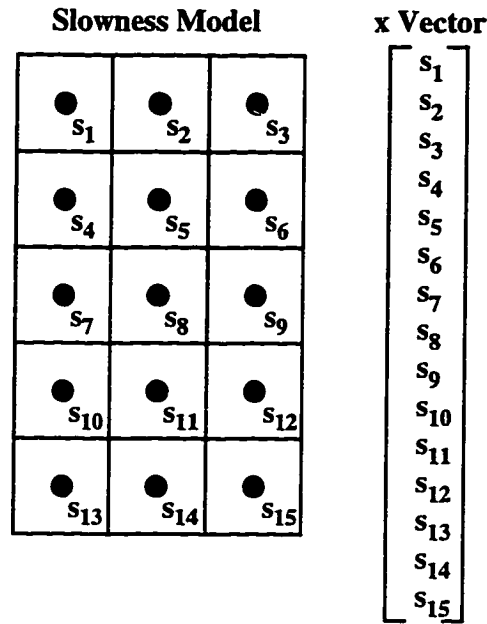


Figure 4.1: A graphical illustration of a simple parameterization of the slowness model and how it is stored as a vector. The slowness model is defined at each node which is located in the center of the constant slowness cell.

### 4.2.1 Direct arrival traveltime tomography

Direct arrival traveltime tomography is the most common method of processing crosswell data. Typically the only parameters being determined are the slowness (1/velocity) values of the model. By substituting  $s$  (slowness) for  $x$  we can rewrite Eqn. 4.1 as:

$$\mathbf{A} \mathbf{s} = \mathbf{t} \quad \text{Eqn. 4.2}$$

The number of elements in  $\mathbf{s}$  equals the number of slowness cells ( $n$ ) in the model and the number of elements in  $\mathbf{t}$  ( $m$ ) equals the number of traveltime observations.

Expressing Eqn. 4.2 in matrix form further clarifies the setup of the problem:

$$\begin{bmatrix} \frac{\partial t_1}{\partial s_1} & \frac{\partial t_1}{\partial s_2} & \frac{\partial t_1}{\partial s_3} & \cdots & \frac{\partial t_1}{\partial s_m} \\ \frac{\partial t_2}{\partial s_1} & \frac{\partial t_2}{\partial s_2} & \frac{\partial t_2}{\partial s_3} & \cdots & \frac{\partial t_2}{\partial s_m} \\ \vdots & \vdots & \vdots & \ddots & \vdots \\ \frac{\partial t_n}{\partial s_1} & \frac{\partial t_n}{\partial s_2} & \frac{\partial t_n}{\partial s_3} & \cdots & \frac{\partial t_n}{\partial s_m} \end{bmatrix} \begin{bmatrix} s_1 \\ s_2 \\ s_3 \\ \vdots \\ s_m \end{bmatrix} = \begin{bmatrix} t_1 \\ t_2 \\ \vdots \\ t_n \end{bmatrix} \quad \text{Eqn. 4.3}$$

From the system of equations shown in Eqn. 4.3 the linear equations corresponding to the various source-receiver traveltime observation can be more easily seen. The variable  $\partial t_i / \partial s_j$  is the length of raypath  $i$  in cell  $j$ . The unknown  $s_j$  is the slowness of the  $j$ 'th cell and  $t_i$  is the traveltime observation corresponding to the  $i$ 'th raypath. Each single equation in the system of equations corresponds to a single traveltime observation. For example, the first raypath, seen in row 1 of the **A** matrix, defines the linear equation

$$\frac{\partial t_1}{\partial s_1} s_1 + \frac{\partial t_1}{\partial s_2} s_2 + \frac{\partial t_1}{\partial s_3} s_3 + \dots + \frac{\partial t_1}{\partial s_m} s_m = t_1 \quad \text{Eqn. 4.4}$$

Now that the setup of direct arrival traveltime tomography has been defined I will describe how reflection traveltimes can be added to the inversion.

#### 4.2.2 Combined direct & reflected arrival tomography

In my previous work in the area of combined direct and reflected arrival traveltime tomography (CDRATT) I assumed the locations of the reflectors were known (Van Schaack and Lazaratos, 1993; Van Schaack, 1994). The shortcoming of this assumption is that typically the reflector locations are *not* known and an iterative approach must be used to refine an initial estimate of the reflector geometries. One example of this approach (Van Schaack and Lazaratos, 1993) is to initiate the combined traveltime inversion assuming flat reflectors. The solution of this traveltime inversion is then used to create upgoing and downgoing reflection images. Updated reflector locations are interpreted from these new reflection images and used in the next non-linear inversion of the traveltime data. This is similar to the approach sometimes used in surface seismic traveltime tomography (Stork, 1988) and is run in an iterative fashion to optimize the stacked results. The disadvantage of this approach is that it is iterative. Tomography and reflection imaging must be performed repeatedly and new reflector geometries must be interpreted each iteration. This is costly in both computer time and manpower.

Nevertheless, for the purpose of completeness, it is useful to describe the simultaneous inversion of direct and reflected arrival with fixed (known) reflector depths. In this case, the addition of the reflection traveltime data to a direct arrival inversion is straightforward. No parameters are added to the **x** vector so **s** = **x** as in Eqns. 4.2 & 4.3. The only change is the addition of a row to **A** and **t** for each reflection traveltime and its associated raypath. Since the reflector location is known the only parameters that can influence the reflection traveltime are the slowness values of the cells through which the raypath passes. So, for

each reflection traveltime, a linear equation in the form of Eqn. 4.4 can be added to the linear system of equations. Once the linear system is defined the inversion can be performed in the same manner as if only direct arrivals were being used.

The theoretical aspects of combining direct and reflected traveltimes to solve for velocity and reflectors depths simultaneously have been studied by Bube and Langan (1995). The focus of their work was to study the effect of adding reflection traveltimes to the crosswell traveltime inversion, in particular, whether the drawback of adding more unknowns, the reflector depths, would outweigh the advantages gained by adding the additional traveltimes. The result of their resolution analysis for two realistic crosswell geometries is that reflector depths are well determined in the crosswell geometry and that reflection traveltime improve the resolution of the slowness field, particularly in the near proximity of the reflector. Their theoretical results, therefore, support the idea that simultaneously inverting direct and reflected arrival traveltimes has practical advantages.

To solve for model slowness and reflector depths simultaneously, both  $\mathbf{A}$  and  $\mathbf{x}$  must be modified. Although I use a more general description of the reflectors in the implementation of the CDRATT inversion I use flat reflectors here, in this discussion, to describe how Eqns. 4.3 & 4.4 are modified. Each flat reflector can be fully described by one parameter, its depth. The notation,  $Zr_j$ , signifies the depth of reflector  $r_j$ . For each reflector that traveltime picks are available an additional parameter is added to  $\mathbf{x}$ . Corresponding to each parameter added to  $\mathbf{x}$ , an additional column is added to  $\mathbf{A}$ . Eqn. 4.5 illustrates one way to modify the linear set of equations shown in Eqn. 4.3 to include reflection traveltimes and solutions for reflector depths.

$$\begin{array}{l}
 \text{Direct arrival raypaths} \\
 \text{Reflected arrival raypaths}
 \end{array}
 \begin{bmatrix}
 \frac{\partial t_1}{\partial s_1} & \frac{\partial t_1}{\partial s_2} & \frac{\partial t_1}{\partial s_3} & \dots & \frac{\partial t_1}{\partial s_m} & 0 & \dots & 0 \\
 \dots & \dots & \dots & \dots & \dots & 0 & \dots & 0 \\
 \frac{\partial t_{n1}}{\partial s_1} & \frac{\partial t_{n1}}{\partial s_2} & \frac{\partial t_{n1}}{\partial s_3} & \dots & \frac{\partial t_{n1}}{\partial s_m} & 0 & \dots & 0 \\
 \frac{\partial t_{n2}}{\partial s_1} & \frac{\partial t_{n2}}{\partial s_2} & \frac{\partial t_{n2}}{\partial s_3} & \dots & \frac{\partial t_{n2}}{\partial s_m} & \frac{\partial t_{n2}}{\partial Zr_1} & \dots & 0 \\
 \dots & \dots & \dots & \dots & \dots & \dots & \dots & \dots \\
 \frac{\partial t_n}{\partial s_1} & \frac{\partial t_n}{\partial s_2} & \frac{\partial t_n}{\partial s_3} & \dots & \frac{\partial t_n}{\partial s_m} & 0 & \dots & \frac{\partial t_n}{\partial Zr_r}
 \end{bmatrix}
 \begin{bmatrix}
 s_1 \\
 s_2 \\
 s_3 \\
 \dots \\
 s_m \\
 Zr_1 \\
 \dots \\
 Zr_r
 \end{bmatrix}
 =
 \begin{bmatrix}
 t_1 \\
 \dots \\
 t_{n1} \\
 t_{n2} \\
 \dots \\
 t_n
 \end{bmatrix}
 \quad \text{Eqn. 4.5}$$

The  $\mathbf{A}$  matrix in Eqn. 4.5 has been assembled with rows related to direct arrival traveltimes placed in the top part and rows related to reflected arrival traveltimes placed in

the bottom part. A new term has been introduced in the  $\mathbf{A}$  matrix,  $\partial t_i / \partial Z r_j$ . This term is the derivative of the traveltimes with respect to changes in the reflector depth. In Eqn. 4.5 I assume a parameterization where slowness and reflector depths are decoupled. For this reason  $\partial t_i / \partial Z r_j$  is always zero for direct arrival raypaths. I also ignore raypaths which contain more than one reflection so there is only one non-zero reflector derivative for each reflected raypath.

### 4.2.3 Summary of basic theory

In this section I have described the basic setup of a linear set of equations for traveltimes tomography. The particular case of interest in this thesis is the combined inversion of direct and reflected arrival traveltimes to simultaneously solve for the slowness field and the location of selected reflectors. The formulation of this inversion has been derived for a basic model to provide the necessary background for a discussion of the implementation of the CDRATT inversion. The exact setup of the linearized system of equations depends on several factors. The items to be discussed are model parameterization, regularization, and the approach taken for solving the non-linear inversion problem.

## 4.3 Parameterization of the model

A number of issues influence the choices made in parameterizing the CDRATT inversion. One issue is accuracy. For example, describing velocity as a 1-D function of depth leads to inversion errors for data sets collected in areas where lateral velocity variations are present. Parameterizing the problem allowing velocity to vary in 2-D may reduce inversion errors but leads to the issue of problem size. Invariably, increasing the number of parameters used to define the model will increase the size of the inversion. Potentially, this may lead to a problem which is overparameterized. Worse yet, a large inverse problem may exceed the capacity of the computer hardware in the areas of memory or speed.

In the implementation of CDRATT used in this thesis I have focused on parameterizing the model to accommodate the features commonly found in STP data sets and the limitations of STP computer hardware. The primary features I have chosen to include in the CDRATT inversion are:

- 2-D isotropic velocity variations,
- deviated source and receiver wells,
- and dipping, non-linear, and/or discontinuous reflector interfaces.

Where possible the code has been designed to ease the accommodation of additional parameters in the future, such as anisotropy and depth statics.

### 4.3.1 Slowness

In the CDRATT inversion the “velocity” model is defined using constant slowness cells. I do this for two reasons: to maintain simplicity and to reduce computer memory requirements. Simplicity is maintained since the inverse problem is defined using the setup shown in Eqn. 4.5. The traveltime derivative,  $\partial t_i / \partial s_j$ , can be calculated in a straightforward manner using this parameterization since it is simply the length of the  $i$  ‘th ray in the  $j$  ‘th cell.

The primary reason I use the constant slowness cell parameterization is that the amount of RAM memory required to solve the inverse problem is minimized. This reduction in memory results from the way the **A** matrix is stored. Any one ray will only intersect a small number of cells in the slowness model. Rather than wasting space storing all the zero traveltime derivatives the **A** matrix is preserved in a compact form where only the non-zero traveltimes derivatives are stored. For example, a horizontal ray traveling from one side to the other through the Fig. 4.1 model would have 12 zero and 3 non-zero traveltime derivatives. Only the 3 non-zero derivatives (and their indices) need be saved.

Another useful way to parameterize the slowness model is by using nodes similar to those in Fig. 4.1 but using them to define the value of the slowness at the corners of a cell. By interpreting the slowness within the cell this parameterization yields a continuous function of slowness in 2-D. One advantage of a continuous function of slowness is that it is much more stable to trace rays in. The memory requirements, however, using this parameterization are double those using the constant slowness cell parameterization. This increase results from the more complex traveltime derivatives that result from this parameterization. Instead of the 3 non-zero derivatives saved in our previous example we would be required to save 6 traveltime derivatives. This is because the slowness at any point in the model is a function of at least 3 nodes.

### 4.3.2 Reflectors

In the basic theory section of this chapter I outlined the setup of the linearized inverse problem. This setup included solutions for reflector location defining the reflectors using a single parameter, depth. This parameterization limits our model to simple flat reflectors. I have implemented a more general description of the reflectors in the CDRATT inversion. The depth of each reflector is defined at a constant interwell interval across the slowness

model. The interval between defined reflector locations is a variable set by the user. Between defined reflector locations the reflector is described using a cubic spline curve. The advantage of using the cubic spline curve is that the 1st derivative of depth with respect to interwell offset is continuous. This improves the ability of the raytracer to link source and receivers for reflected raypaths.

Discontinuous reflectors are handled as independent reflecting horizons. The starting estimate for each reflecting horizon where traveltime picks are obtained is flat, continuous, and connects from one side of the slowness model to the other. The actual extent of the reflector is determined following the inversion and is based on the ray coverage along the reflector. This approach for handling discontinuous reflector does not provide any information about which discontinuous reflector segments are associated with which others. As with surface seismic imaging, determining fault locations and throw would be done in the interpretation phase.

## 4.4 Forward modeling — raytracing & traveltimes

I use an initial value raytracer and solve the two-point problem using an iterative approach. One drawback of the discrete constant slowness cell parametrization of the model is that it suggests raytracing by launching rays and calculating changes in trajectory at cell boundaries using Snell's Law. The resulting rays tend to be undesirable since they can make sharp changes in trajectory at each cell boundary which does not conform to the assumptions made in justifying the use of ray theory in the first place. Unfortunately, as mentioned previously, parameterizing the slowness model using gradients leads to inverse problems which are too large to solve. To overcome this dilemma I have adopted a hybrid parameterization of slowness.

I implement a hybrid parametrization of slowness starting with a model where slowness values are defined at node points on an evenly spaced grid. This gridding scheme is identical to that shown in Fig. 4.1. The difference is in how the value of slowness between nodes is allowed to vary. For raytracing, where better results are obtained with a continuous slowness field, I interpolate the slownesses as needed using bi-linear interpolation. To calculate traveltimes and the traveltime derivatives required to set up the inverse problem I assume each node defines the center of a constant slowness cell.

While this hybrid scheme might seem somewhat inconsistent it roughly parallels the philosophy used in straight ray tomography. In straight ray tomography the calculation of the raypaths and the discretization of the slowness field (for purposes of setting up the inverse problem) are completely decoupled. Likewise, in this hybrid parameterization I

obtain the most reliable raypaths using the best parameterization and then, ignoring the origin of the raypaths, use them in a model parameterization ideal for the inverse problem. Results of synthetic tests are presented in the next chapter which support my opinion that this hybrid approach of model parameterization is effective and sufficiently accurate to obtain good results.

#### 4.4.1 Initial value raytracing

I use a modified version of the initial value raytracer described by Harris (1992). This raytracer calculates raypaths in smoothly varying heterogeneous media. Raytracing is performed in a piece-wise fashion using the Runge-Kutta method to solve the ordinary differential equations defining the raypath.

I have modified the original code described by Harris to obtain slightly better performance. The original version calculates the slowness gradient at each point along the raypath from interpolated slowness values. To improve speed and efficiency I calculate the slowness gradient in the x and z directions at each node point prior to raytracing. I then obtain the gradient when required by interpolating the precalculated gradients. Bi-linear interpolation is used both to interpolate slowness values to calculate the gradients and to interpolate the gradients themselves.

#### 4.4.2 Calculating reflected raypaths

Reflected raypaths are calculated using the same initial value raytracing code as direct raypaths. Raypaths are calculated first for all direct arrivals and then for all reflected arrivals. To obtain a reflected raypath for a particular reflector the ray is initially launched in the same fashion as a direct ray. The ray is monitored as it is calculated step by step until it crosses the reflecting horizon.

Once the ray crosses the reflecting horizon I calculate the exact reflection point. The reflection point calculation uses an iterative approach. First points on the reflector are obtained using the cubic spline approximation which bracket the possible intersection point. The reflector is assumed to be linear between these points and an intersection point with the raypath is found. This intersection point is used to calculate a new point on the reflector which replaces one of the two previous reflector points so the possible reflection point remains bracketed. This routine is performed iteratively until the intersection point is found to a user-defined tolerance.

The intersection point of the ray and the reflector is used to calculate the local incidence angle of the ray on the reflector. This angle is computed using the local raypath



trajectory and a derivative function of the cubic spline curve to determine the local reflector dip. From this information a reflected trajectory is computed and the ray is re-launched. The ray then proceeds until it intersects the well or leaves the model.

#### 4.4.3 The two-point raytracing problem

The two-point problem is solved using a standard iterative approach which is a derivation of a code described by Langan et al (1985). Rays are traced by receiver gather from receiver to source. I do this partly for philosophical reasons, to parallel the acquisition method, and partly to aid the calculation of traveltime residuals.

The first step in solving the two-point problem is to shoot a reference fan for the receiver gather under consideration. The rays are shot so as to provide a relatively uniform coverage at the source well. For each source-receiver pair for which a raypath is desired the algorithm finds rays from the reference fan which bracket the pair. Attempts are made to connect the source and receiver using the reference fan data as a starting point and a derivative-based search algorithm. Rays are shot from receiver to source until a ray is “captured” within a user defined “capture tolerance” or until a user-specified number of iterations is reached and the process is aborted.

It is possible to find more than one pair of reference rays bracketing the source. This will occur when triplications are present. To discriminate between these various rays, the user sets a flag indicating whether rays of minimum traveltime or minimum path length are desired. A minimum path length raypath corresponds to the “energetic” direct arrival ray. Raypaths for all possible source-receiver combinations are calculated and the desired path is stored.

#### 4.4.4 Calculating traveltimes and traveltime derivatives

Once the raypath is obtained its traveltime is calculated using the constant slowness cell parameterization. The traveltime of raypath  $i$ ,  $t_i$ , is calculated using this equation,

$$t_i = \sum_{j=1}^m l_{ij} s_j \quad \text{Eqn. 4.6}$$

In Eqn. 4.6  $l_{ij}$  is the length of the  $i$  ‘th ray in the  $j$  ‘th cell and  $s_j$  is the slowness of the  $j$  ‘th cell.

The traveltime derivative,  $\partial t_i / \partial s_j$ , for the constant slowness cell parameterization is simply the length of the ray in the cell,  $l_{ij}$  from Eqn. 4.6. I currently use an estimate of this

which is accurate to 1/10 of a foot. To obtain this estimate I resample the ray in 1/10 ft increments and count the number of segment endpoints which fall in each cell. The advantage of this approximation is speed and simplicity.

#### 4.4.5 Calculating reflector depth derivatives

Traveltime derivatives with respect to the reflector depth parameters,  $\partial t_i / \partial Z r_j$ , are calculated within the raytracing process. To calculate these derivatives I use the expression derived by Bishop et al. (1985) for upgoing reflection events (e.g. those found in surface seismic reflection tomography). The expression for the traveltime depth derivative of reflector parameter  $j$  when the reflection point,  $(x_R, z_R)$ , is located (in offset) between  $x(r_j)$  and  $x(r_{j-1})$  is

$$\frac{\partial t_i}{\partial Z r_j} = \pm 2s(x_R, z_R) \cos \beta \cos \theta \left( \frac{x_R - x(r_{j-1})}{x(r_j) - x(r_{j-1})} \right) \quad \text{Eqn. 4.7}$$

In this equation,  $s(x_R, z_R)$  is the local slowness at the reflection point,  $\beta$  is the dip of the reflector from the horizontal, and  $\theta$  is the local angle of incidence of the raypath on the reflector. To account for downgoing reflection events the derivative is multiplied by -1. This procedure is represented by the +/- expression at the front of Eqn. 4.7.

### 4.5 Solving the inverse problem

To solve the tomographic inverse problem I use a continuation approach described by Bube and Langan (1994). The basis of this approach is to add regularization to the inverse problem in the form of smoothing penalty terms. The non-linear system of equations is then solved with penalty weights fixed using the Gauss-Newton (G-N) method. After the non-linear problem is solved the penalty weights are relaxed and the non-linear problem is solved again. This procedure is repeated until an optimum solution is reached. In this approach a “continuation step” refers to the solution of a non-linear problem through a series of linearized steps while holding the smoothing penalties constant. A “G-N step” is the solution of a single linearized system of equations within the larger continuation step.

There are several advantages to this approach. One is that it provides regularization to the inverse problem. A second, related advantage, is that the optimum weights for the regularization do not need to be known *a priori*. A range of weights is run during the inversion so that initial iterations are dominated by the smoothing terms and later

inversions are dominated by the data. Although a wide variety of smoothing terms are possible I have found, like Bube and Langan (1994), that penalty terms for the horizontal and vertical first spatial derivatives of slowness work well. Additionally, in my inversion, I have found that I must add a smoothing penalty term for the second derivative of the reflector depth with respect to offset. In the next sections I will further discuss the details of these penalty terms.

#### **4.5.1 Regularization — slowness field**

In my crosswell inversion I use smoothing penalty terms for horizontal and vertical spatial derivatives of slowness in the same manner as Bube and Langan (1994). Typically, I weight the horizontal derivatives about four times heavier than the vertical derivatives although this is a user-defined variable. This preferential weighting is consistent with the lower resolution of the typical crosswell inversion in the horizontal direction. Also, there is typically less lateral variation in slowness than vertical variation in many geologic settings.

#### **4.5.2 Regularization — reflector geometries**

Because I allow the possibility of reflectors which do not extend completely from one well to the other there must be regularization added to the solution of the reflector depths. The main reason regularization is required is because of the cubic spline parameterization of the reflectors. If, for example, a reflector only extends half way between the wells only about half of the reflection depth derivatives for that reflector will be non-zero. The reflector depth parameters for which the depth derivatives are always zero lie in the null space of the model. The least-squares solver used in my program will not provide any perturbations to those parameters.

In a CDRATT inversion containing discontinuous reflectors there will exist adjacent reflector points where one is updated during the inversion and the other remain unmodified since it lies in the null space of the inversion. The unfortunate side effect of this is that the cubic spline solution across this discontinuity will vary wildly. Even worse, these wild variations will not be confined to the area of the discontinuity. Once a reflector geometry acquires these sharp oscillations it becomes difficult to link rays through this reflector.

To solve this problem I have added a smoothing penalty term to the inversion to minimize second derivative variations of the reflector depth with respect to horizontal offset. The effect of this penalty term on discontinuous reflectors is to preserve the slope of the reflector when no other information is present. Like the smoothing penalty terms

applied to the slowness field, I decrease the weight of this reflector penalty term at the beginning of each continuation step. I have found in synthetic examples shown in chapter 4 that the weight of the reflector second derivative penalty term need not be very strong to maintain the stability of the reflector solutions.

### 4.5.3 Problem setup

The least-squares solution of the linearized G-N step is the minimum of

$$\|A\delta\mathbf{x} - \delta\mathbf{t}\|^2 + c_h\|D_h\delta\mathbf{x}\|^2 + c_v\|D_v\delta\mathbf{x}\|^2 + c_z\|D_z\delta\mathbf{x}\|^2 \quad \text{Eqn. 4.8}$$

In Eqn. 4.8,  $A$  is the matrix of derivatives of the traveltimes with respect to each of the parameters of the model. In this case,  $A$  contains derivatives of traveltimes with respect to the slowness in each cell and derivatives of traveltimes with respect to the depth of the reflectors. The vector  $\delta\mathbf{t}$  contains the traveltime residuals, e.g. the differences between traveltimes calculated using the starting model  $\mathbf{x}^k$  and traveltimes observed in the experiment:

$$\delta\mathbf{t} = \mathbf{t}(\mathbf{x}^k) - \mathbf{t}_{obs} \quad \text{Eqn. 4.9}$$

In Eqn. 4.9 the vector,  $\delta\mathbf{x}$ , is the perturbation to the starting model  $\mathbf{x}^k$  required to minimize Eqn. 4.8. The result of the  $k$ 'th G-N step is the  $k+1$ 'th updated model,  $\mathbf{x}^{k+1}$ , where

$$\mathbf{x}^{k+1} = \mathbf{x}^k + \delta\mathbf{x} \quad \text{Eqn. 4.10}$$

The remaining terms in Eqn. 4.8 are the smoothing penalty terms. The constants  $c_j$  are the weights of the various penalty terms relaxed prior to the beginning of each new continuations step. The matrix operators,  $D_h$ ,  $D_v$ , and  $D_z$ , are used to calculate the derivatives used in the smoothing penalties and are constant through the entire inversion.

The final version of the linearized system of equations solved in the CDRATT inversion is show in a schematic fashion in Equation 4.11. I have broken up the  $A$  matrix into 5 distinct parts, each designated by a row. The first row represents derivatives related to direct arrivals only. Notice in the first row that the derivatives of traveltimes with respect to reflector depths are zero as you would expect for non-reflected raypaths. The second row

represents all reflected arrival raypaths which have both slowness and depth derivatives. The next three rows are the smoothing penalty terms.

The right hand side of Eqn. 4.11 contains the traveltime residuals, the difference between model and observed times, and weighting terms for the regularization penalties. To keep the penalty terms properly balanced they are normalized by the Frobenius norm of subsets of the  $\mathbf{A}$  matrix (Bube and Langan, 1994). The values  $c_h$  and  $c_v$  are calculated by taking the current penalty weight and scaling it by the square of the Frobenius norm of the traveltime derivatives with respect to slowness. The value  $c_z$  is scaled by the square of the Frobenius norm of the traveltime derivatives with respect to depth. The constant  $C_{start}$  provides the user the ability to drive the derivatives toward an input slowness model or towards flatness (when  $C_{start}$  is homogeneous). I typically initialize  $C_{start}$  to be homogeneous and equal the average slowness of the data set.

$$\begin{bmatrix} \dots & \frac{\partial t_1}{\partial s_j} & \dots & 0 \\ \dots & \frac{\partial t_n}{\partial s_j} & \dots & \frac{\partial t_n}{\partial Z_{r_r}} \\ \dots & \sqrt{c_h} \mathbf{D}_h & \dots & 0 \\ \dots & \sqrt{c_v} \mathbf{D}_v & \dots & 0 \\ \dots & 0 & \dots & \sqrt{c_z} \mathbf{D}_z \end{bmatrix} \begin{bmatrix} \dots \\ \delta s_m \\ \dots \\ \delta Z_{r_r} \end{bmatrix} = \begin{bmatrix} \delta t_{dir} \\ \delta t_{ref} \\ \sqrt{c_h} \mathbf{D}_h \delta(s_m - C_{start}) \\ \sqrt{c_v} \mathbf{D}_v \delta(s_m - C_{start}) \\ -\sqrt{c_z} \mathbf{D}_z \delta Z_{r_r} \end{bmatrix} \quad \text{Eqn. 4.11}$$

## 4.6 Conclusions

In this chapter I present an approach for simultaneously processing direct and reflected arrival crosswell information using traveltime tomography. My implementation of this approach is Combined Direct and Reflected Arrival Traveltime Tomography (CDRATT). The results of a CDRATT inversion are a slowness model and the locations of selected reflectors. The 2-D isotropic slowness model is defined using a cell parameterization and reflectors are defined using cubic splines. The “ideal” solution minimizes the difference between the observed data, the direct arrival traveltimes and reflected arrival traveltimes from selected reflectors, and traveltimes calculated tracing rays through the model.

The CDRATT inversion uses a continuation approach for solving the non-linear tomography problem. Smoothing penalty terms are added to the inversion providing regularization for both the slowness and reflector solutions. The inverse problem is solved in a series of continuation steps where the smoothing penalty terms are slowly relaxed.

Each continuation step consists of a number of linearized Gauss-Newton steps solving the non-linear inverse problem while the weights of the smoothing penalty terms are held constant. Solutions of early continuation steps provide a smooth slowness model and nearly linear reflectors. In later solutions the slowness model is allowed more 2-D variations while the reflectors are allowed to adopt increasingly non-linear fluctuations.

# **CHAPTER 5**

## **TRAVELTIME TOMOGRAPHY USING DIRECT AND REFLECTED ARRIVALS: VALIDATION**

### **5.1 Introduction**

In Chapter 4 I presented the theory and implementation of Combined Direct and Reflected Arrival Traveltime Tomography (CDRATT). In this chapter I present the results of several combined direct and reflected arrival inversions of synthetic data as a validation of the technique. I focus primarily on the ability of CDRATT to accurately recover reflector depths. Two of the synthetic studies are designed to test the ability of the CDRATT inversion to handle non-linear reflectors and discontinuous reflectors. In the final study I invert a synthetic data set modeled after an actual field experiment.

### **5.2 Forward modeling of synthetic data sets**

The synthetic data sets found in this chapter were calculated using a finite-differences eikonal-based program that I have developed. This program is a derivation of an algorithm introduced by Mo (1994) and was discussed previously in Chapter 3. There are several advantages to using the finite-differences eikonal solver as a forward modeler. One advantage is that no raytracing or raypaths are required, making it very fast. Another is that reflection traveltimes can be calculated very easily for arbitrary reflection surfaces.

There is an additional benefit because the forward modeler is different from the initial-value ray tracer used in the inverse problem. The approaches used by these methods to calculating traveltimes are quite different. Nevertheless, traveltimes obtained using these programs should be similar if they are implemented correctly since both modelers are based on ray theory. Different approaches for calculating traveltimes in the forward and inverse problems provide a more thorough validation of the various elements of the process and are more likely to expose implementation errors.

#### **5.2.1 Calculating direct arrival traveltimes**

Calculating direct arrival traveltimes is accomplished in one step using the finite-difference eikonal code. For each receiver location a traveltime map is generated (to maintain consistency with other codes I prefer to “shoot” from receiver to source). Receiver

to source traveltimes are read from the traveltime map location which coincides with the source. Bi-linear interpolation is used when the source location does not reside on a grid node. The traveltimes are recorded for all source locations after which the code increments to the next receiver location. All receivers are “shot” in turn until the entire direct arrival traveltime data set has been calculated

### 5.2.2 Calculating reflected arrival traveltimes

The forward modeling of reflected arrival traveltimes is based on the principle of wavefronts used in the XSP-CDP mapping program described in Chapter 3. Combined traveltime maps are used to calculate reflection points, in a 2-D velocity model with arbitrary reflector geometries, which define the mapping trajectories in the XSP-CDP mapping program. The reflection point for each source-receiver-reflector combination is defined by the location of the stationary point of total traveltime along the reflecting horizon. To use this technique for forward modeling one need only record the traveltime obtained from each the source-receiver-reflector combination.

Reflection traveltimes can be calculated for any number of reflectors at little additional computational expense using the combined traveltime approach. To minimize computations though, I calculate reflection traveltimes for all desired reflectors before calculating the combined traveltime map for the next source-receiver pair. A subset of computed reflection traveltimes were used in the synthetic examples shown in this chapter to provide data sets that were more like those that would be obtained from field experiments, in terms of coverage and the ability to pick the data.

A NOTE ON EFFICIENCY: Traveltime maps for all source and receiver locations can be calculated and stored in RAM prior to the calculation of reflection traveltimes. From this collection of maps, a combined map can be created for any source-receiver combination simply by adding the appropriate source and receiver maps directly from memory.

## 5.3 Synthetic Study #1

The primary goal of the first synthetic study is to test the ability of direct and reflected arrival tomography to recover the geometries of straight and curved reflectors. I have created a simple model, shown in Figure 5.1, consisting of 3 layers and 4 reflectors. The layers are constant velocity although a mild 2-D filter has been applied to the model to smooth the interfaces slightly.

The forward modeler used to calculate the synthetic traveltimes uses the same cubic spline reflector parameterization as the CDRATT inversion algorithm. The cubic spline



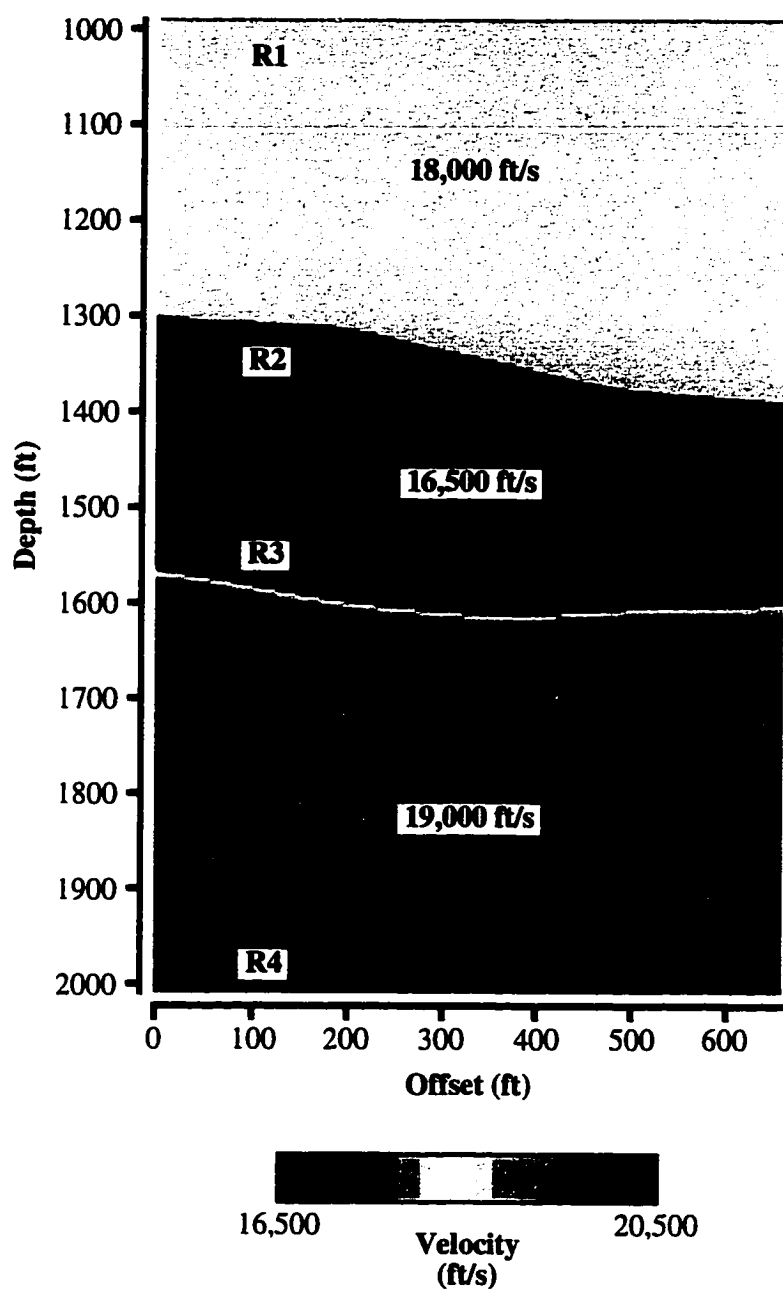


Figure 5.1: This figure shows the velocity distribution of model #1. The reflectors are defined by a cubic spline curve calculated from 8 evenly spaced points across the model.

node definitions of the Study #1 model are shown in Table 5.1. In this example the top and bottom reflectors are linear and horizontal and Reflectors 2 & 3 are curved. The geometry of these reflecting horizons can be seen graphically in Fig. 5.1.

**TABLE 5.1. Synthetic model #1 reflectors**

<b>Offset (ft)</b>	<b>0.0</b>	<b>94.29</b>	<b>188.57</b>	<b>282.86</b>	<b>377.14</b>	<b>471.43</b>	<b>565.71</b>	<b>660.0</b>
<b>Reflector 1</b>	1003.0	1003.0	1003.0	1003.0	1003.0	1003.0	1003.0	1003.0
<b>Reflector 2</b>	1302.0	1310.0	1315.0	1335.0	1355.0	1375.0	1385.0	1392.0
<b>Reflector 3</b>	1569.0	1584.0	1600.0	1610.0	1615.0	1610.0	1607.0	1604.0
<b>Reflector 4</b>	1998.0	1998.0	1998.0	1998.0	1998.0	1998.0	1998.0	1998.0

### **5.3.1 Study #1: acquisition geometry and data specifications**

The synthetic survey is designed with 201 sources and 201 receivers spaced every 5.0 ft along the sides of the model shown in Fig. 5.1. The range of the sources and receivers is from 1000.0–2000.0 ft and the distance between the source and receiver wells is 660.0 ft. Direct and reflected arrival traveltimes were initially calculated for all source-receiver-reflector combinations in the forward modeling. In order to create a data set more closely resembling one that might come from the field some source-receiver-reflector combinations were discarded.

The direct arrival data set was edited by discarding traveltimes for source-receiver pairs at near and far offsets. Near offset traveltimes are often thought to be unreliable in field data sets due to head waves. Far offset traveltimes can be difficult to pick from field data due to poor signal-to noise. So, in this example, I muted traveltimes if the source and receiver were within 75 ft of each other in depth, approximately  $\pm 6.5^\circ$  about the horizontal, and if the source/receiver offset was greater than ~940 ft, about  $\pm 55.0^\circ$ . This aperture is representative of the direct arrival traveltimes that might be obtained in a 600 ft survey.

There are several field data observations which provide a guide for editing synthetic reflected arrival traveltimes. One is that reflections are most visible in processed ~600 ft offset surveys for angles of incidence ranging from approximately  $40\text{--}65^\circ$  (Lazaratos, 1993; Lazaratos, personal comm.). A second observation is that it is difficult to reliably pick traveltimes of a single reflector for both up and downgoing reflections.

So, based on these observations, I restricted reflection traveltimes for each reflector to be exclusively upgoing or downgoing, and I restricted traveltimes for each reflector to fall with a range of Common Mid-depth elevations chosen to keep the incidence angles of the rays approximately  $40\text{--}65^\circ$ . Crosswell Common Mid-depth Gathers (CMG's), discussed in Chapter 2, have the property that the angle of incidence of all rays reflecting off of a flat

reflector in a 1-D velocity field is the same. For this reason CMG's can be used, as an approximation, to edit reflection traveltimes in terms of the angle of incidence. Table 5.2 lists the edited reflected arrival traveltimes based on the direction of the reflection and the CMG range.

**TABLE 5.2. Specifications of Example 1 reflection traveltime data**

	Direction	CMG Range (ft)	# Traveltimes
<b>Reflector 1</b>	downgoing	1187.0–1390.0	6887
<b>Reflector 2</b>	downgoing	1500.0–1702.0	6456
<b>Reflector 3</b>	upgoing	1217.0–1421.0	6239
<b>Reflector 4</b>	upgoing	1609.0–1812.0	6501

### 5.3.2 Synthetic Study #1: inversion and results

I ran a direct and reflected arrival inversion on the synthetic data set starting with a homogeneous velocity model (17,800 ft/s) and flat reflectors defined by 8 nodes. The starting depth of the reflectors was 1000.0, 1347.0 1586.0, and 2000.0 ft. I set the initial horizontal smoothing penalty weight equal to the traveltime data weight and the vertical smoothing penalty to 1/4th of the horizontal value. The initial value of the reflector second derivative smoothing penalty weight was 1/100th the horizontal weight at the beginning of the inversion. The horizontal and vertical smoothing penalty terms were relaxed an order of magnitude every 4 continuation steps and the reflector penalty term was relaxed an order of magnitude every 2 continuation steps.

The ideal, or “best”, answer of this inversion is the result of continuation step 12. By this step the horizontal penalty term, the strongest of the three, has only 4% of the weight of the traveltime data. Traveltime residuals are ~58μs root-mean-square (rms) for the 24,327 reflected rays and ~28μs rms for the 33,993 direct arrival rays. Figure 5.2 shows the velocity results of the traveltime inversion. The velocity tomogram recovers the homogeneous nature of the 3 zones reasonably well. The curved nature of the interfaces bounding the low velocity central layer is also seen in the tomogram although the interfaces themselves are a somewhat blurred.

The recovered reflector parameters are shown in Table 5.3. Unfortunately, a direct comparison cannot be made between the recovered reflector parameters and the original model parameters, listed in Table 5.1. In spite of the fact that 8 parameters are used for each reflector description there is a slight difference in the offsets in the two parameter sets which can be noted across the top of each table. The difference is because the tomogram is 670.0 ft across while the source-receiver offset is 660.0 ft. The raytracer used in the

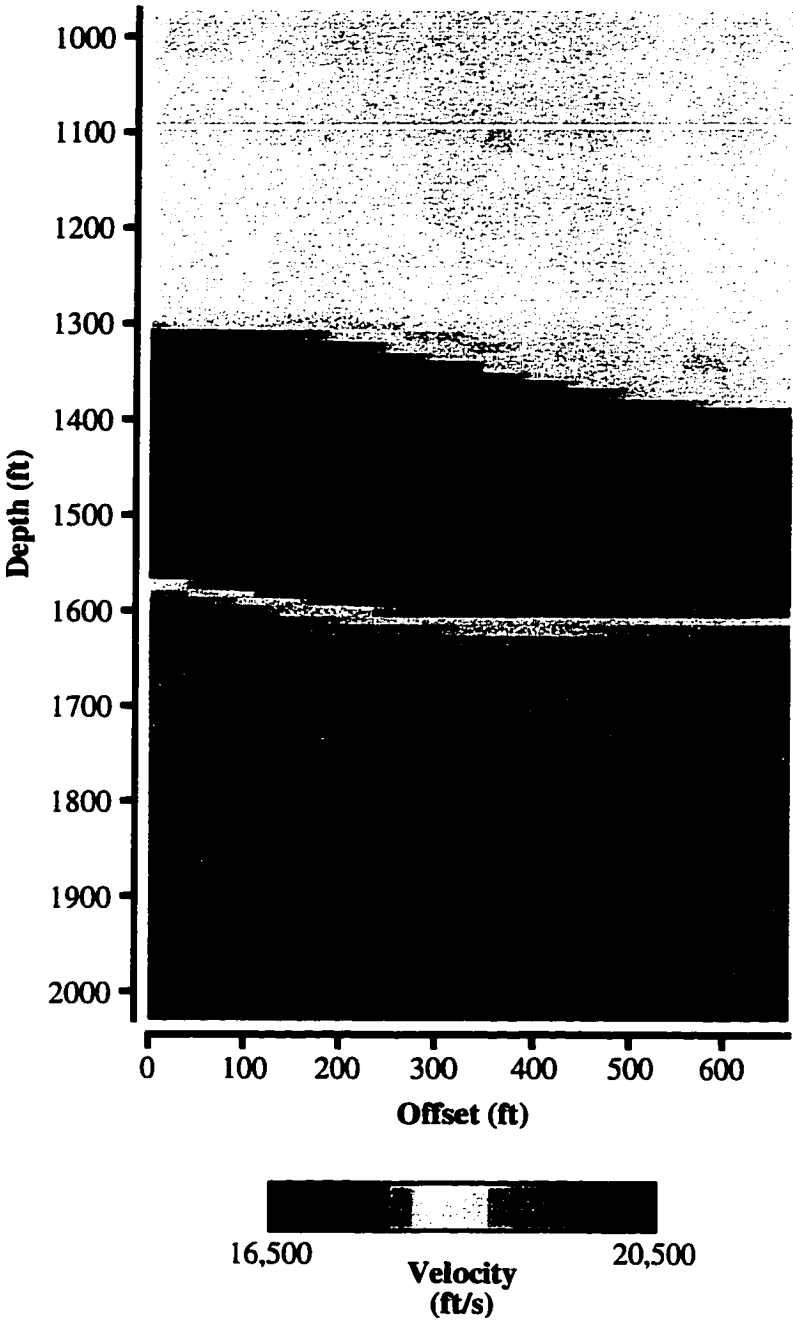


Figure 5.2: The velocity tomogram resulting from 12 continuation steps of a combined direct and reflected arrival traveltimes inversion. Compare this result with the original velocity model used to create the synthetic data seen in Fig. 5.1.

inversion program requires the sources (on the right side of the model) to lie *within* the model so an extra pixel was added to the right of the model for the inversion.

**TABLE 5.3. Example 1 reflector depth inversion results**

Offset (ft)	0.0	95.7	191.4	287.1	382.8	478.6	574.3	670.0
<b>Reflector 1</b>	1002.7	1002.3	1002.1	1002.6	1002.8	1002.9	1002.8	1003.0
<b>Reflector 2</b>	1301.4	1308.9	1315.3	1334.8	1354.6	1373.9	1383.8	1392.3
<b>Reflector 3</b>	1569.7	1586.6	1603.1	1613.1	1617.9	1612.7	1609.4	1603.9
<b>Reflector 4</b>	1998.0	1998.5	1998.9	1998.5	1998.4	1998.5	1998.3	1998.0

While the errors in depth due to the slightly different offset are small, increasing from left to right, a more direct comparison of the recovered reflector depths and the model values has been assembled in Table 5.4. The recovered reflector depths seen in Table 5.3 have been interpolated using the cubic spline definition to the same offset values as the model.

The range of errors in the recovered reflector depths seen in Table 5.4 is -2.3–3.1 ft. The rms error of the recovered reflector depths is 1.4 ft. The resolution of reflector depth is a fraction of the 10.0 ft constant velocity cells used to define the velocity model. The magnitude of these errors supports the theoretical predictions of Bube and Langan (1995) for a 600 ft tomographic inversion. The primary sources of error are Reflectors 2 and 3. The calculated location of Reflector 2 is uniformly shallow while Reflector 3 is uniformly deep. The shallow or deep sense of the reflector errors can be explained as resulting from the direction of the reflection raypaths with respect to the velocity contrast.

**TABLE 5.4. Resampled\* reflector depth inversion results and synthetic model #1 reflector depths**

Offset (ft)	0.0	94.29	188.57	282.86	377.14	471.43	565.71	660.0
<b>Ref. 1 model</b>	1003.0	1003.0	1003.0	1003.0	1003.0	1003.0	1003.0	1003.0
<b>Ref. 1 result*</b>	1002.7	1002.3	1002.1	1002.6	1002.7	1002.9	1002.8	1002.9
<b>Ref. 2 model</b>	1302.0	1310.0	1315.0	1335.0	1355.0	1375.0	1385.0	1392.0
<b>Ref. 2 result*</b>	1301.4	1308.8	1315.0	1333.8	1353.4	1372.7	1383.2	1391.2
<b>Ref. 3 model</b>	1569.0	1584.0	1600.0	1610.0	1615.0	1610.0	1607.0	1604.0
<b>Ref. 3 result*</b>	1569.7	1586.3	1602.7	1612.7	1617.9	1613.1	1609.7	1604.7
<b>Ref. 4 model</b>	1998.0	1998.0	1998.0	1998.0	1998.0	1998.0	1998.0	1998.0
<b>Ref. 4 result*</b>	1998.0	1998.5	1998.9	1998.5	1998.4	1998.5	1998.3	1998.0

\*The reflector inversion results have been interpolated using a cubic spline interpolation to obtain reflector depths for the same reflector x offsets as the original model.

Reflection traveltimes obtained from Reflector 3 are for upgoing raypaths. The ability of the CDRATT inversion routine to exactly locate a reflector defined by a sharp interface

is related to the ability of the inversion to define the interface itself. Since the velocity gradient in the vertical direction is somewhat smooth the reflector must be shifted slightly to compensate for the gradient. In the case of Reflector 3, a low velocity zone overlies a high velocity zone and the raypaths travel primarily through low velocities. The smooth gradient causes the raypaths to travel through velocities which are a little too high near the reflector. This results in a calculated traveltime which is too low if the reflector is properly located. To compensate for this the reflector is shifted down slightly to lengthen the raypaths and increase the traveltimes. The same reflector would be shifted up slightly if the model consisted of a high velocity zone overlying a low velocity zone. This same reasoning applies to Reflector 2 except that the direction of the correction is opposite since the location of this reflector is calculated using downgoing rays.

## 5.4 Synthetic Study #2

The second example is designed to test the ability of the direct and reflected arrival traveltime inversion to recover reflector geometries when the reflectors are discontinuous. The model used to generate the direct and reflected arrival traveltimes is shown in Figure 5.3. This model includes 5 dipping layers that have been thrown offset by a steeply-dipping normal fault. I have also included a low velocity layer near the bottom of the model with a velocity contrast across the fault. This situation is designed to mimic a possible field experiment where a target exists near the bottom of the survey. This is a situation where traditional direct arrival tomography has poor lateral resolution.

The dimensions of the model shown in Fig. 5.3 are similar to those of the first synthetic model (Fig. 5.1) except that the new model is 650.0 ft across rather than 660.0 ft. The interfaces are linear, except across the fault, and dip uniformly at  $8.75^\circ$  from the receiver well to the source well. Each reflector can be completely described by the point at which it intersect a well and the point it intersects the fault. The broken reflectors have been numbered separately to maintain a consistency with the inversion routine which solves for the broken pieces of a discontinuous reflector as separate individual reflectors. The geometries of the reflectors are given in Table 5.5.

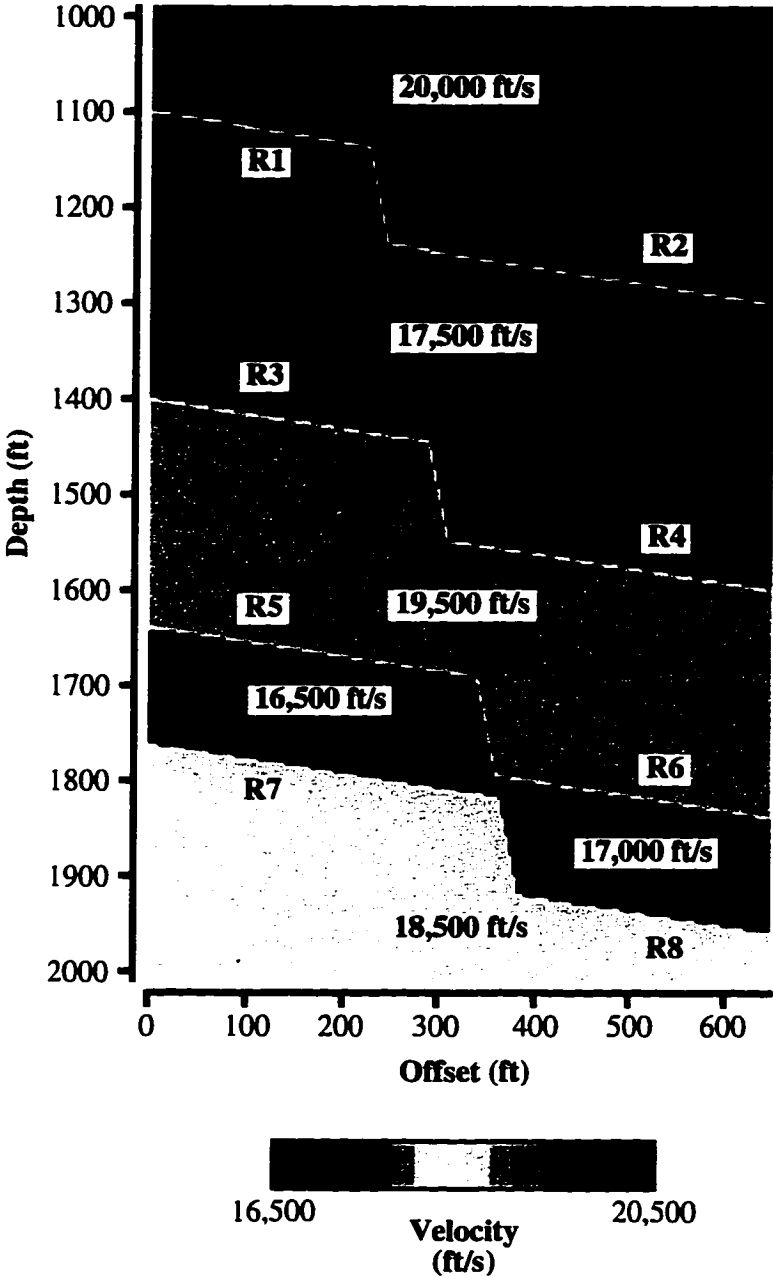


Figure 5.3: Velocity model used to generate traveltime data for synthetic study #2. Reflectors are numbered from top to bottom. Discontinuous reflectors are defined by the individual segments. The fault plane is not used to generate reflections for the synthetic data set. Reflector depths can be found in Table 5.5

**TABLE 5.5. Synthetic model #2 reflector data**

	Receiver Well intersection depth (ft)	Fault Plane intersection point x,z (ft)	Source Well intersection depth (ft)
<b>Reflector 1</b>	1100.0	227.0, 1134.9	null
<b>Reflector 2</b>	null	247.6, 1238.1	1300.0
<b>Reflector 3</b>	1400.0	288.9, 1444.4	null
<b>Reflector 4</b>	null	309.5, 1547.6	1600.0
<b>Reflector 5</b>	1640.0	338.4, 1692.1	null
<b>Reflector 6</b>	null	359.0, 1795.2	1840.0
<b>Reflector 7</b>	1760.0	363.2, 1815.9	null
<b>Reflector 8</b>	null	383.8, 1919.0	1960.0

### 5.4.1 Study #2: acquisition geometry and data specifications

The source and receiver acquisition geometry of synthetic Survey #2 is almost identical to that of Survey #1 except that the source-receiver offset is 650.0 ft. There are 201x201 sources and receivers spaced evenly every 5.0 ft from 1000.0–2000.0 ft. As with Survey #1, traveltimes were initially calculated for all source-receiver-reflector combinations and then edited to provide a more realistic traveltime data set. Direct arrival traveltimes have been prepared in a slightly different manner in this example. All near-offset direct-arrival traveltimes are used in the inversion. Far offset traveltimes are limited to  $\pm 50.0^\circ$ , about 775 ft in offset. Reflected traveltime arrivals have been edited in much the same way as in the Study #1. The reflection data for each reflector are edited to include traveltimes of either upgoing or downgoing events. The traveltimes are further edited to provide a reasonable range of incidence angles. Table 5.6 provides information on the traveltimes used for the various reflectors.

**TABLE 5.6. Specifications of Example 2 reflection traveltime data**

	Direction	# Traveltimes
<b>Reflector 1</b>	downgoing	1495
<b>Reflector 2</b>	downgoing	6976
<b>Reflector 3</b>	downgoing	3841
<b>Reflector 4</b>	upgoing	4091
<b>Reflector 5</b>	upgoing	5290
<b>Reflector 6</b>	upgoing	5060
<b>Reflector 7</b>	upgoing	6471
<b>Reflector 8</b>	upgoing	2811



### 5.4.2 Synthetic Study #2: inversion and results

I ran a direct and reflected arrival inversion on synthetic data set #2 starting with a homogeneous model (18,380 ft/s) with 10.0 ft cells and flat reflectors each defined by 34 nodes. The initial reflector depths of Reflectors 1–8 respectively were: 1090.0, 1290.0, 1395.0, 1610.0, 1755.0, 1850.0, 1870.0, and 1970.0 ft. Since part of the information desired from the inversion is an estimate of the reflector extent, the reflectors were parameterized using a higher number of nodes. From the final model the segments of each reflector that create reflections are interpreted to define the reflector extent.

The initial values of the smoothing penalties weights in this inversion differ slightly from the values used in Study #1. Like Study #1, the initial weight of the horizontal smoothing penalty equals the weight of the traveltimes data and the vertical smoothing penalty weight is 1/4th of the horizontal weight the entire inversion. But, in this inversion, the initial reflector second derivative smoothing penalty weight *equals* the horizontal weight. The reflector smoothing was initialized at a higher value in this example to help stabilize the larger number of nodes used to define each reflector. Another difference in this inversion is that *all* smoothing penalty terms were relaxed an order of magnitude every 4 continuation steps.

The ideal, or “best”, answer is the result of continuation step 10. Traveltime residuals are  $\sim 108\mu\text{s}$  rms for the 33,884 reflected rays and  $\sim 120\mu\text{s}$  rms for the 37,873 direct arrival rays. Note in this example that the direct arrival traveltime residuals are slightly higher than the reflected arrival residuals. This result is due to an increased ratio of reflected traveltimes to direct arrival traveltimes and the inclusion of near-offset direct-arrival traveltimes which have higher residuals. The final tomogram is shown in Figure 5.4. Note that the resolution is similar to that of Study #1. The existence of the fault can be seen in the tomogram especially at the bottom of the image. The different velocities of the thin faulted layer near the bottom are also apparent in the tomogram.

The reflector depth results obtained in this example are interpreted in a slightly different manner than in Study #1 although the inversions are run in much the same way. The lateral extent of the reflectors is never known *a priori* so each reflector is initially assumed to extend all the way across the model. After the inversion is complete an estimate of the lateral extent of the reflectors can be recovered based on the raypath coverage of each reflector segment. By using 34 nodes to describe the reflectors across the 660.0 ft model the distance between nodes is 20.0 ft. The coverage is maintained by keeping track of the number of non-zero derivatives of each reflector depth parameter. In this inversion the average number of non-zero derivatives for all reflector parameters is 490.6. I have set the cutoff for the number of non-zero parameters to qualify a segment as being “covered” as 6

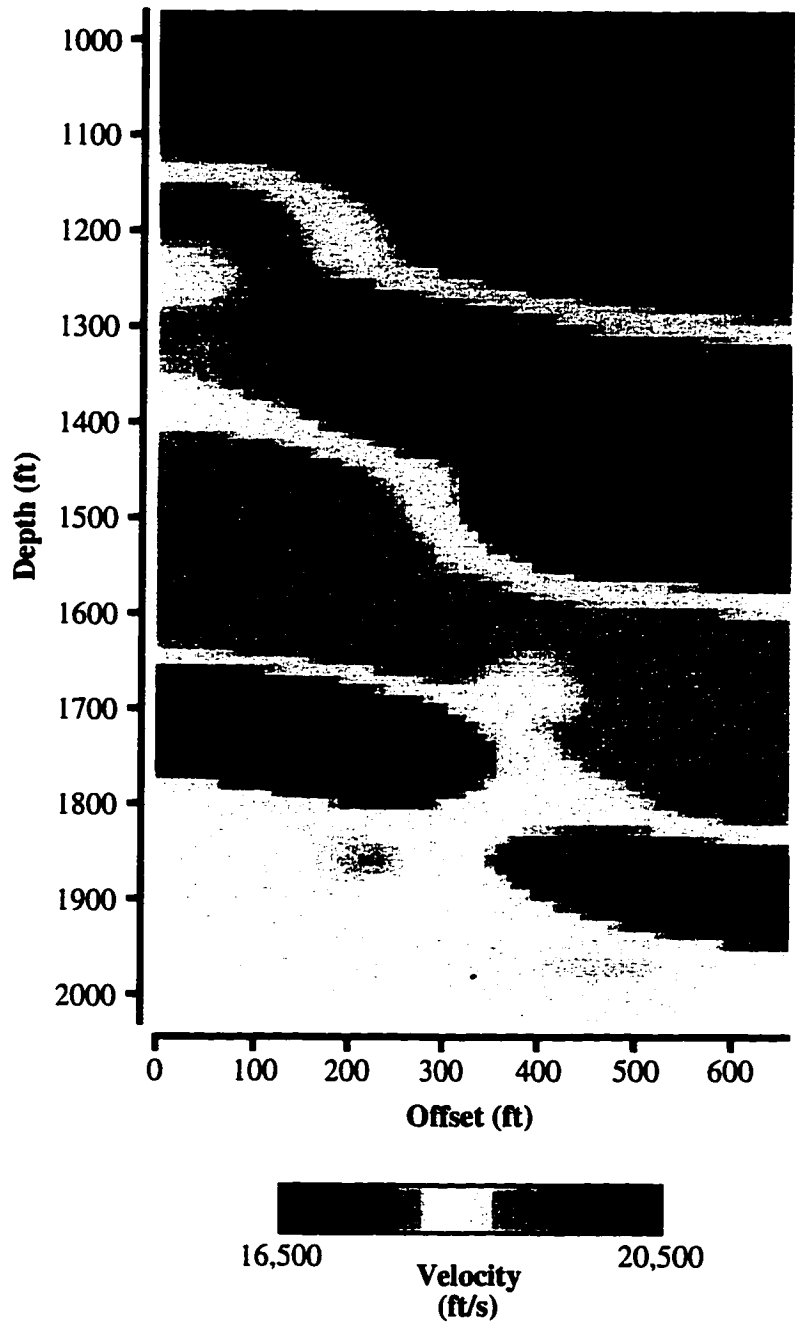


Figure 5.4: The resulting velocity tomogram obtained after 10 continuation steps of a combined direct and reflected arrival traveltimes inversion. This result should be compared to the velocity model shown in Fig. 5.3 which was used to generate the traveltimes data.

to remove some spurious segments. This cutoff value removes only 6 reflector covered segments. To aid in the visualization of the reflector recovery I have plotted the covered reflector solutions in Figure 5.5 as an overlay to the original model.

Figure 5.5 shows that direct and reflected arrival traveltimes inversion locates the reflectors fairly well in depth and also in extent. The largest errors in depth appear in Reflectors 1, 2, 7, and 8. A mispositioning phenomena similar to that seen in Study #1 is apparent in the final reflector solutions. Reflectors 1 and 2, determined by downgoing reflections, with a high velocity layer overlying a low velocity layer, are too shallow. These reflectors are mispositioned like Reflector 2 in Study #1. Reflectors 7 and 8, determined by upgoing reflectors, with a low velocity layer overlying a high velocity layer, are too deep. These reflectors are like Reflector 3 of the first study. The magnitude of the errors is a bit larger this time, though.

To provide a graphic display of the reflector depth errors, they have been plotted in Figure 5.6. The extent of the reflector depth errors is from about -10–12 ft, a bit larger than found in the previous example. Note that the largest errors occur in reflectors near the top and bottom of the image. There are several possible explanations to be investigated in future work. First, the top and bottom layers are covered by relatively few direct arrival raypaths. This may make it more difficult to calculate a sharp velocity gradient at these interfaces. Second, this inversion ran only 10 continuation steps before it became unstable. This means the smoothing penalty terms are still relatively strong compared to Study #1. This prevents velocity gradients in the final iteration as large as those allowed in Study #1. Finally, the forward modeler used to calculate the direct arrival traveltimes is more prone to errors near sharp, nearly-horizontal interfaces. There may be significant errors in the traveltimes data preventing the inversion from calculating the sharp interfaces more accurately.

## 5.5 Synthetic Study #3

Synthetic study #3 is based on field data set Mc68-02b collected as part of the McElroy Reservoir Geosciences Project (MRGP) (Harris et al., 1995). This example is designed to parallel the Mc68-02b survey in terms of processing, source/receiver/reflector acquisition geometry, and model characteristics. The results of the CDRATT velocity estimation and imaging of Survey Mc68-02b are the focus of Chapter 6. One goal of Synthetic Study #3 is to obtain an estimate of the resolution potential of the field survey. The synthetic data are calculated using a velocity and reflector geometry model containing many of the features of the McElroy site. Figure 5.7 shows the model used to create the synthetic data. This

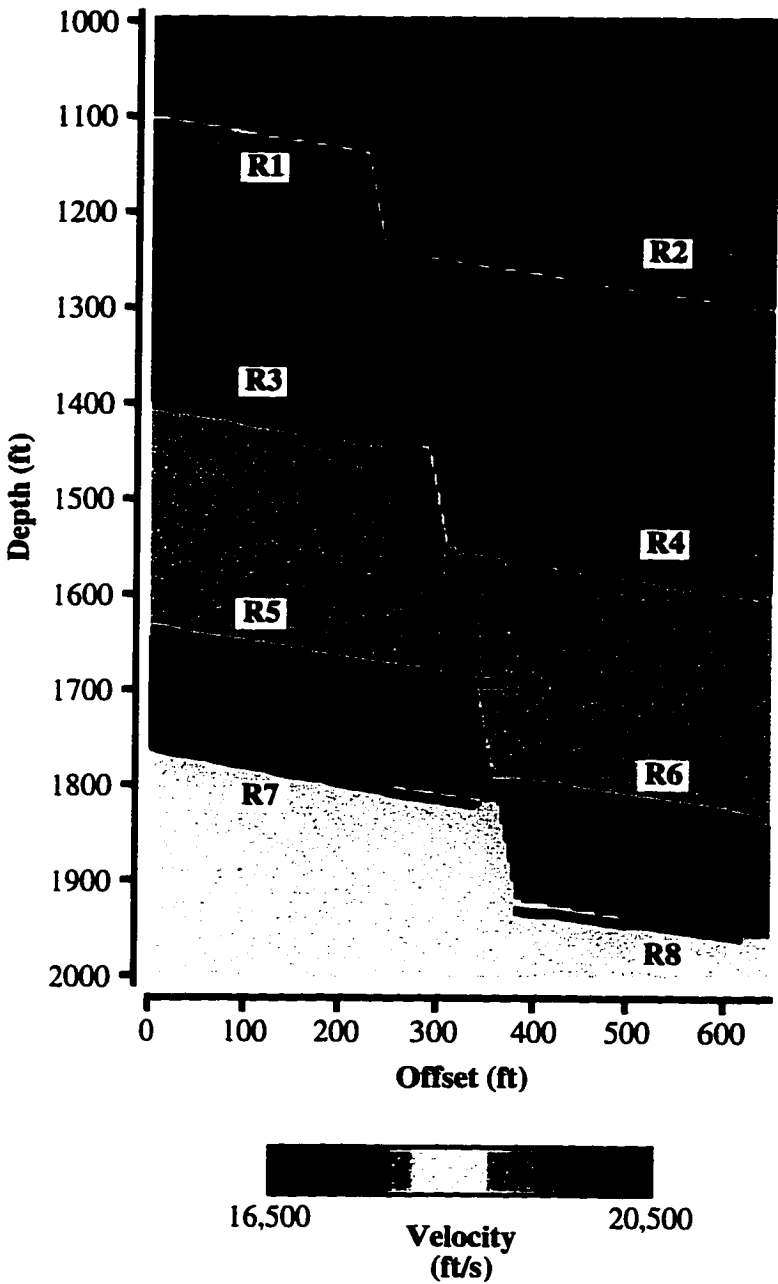


Figure 5.5: The reflector depth locations obtained from the traveltimes inversion plotted on top of the original velocity model used to generate the synthetic data. The reflectors are actually defined across the entire velocity image but only reflector parameters with a significant number of non-zero depth derivatives have been plotted.

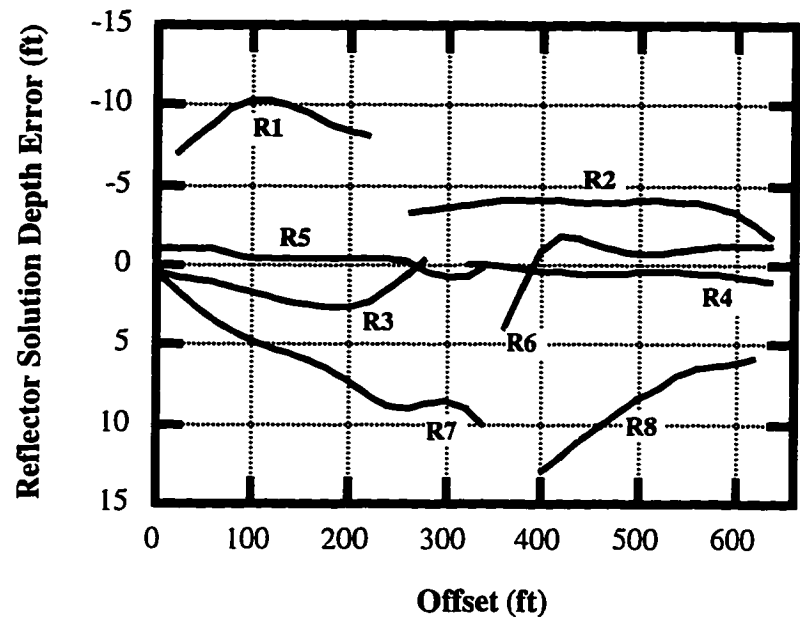


Figure 5.6: The difference between the reflector depths obtained from the traveltime inversion and the actual model depths shown in Fig. 5.5. Note that the largest errors are in the reflector depths near the top and bottom of the model.

model is based on a smoothed version of the receiver well (JTM1202) S-wave sonic log and local information on the reflector geometries.

The interpreted geometries of the reflectors at the McElroy site are based on traveltime picks and crosswell reflection images collected at the McElroy test site (Lazaratos et al., 1995). To interpret reflector geometries from the field data set requires reflection traveltimes for Reflectors R1–R9, seen in Fig. 5.7, and the direct arrival traveltimes. The intersection of the direct and reflected arrivals provides an estimate of the intersection of the reflecting horizons and the wells. An analysis of the crosswell reflection image shows that although the picked reflectors are dipping to various degrees that they are basically linear. The reflectors used in the design of the synthetic model, shown in Fig. 5.7 reflect these observations.

Table 5.7 provides the details of the reflection depths of the synthetic model. Since the reflectors are linear they can be completely defined by their intersection points with the wells. The primary difference between the setup of the field and synthetic survey is that the well deviations of the field survey were not incorporated into the synthetic model. In the synthetic model the wells are assumed to be vertical with an offset of 195.0 ft. Note that Reflectors 3 and 4 are identical in location. They are defined as separate reflectors to maintain consistency with the Mc68-02b CDRATT inversion.

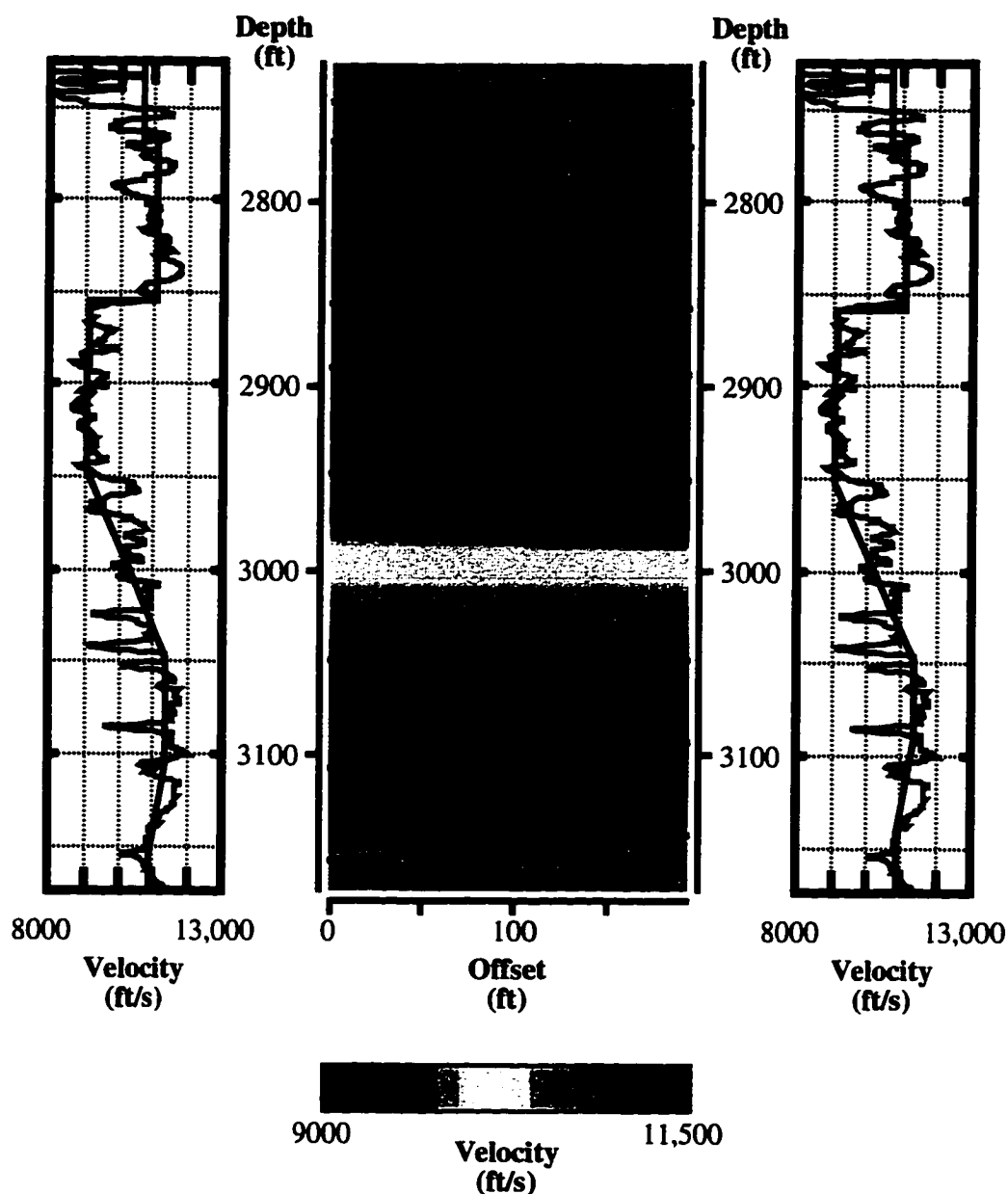


Figure 5.7: The synthetic model used in Study #3. The simple velocity profile is an approximation of the receiver well *S*-wave sonic log. The velocity profile on the right side is perturbed to reflect the change in reflector depths across the model. The location and nature of these reflectors is believed to reflect the geology at the McElroy site. Arrows on the reflectors indicate the nature (upgoing or downgoing) of the reflected arrival traveltime picks obtained from the field data set. The synthetic traveltime picks were edited to include picks for the same source-receiver-reflector combinations as the field data set.

**TABLE 5.7. Synthetic model #3 well intersection depths**

	Receiver Well intersection depth (ft)	Source Well intersection depth (ft)
<b>Reflector 1</b>	2746.0	2748.5
<b>Reflector 2</b>	2767.5	2772.5
<b>Reflector 3</b>	2855.0	2860.0
<b>Reflector 4</b>	2855.0	2860.0
<b>Reflector 5</b>	2890.0	2895.0
<b>Reflector 6</b>	2947.5	2952.5
<b>Reflector 7</b>	3048.5	3048.5
<b>Reflector 8</b>	3107.0	3092.0
<b>Reflector 9</b>	3157.5	3142.5

### 5.5.1 Study #3: acquisition geometry and data specifications

The synthetic data are edited to have non-zero traveltimes for the same source-receiver-reflector combinations as the Mc68-02b field data set. The primary difference in the synthetic data set is that it is designed with vertical, non-deviated wells. The synthetic consists of 162 sources from 2745.0–3147.5 ft by 167 receivers located from 2745.0–3160.0 ft, every 2.5 ft. Direct arrival *S*-waves are not produced by the piezoelectric source at near offsets and the minimum offset for which direct arrival traveltimes in the field data set are available is about 55 ft. Study #3 reflects this lack of coverage. Direct arrival traveltimes are available for all larger offsets. Table 5.8 provides information about the reflected traveltime picks. These also mirror the traveltime picks available from the field data set.

**TABLE 5.8. Field and synthetic reflection traveltime coverage**

	Direction	# Traveltimes
<b>Reflector 1</b>	downgoing	4392
<b>Reflector 2</b>	downgoing	4275
<b>Reflector 3</b>	downgoing	4940
<b>Reflector 4</b>	upgoing	783
<b>Reflector 5</b>	downgoing	2664
<b>Reflector 6</b>	downgoing	3872
<b>Reflector 7</b>	upgoing	6399
<b>Reflector 8</b>	upgoing	4264
<b>Reflector 9</b>	upgoing	4203

### 5.5.2 Synthetic Study #3: inversion and results

The CDRATT inversion was run limiting direct arrival traveltimes to an aperture of  $\pm 65.0^\circ$ , equivalent to approximately 420 ft in offset. At the beginning of the inversion the weights of the second derivative reflector smoothing penalty and the horizontal smoothing penalty were set equal to the weight of the traveltime data while the vertical smoothing weight was 1/8th the weight of the horizontal smoothing. The penalty weights were relaxed at a rate of one order of magnitude every 4 continuation steps. The initial velocity model was homogeneous (10,200 ft/s), the average velocity of the direct arrival traveltimes (of the field data set). The cell size of the model is 5.0 ft by 5.0 ft. The reflectors are defined with 21 nodes each, equal to 10.0 ft between nodes. Like Study #1 and Study #2, the CDRATT inversion was started with flat reflectors. The starting depths for Reflectors 1–9 respectively was: 2750.0, 2770.0, 2860.0, 2855.0, 2890.0, 2950.0, 3050.0, 3100.0, and 3150.0.

The results of the 10th continuation step of the synthetic data inversion are optimal for a direct comparison with the field data inversion. Traveltime residuals are  $\sim 24\mu\text{s}$  rms for the 35,237 reflected rays and  $\sim 18\mu\text{s}$  rms for the 20,163 direct arrival rays. These residuals are very near the resolution of the code used to calculate the traveltimes of the raypaths. The velocity tomogram, shown in Figure 5.8 shows the simple features of the velocity model with few artifacts.

The calculated reflector depths have a range of errors of -1.27–0.73 ft and an rms depth error of 0.54 ft,  $\sim 6.5$  inches. This result confirms the theoretical estimate of Bube and Langan (1995) for a  $\sim 180$  ft crosswell profile. Table 5.9 provides an abbreviated listing of the inversion results along with the model parameters. Every other reflector depth parameter (in offset, 11 out of 21) is shown in this listing. One observation that can be made from the data in Table 5.9 is that the largest depth errors occur in Reflectors 3 and 4. These reflectors occur at the interface of two zones with a high velocity contrast. The slow layer lies beneath the fast layer.

The errors in Reflectors 3 and 4 are of the same type that has been discussed in Studies #1 and #2. Reflector 3, determined by downgoing reflections in the slower layer, is slightly shallow over its entire length. Reflector 4, determined by upgoing reflections in the faster layer, is also shallow. This is the situation predicted but not observed in Studies #1 and #2. Due to the velocity gradient in the vicinity of the correct reflector location, the upgoing reflected ray travels through slow material near the interface. The increase in traveltime caused by the slow material forces the reflector up so that the raypath is shortened and the traveltime is compensated.



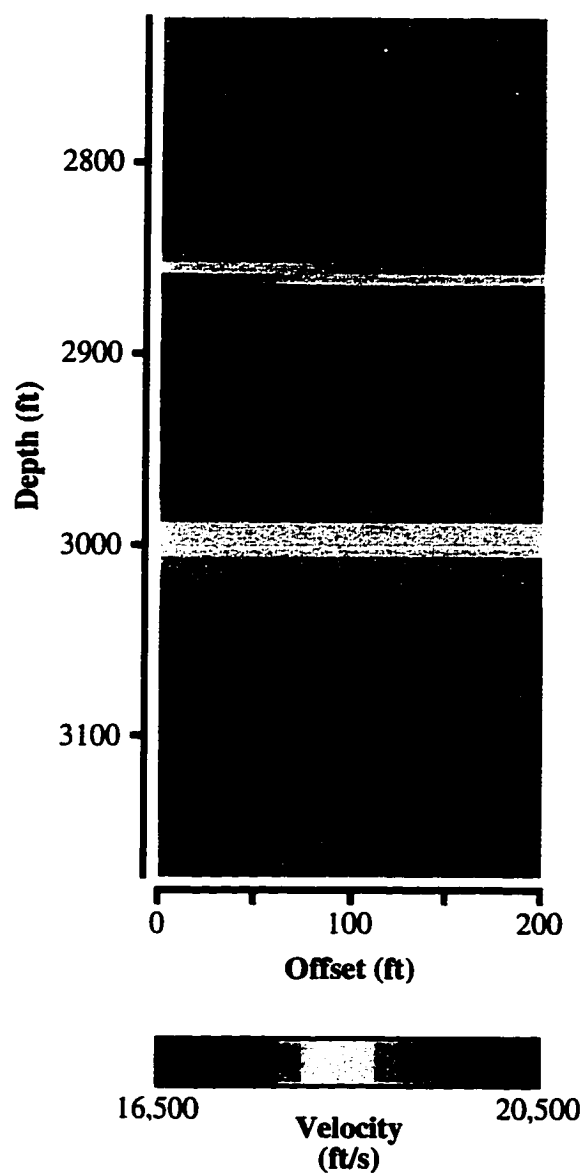


Figure 5.8: The tomogram result of the 10th continuation step of the synthetic data inversion. The rms error of the 55,400 direct and reflected traveltimes used in this inversion is  $20.3 \mu\text{s}$ . This tomogram can be compared with the model used to generate the synthetic data shown in Fig. 5.7.

**TABLE 5.9. Reflector depth inversion results and synthetic model #3 reflector depths**

Offset (ft)	0.0	20.0	40.0	60.0	80.0	100.0	120.0	140.0	160.0	180.0	200.0
<b>R1 model</b>	2746.0	2746.3	2746.5	2746.8	2747.0	2747.3	2747.5	2747.8	2748.1	2748.3	2748.6
<b>R1 result</b>	2745.9	2746.0	2746.1	2746.3	2746.5	2746.9	2747.2	2747.6	2747.9	2748.2	2748.5
<b>R2 model</b>	2767.5	2768.0	2768.5	2769.0	2769.6	2770.1	2770.6	2771.1	2771.6	2772.1	2772.6
<b>R2 result</b>	2767.6	2768.1	2768.6	2769.1	2769.6	2770.1	2770.7	2771.3	2771.9	2772.4	2772.7
<b>R3 model</b>	2855.0	2855.5	2856.0	2856.5	2857.1	2857.6	2858.1	2858.6	2859.1	2859.6	2860.1
<b>R3 result</b>	2854.5	2854.7	2855.1	2855.5	2855.9	2856.3	2856.8	2857.5	2858.1	2858.8	2859.5
<b>R4 model</b>	2855.0	2855.5	2856.0	2856.5	2857.1	2857.6	2858.1	2858.6	2859.1	2859.6	2860.1
<b>R4 result</b>	2854.2	2854.7	2855.1	2855.6	2856.1	2856.5	2857.0	2857.6	2858.1	2858.7	2859.3
<b>R5 model</b>	2890.0	2890.5	2891.0	2891.5	2892.1	2892.6	2893.1	2893.6	2894.1	2894.6	2895.1
<b>R5 result</b>	2889.9	2890.5	2891.1	2891.7	2892.3	2892.7	2893.2	2893.6	2894.1	2894.5	2894.9
<b>R6 model</b>	2947.5	2948.0	2948.5	2949.0	2949.6	2950.1	2950.6	2951.1	2951.6	2952.1	2952.6
<b>R6 result</b>	2947.5	2948.0	2948.5	2949.0	2949.4	2949.9	2950.5	2951.0	2951.5	2952.0	2952.5
<b>R7 model</b>	3048.0	3048.0	3048.0	3048.0	3048.0	3048.0	3048.0	3048.0	3048.0	3048.0	3048.0
<b>R7 result</b>	3048.5	3048.5	3048.5	3048.5	3048.5	3048.4	3048.4	3048.5	3048.5	3048.5	3048.7
<b>R8 model</b>	3107.0	3105.5	3103.9	3102.4	3100.8	3099.3	3097.8	3096.2	3094.7	3093.2	3091.6
<b>R8 result</b>	3107.0	3105.5	3103.9	3102.4	3100.9	3099.3	3097.7	3096.2	3094.6	3093.1	3091.7
<b>R9 model</b>	3157.0	3155.5	3153.9	3152.4	3150.8	3149.3	3147.8	3146.2	3144.7	3143.2	3141.6
<b>R9 result</b>	3157.6	3156.1	3154.6	3153.0	3151.4	3149.8	3148.3	3146.7	3145.2	3143.7	3142.3

## 5.6 Conclusions

The results of the CDRATT inversions shown in this chapter support the theoretical predictions that reflector locations are well resolved in crosswell data in spite of mediocre velocity resolution (Bube and Langan, 1995). Synthetic Surveys #1 & #2 achieved a resolution in reflector depths very close to the 0.5–2.5 ft value predicted for a 600 ft offset crosswell geometry. In these studies reflector depths were located with an rms accuracy of about 1.4 ft and 4.5 ft respectively. In Synthetic Study #3, designed around Survey Mc68-02b which is studied in Chapter 6, reflector depths were recovered with an rms error of 6.5 inches. These results provide a good match with predicted resolution values even though the resolution analyses were performed using a simple homogenous velocity model and flat reflectors. The synthetic studies presented here all included 2-D velocity models and reflector geometries.

More important, with respect to aligning reflections in the mapped domain to obtain good stacking, the rms reflection traveltime residuals of the synthetic studies were very small, ranging from approximately 25–120 $\mu$ s. How does this temporal error relate to the spatial alignment of reflections in the mapped domain? Assume a source wavelet, where

the source center frequency is 1000 Hz and the medium velocity is 10,000 ft/s. Also, assume an acquisition geometry similar to Synthetic Study #3, where the distance between wells is 195 ft, and the vertical mapping trajectory midway between the wells (e.g. source depth equals receiver depth and a horizontal reflector). In this case the spatial wavelength of the mapped wavelet is 10 ft (at normal incidence). A traveltime of 100 $\mu$ s corresponds to 1 ft in this medium. So, a 100 $\mu$ s traveltime residual for a reflected raypath is equivalent to a vertical mispositioning of the mapped wavelet of 0.5 ft at normal incidence, 0.7 ft at 45°, and 1.2 ft at 65°. This suggests that, for this example, reflections would be aligned about the calculated reflector locations with an accuracy of  $\sim 1/10$  of a wavelength, or better, for a wide range of incidence angles.

The synthetic examples studied in this chapter show that CDRATT inversion is a good choice as a crosswell velocity estimation tool when reflection traveltimes can be obtained. This is supported by several results. First, the CDRATT correctly locates reflectors. Second, the low traveltime residuals indicate that the alignment of the picked events about the calculated reflector positions is better than  $1/10$  of a wavelength for typical crosswell geometries and acquisition parameters. Third, and final, the CDRATT inversion results are obtained from the traveltime data in one step without any repicking of the reflection events. So, to summarize, the results are accurate and the process is not labor intensive. These are ideal traits for a velocity estimation procedure.

# **CHAPTER 6**

## **THE CDRATT VELOCITY ESTIMATION METHOD: McELROY FIELD STUDY**

### **6.1 Introduction**

The fundamental goal of this thesis is to provide a consistent method for velocity estimation and reflection imaging of crosswell seismic data. In Chapter 1 I describe an approach for crosswell reflection velocity estimation using Combined Direct and Reflected Arrival Traveltime Tomography (CDRATT). To implement the CDRATT velocity estimation method required the development of several new processing/inversion tools. Two of the most important are the CDRATT inversion and XSP-CDP reflection imaging using the CDRATT model. In Chapters 2-5 I describe the theory and design of these tools and validate their performance.

In this chapter I demonstrate the effectiveness of the CDRATT velocity estimation method on a field data set. This example uses data collected from the McElroy oilfield located in west Texas. The data were collected by Stanford University as part of an ongoing reservoir monitoring and characterization project, the McElroy Reservoir Geosciences Project (MRGP). As part of this field data demonstration I describe the picking of reflection traveltimes. This is an important procedure since reflection traveltimes are required to use the CDRATT velocity estimation method but have not been obtained from crosswell data prior to this work.

I provide a comparison of tomograms created with and without the use of reflection traveltime data. In the example shown in this chapter the largest improvements in imaging take place near the top and bottom edges of the surveyed area. The importance of extending the accuracy of the crosswell imaging techniques to the edges results from the targets in crosswell studies undertaken in the oil field environment so often being near the bottom of the survey. This is true since wells are not often drilled far beyond the reservoir depth.

The addition of reflection traveltimes results in an improved correlation of velocity of the tomogram at the wells when compared to the *S*-wave well logs. The largest improvement is found comparing the CDRATT tomogram with the 2-D Direct Arrival Only (DAO) tomogram. The 1-D DAO tomogram also has a slightly better correlation with the well logs than the 2-D DAO tomogram. The CDRATT tomogram matches the average velocity of the well logs better than the 1-D DAO tomogram though. In fact, for the receiver

well where the *S*-wave log was collected, JTM1202, the mean error of the CDRATT tomogram is only 0.2%, more than four times better than the 1-D DAO result.

In the last sections of this chapter I compare data mapped using a CDRATT model with data mapped using the 1-D and 2-D DAO tomograms and show that the CDRATT model provides better alignment of reflections prior to stack and, subsequently, higher resolution stacked reflection images. The difference in stacking quality between the 2-D DAO and CDRATT mapped data shows that the addition of reflection information to the traveltime inversion results in a velocity model that is superior for crosswell reflection imaging. The effects of this are most significant near the top and bottom edges of the stacks. This corresponds to the region where the most amount of information is added to the tomographic inversion in the form of increased angular coverage.

## 6.2 Field data example: McElroy Survey Mc68-02b

The data used in this field example are part of an ongoing reservoir characterization and monitoring project, the McElroy Reservoir Geosciences Project (MRGP). As part of this project three surveys were collected over a period of approximately 4 years between two wells in the McElroy field in west Texas: JTM1068 and JTM1202. The survey used in this example, Survey Mc68-02b, was the second of these surveys and was collected in February of 1993. Research work in multi-gather crosswell reflection imaging by Lazaratos (1993) focused on the first of these surveys, Survey Mc68-02a, collected in December of 1991.

I chose to use Survey Mc68-02b for several reasons. 1) Data quality are extremely good with a high signal-to-noise ratio, accurate timing and depth measurements, a broad angular coverage, and fine source and receiver sampling. These features allow the data to be processed effectively to enable accurate picking of direct and reflected arrival traveltimes. 2) As part of the MRGP, the geology of this area has been well studied which provides information needed to judge the effectiveness of the CDRATT velocity estimation method. 3) While the geology of the area is relatively simple several important features, such as an angular unconformity, provide some challenge to the imaging method.

In this section I first provide a description of the site geology followed by details of the crosswell experiment. After this I describe the reduction of the trace data to direct and reflected arrival traveltimes. The next section describes the CDRATT inversions performed on these data followed by the generation of reflection images from the inversion results.

### 6.2.1 Site description

The crosswell seismic data used in this example were collected in an experiment performed in the McElroy field located in west Texas, as shown in Figure 6.1. The McElroy field is positioned along a north-south-trending asymmetrical anticline with a steeply dipping eastern limb and a more gently dipping western limb. In the vicinity of the crosswell experiment the structure is fairly flat although mildly increasing dips can be found toward the bottom of the surveyed section. The target of the crosswell imaging study was the Permian-aged San Andres/Grayburg formations located at a depth of approximately 2900 ft. The Grayburg formation is the primary reservoir unit in this area.

Details of the geology at the experiment site are shown in Figure 6.2. Included in this figure is a *P*-wave velocity tomogram created from data acquired in Survey Mc68-02a (Harris et al., 1995). This tomogram helps highlight several of the larger units in the survey area. The principal producing interval, the D5, is between 2862–2945 ft in the shallow-shelf dolostones of the Grayburg formation. Average porosity is about 10% but varies higher because of solution enhancement and lower because of secondary deposition of evaporites. These alterations are of irregular geometry and result in significant spatial variations in both porosity and permeability. As a result of this heterogeneity, oil recovery varies substantially across the field, with the highest production coming from the central area and the lowest in the flanks. The Grayburg lies unconformably over the San Andres formation as a result of a regression which exposed the San Andres carbonate platform (Harris et al., 1984; Walker and Harris, 1986).

The observation that substantial amounts of noncontinuous pay occur in the McElroy field has led to pattern flooding in place of peripheral floods and extensive infill drilling. Unfortunately the fine stratification of porosity found in the McElroy field limits the effectiveness of standard surface seismic during exploration and development. The porous zones of interest are thin and heterogeneous enough that they are poorly resolved using surface seismic (Harris and Walker, 1988). In addition, although the structure is reasonably simple, there can be difficulty correlating reservoir zones from well to well (Lemen et al., 1990). In an attempt to overcome these problems and assist in the evaluation of a CO<sub>2</sub> pilot project a series of crosswell seismic experiments were designed to assist in time-lapse reservoir monitoring and reservoir characterization, the fundamental goal of the McElroy Reservoir Geosciences Project.

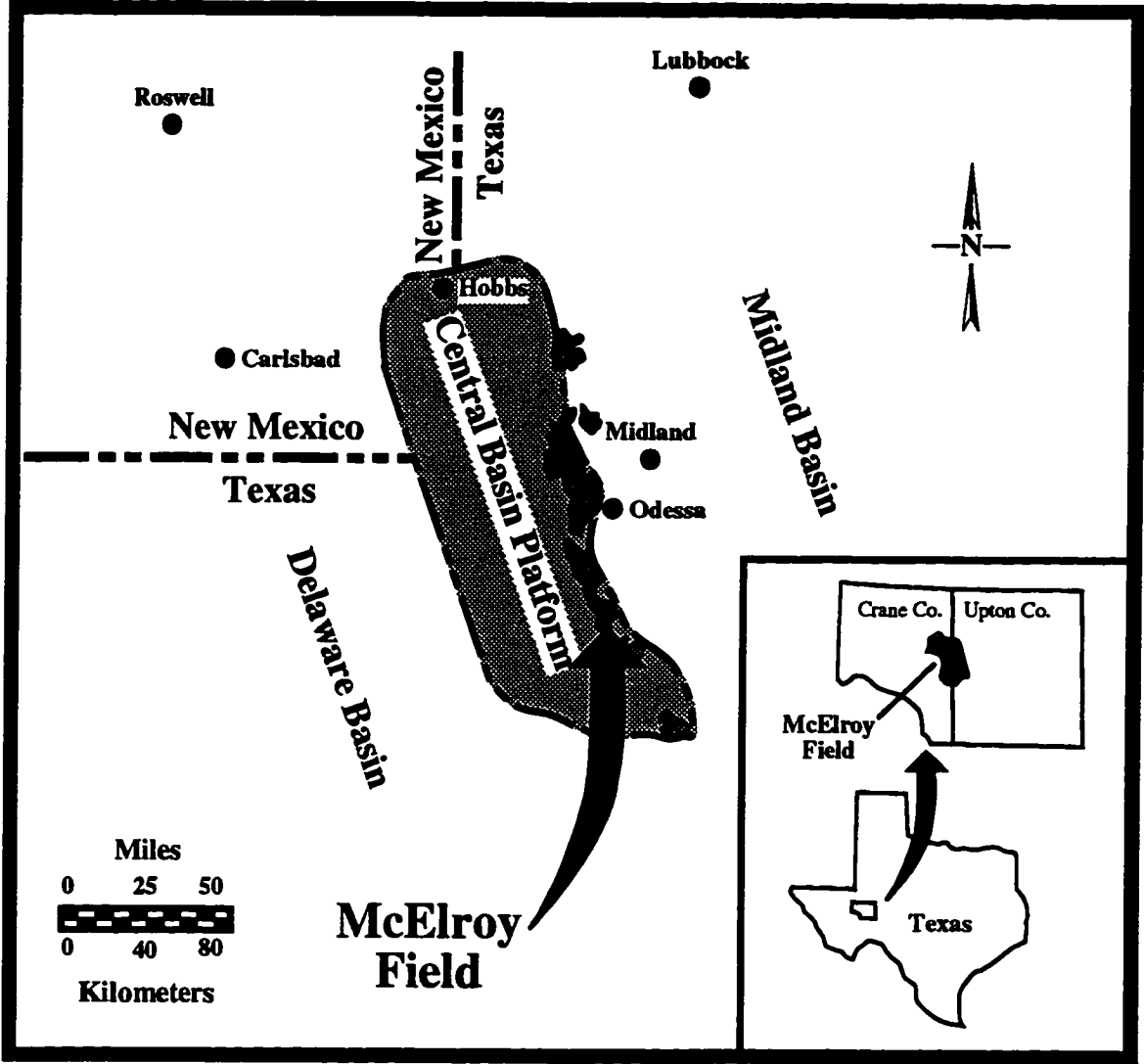


Figure 6.1: This map of the Permian Basin regions show the location of the McElroy Field located on the eastern margin of the Central Basin Platform.

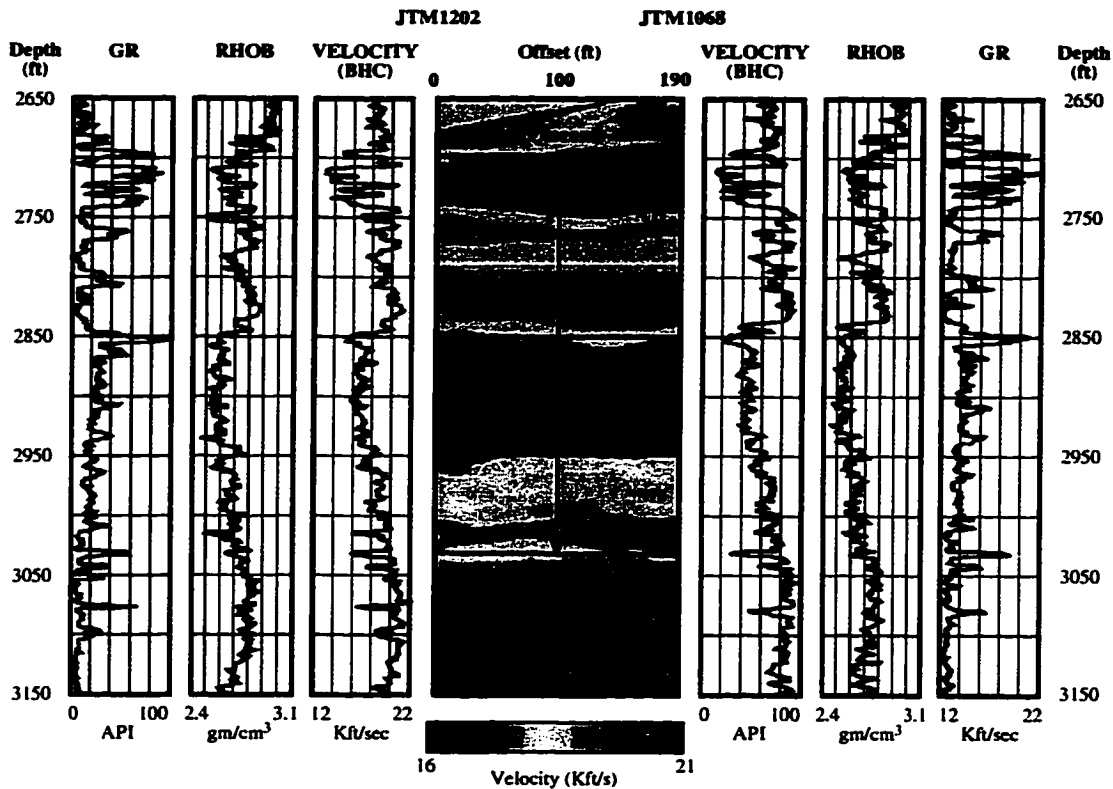


Figure 6.2: The logs collected at the experiment test site show the predominantly layer-cake geology of the McElroy experiment site. The targeted units show up distinctly on the  $P$ -wave tomogram created from data collected in Survey Mc68-02a.

### 6.2.2 Survey description and data acquisition

The  $\text{CO}_2$  injection pilot project is being conducted in section 205 in the southwest portion of the McElroy field. The location of the pilot  $\text{CO}_2$  flood area and the crosswell surveys within section 205 are shown in Figure 6.3. The study area is part of three 20-acre five spot patterns. Of the two surveys shown in Fig. 6.3 I consider only the survey collected between wells JTM1202 and JTM1068, Survey Mc68-02b.

JTM1202 was drilled as an observation well for the  $\text{CO}_2$  pilot project. This well was cased through the production zone with fiberglass casing to permit monitor logging. The other well in the Mc68-02b survey, JTM1068, was transformed to a  $\text{CO}_2$  injector around March 1993. At the time Survey Mc68-02b was acquired, February 1993, JTM1068 was under water injection in an attempt to bring up and stabilize the reservoir pressure. Prior to this it had been a producing well. One purpose for the acquisition of Survey Mc68-02b prior to  $\text{CO}_2$  injection was to establish a baseline measurement for the time-lapse monitoring aspect of MRGP.



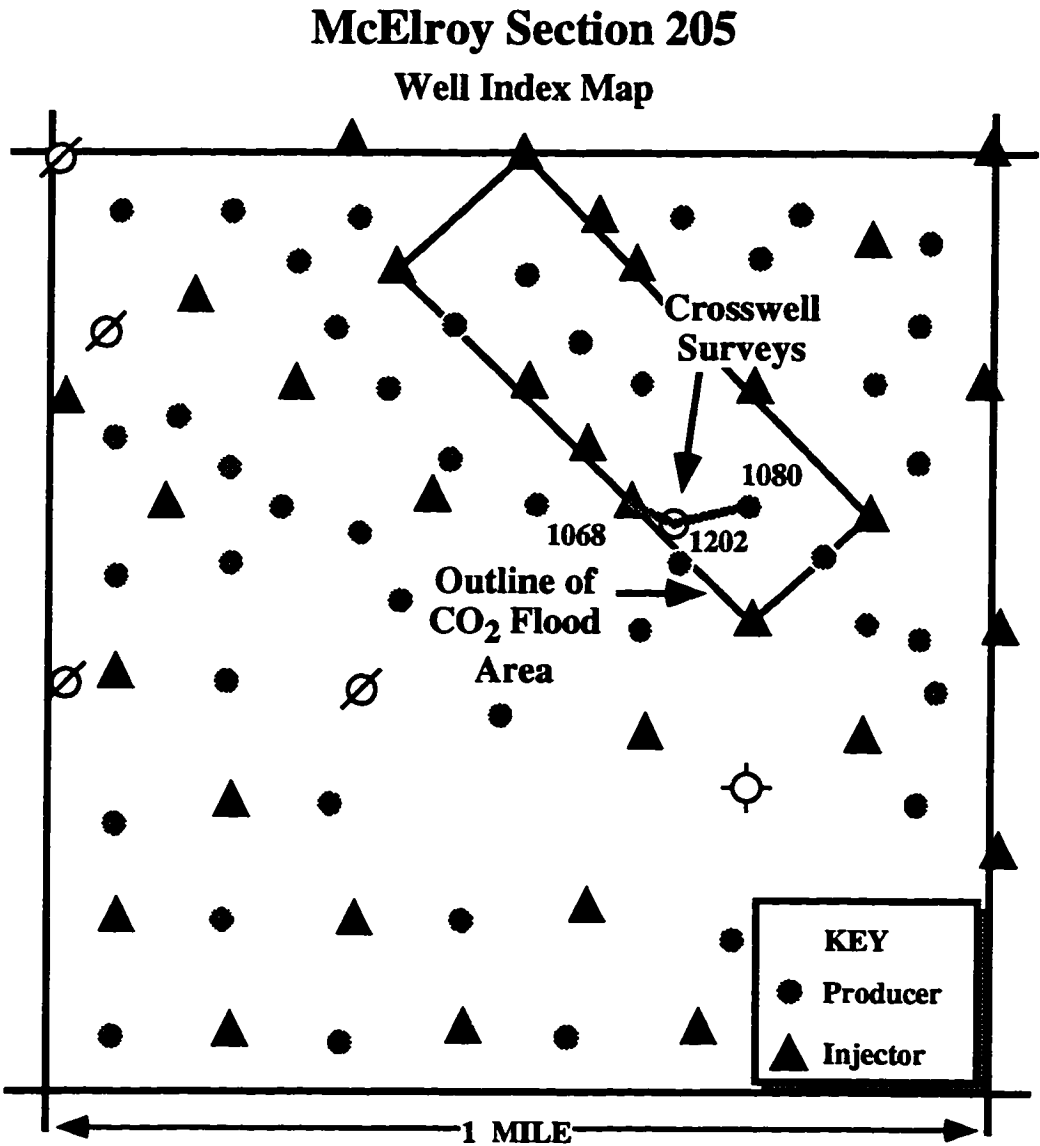


Figure 6.3: The pilot site has three 20-acre five spots. The survey used in this thesis was collected between wells JTM1068, an injector, and JTM1202, an observation well.

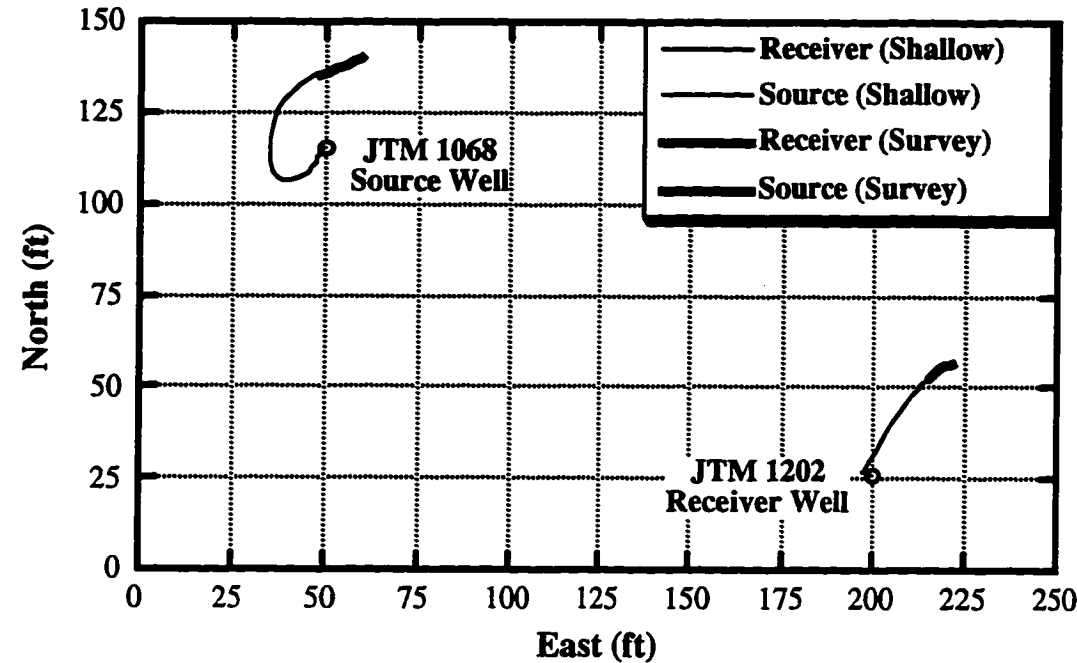


Figure 6.4: A map view of the well deviations found in Survey Mc68-02b. The bold sections of the well trajectories correspond to the range of depths over which the crosswell data were acquired.

A map perspective of wells JTM1202 and JTM1068 is shown in Figure 6.4. The northeasterly drift of the wells over the surveyed region, shown in bold, is evident in this figure. The well drift over the surveyed zone is relatively small for both wells, about 10 ft, and is roughly orthogonal to the plane of the survey. This type of well deviation, which is small in the first place, is effectively compensated using the rotation-translation deviation correction algorithm applied in the CDRATT inversion.

The acquisition geometry of Survey Mc68-02b is shown in Figure 6.5. The data set consists of 241 sources by 241 receivers spaced at a 2.5 ft interval over the surveyed zone. As seen in Fig. 6.5 the source locations range from 2547.5–3147.5 ft (wireline depth) while the receiver locations range from 2575.0–3175.0 ft (wireline depth). Source and receiver wireline depths are tied to the JTM1202 sonic log of November 8, 1991 (log measured from the kelly bushing). The average distance between wells over the surveyed region is 188 ft.

The data were collected with a piezoelectric bender source and a string of hydrophone receivers. The source was run in a vibrator-like mode using a linear sweep from 250–2000 Hz over 200 ms. Two sweeps were stacked at each shot point. Data were acquired using the “shooting-on-the-fly” logging technique. In this technique the receiver string is held stationary at the appropriate depth while the source is logged up the hole, firing at the

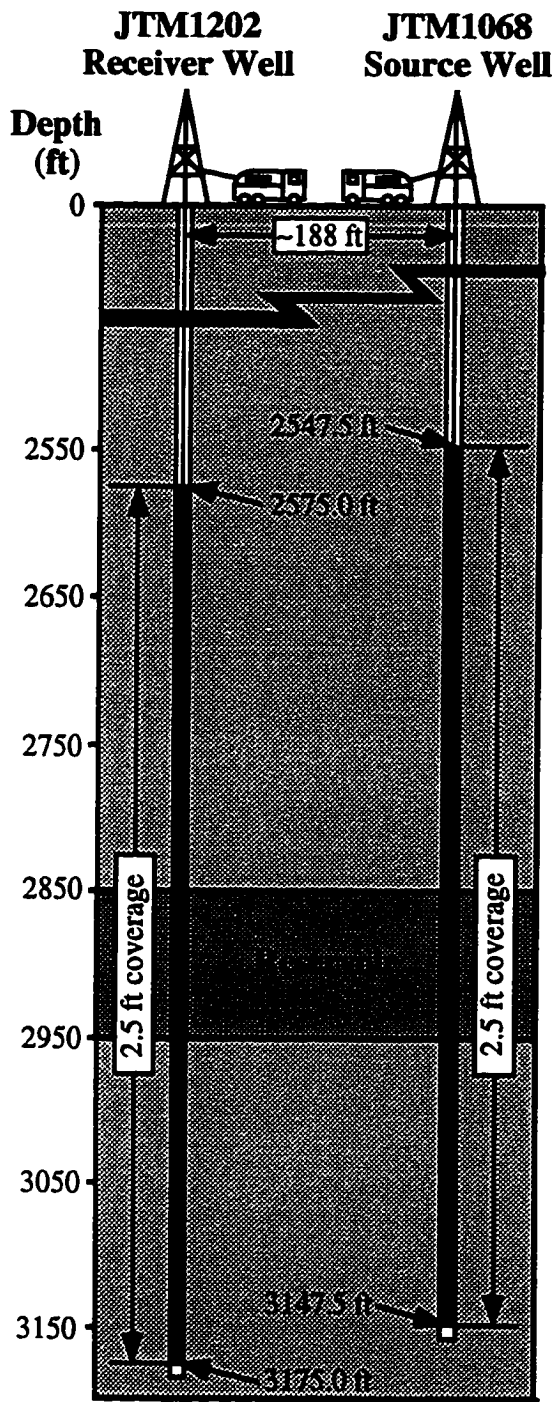


Figure 6.5: The acquisition geometry of Survey Mc68-02b. The depths shown are tied to the kelly bushing at well JTM1202.

appropriate depths. After the source completes its run through the survey interval the receivers are repositioned at another depth and the process is repeated. This technique has two fundamental advantages over the standard “stop and shoot” technique: 1) moving the source from location to location is done automatically with minimal operator effort and 2) the constant motion of the tool up the hole allows precise depth positioning. These advantages combine to allow larger volumes of high-quality finely-sampled (in depth) data to be acquired than is possible in standard acquisition methods. This technique, introduced by Stanford University, has resulted in 10-fold increase in data set sizes with virtually no increase in acquisition time. Additional details on the data acquisition and hardware can be found in Harris et al. (1995).

### 6.2.3 Data description

The data used in this example are actually a subset of the entire Mc68-02b crosswell survey. The survey was windowed for several reasons. One important reason is related to computer hardware resources. The entire survey of 241 by 241 traces can potentially yield over 58,000 direct arrival traveltimes. This results in an inversion problem that is near the limits of what the 96Mb of computer RAM can accommodate on the DEC Alpha stations that these problems were run on. A second reason for decimating the data set is that direct and reflection traveltimes for source and receiver combinations above the Grayburg formation (Fig. 6.2) are difficult to obtain with confidence. This is primarily due to the large velocity contrast between the ~14,000 ft/s McElroy formation and the ~20,000 ft/s velocity found in the A1 unit of the Grayburg formation. This contrast results in head waves and strong transmission attenuation. For these reasons, and because the primary targets of the imaging study were the Grayburg/San Andres formations, the survey was windowed as shown in Figure 6.6. Traces from sources and receivers located above 2745 ft were discarded in addition to traces from below 3160 ft. This decimation reduces the Mc68-02b data set to 167 receivers by 162 sources, a total of 27,054 traces.

The crosswell data collected at the McElroy test site contain a wide variety of seismic wave modes (Van Schaack, 1995). An analysis of a typical gather collected during Survey Mc68-02a is shown in Figure 6.7. As can be seen in this gather, both *P*- and *S*-waves are present in the crosswell data. In this demonstration of the CDRATT velocity estimation method I pick and process only *S*-wave direct and reflected arrival events. The primary reason I focus on the *S*-wave events is because of the strong signal level of the *S*-wave reflections which eases processing and the picking of traveltimes. *S*-wave reflection events are evident in the unprocessed gather shown in Fig. 6.7 while *P*-wave reflections are far more subtle. This difference in relative amplitudes is not a fundamental property of

crosswell data but a result of the acquisitions hardware including the piezoelectric bender source and the hydrophone receivers.

Figure 6.8 provides a schematic view of the radiation pattern of the piezoelectric bender source and the sensitivity pattern of a hydrophone receiver within fluid filled boreholes. The radiation pattern of the radial-force fluid-coupled source has been estimated by a number of researchers such as Lee and Balch (1982), Meredith (1990), and Gibson (1994). The newer work addresses issues such as low formation velocity and the effects of casing and cement. An important prediction consistent in all their work is the radiation of *S*-waves with a  $\sin 2\theta$  dependent radiation pattern, a quadrapole. The  $\sin 2\theta$  dependence creates the four-leafed pattern plotted in the source representation shown in Fig. 6.8. The *P*-wave radiation pattern is peanut-shaped with the peak energy perpendicular to the borehole.

The sensitivity pattern of a hydrophone receiver can be estimated from work done by Schoenberg (1986). Schoenberg describes the pressure field within a fluid-filled borehole

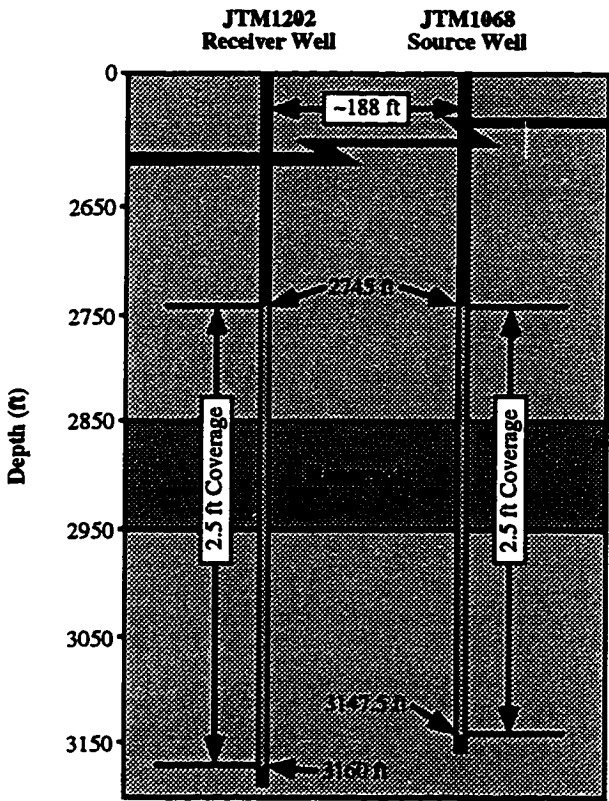


Figure 6.6: The windowed Survey Mc68-02b used in the inversions and imaging shown in this chapter. The survey was windowed to reduce the size of the CDRATT inversion problem and avoid the slow McElroy formation, just above 2750 ft, while maintaining the fullest possible coverage of the reservoir zone.

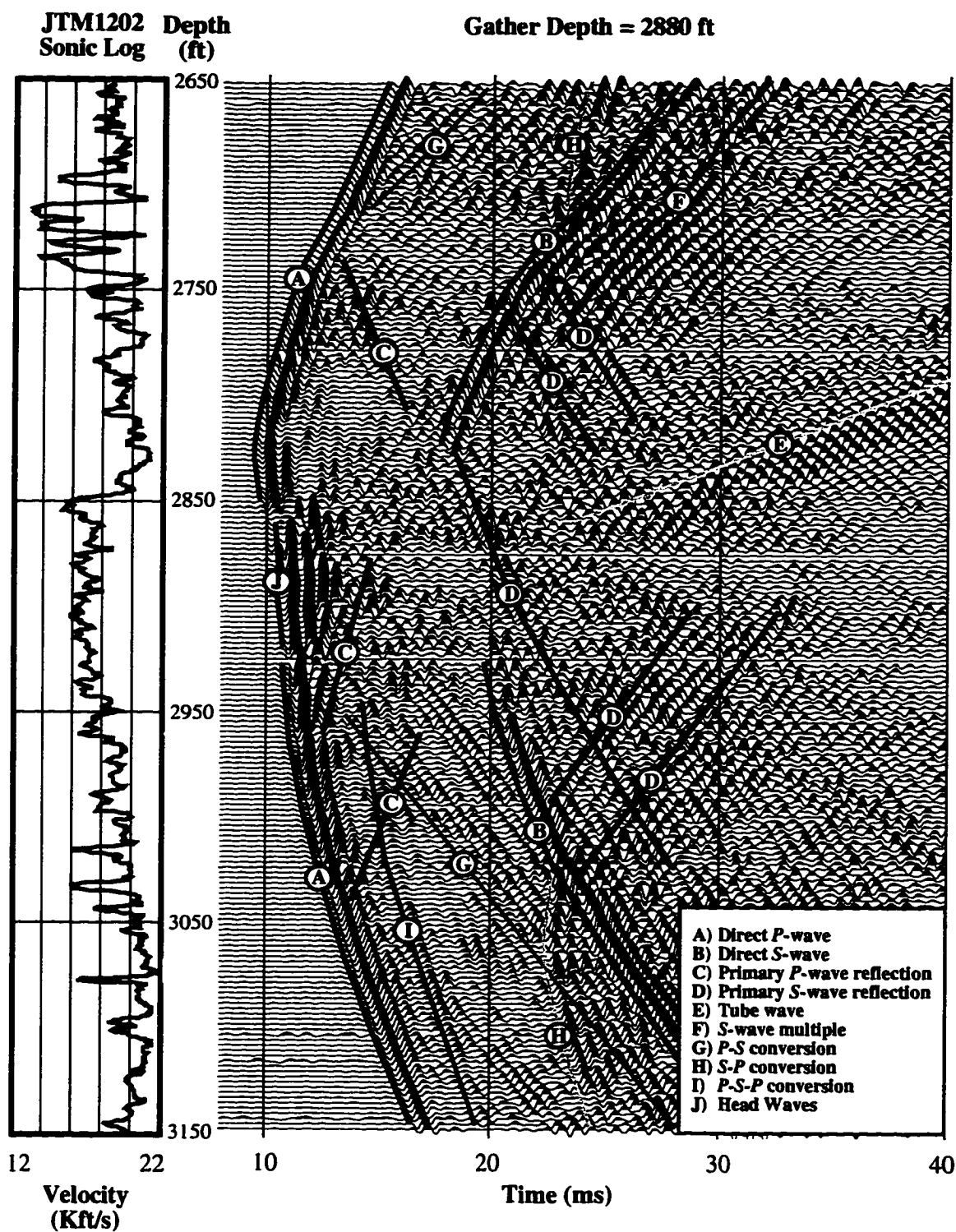


Figure 6.7: An interpretation of the many wave modes present in a crosswell seismic gather. Note the null in the S-wave direct arrivals around the depth of 2880 ft, the gather depth.

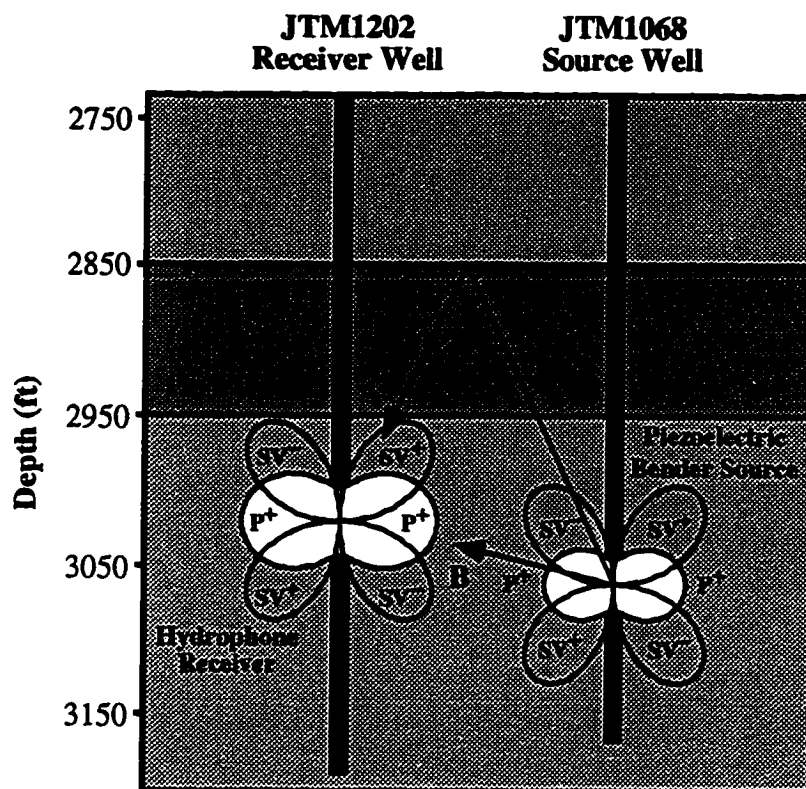


Figure 6.8: This figure illustrates the theoretical source radiation pattern of a piezoelectric bender source and the receiver sensitivity pattern of a hydrophone receiver. The source radiates the most *S*-wave energy at 45 degrees from the horizontal. The receiver is also most sensitive to *S*-waves at these angles. These patterns predict stronger *S*-wave reflections than *P*-wave and zero energy in the *S*-wave direct arrival when the source and receiver are at approximately the same depth.

resulting from incident *P*- and *S*-waves. Using this work to describe the response of a hydrophone receiver assumes that the hydrophone provides a direct measure of pressure and that the hardware within the borehole has a minimal effect on the pressure field. The sensitivity pattern of the hydrophone receiver, shown in Fig. 6.8, is remarkably similar to the radiation pattern of the source. Both the four-leafed *S*-wave sensitivity and the peanut-shaped *P*-wave sensitivity are predicted. In addition, Schoenberg's work predicts the maximum sensitivity of the hydrophone receiver is greater for *S*-waves than *P*-waves.

The piezoelectric source and hydrophone receiver approximations explain why reflected *S*-waves have better signal-to-noise ratio than *P*-wave reflections. As seen in Fig. 6.8, peak *S*-wave source power and receiver sensitivity occur at  $\pm 45^\circ$  from the vertical. *S*-wave reflections are then created and monitored at angles optimal for good signal-to-noise ratio, such as that shown by ray "A". This same ray is not optimally located within the *P*-wave radiation and sensitivity patterns to obtain strong *P*-wave reflections. On the other

hand, for nearly horizontal rays such as ray “B”, this situation is reversed, *P*-waves are strong and *S*-waves are weak. The “hole” in the *S*-wave radiation and sensitivity occurring at small angles is apparent within the field gather shown in Fig. 6.7. Note that the amplitude of the *S*-wave direct arrival goes to zero at low angles.

In summary, this Mc68-02b survey example focuses on the *S*-wave direct and reflected arrivals because their signal-to-noise ratio is highest. This makes the traveltime picking of these events straightforward. *P*-wave events can also be used although more care is required to accurately pick the reflection data. To better illustrate the potential of CDRATT velocity estimation to field data I have used the more reliable *S*-wave events.

## 6.3 Traveltime picking

Traveltime picking is one of the more critical aspects of the CDRATT velocity estimation. In this step a large volume of seismic data is reduced to a set of traveltimes which can be processed using the CDRATT inversion. In addition to reducing the data set to a manageable size this process eliminates extraneous data making the inversion more robust. Since accurate traveltime picking is so crucial I describe some of the details of my picking methods in this section. The picking of reflection traveltimes from crosswell data is new and required the development of a focused approach to obtain reliable times. The reflection traveltimes shown in this section are the first ever picked and processed in a crosswell traveltime inversion.

### 6.3.1 Direct arrivals

Picking direct arrival *S*-wave traveltime picks is relatively straightforward in the windowed Mc68-02b data set. Figure 6.9 shows a typical Common Shot Gather (CSG) where the source location is slightly above the reservoir unit at 2800 ft. Both direct *P*- and *S*-waves can be seen clearly in this gather. The null in the *S*-wave direct-arrival wavefield, resulting from the radiation and sensitivity patterns discussed in the last section, can be seen in this gather at near offsets, where the receiver depth is within ~40 ft of the source depth.

An illustration of the CSG ray coverage and the direct arrival traveltime pick map are shown in Figure 6.10. The pick map contains direct arrival traveltime picks for the entire data set. The black horizontal line on the traveltime pick map, near the top, indicates the location of the traveltime picks corresponding to the single gather shown in Fig. 6.9. For a single source depth the traveltimes are saved in the pick map from left to right, shallow to deep. The diagonal blue element within the pick map corresponds to the near-offset no-data zone.



6.3.2 Reflected arrivals

Prior to work by Lazaratos (1993) reflection imaging of crosswell data was performed primarily to demonstrate principles and potential pitfalls of this technique. In his work, solutions were provided for a number of technical issues which made it difficult to obtain high signal-to-noise crosswell reflection images from field data. Many of these solutions were made possible due to a significant advancement in data acquisition referred to earlier, “shooting on the fly”.

The acquisition technique of shooting on the fly allows crosswell data to be acquired much more efficiently and with better depth accuracy than had been possible using the standard “stop and shoot” method. As a by-product of this increase in efficiency it became feasible to collect crosswell data with a fine spatial sampling interval. In the past, 10 ft and 5 ft source and receiver sample intervals were common. The new technique makes feasible 2.5 ft and even 1 ft sample intervals. The primary benefit of the finer sampling is that it prevents the spatial aliasing of seismic events in the trace records. This allows the effective application of digital signal processing techniques (Rector et al., 1994; Rector et al., 1995).

Theoretically, including reflection traveltimes in a tomographic inversion is relatively straightforward. Implementing the required algorithm code changes to utilize these

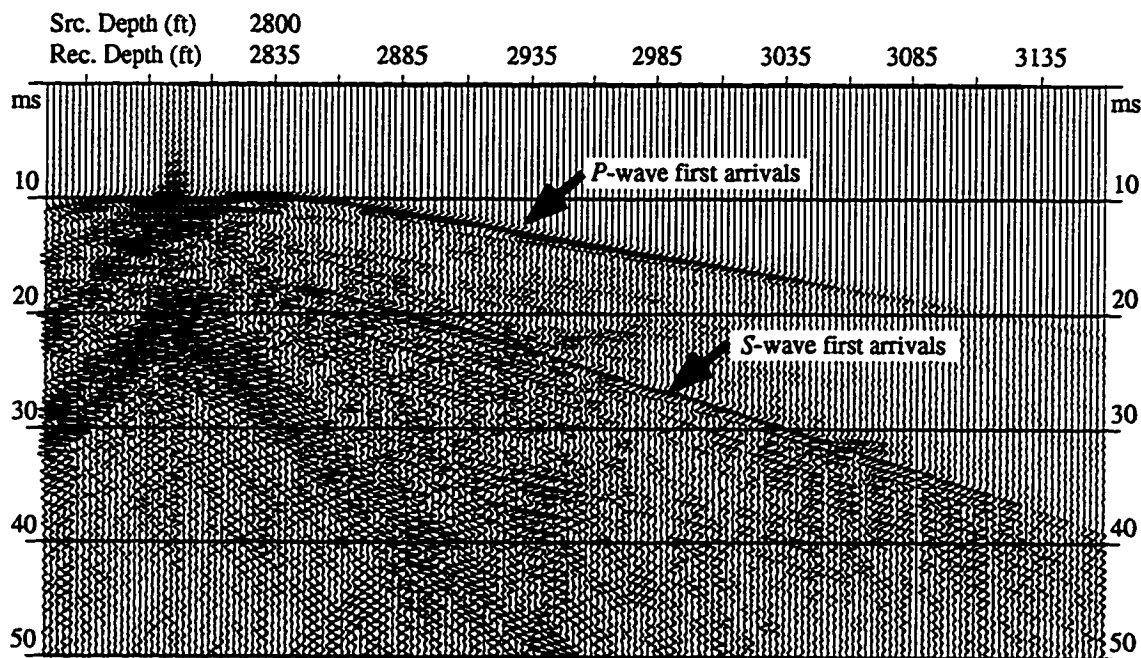


Figure 6.9: A Common Shot Gather where the source is located at a depth of 2800 ft. Direct arrival S-wave traveltimes can be picked with little difficulty from this unprocessed gather.

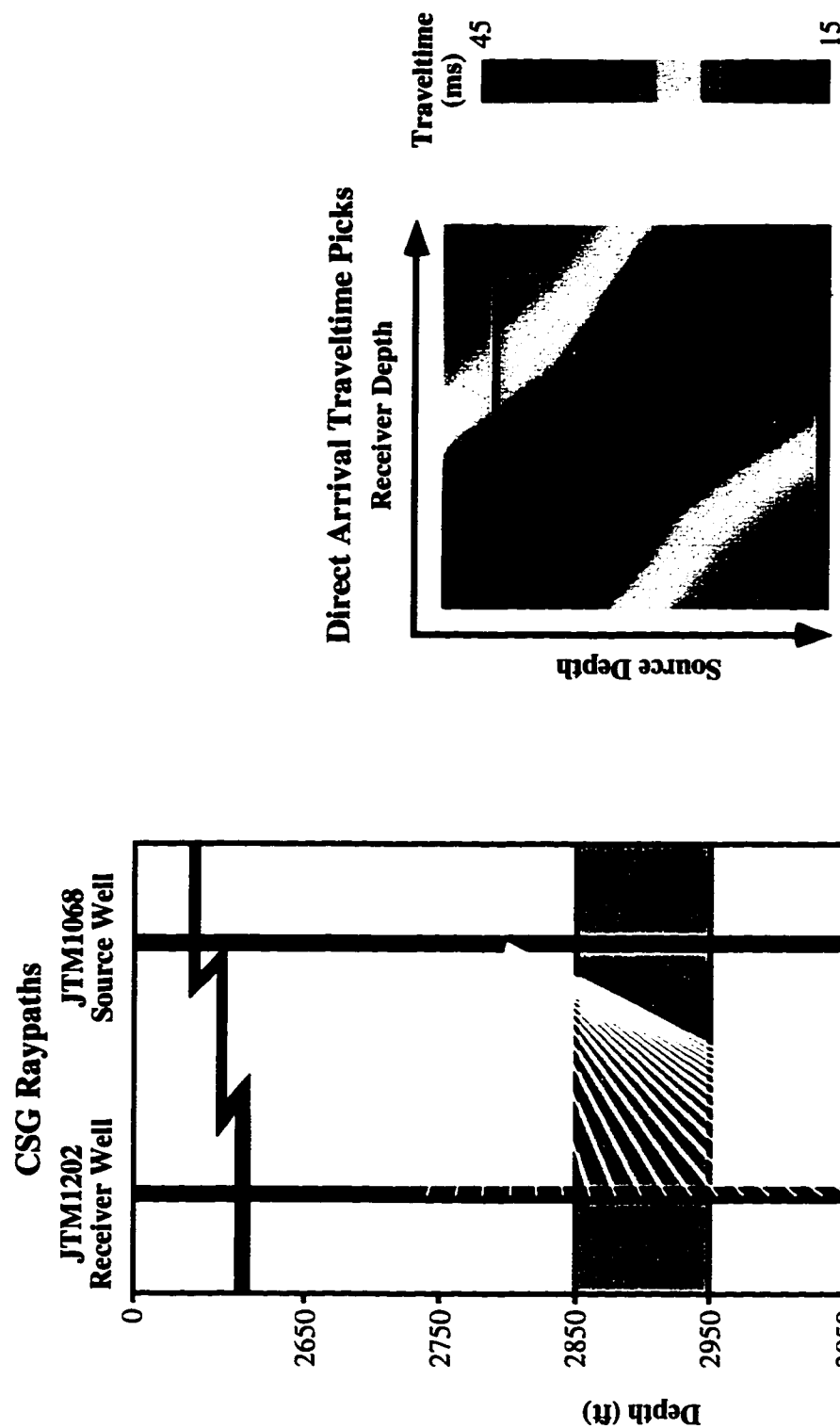


Figure 6.10: The figure on the left provides a cartoon illustration of the approximate geometry and ray paths corresponding to the CSG shown in Figure 6.9. Directly above is a traveltime pick map for the direct arrival S-waves. Traveltime picks corresponding to the CSG at left would lie along the black line above.

traveltimes in the inversion is also reasonably straightforward. The primary difficulty in reflection tomography is obtaining accurate traveltime picks for reflection events. While reflections can occasionally be seen in raw data, for example those shown in Fig. 6.7, they are difficult to pick without enhancement. Only recently, since crosswell data began being acquired at fine spatial sampling intervals, have signal processing procedures been effective at enhancing reflections in crosswell data. This recent advance, plus some re-ordering and selective sorting of the data I have devised, has made picking reflection events feasible. These breakthroughs have been necessary to make the CDRATT velocity estimation possible and, to my knowledge, the reflection traveltime picks used in this thesis are the first to be obtained from any crosswell field data set.

A crosswell seismic survey can be organized in a manner similar to a large multi-offset VSP survey and processed as such. On the other hand, the acquisition geometry and volume of data collected in crosswell surveys offers the opportunity for more complex and effective multi-domain filtering not possible with offset VSP's. This type of processing sequence has been documented in Rector et al. (1994) and Rector et al. (1995) and will not be discussed here in detail. Since data used for the reflection traveltime picking in this example were processed by Lazaratos using this approach, however, a brief description of the Lazaratos' processing flow will be included for completeness.

The basic processing sequence used to enhance the *S*-wave reflections is shown in Figure 6.11. This flow is a multi-step process which calls for sorting the data into Common Shot Gathers (CSG), Common Receiver Gathers (CRG), and Common Offset Gathers (COG), and applying filters in each of these sort domains. Each of these filters is designed to either enhance the desired *S*-wave reflection events, or attenuate undesired events. At the end of this flow the processed data are filtered again into upgoing and downgoing data sets. Creating a total of four processed data sets.

Why four data sets? As can be seen in Fig. 6.11 the data are separated into two parallel flows. The flow down the left side is designed to enhance reflections near the source well while the flow on the right side enhances reflections near the receiver well. Actually the reflections are not processed effectively only at the wells but in one half of the image area or the other. Away from the "good" side the quality of the processed reflections degrade. To create upgoing and downgoing reflection images from this processed data Lazaratos (1993) mapped these four data sets separately. The mapped data were then stacked to create four separate reflection images: upgoing source half, upgoing receiver half, downgoing source half, and downgoing receiver half. The last step of his imaging procedure consisted of splicing the two "good" half sections of the resulting reflection images at the middle discarding the "bad" halves.

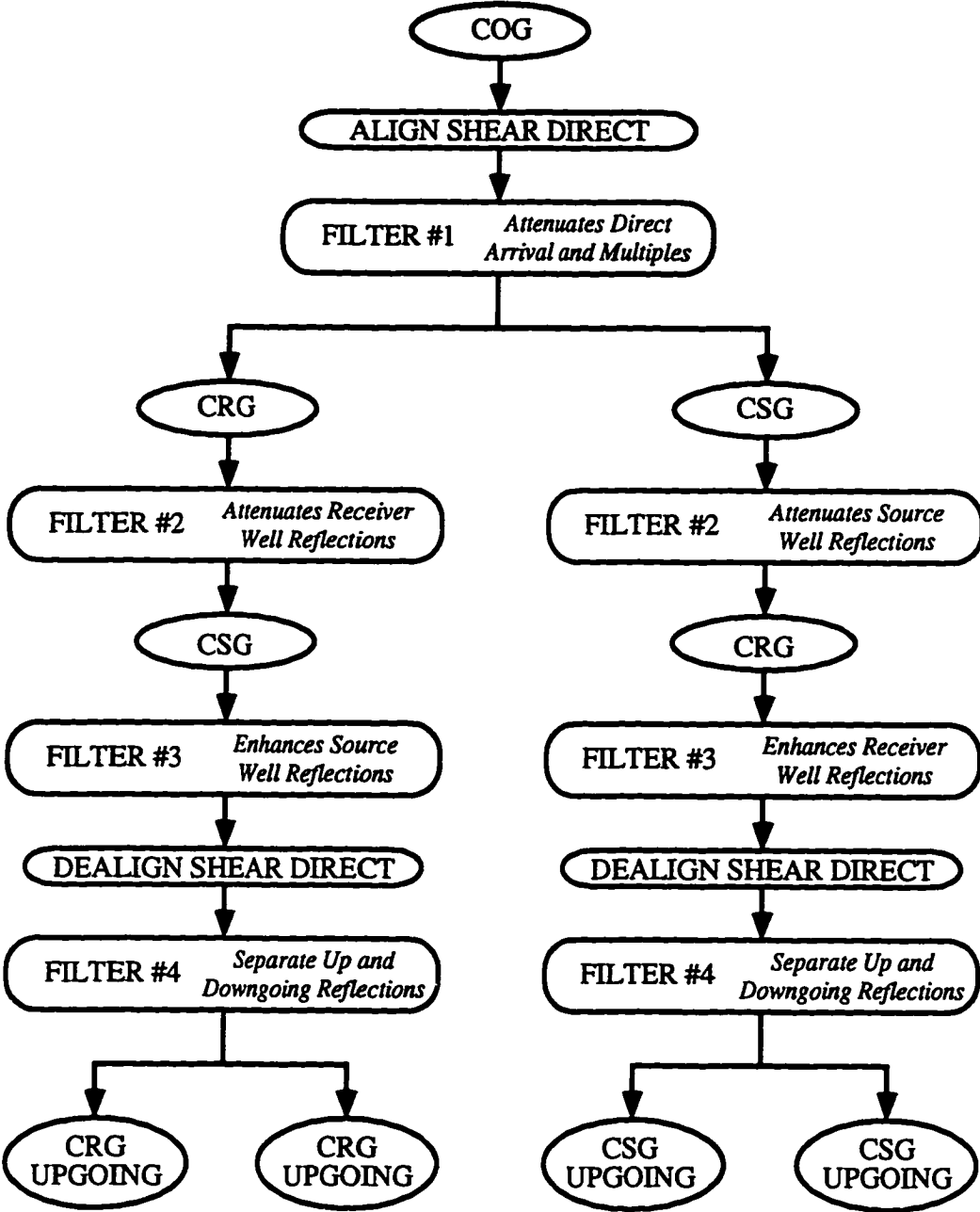


Figure 6.11: The processing sequence used by Lazaratos (1993) to separate and enhance S-wave reflections in the Mc68-02b data set. The enhanced data resulting from this flow are used to pick reflection traveltimes and for reflection imaging.

It is undesirable to have to pick a reflection event from two data sets, one for the receiver well half and the other for the source well half. To avoid this I combine the appropriate traces from each of the four processed data sets to create just two data sets, one consisting of upgoing reflections and the other downgoing reflections. This procedure is shown schematically in Figure 6.12. Once this has been done the data are ready for reflection picking.

A second application for these combined data sets, beyond picking, is that they can be used to map upgoing and/or downgoing reflections in a single step to create a well-to-well image without splicing. This procedure can cut the effective mapping time in half.

Once the reflection events have been enhanced, picking reflection traveltimes proceed in a fashion similar to direct arrival traveltime picking. One difference is that individual reflection events are identified and picked in sequence. A second difference is that the sort domain plays an important role in making it practical to identify and track each reflection event. Figure 6.13 shows crosswell seismic data before and after the wavefield processing to enhance reflections. A number of points are illustrated in Fig. 6.13: attributes of the Common Mid-depth Gather (CMG) in which the data are sorted, the effect of the wavefield processing, and the selection and picking of “Reflection 7” and its attributes. I will discuss each of these in turn.

The data shown in Fig. 6.13 have been sorted into Common Mid-depth Gather (CMG). Common Mid-depth Gather are defined as gathers where the average depth of the source and receiver is constant. In the case of the gathers shown in Fig. 6.13, the CMG depth is 2970 ft. A ray trace representation of this gather is shown in Fig 6.14. One property of the CMG which is useful for reflection picking is that for vertical wells, flat reflectors, and constant velocity, the reflection events are flat, or at a constant time. This is because the

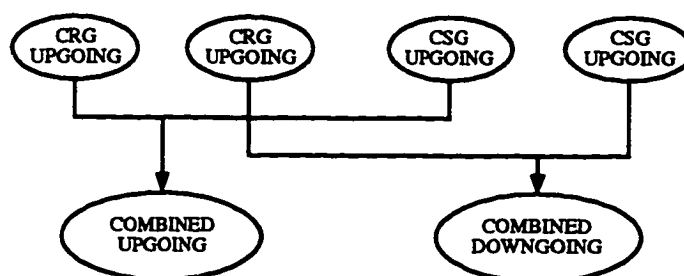


Figure 6.12: The above procedure shows the four data sets resulting from the processing flow found in Fig. 6.11 which are then edited and combined to create one upgoing data set and one downgoing data set.

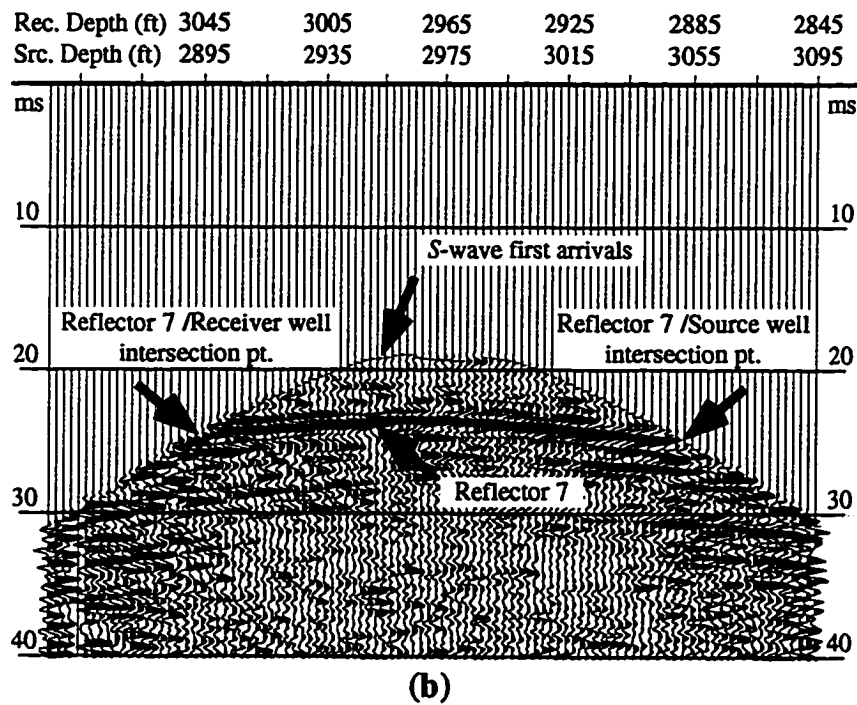
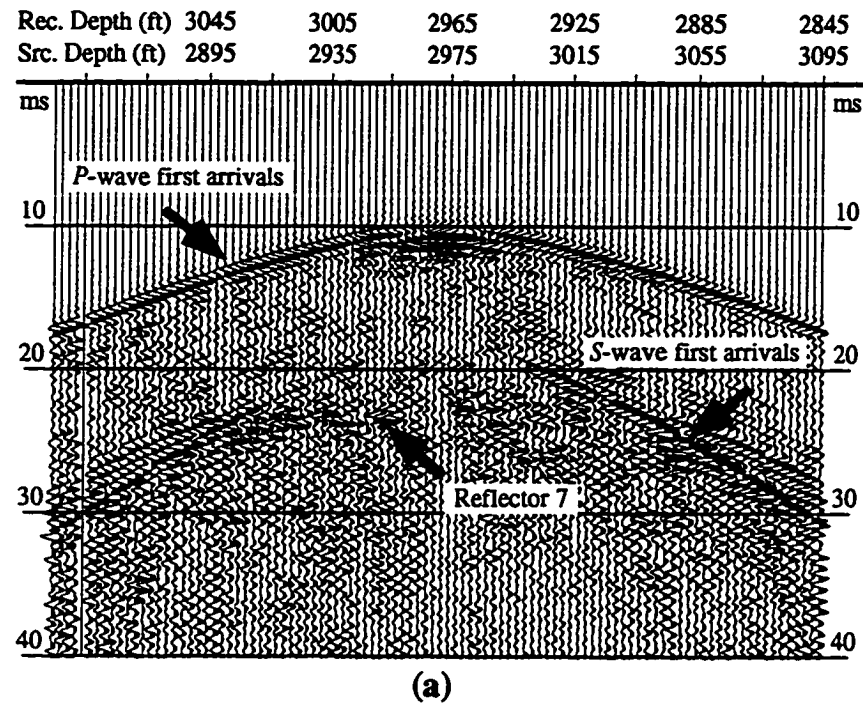


Figure 6.13: A Common Mid-depth Gather (CMG) before and after the processing designed to enhance upgoing S-wave reflections. Note that reflections can be seen going well to well in this gather.

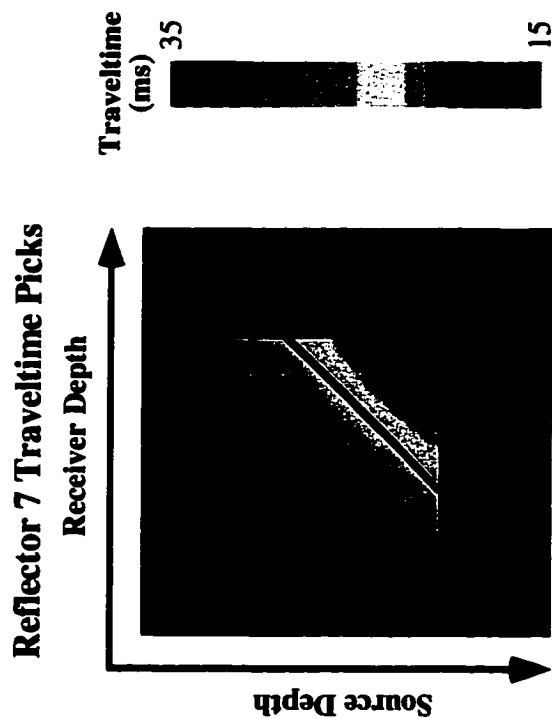
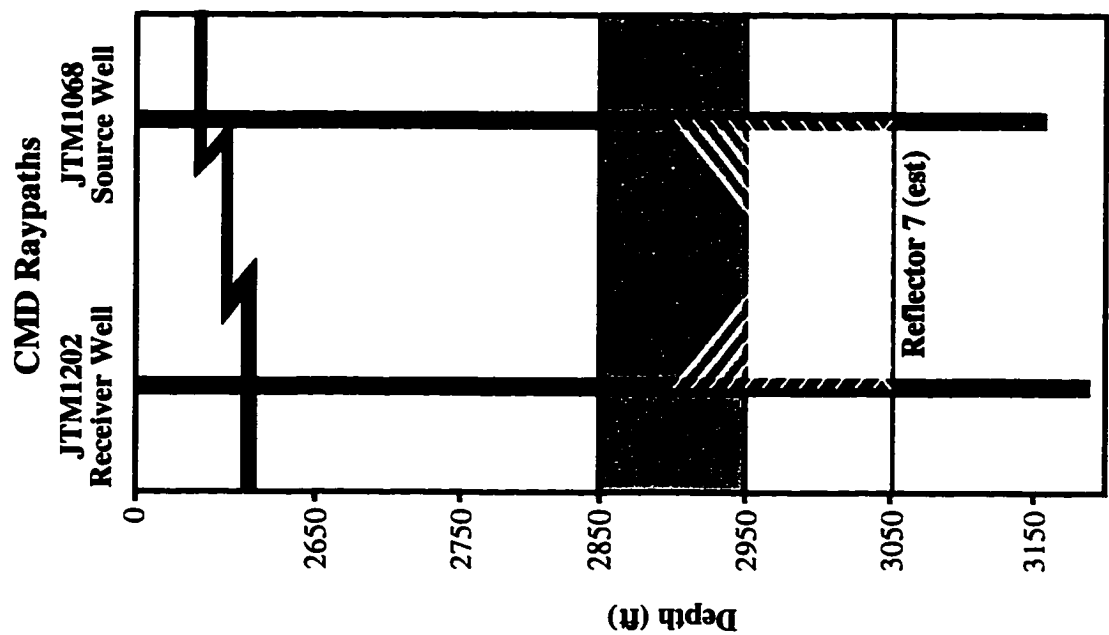


Figure 6.14: The figure on the left provides an illustration of the approximate geometry and ray paths corresponding to the CMG shown in Figure 6.13. Directly above is a traveltime pick map for the reflected arrival S-waves for Reflector 7. Traveltime picks corresponding to the CMG at left would lie along the black diagonal

raypaths, seen in Fig. 6.14, are all the same length. Dipping reflectors and velocity variations can result in perturbation of the reflection event from the horizontal, such as that seen in Reflector 7 in Fig. 6.13b. For the most part, however, reflector moveout is minimized. This property makes the CMG ideal for picking reflections.

A second point illustrated in Fig. 6.13 is the effectiveness of the processing procedure in enhancing reflection events. In Fig. 6.13a reflections can be seen within the data but with some difficulty, due to the low signal-to-noise ratio. Fig. 6.13b shows the same gather after processing. Now the reflections are much more apparent. All events earlier in time than the direct *S*-wave arrival have been removed as part of the processing. Undesired events, later than the *S*-wave direct arrival, have been attenuated leaving primarily upgoing *S*-wave reflections.

Finally, the last point illustrated by the processed data is related to the attributes of the reflections. I have denoted a single strong reflector within this gather as Reflector 7. With processing this reflector now has sufficient signal strength to be picked using standard picking practices. In crosswell data the intersection of a reflector with its direct arrival counterpart (e.g. *S*-wave reflections with *S*-wave direct arrivals) corresponds to the intersection of the reflection event with a well. Reflector 7 can be seen to intersect with the direct arrivals at two points, one corresponding to the receiver well and the other, the source well. The intersection depth of the reflector and the source well can be determined from the CMG by noting the source depth at the intersection of the reflector and direct arrival at the source well, similarly with the receiver well. The approximate well intersection depths for Reflector 7 are 3050 ft at both wells. The bowing up of the reflector in the CMG may indicate actual reflector bowing or perhaps variations in velocity, well deviations etc. The true geometry of the reflector can be determined using the CDRATT inversion and reflection imaging.

The reflection picking procedure is straightforward once the seismic data have been processed. Strong reflection events are identified within the data and picked, one by one, over a range of common mid-depth values. Each picked reflector results in a traveltime pick map similar to the one created from direct arrival picking. An example of this pick map for Reflector 7 is shown in Fig. 6.14. The location of the traveltime picks within this map corresponding to the 2970 ft CMG, shown in Fig. 6.13, is denoted by the black diagonal line. Note that a majority of the values within the pick map are zero, equivalent to “no data” locations. These no data locations are due to either a signal level which is insufficient to make an accurate pick or source-receiver combinations for which a reflection off the particular interface is impossible.



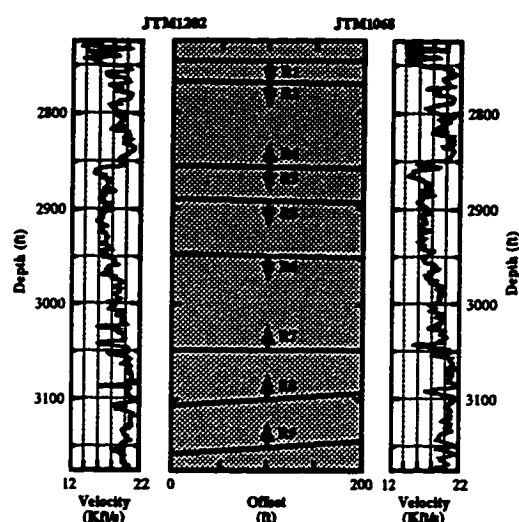


Figure 6.15: The orientation (upgoing/downgoing) and estimated geometries of reflections events picked from the Mc68-02b survey. The reflector geometries are estimated by observing the intersection of the events and the wells and assuming linearity between these points. Note below 3050 ft the reflection events begin dipping to the left. This interpretation would be unlikely using only the well logs shown.

A total of nine reflection events were identified and picked from the Mc68-02b data set. These events are shown diagrammatically in Figure 6.15. The reflectors in this figure are defined by their intersection points with the wells with an assumption of linearity between these points. Note that Reflectors 3 & 4 are co-located. In my picking procedure upgoing and downgoing reflections are always defined as independent reflection events. This is to avoid inconsistencies which might result from phase shifting of the data during processing or misidentification of events. Note also the rough estimates of reflection geometries suggests a change in dip angle below 3050 ft, the location of the San Andres/Grayburg unconformity. For the most part, however, reflection events above 3050 ft are reasonably flat, with perhaps a very slight dip towards JTM1068.

### 6.3.3 The Mc68-02b CDRA TT traveltime data set

The complete set of traveltimes used in the Mc68-02b CDRA TT inversion are shown in Figure 6.16. This data set consists of 20,169 direct arrival traveltimes and a total of 35,792 reflected arrival traveltimes for nine reflectors. Of the nine reflection events, four correspond to upgoing reflections, and five to downgoing reflections. Overall, there are 55,961 traveltimes available for the CDRA TT inversion. As mentioned earlier in this

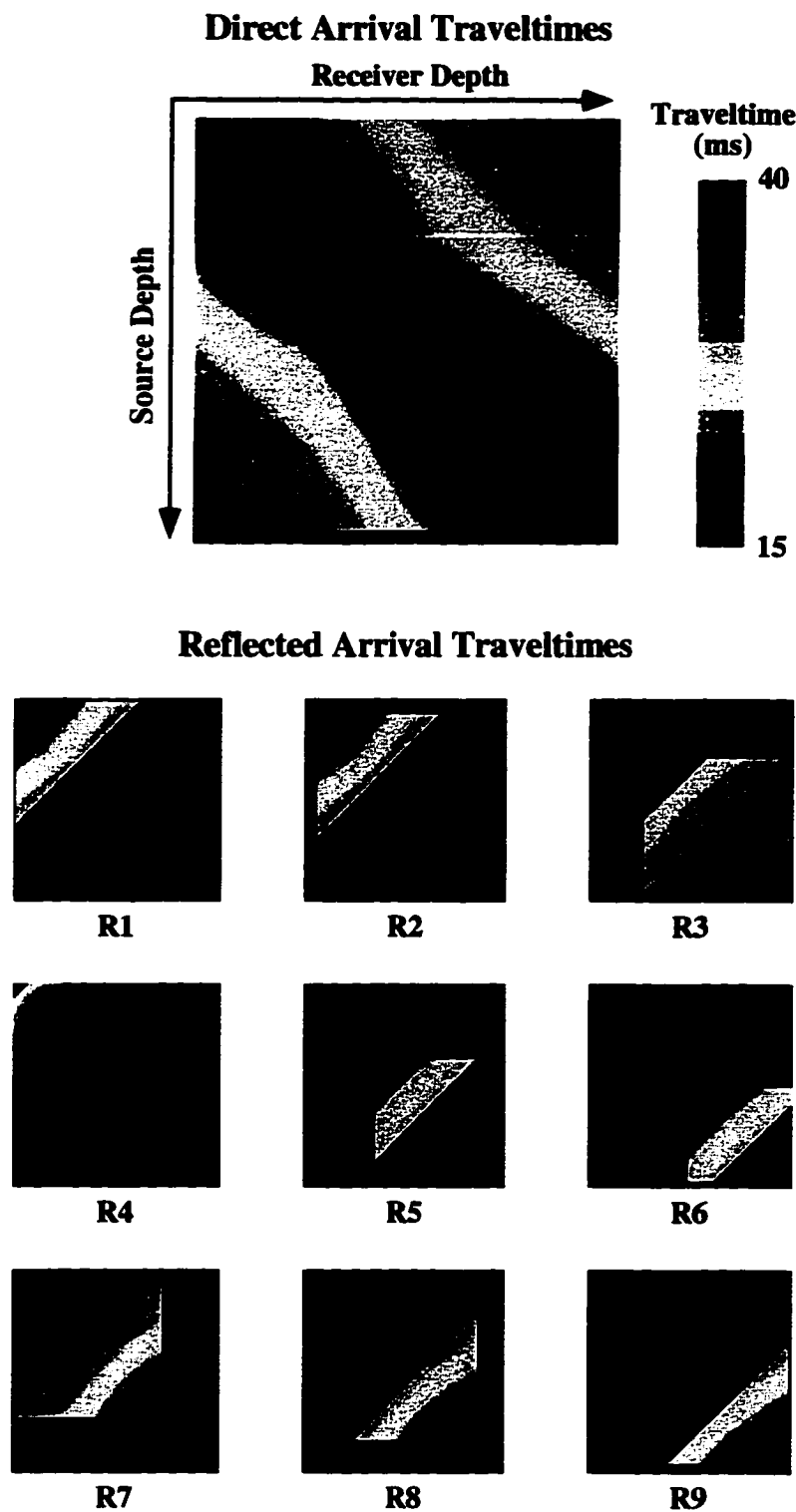


Figure 6.16: The complete set of direct and reflected arrival traveltimes obtained from the windowed Mc68-02b data set. The above images represent 20,169 direct arrival traveltimes and a total of 35,792 reflected arrival traveltimes.

section, this total is close to the limit allowed by the computational resources of our research group.

A special effort was made to identify and pick reflection events near the top and bottom edges of the survey. These are Reflectors 1 & 9. One potential advantage of including reflection events in a crosswell traveltime inversion is the possibility of increasing the angular coverage near the top and bottom edges of the survey. This is typically where the most troublesome inversion artifacts form. The Mc68-02b crosswell experiment was designed so that the reservoir is in the middle of the survey, with the best angular coverage. Many times, however, the target lies at the bottom of the survey since wells are not commonly drilled beyond the deepest potential reservoir. In these cases the additional angular coverage offered by the reflection traveltimes may be particularly advantageous.

## 6.4 Traveltime inversion

A total of six traveltime inversions were run using the Mc68-02b traveltime data set. These inversions were run in exactly the same way with the following three variations.

1. The first inversion was run using only direct arrival traveltimes and allowing the velocity to vary only in depth, a 1-D inversion. This type of model is similar to that used by Lazaratos (1993) and was run to provide a comparison of his approach with the CDRATT velocity estimation method.
2. The second inversion was also run using direct arrival traveltimes only but in this case 2-D velocity variations were allowed. This inversion was run to provide a baseline to see the effect of adding reflection traveltime information on crosswell velocity and reflection imaging. With this inversion result I address the question of whether the velocity model acquired using only direct arrivals is consistent with the reflection data.
3. The final four inversions were all run using CDRATT. In these inversions the number of nodes used to define the reflectors was varied from 2 to 21. The purpose of these tests is to show the effect of different reflector parameterizations on the CDRATT solutions.

The rest of the processing parameters were left unchanged in these inversions. A summary of the more important parameters is shown in Table 6.1. The goal of the traveltime inversion is to obtain a model which provides the closest agreement between observed (in the data) and calculated (through the model) traveltimes. The accuracy of this agreement is measured in terms of traveltime residual, the difference of these two numbers. A listing of the traveltime residuals for each inversion is provided in Table 6.2. Included in this table are the number of direct and reflected arrival rays used in each inversion. These numbers show a rms residual error less than the acquisition sample interval, 200  $\mu$ s, for all the inversions run. By this measure *all* the inversions are relatively successful in obtaining a

**TABLE 6.1.**  
**Direct Arrival Only and CDRATT Tomographic Inversion Parameters**

<b>Traveltime Inversion Parameters</b>	<b>Description</b>
Model size	41 x 91 nodes - total 3731
Pixel size	5 ft by 5 ft (each node represents the velocity in the pixel)
Starting model	Constant velocity 10,200 ft/s
# Shots	162
# Receivers	167
# Reflectors	9 (no reflectors used in the direct arrival only inversions)
Min/max aperture	+/- 65 degree limit on direct arrival raypaths
Horiz./vert. damping	Ratio of horizontal to vertical model regularization = 8
Relaxation	Rate at which the penalty terms are relaxed per continuation step = $10^{-2}$ .
Continuation steps	All results come from the 10th continuation step of the inversion.
Well deviation corrections	All inversions use the same well geometries. These geometries were obtained using a projection method.

model which explains the data, although some better than others. There are, however, other measures of model accuracy.

In the sections that follow the quality of these inversion models will be discussed in terms of these other criteria: absence of artifacts, reflector geometries, conformance with the well logs and local geologic knowledge, quality of reflection images, etc. The goal of these sections is to demonstrate the validity and accuracy of the CDRATT imaging approach.

**TABLE 6.2.**  
**Traveltime Residuals of Direct Arrival Only (DAO) and CDRATT Inversions**

<b>Inversion Type &amp; Reflector Parameterization*</b>	<b>Total Residual (RMS <math>\mu</math>s)</b>	<b>Direct Arrivals Residual (RMS <math>\mu</math>s)</b>	<b>Reflected Arrivals Residual (RMS <math>\mu</math>s)</b>	<b>Direct Arrivals Used</b>	<b>Reflected Arrivals Used</b>
Direct only 1-D	132.9	132.9	N/A	20147	0
Direct only 2-D	62.0	62.0	N/A	20147	0
CDRATT T2 2-D	113.1	85.2	126.2	20147	35615
CDRATT T5 2-D	109.6	80.4	123.0	20147	35780
CDRATT T11 2-D	105.7	77.4	118.7	20147	35770
CDRATT T21 2-D	104.3	77.1	116.9	20147	35767

\* Reflector parametrization refers to the number of spline points used to define the reflector, e.g. T21 indicates that 21 points were used to parameterize the reflectors in this inversion.

### 6.4.1 Direct arrival only (DAO) traveltimes inversions

Two traveltimes inversions were run using direct arrivals only. The first of these inversions uses a 1-D velocity parameterization. The resulting 1-D velocity tomogram is shown in Figure 6.17. The second DAO inversion was run using a 2-D velocity parametrization and the results of this inversion are shown in Figure 6.18. Displayed alongside each tomogram are the open hole *S*-wave well logs and slices of the tomogram velocity field near those wells. Unfortunately, while an open hole *S*-wave sonic log was collected from JTM1202 only a *P*-wave log was acquired from JTM1068. For comparison purposes a “synthetic” *S*-wave log was calculated for JTM1068 using a smoothed version of the  $V_p/V_s$  ratio calculated in JTM1202 and JTM1068’s *P*-wave log. The well logs are displayed in red and the tomogram slices are displayed (in blue).

Several observations can be made from a comparison of the 1-D and 2-D direct-arrival tomograms. The first observation comes from a comparison of the tomogram slices at the wells with the corresponding well logs. Plots of the well logs and tomogram slice velocities (shown in Figs. 6.17 and 6.18) show that the vertical resolution of the tomograms is much less than that of the well logs, as expected. The tomogram slices appear to capture the average velocities represented by the well logs fairly well, though.

Table 6.3 summarizes the rms and mean differences between the 1-D and 2-D tomogram slices and the well logs. In fact, the mean of the percentage difference for both wells is low, 2% and less for both wells. At well JTM1202, where actual *S*-wave measurements were taken, this value is even lower, closer to 1%. One point to note is that the correlation of the 1-D traveltimes inversion results and the well logs is nominally better than the 2-D inversion results. This suggests that the 1-D velocity parameterization constrains the inversion in a way that makes the results correlate better at the wells.

**TABLE 6.3.**  
Correlation of Tomogram Slices with *S*-wave Well Logs

	JTM1202 % Difference of Tomogram Slices & Well logs		JTM1068 % Difference of Tomogram Slices & Well logs	
	rms	mean	rms	mean
1-D vel. tomogram	8.6	0.9	9.5	1.9
2-D vel. tomogram	9.4	1.2	10.3	2.0

The next observation is that the velocity of the tomogram slices in Figs. 6.17 and 6.18 appear quite similar to each other. The resolution of the two tomograms (in the vertical

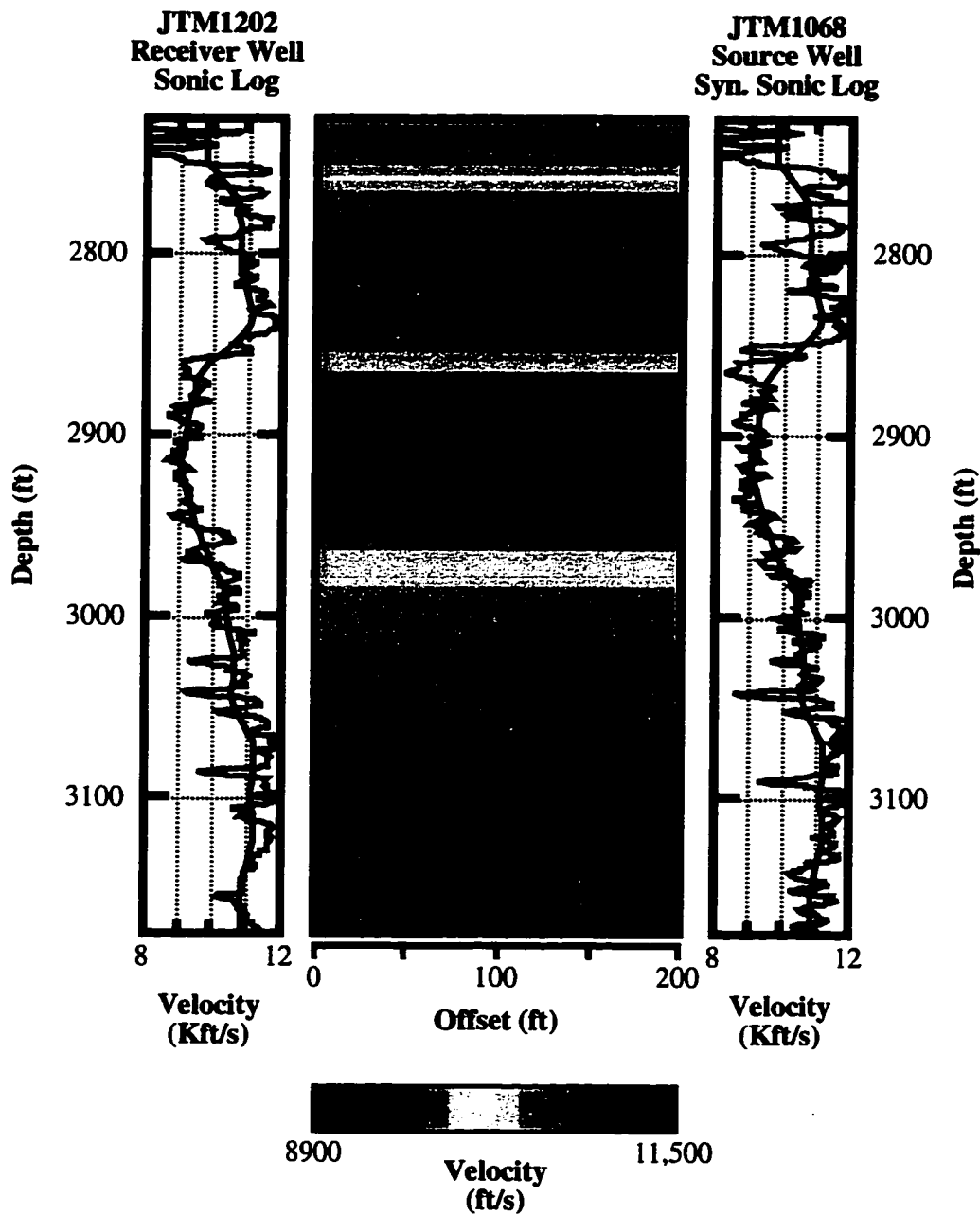


Figure 6.17: A 1-D direct arrival only traveltime inversion of the Mc68-02b data. Along the sides are *S*-wave well logs each displayed with a slice of the velocity tomogram taken from near the well.

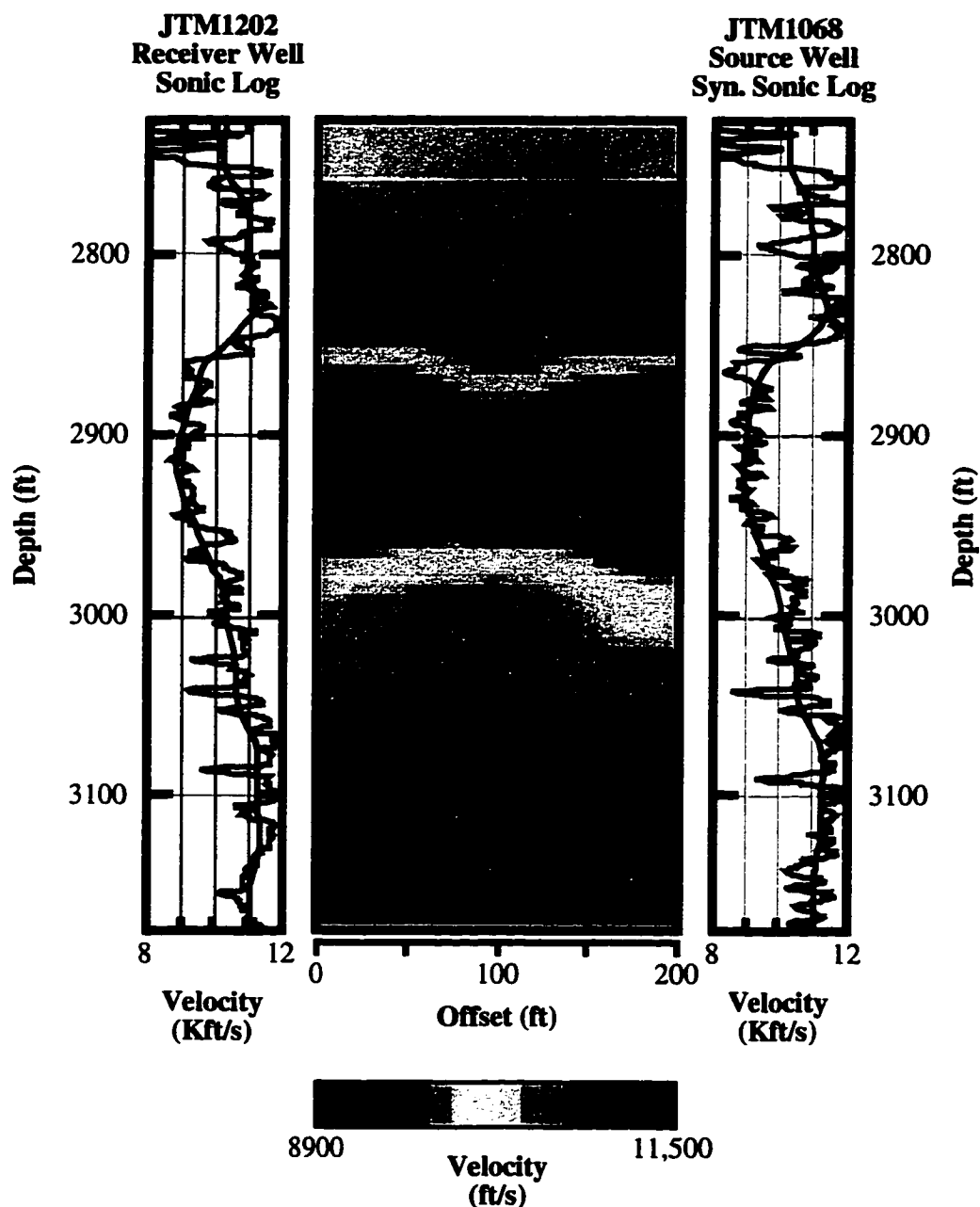


Figure 6.18: A 2-D DAO travelt ime inversion of the Mc68-02b data set. A comparison of this result with that shown in Fig. 6.17 illustrates the changes resulting from a modification in the velocity parametrization, 1-D to 2-D. Although the rms travelt ime residual of this tomogram is significantly lower the correlation with the well logs is slightly poorer and there are obvious velocity artifacts at the top and bottom of the

direction) is almost identical in spite of the different velocity parameterizations. In fact, the rms difference between the two receiver well slices and the two source well slices is only about 2% and the average difference is about 0.25%. The largest difference between the two slices along the well is near the top, above 2750 ft, where the difference is about 5 percent. At this depth, however, there is no ray coverage and the velocity is determined almost exclusively by the penalty terms on high velocity gradients between pixels.

The third observation relates to lateral velocity variations in the 2-D tomogram. Although the geology of the area is layer-cake, the 2-D tomogram shows a fair amount of lateral variation symmetric about the vertical axis of the tomogram. This form of symmetry is common in many direct arrival tomograms. Since it is unlikely that the geology is actually symmetrical in this way in so many surveys this feature is commonly believed to be an inversion artifact. The nature of these “artifacts” is that they tend to be strongest near the top and bottom edges of the tomogram. In the case of the 2-D tomogram in Fig. 6.18 the lateral velocity variations near the top are easily seen and appear as a lower velocity “V” shaped structure. These variations are even more evident viewing the tomogram in units of “slowness”,  $\mu\text{s}/\text{ft}$ , as shown in Figure 6.19. In this figure the “V” shaped anomalies can be seen at both the top *and* bottom of the surveyed area. The exact cause of these artifacts is still being studied but a general observation has been that they are typically *not* seen in tomograms calculated from synthetic data sets. This suggests that they may be due to acquisition effects such as incorrect well geometries, timing errors, picking errors, or from incorrectly modeled media effects, such as velocity anisotropy. Regardless, the observation that they typically show up where the ray coverage is poorest, near the edges, implies that improving angular coverage in those regions, perhaps using reflection traveltimes, may reduce the magnitude of these artifacts.

The final point is a short discussion of the traveltimes residuals of the tomographic inversions, shown in Table 6.2. The rms residual traveltime error for the 1-D inversion is 139.9  $\mu\text{s}$ . This about 3/4 of the sampling rate of the seismic data, 200  $\mu\text{s}$ . This rms residual amounts to about 0.7% for the fastest traveltimes at near offsets, which are about 20 ms, and less for the far offsets. As might be expected, allowing more velocity parameters in the form of a 2-D velocity model, allows the inversion to reduce this error even further. The rms residual traveltime error of the 2-D inversion is about half that of the 1-D, 62.0  $\mu\text{s}$ . This amounts to about 0.3% rms difference between the modeled direct arrival traveltimes and the experiment data at near offsets.

In summary, the results of the 1-D and 2-D direct arrival traveltime inversions show good agreement with well log data and each other at the wells. Also, both inversions provide velocity models that can explain the traveltime data with an rms error of better than



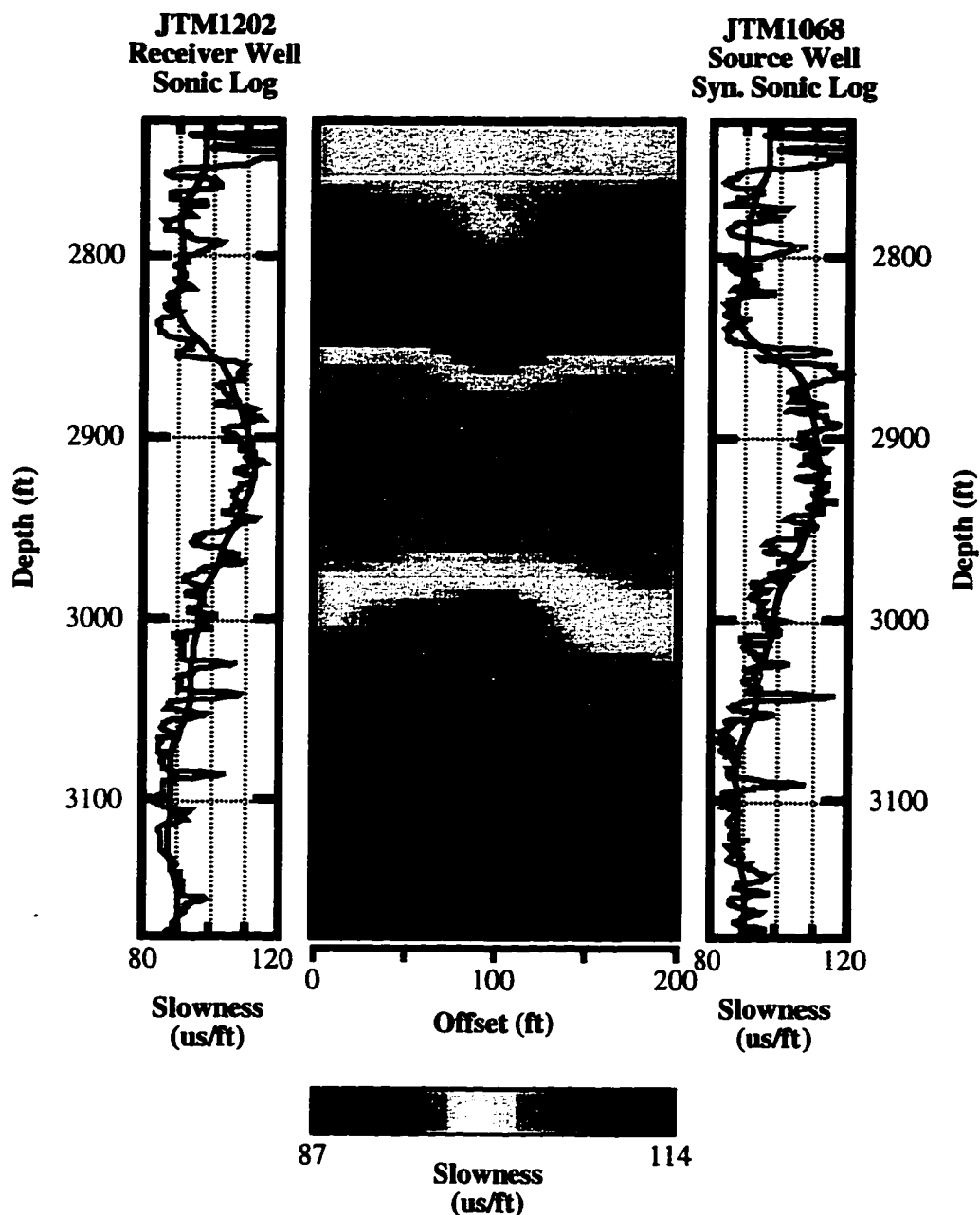


Figure 6.19: This figure provides another look at the 2-D DAO inversion result. The model here is plotted in terms of inverse velocity, slowness. This display mode enhances some of the axis-symmetric inversion artifacts present at the top and bottom of the tomogram.

1%. In spite of this the 1-D and 2-D models are distinctly different in nature. The 2-D velocity model shows fairly strong lateral variations that are symmetric about the axis of the survey and strongest at the top and bottom of the velocity image. These velocity models provide a baseline for comparison with the results of the CDRATT inversion. In Section 6.4.3 these models are compared with the CDRATT velocity model. In Section 6.5 the effectiveness of using these different models to image crosswell reflections is tested.

## 6.4.2 CDRATT inversion — choice of reflector parametrization

In this section I process the Mc68-02b data set shown in Fig. 6.16 using the CDRATT inversion method. The velocity model is parameterized in the same way as the 2-D DAO model. The reflectors, however, can be defined with a variable number of nodes. Part of this section is devoted to determining the optimal parameterization of the reflectors for the Mc68-02b data set.

The combined inversion of the Mc68-02b direct and reflected arrival traveltimes is accomplished using the same parameters as those used in the 2-D DAO inversion. The only addition to the CDRATT model is the reflector geometries. Reflectors are defined at nodes containing the reflector depths. These nodes are spaced evenly from one side of the model to the other. The reflector location between the nodes is defined using a cubic spline algorithm. In any one inversion, all reflectors are defined with the same number of nodes, a number set by the user. Defining the reflector with just two nodes, each which would be located on the side edges of the model, limits the inversion to simple linear reflectors. Although these reflectors may dip, the reflector location in between the node points is just a linear interpolation of the reflector depths at the edge. By defining the reflector using more nodes, both dipping *and* curved reflectors can be described.

Describing the reflectors using many nodes allows complex reflector geometries to be defined. Overparameterizing the reflectors, however, can result in a less robust inversion and excessive computational time. The task then is to determine the optimal number of reflector nodes for the inversion. As a test I have run four CDRATT inversions using 2 nodes, 5 nodes, 11 nodes, and 21 nodes per reflector. The models resulting from each of these inversions are shown in Figure 6.20. The traveltime residuals for direct arrivals, reflected arrivals, and combined direct and reflected arrivals, corresponding to each of the inversions are shown in Table 6.2

All of the CDRATT velocity models shown in Figure 6.20 look quite similar. The apparent similarity is supported by the fact that the rms traveltime residuals vary only a little, from 113.1  $\mu\text{s}$  to 104.3  $\mu\text{s}$ , for inversions T2 to T21 respectively. The rms traveltime residuals of the direct arrivals are slightly higher, 85.2  $\mu\text{s}$  to 77.1  $\mu\text{s}$ , than was seen in the

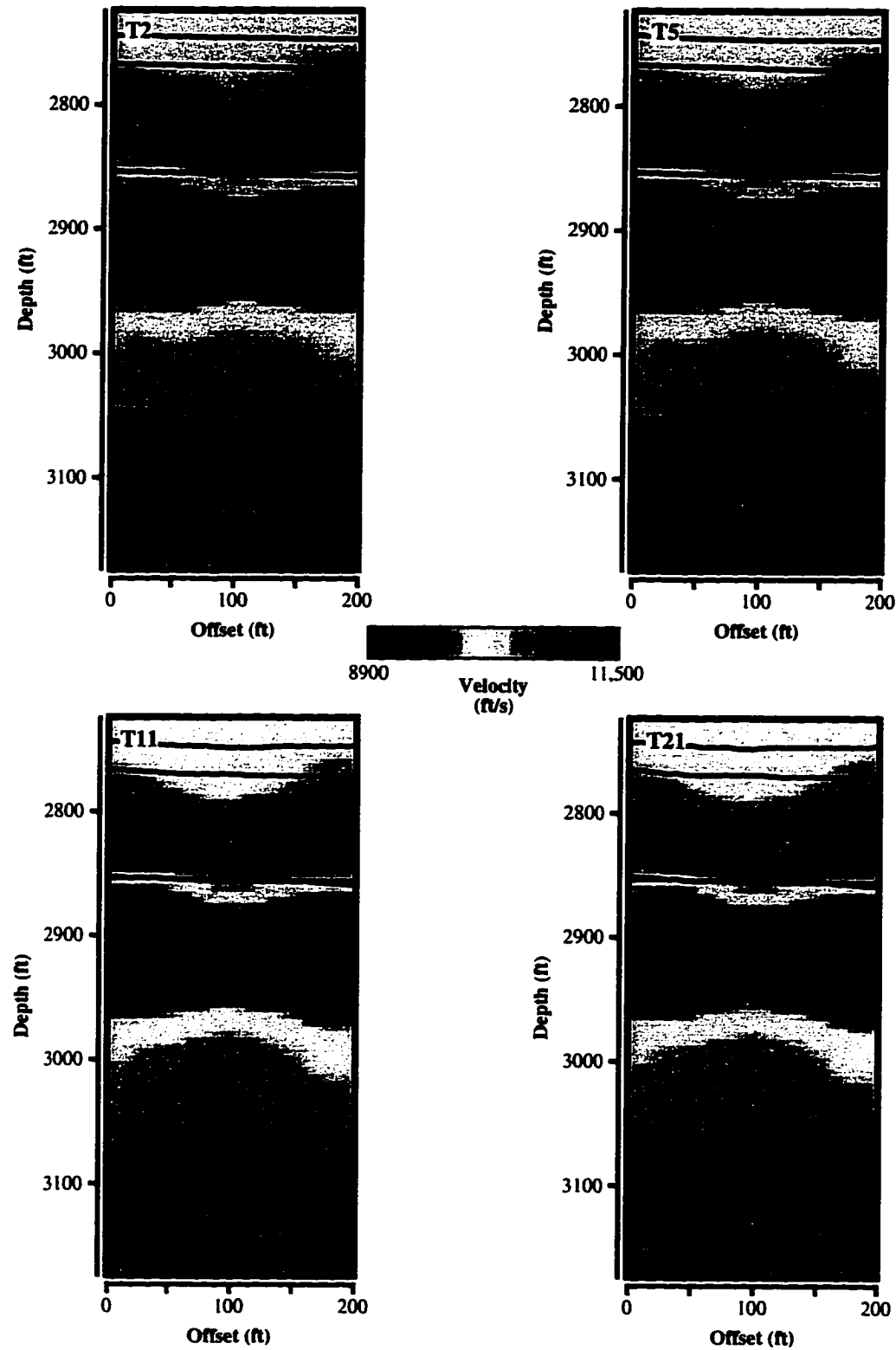


Figure 6.20: The spectrum of CDRATT models created for reflector parameterizations using 2, 5, 11, and 21 nodes. The images show both the calculated velocity field and the calculated reflector solutions for each of the inversions.

2-D DAO inversion, 62.0  $\mu$ s. This is expected since the models must satisfy the additional reflection data also.

**TABLE 6.4.**  
**Velocity Changes of CDRATT Inversions with respect to the 2-D DAO Inversion**

Inversion Comparison	Min% dif.	Max% dif.	% dif. rms	% dif. average
CDRATT T2/Direct only	-3.69	3.25	1.29	-0.28
CDRATT T5/CDRATT T2	-1.22	1.34	0.43	-0.14
CDRATT T11/CDRATT T5	-1.13	1.07	0.37	-0.13
CDRATT T21/CDRATT T11	-.50	.36	0.12	-0.02

As can be seen in Figure 6.21, the velocity models *are* very similar. In this figure I have calculated the percent difference in velocity between each model and the next less complex model (in terms of reflector parameterization). Table 6.4 provides some statistics for these comparisons. The largest change in the velocity models in Figure 6.21 is between the 2-D DAO result and the CDRATT T2 velocity model, due to the addition of reflector information. Increasing the number of reflector nodes leads to a relatively large change in velocity until 21 nodes are used to define each reflector. The difference between the CDRATT T11 and T21 velocity models is very small compared to the changes seen up to then.

The calculated reflector geometries seen in Fig. 6.20 are similar to the geometries estimated from the well intersection points shown in Fig. 6.15. Reflectors above 3050 ft show a very mild dip from the receiver well to the source well. The two reflectors below 3050 ft dip more steeply in the opposite direction. A summary of the intersection points of the reflectors with the model edge is shown in Table 6.5. The reflector geometries of all reflectors agree with the estimated well intercept depths to within a fraction of the velocity model pixel size, 5 ft. Variations in reflector geometries between the different CDRATT inversions agree, in general, to within 1 ft or so. The most obvious difference between the calculated reflector geometries, seen in Fig. 6.20, are small perturbations from linearity for reflectors 1, 2, 7, 8, & 9. These perturbations increase in magnitude as more points are used to define the reflectors but are nominally less than 4 ft for all reflectors, even in the CDRATT T21 results.

The reflector geometry results of the CDRATT T21 inversion contains a greater degree of rapid fluctuations than the other inversions. This is in contrast to the local geologic knowledge which supports smoother reflection interfaces. A close examination of the parameter coverage, how many non-zero depth derivatives are obtained for each reflector

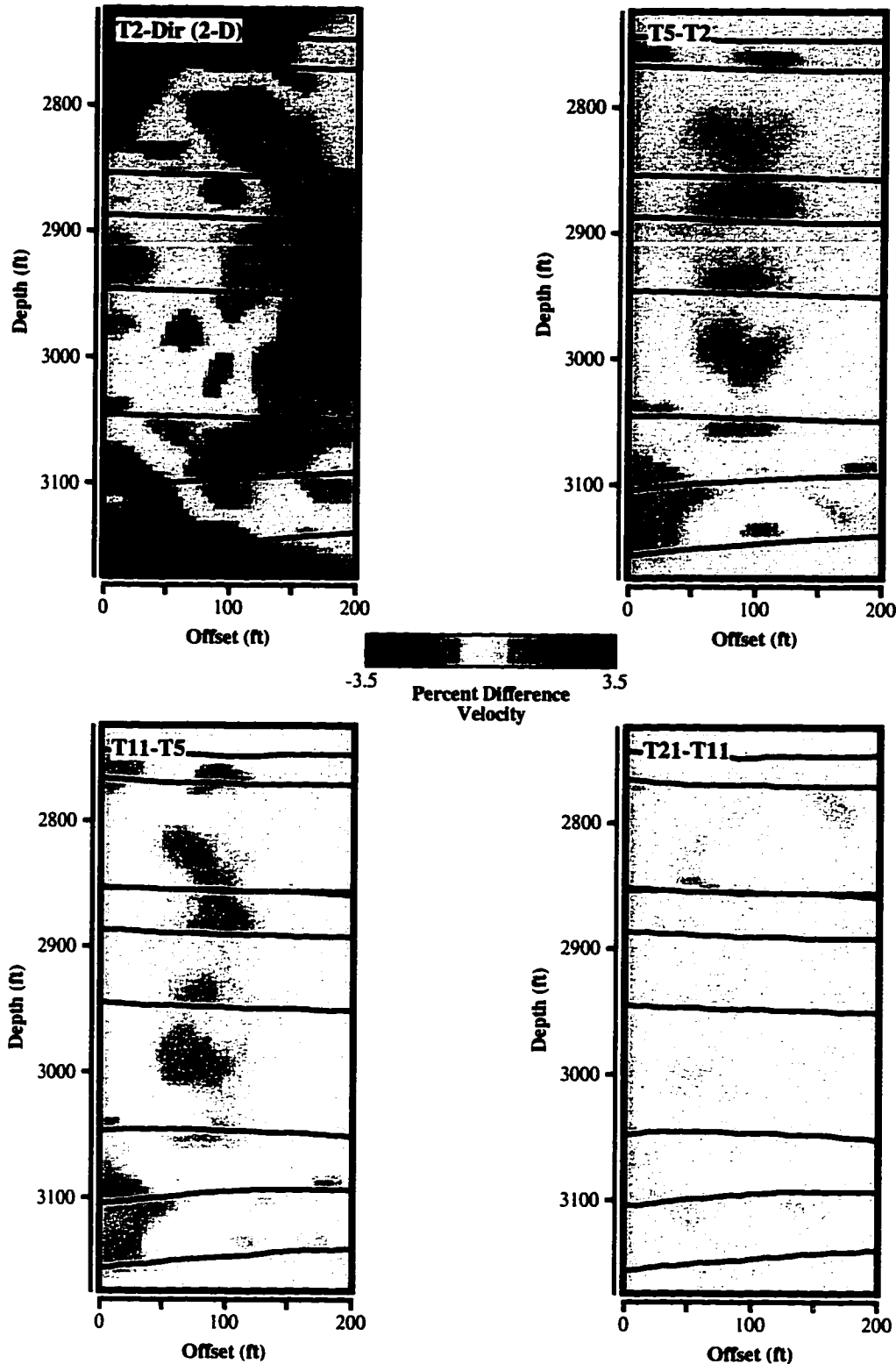


Figure 6.21: This sequence of images shows the percent change in velocity between each CDRATT inversion and the next less complex reflector parameterization. The upper-left image, showing the largest changes, is the difference between the CDRATT T2 and the 2-D DAO velocity models.

**TABLE 6.5.**  
**A Comparison of Model Edge Intersection Points of Reflectors (approx. well intersections)**

Model >>	Well/ref inter.		CDRATT T2		CDRATT T5		CDRATT T11		CDRATT T21	
Offset (ft) >>	0	200	0	200	0	200	0	200	0	200
Reflector 1	2746.0	2748.5	2744.9	2748.4	2744.4	2747.8	2743.9	2747.0	2743.8	2746.6
Reflector 2	2767.5	2772.5	2768.0	2772.4	2767.6	2772.3	2766.9	2772.1	2766.4	2772.1
Reflector 3	2855.0	2860.0	2854.0	2859.2	2854.1	2859.5	2854.3	2860.0	2854.5	2860.5
Reflector 4	2855.0	2860.0	2854.8	2859.0	2854.6	2858.8	2853.5	2857.8	2852.5	2857.0
Reflector 5	2890.0	2895.0	2888.2	2894.0	2887.8	2893.7	2887.7	2893.5	2887.7	2893.6
Reflector 6	2947.5	2952.5	2946.7	2952.4	2946.2	2952.1	2946.0	2951.8	2946.0	2951.4
Reflector 7	3048.5	3048.5	3046.3	3051.0	3047.4	3051.7	3048.4	3052.4	3049.5	3053.8
Reflector 8	3107.0	3092.0	3104.0	3092.1	3105.2	3093.4	3106.0	3094.7	3106.1	3095.0
Reflector 9	3157.5	3142.5	3157.3	3140.6	3157.3	3140.8	3157.5	3141.1	3157.5	3141.0

depth parameter, shows that there is relatively uniform reflector coverage, even near the wells. This suggests the inconsistency is a symptom of the node points being too close together. The spline reflector parameterization is more stable when the distance between nodes is greater.

I believe that the CDRATT T11 inversion uses the optimal reflector parametrization for the Mc68-02b experiment. This choice is made on the basis of two observations: 1) that the velocity model is stable and doesn't change significantly with additional reflector nodes and 2) that the reflectors, while still non-linear, are stable and capable of modeling the complexity of the McElroy geology.

### 6.4.3 CDRATT inversion — analysis of results

In the last section I compared the CDRATT inversion results for various reflector parameterizations. Of these results the CDRATT T11 model was judged to be optimum. In this section I compare the velocity component of this model to the DAO results shown previously. The purpose of this comparison is to determine the effect of including reflection traveltimes on the tomogram velocities and distribution of those velocities.

Figure 6.22 provides an enlarged view of the CDRATT T11 tomogram and plots of the tomogram slices at the well with the well logs. Upon initial examination there are no obvious improvements in the well log tie of the CDRATT velocity model. The CDRATT tomogram slices appear to represent the average well log velocities in the same way as the 2-D DAO tomogram (Fig. 6.18). Table 6.6 provides the statistics of these correlations for comparison purposes. As was noted before, in Table 6.3, the 1-D DAO tomogram provides a slightly better correlation with the well logs than the 2-D DAO tomogram. The data in

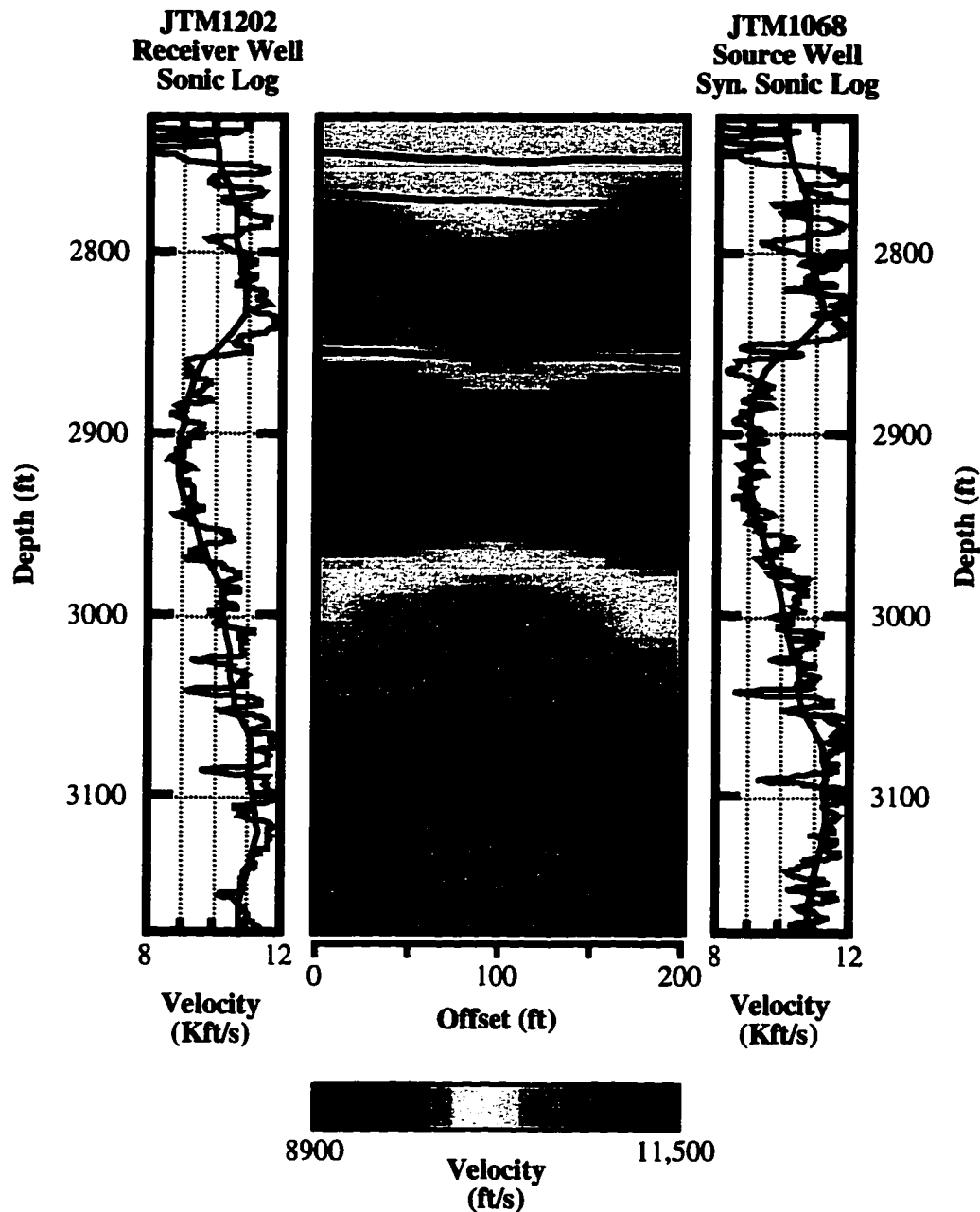


Figure 6.22: The optimal CDRATT solution obtained using an 11 node reflector parameterization. CDRATT inversions run using more nodes result in only small changes in the velocity model but larger instabilities in the reflector solutions.

**TABLE 6.6.**  
**Comparison of DAO and CDRATT Tomogram Slice Correlations with S-wave Well Logs**

	JTM1202 % Difference of Tomogram Slices & Well Logs		JTM1068 % Difference of Tomogram Slices & Well Logs	
	rms	mean	rms	mean
1-D vel. tomogram	8.6	0.9	9.5	1.9
2-D vel. tomogram	9.4	1.2	10.3	2.0
CDRATT T11 Tomogram	9.0	0.2	10.0	1.7

Table 6.6 show, however, that while the 1-D DAO inversion has slightly less rms difference between the well logs and tomogram slices, the CDRATT tomogram matches better the average velocity of the well logs. In fact, for the receiver well where the S-wave log was collected, JTM1202, the mean error of the CDRATT tomogram is only 0.2%, more than four times better than the 1-D DAO result.

Another point of comparison is in the tomogram velocities at the top and bottom of the CDRATT tomogram where inversion artifacts are often found. A comparison of the 2-D DOA tomogram and the CRATT T11 tomogram, Figs. 6.18 and 6.22, show small but noticeable differences near the top and bottom of the surveyed area. These differences are more obvious in a direct comparison of the two tomograms shown in Figure 6.23. The image in Fig. 6.23 shows the velocity change, in percent, between the two tomograms, with the 2-D DOA tomogram used as the reference. As suggested by Figs. 6.18 and 6.22, the largest differences are found at the top and bottom of the difference tomogram. This was expected since the largest change in angular coverage, due to the addition of reflection traveltimes, is in these regions. The maximum velocity changes are at the top and bottom, middle, immediately within Reflectors 1 & 9. The change at these points, blue-green on the difference tomogram, represents a *decrease* in velocity of about 4%. Directly below the top change, to about a depth of 2850 ft, the difference tomogram shows an *increase* in velocity of about 1.5%. Elsewhere in the image, primarily between 2850 ft and 3050 ft, the difference in velocity is less than  $\pm 1\%$ .

#### 6.4.4 CDRATT inversion — conclusions

While the addition of reflection traveltimes does not completely eliminate artifacts in the velocity tomogram they do have a large effect near the top and bottom edges of the tomogram if reflections are picked in the vicinity. This supports the prediction that improving the angular coverage near the survey edges will lead to improvements in the velocity tomogram by reducing the non-uniqueness of the inversion problem. Also, more



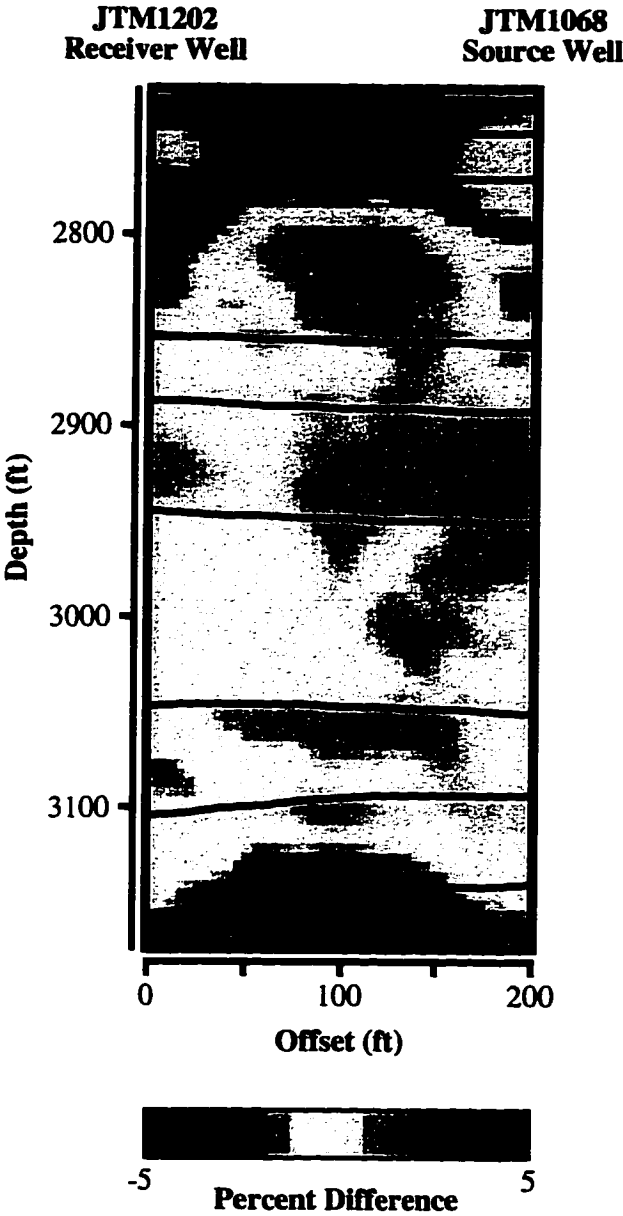


Figure 6.23: A map of the tomogram velocity changes occurring due to the addition of reflection traveltimes to the traveltimes inversions. This image is the percent difference between the 2-D DAO inversion and the CDRATT T11 inversion using the DAO inversion as the reference. As can be seen in the image above the primary changes in velocity are located at the top and bottom of the tomogram where the addition of reflection information provides the largest change in angular ray coverage.

subtly, the effect of the individual reflectors can be seen in Fig. 6.23 as higher frequency variations (spatially) in the velocity field immediately adjacent each reflector. This supports the prediction by Bube and Langan (1995) that the addition of reflection information will increase the resolution of the velocity field primarily *near* the reflectors. It has also been shown that, at least in this example, the addition of reflection traveltimes allows a closer correlation with the well logs to be achieved.

Overall, I have shown that the addition of reflection traveltimes to the crosswell velocity inversion problem provides a measurable improvement in velocity imaging. These improvements are not dramatic, as expected. Bube and Langan (1995) predicted a modest improvement in velocity imaging but that it would be reflector *locations* that would be well resolved. While the calculated reflection geometries compare well to those estimated from the intersection of the reflection events and direct arrival events (which occur at the well) quantifying their accuracy and resolution is difficult. The primary use, though, of the reflection geometries obtained in the CDRATT inversion is in the mapping of the reflection data. In the next section the effectiveness of the CDRATT model for crosswell reflection imaging, the focus of this thesis, is explored.

## 6.5 Reflection imaging

Reflection imaging of the crosswell seismic data is the final step of the CDRATT velocity estimation method. At this point though, the optimal velocity model has already been calculated. Still, although the CDRATT model has been defined and the mapping trajectories are completely determined, careful processing is needed to obtain the optimal reflection images.

A number of techniques have been devised for crosswell reflection imaging which allow a better quality stacked image to be created. One of the most effective of these techniques is “residual moveout corrections” (Lazaratos, 1993). These corrections are designed to compensate for the misalignment of events in the mapped domain prior to stacking. Misalignment of *S*-wave events of only 1–1.5 ft could have a significant detrimental effect on the quality of the stack for the typical wavelengths found in the McElroy data set. A number of theories have been proposed to explain these misalignments. Although effective at creating a higher resolution stack, the philosophy of the “residual moveout correction” approach is to correct the misalignments after mapping, ignoring their source.

One of the key points in CDRATT velocity estimation is that accurate data acquisition, processing, *and* a mapping model that is consistent with both direct *and* reflected arrivals

should be sufficient for effective reflection imaging under normal conditions. In other words, residual moveout corrections should be unnecessary using a model provided by CDRATT velocity estimation. In this section I will test this prediction by studying the results of mapping the Mc68-02b data with the CDRATT model.

### 6.5.1 Brute stacks

The simplest stack of crosswell reflection data is made by mapping all the available data and stacking it directly. This is sometimes referred to as the “brute” stack because no post-map processing or editing is done; the data are simply thrown together in a “brute” force approach. In this first example I have done exactly this. I have mapped the upgoing and downgoing processed seismic data separately using the CDRATT T11 model and stacked all the mapped gathers directly with no preliminary editing. The results of this brute stack are shown in Figure 6.24. The red lines on the upgoing and downgoing reflection images are the CDRATT T11 reflector solutions.

The reflections in the brute stack are quite coherent without any editing of the mapped data prior to stacking. The downgoing reflection image shows reflections from 2900–3000 ft with spatial wavelengths of only 5–10 ft and the well-known angular unconformity at 3050 ft is readily apparent in the upgoing reflection image. Some noise is apparent in the top section of the upgoing image and bottom section of the downgoing image as a result of wavelet stretching. This phenomena, documented by Lazaratos (1993), results from the stack (at that location) consisting of primarily wide angle reflections. These wide angle reflections are stretched in the mapping procedure in a manner similar to NMO stretch in surface seismic processing. As with surface seismic processing, the ideal approach for eliminating the effect of this stretch is to remove the wide angle reflection events prior to stacking. In spite of the lack of processing the brute stacks show strong, coherent, well-to-well reflections. The brute stack result shows the importance of a good velocity model in eliminating the need for post-map processing procedures.

The geometry of the reflections in the reflection image tie well with the CDRATT solutions. This is not required to be true as Lazaratos (1993) showed in his work by imaging the McElroy angular unconformity using a simple horizontal reflector assumption. The close agreement between the CDRATT reflector solutions and the reflections in the reflection image has an important consequence. One of the requirements for accurately locating reflection events using the mapping method is accurate reflector geometries. While reflection events may stack reasonably well without the true reflector geometries, as shown by Lazaratos, they can not be correctly positioned. One possible solution to this, suggested by Lazaratos, is to migrate the reflection images post-stack. This step is

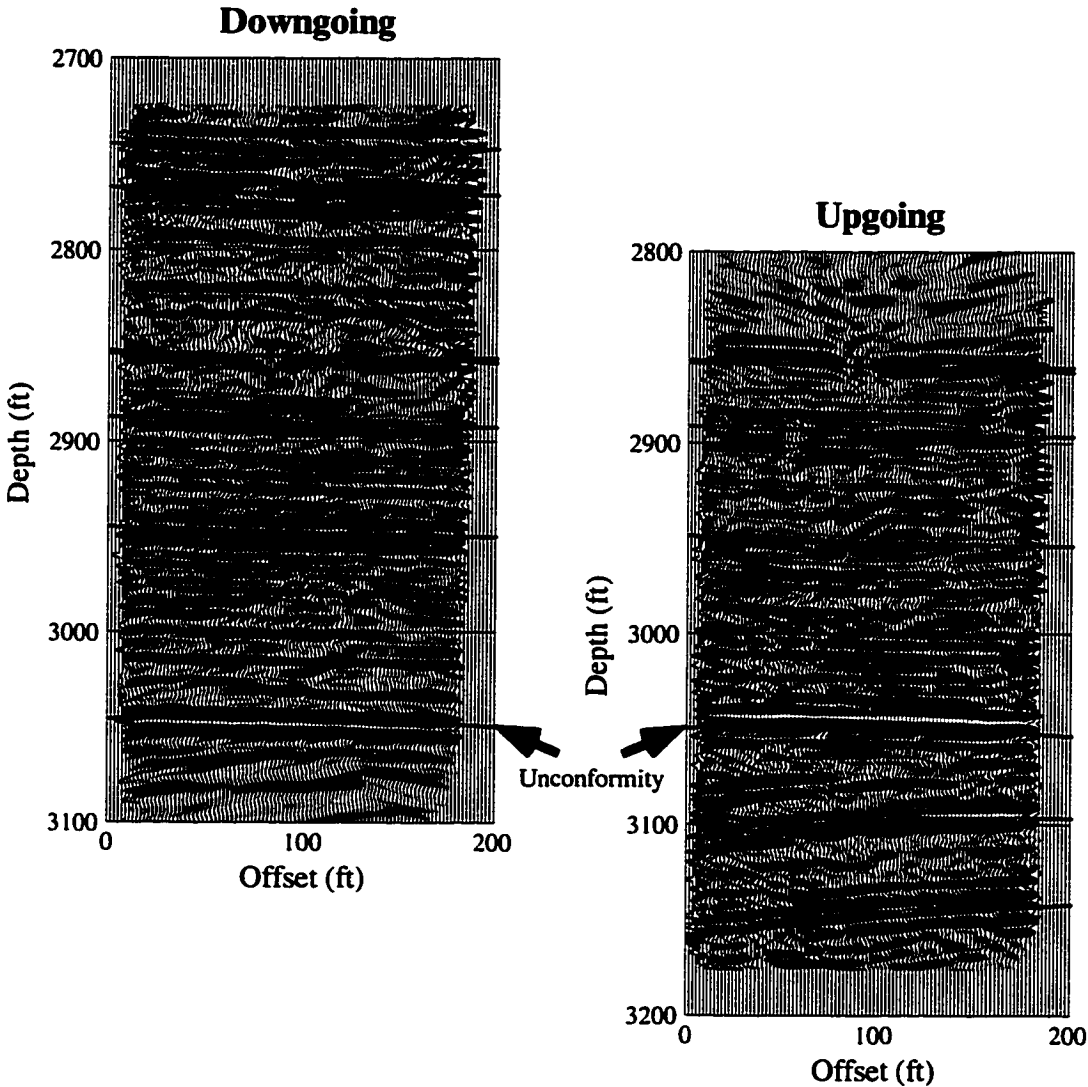


Figure 6.24: These reflection images are “brute” stacks of the Mc68-02b processed seismic data mapped using the CDRATT T11 model. The red lines are the reflector solutions of the CDRATT traveltime inversion. The reflection sections are created by stacking all available mapped data with no post-map or post-stack processing.

unnecessary using the CDRATT model when the calculated reflection geometries correspond well with the geometries in the reflection image. This provides a second role for the CDRATT reflector geometries, in addition to calculating the mapping trajectories, as a quality control reference for interpretation of the reflection images.

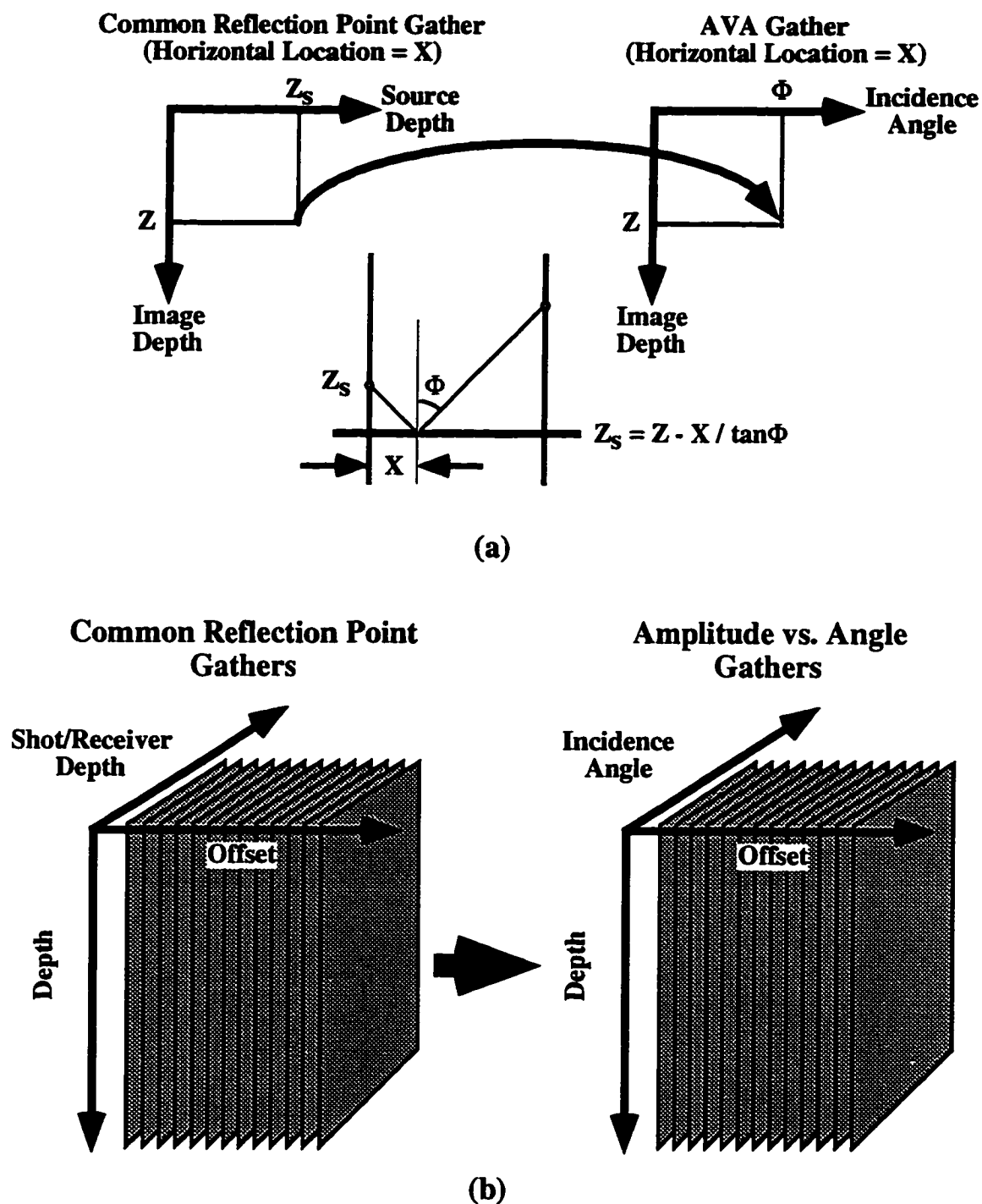
### 6.5.2 Limited angle stacking

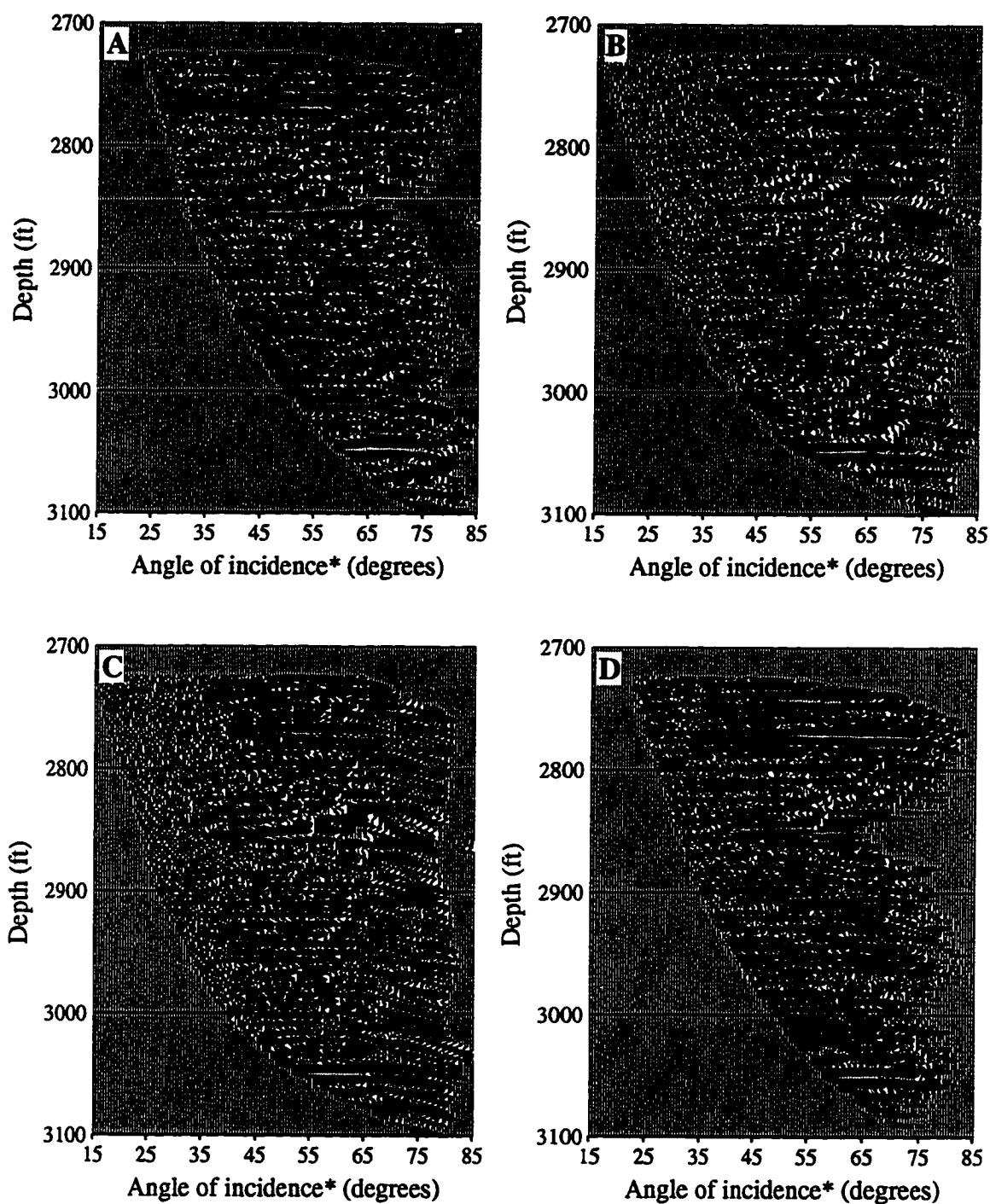
The brute stack reflection images shown in Fig. 6.24 are fairly low noise without *any* post-map processing. In spite of this there are immediate benefits to be obtained by applying a simple filter prior to stacking to limit the effective range of reflection angles stacked. This process was described by Lazaratos in his thesis. The two main benefits of limiting effective reflection angles are that excessively stretched data are removed and the wavelet varies less within the reflection image.

An effective implementation of this filter (Lazaratos, 1993) uses a transformation of the mapped data cube into the Amplitude vs. Angle (AVA) domain. The basics of this transformation are shown in Figure 6.25. The transformation itself is described in Fig. 6.25a. The implementation shown uses a straight ray assumption. This approach can be modified easily to calculate the transformation angle more accurately if needed but the straight ray assumption has been adequate for these tests. Each point in the Common Reflection Point (CRP) domain is transformed to a unique point in the Amplitude vs. Angle domain. This is done on a gather by gather basis. The final result is a data cube organized like the AVA cube in Fig. 6.25b. The transformed data cube can be sorted into Common Angle Gathers (CAG's) and AVA gathers. Each AVA gather contains all the data that can be stacked to create a single image trace. This is an ideal domain to filter the data to preserve a uniform range of incidence angles in the final stack.

Examples of data in the AVA domain are shown in Figures 6.26 and 6.27. Figure 6.26 shows AVA gathers of downgoing reflection data for offsets in the Mc68-02b reflection image of 25, 75, 125, and 175 ft, corresponding to "A" through "D" respectively. Figure 6.27 is set up in a similar fashion but illustrates upgoing reflection events. In the reflection imaging process each one of these gathers is stacked to create a single trace. To obtain an optimal stack events should be horizontal to minimize destructive interference. Reflection events in the displayed AVA gathers are well lined up in this desired fashion.

If all the data in each AVA gather shown in Figs. 6.26 and 6.27 are stacked the range of incidence angles contributing to the final trace varies over the entire range of depths. The drawback of this is that the bandwidth of the final wavelet is a function of the incidence angles stacked. To minimize the variability of the wavelet a subset of the AVA gathers should be chosen for stacking. This filter, in addition to providing a more stationary





\* straight ray approximation

Figure 6.26: This figure shows downgoing mapped reflection data in the AVA domain. The gathers represent offsets in the Mc68-02b image located at 25, 75, 125, and 175 ft, “A” through “D” respectively. The data were processed to enhance downgoing reflections prior to mapping.

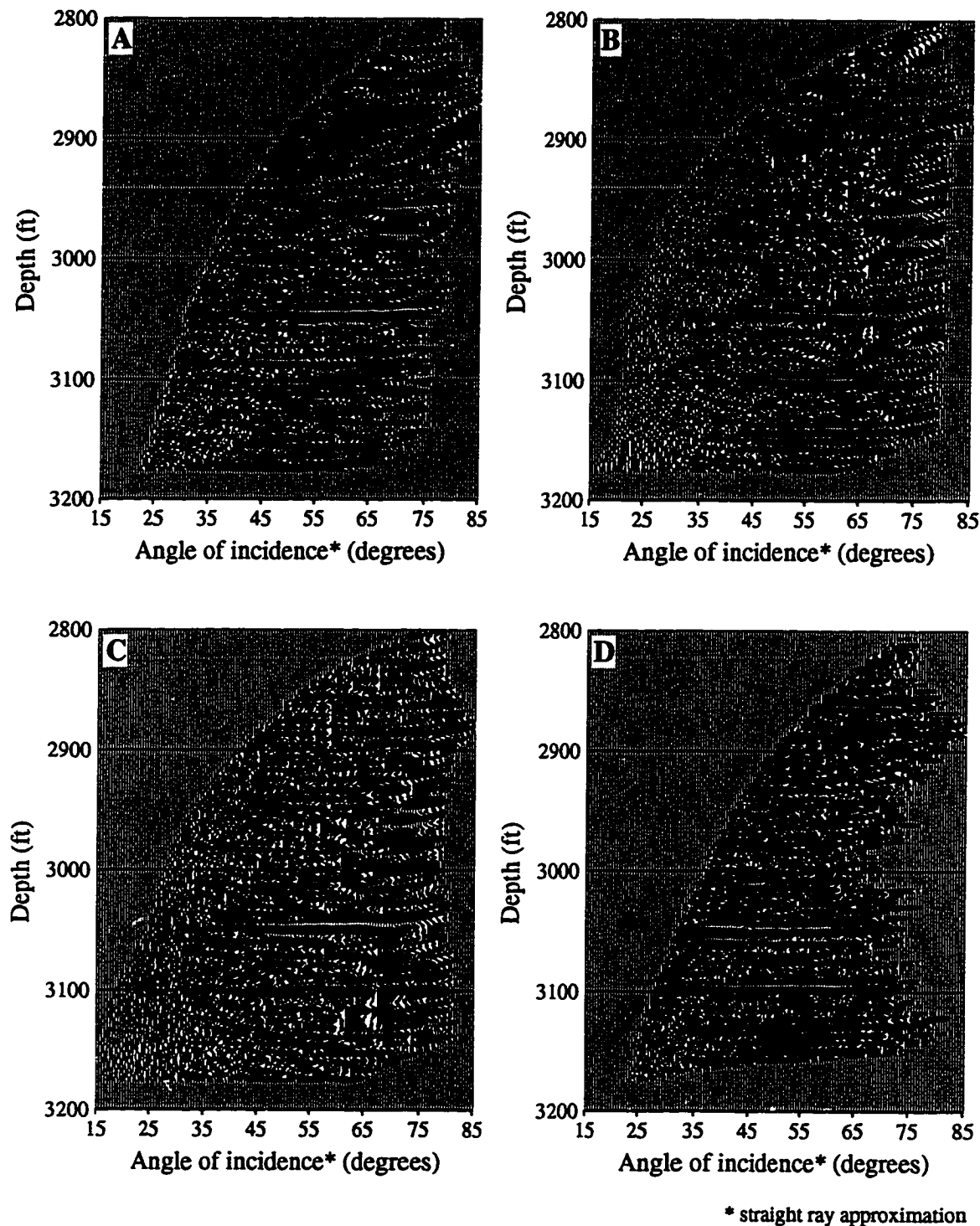


Figure 6.27: This figure shows upgoing mapped reflection data in the AVA domain. The gathers represent offsets in the Mc68-02b image located at 25, 75, 125, and 175 ft, “A” through “D” respectively as in Fig. 6.26. The data were processed to enhance downgoing reflections prior to mapping.



wavelet, is also used to remove stretched and noisy data. Balancing the desire to make the range of incidence angles stacked very small are the benefits achieved through using the broadest range of angles: a more broadband wavelet and a greater number of traces to enhance the signal-to-noise benefits of stacking. Keeping all these conflicting requirements in mind I have chosen a range of incidence angles spanning 35–65 degrees. This range provides a large number of traces to stack (60), eliminates most of the noisy and stretched data, and provides a more stationary wavelet.

The results of the limited angle stacking are shown in Figure 6.28. The most obvious difference in these new stacks are that the very top of the upgoing stack and very bottom of the downgoing stack have been muted. This is because these sections contained only angles greater than 65 degrees. A closer examination of the brute and limited angle stacks shows that a fair amount of noise has been removed from the limited angle stack improving the coherency of the fainter reflection events. This is particularly obvious in the upgoing reflection image between 2900 and 3050 ft.

### 6.5.3 Comparison of CDRATT and DAO models

A velocity model that is consistent with the reflected arrivals should lead to AVA gathers where the reflection events are better lined up. This is the goal of CDRATT velocity estimation. If the events are lined up well they should stack in a coherent fashion providing the best stack. In this section I will examine the effectiveness of CDRATT velocity estimation by comparing the alignment of events in the AVA domain for data mapped using models calculated with the following methods: 1-D DAO, 2-D DAO, and CDRATT T11.

Figure 6.29 shows mapped Mc68-02b downgoing seismic data in three AVA gathers. These AVA gathers represent the identical data mapped using three different models: the 1-D DAO model (Fig. 6.29a), the 2-D DAO model (Fig. 6.29b), and the CDRATT T11 model (Fig. 6.29c). Since no reflector information is provided by the DAO inversions a horizontal reflector assumption was made. Previously, in the section of this chapter comparing the tomographic results, I showed that the largest change in the velocity tomogram due to the addition of reflection traveltimes is near the top of the image. This is the area of focus in this example since the data mapped near this region should, potentially, have the largest errors. The AVA gathers are for an offset of 175 ft which corresponds to AVA gather “D” in Fig. 6.26 between the depths of 2700 and 2800 ft.

In this example I focus on two of the reflectors picked and used in the CDRATT inversion, Reflectors 1 & 2. Reflector 1 corresponds to a peak in the downgoing reflection section located at a depth of approximately 2747 ft and Reflector 2 corresponds to a trough

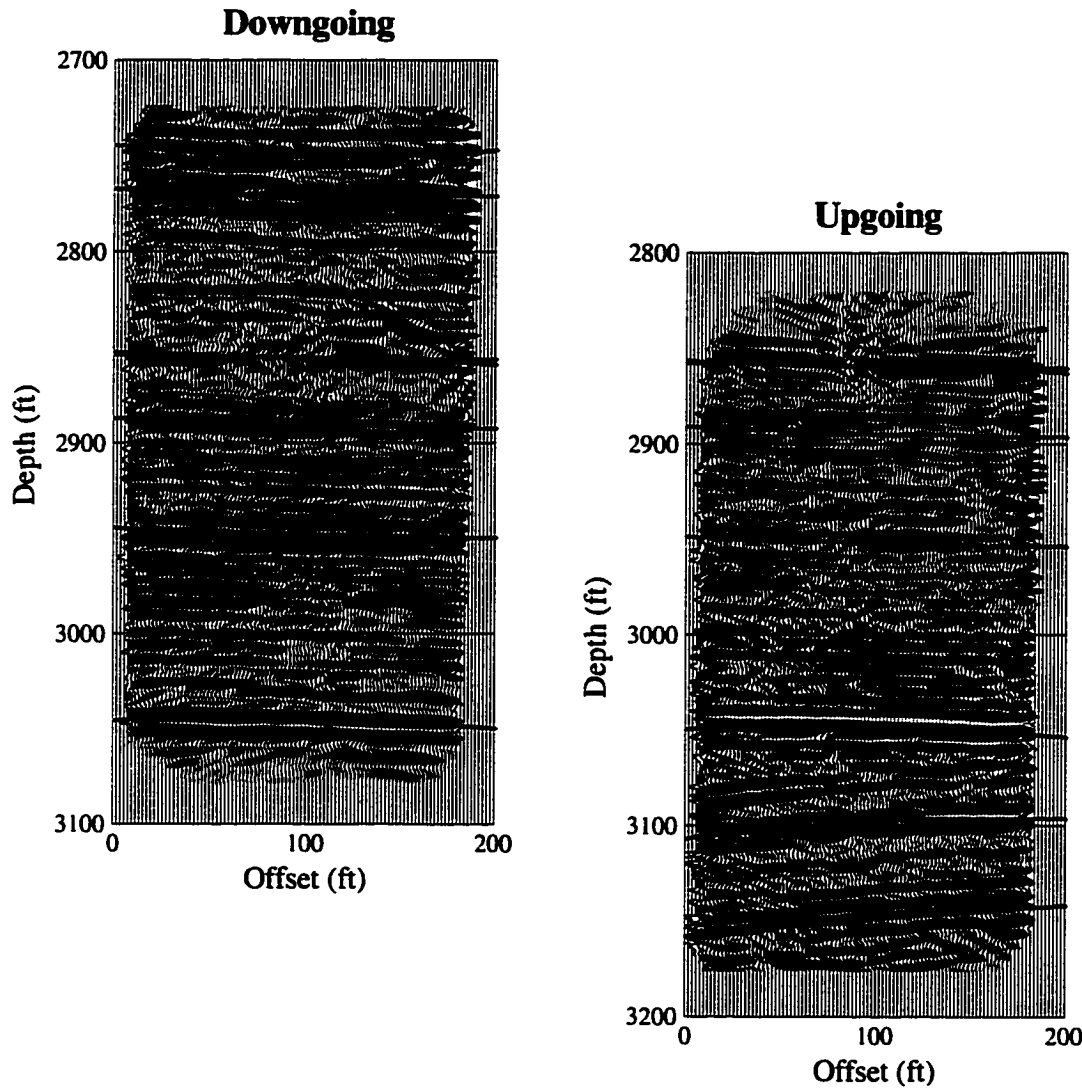


Figure 6.28: These reflection images are limited angle stacks of the Mc68-02b processed seismic data mapped using the CDRATT T11 model. These images provide an improvement in signal-to-noise ratio over the “brute” stacks shown in Fig. 6.24. The reflection sections are created by stacking data between the angles of 35 and 65 degrees with no post-map or post-stack processing.

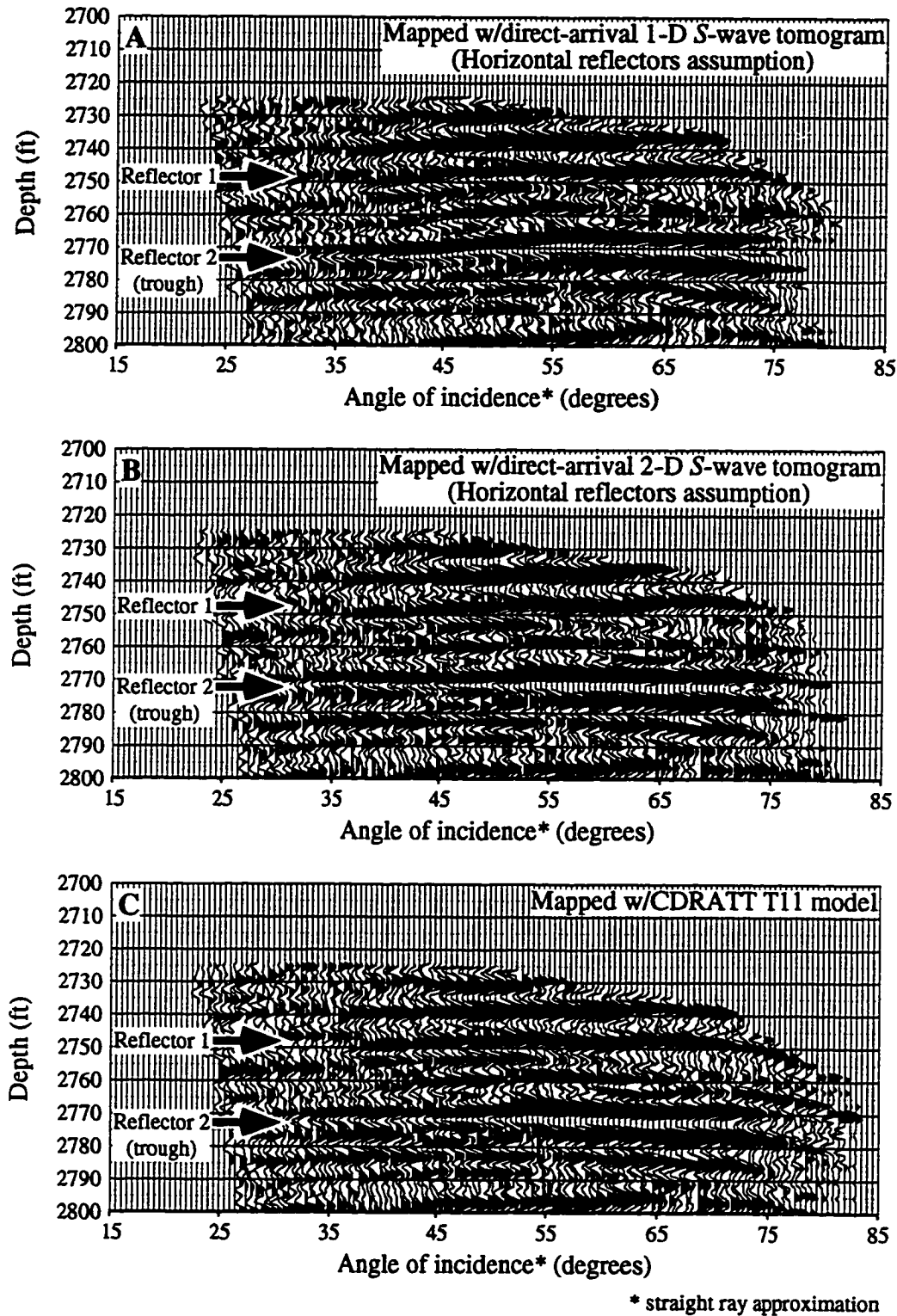


Figure 6.29: These three images show downgoing mapped data in the AVA domain for an image offset of 175 ft. The identical data were mapped using three different models: A) 1-D DAO, B) 2-D DAO, and C) CDRATT T11. To stack reflection events effectively they should be aligned horizontally. Image "C" shows the best alignment.

in the downgoing section located at about 2772 ft. In Fig. 6.29a, mapped with the 1-D DAO model, the depths of Reflectors 1 & 2 vary almost 5 ft over the range of angles present in the AVA gather. This corresponds to nearly a half a wavelength of the dominant frequency and would result in significant destructive interference if stacked. This moveout motivates the development of the velocity estimation approach described in this thesis. In Fig. 6.29b the same data mapped with the 2-D DAO model is shown. The 2-D DAO model aligns the reflections more effectively than the 1-D DAO model but, while Reflector 2 appears well lined up, there still is a noticeable amount of moveout in Reflector 1. The final AVA gather, Fig. 6.29c, presents the results of mapping with the CDRATT T11 model. In this image both Reflectors 1 & 2 are lined up well over a wide range of angles. The biggest differences in Figs. 6.29b and 6.29c occur near the very top of the image. This is expected since the largest difference in these velocity models (Fig. 6.23) occurs in this region.

The 2-D DAO model provides a significant improvement over the 1-D DAO model in lining up reflections in the AVA gather. How significant is the small amount of remaining moveout on the final stack? Figure 6.30 shows the results of stacking the 1-D DAO and CDRATT mapped AVA downgoing data over a range of angles of 35–65 degrees. While both images agree well below Reflector 2 there is a significant difference in the images above this. In the CDRATT imaged section Reflector 1 and an event above it are strong and coherent from well to well. In the section imaged with the 2-D DAO model these same reflectors are broken, discontinuous, and of low amplitude. The mild residual moveout resulting from the 2-D DAO model is sufficient to have a severe impact on the image quality near the edge of the survey.

To complete the comparison I've included Figure 6.31, the entire upgoing and downgoing limited angle (35–65 degrees) stacked sections created using the 2-D DAO model. Compare these stacks to the limited angle CDRATT stacks shown in Fig. 6.28. Small differences in the dipping reflector at ~3150 ft can be observed near the bottom of the upgoing section similar to the differences at ~2740 ft in the downgoing sections shown in Fig. 6.30. This reflects another zone where the 2-D DAO and CDRATT velocity models differ significantly. The rest of the stacked sections correlate well. This is expected since the velocity models don't vary significantly through the middle of the survey.

The difference in stacking quality between the 2-D DAO and CDRATT mapped data shows that the addition of reflection information to the traveltime inversion results in a velocity model that is superior for crosswell reflection imaging. In the example shown the effects of this are most significant near the top and bottom edges of the stacks. This corresponds to the region where the most amount of information is added to the tomographic inversion in the form of increased angular coverage.

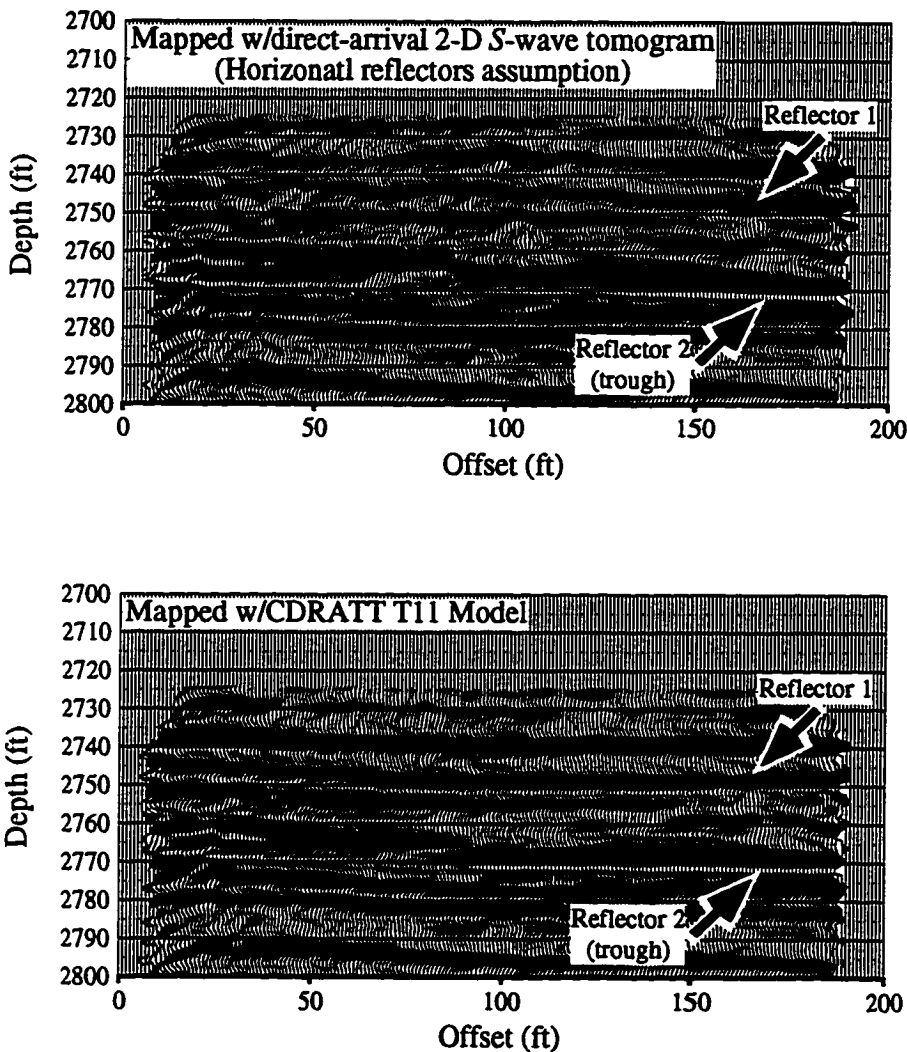


Figure 6.30: This figure provides a comparison of 35–65 degrees limited angle downgoing stacks created using data mapped with the 2-D DAO model and the CDRATT T11 model. Reflectors above 2770 ft in the DAO stack show poor coherency and resolution. The same reflections are sharp and of high amplitude in the CDRATT stack

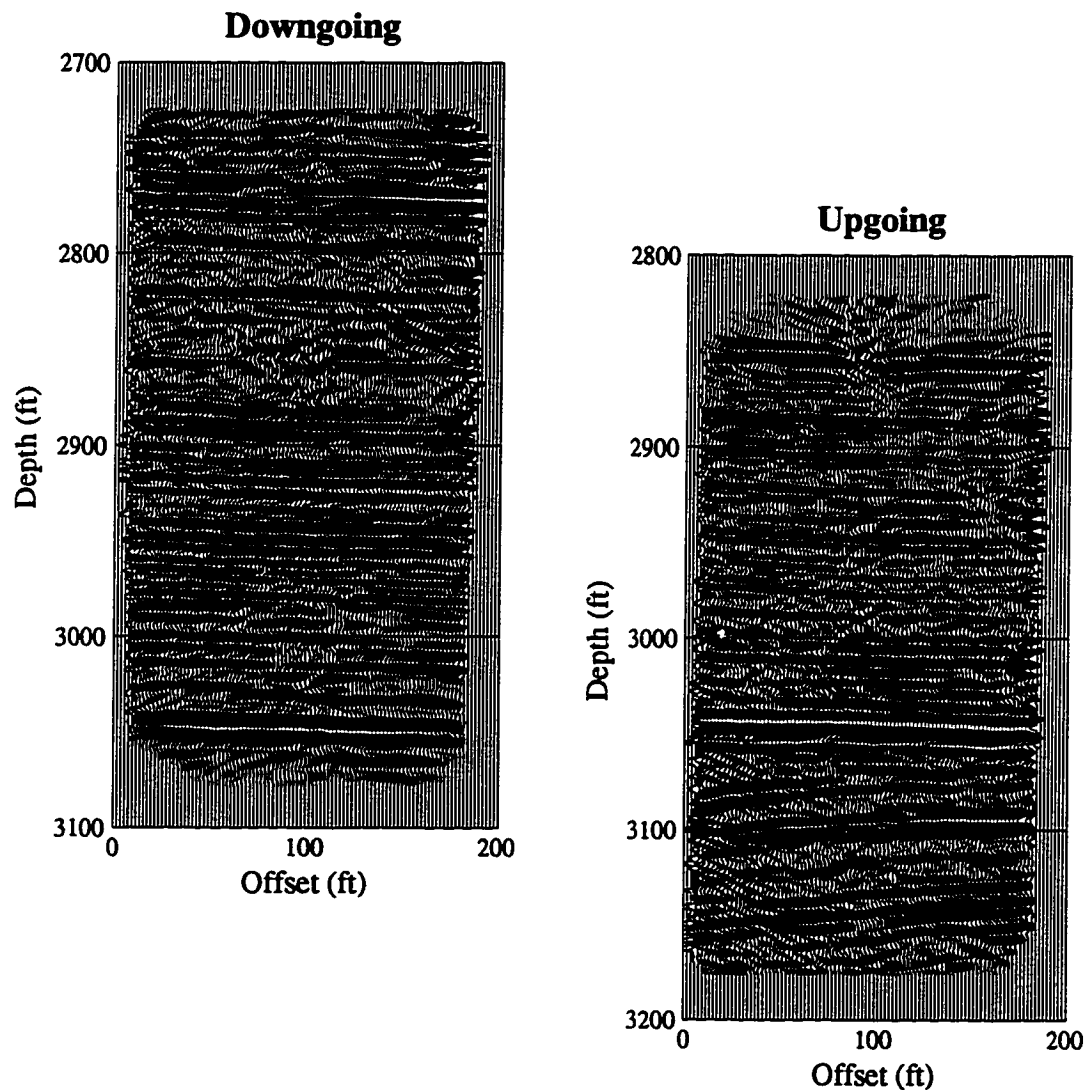


Figure 6.31: These upgoing and downgoing 35–65 limited angle stacks were created using reflection-enhanced seismic data and the 2-D DAO model. These images allow a comparison over the entire image with the CDRATT mapped data shown in Fig. 6.28. Note that the reflections below 3100 ft are also poorly stacked compared to the CDRATT images.

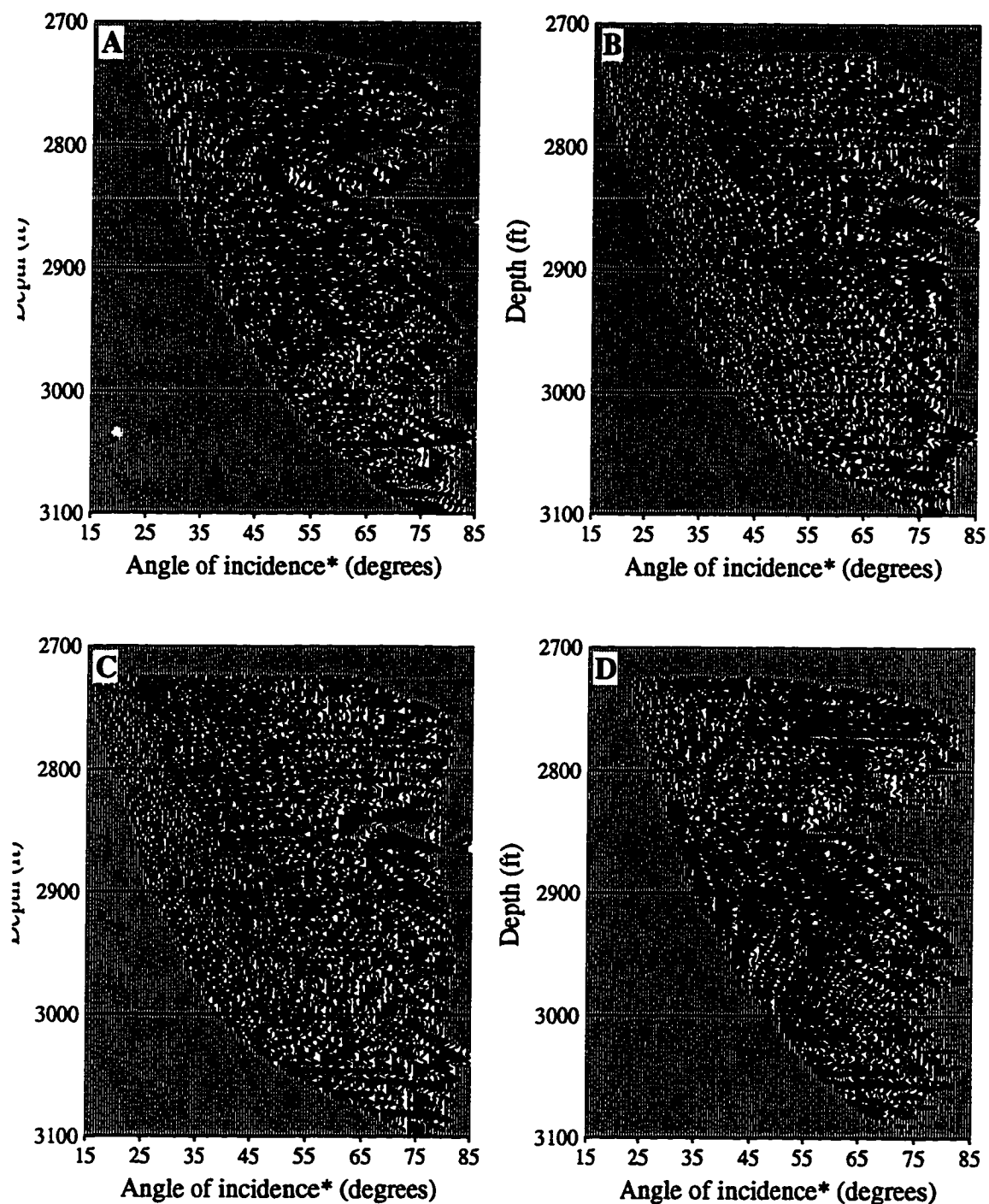
### 6.5.4 Reflection imaging without wavefield processing

All of the reflection images shown so far have been created using seismic data that have been processed to enhance upgoing and downgoing reflection events using a multi-step process which is outlined in Fig. 6.11. Reflection enhancement is required in the procedure for picking accurate reflection traveltimes and thus necessary in the CDRATT velocity estimation method. There is the question of its importance with respect to reflection imaging. This question can not be answered confidently in general due to the different noise levels, hardware response, etc., found in the variety of crosswell surveys collected. It can be tested with the Mc68-02b data though.

In this section I have created stacked sections of the Mc68-02b data in precisely the same manner as described in the limited angle stacking section previously. The only difference in this example is that the data which are mapped are completely unprocessed. No filtering, event removal, or event enhancement techniques were applied prior to mapping with the CDRATT T11 model. Following the initial mapping the data were transformed to the AVA domain as described previously. Figures 6.32 & 6.33 provide examples of these AVA gathers for downgoing and upgoing reflections respectively. For comparison purposes these gathers correspond to the AVA gathers created from the processed data shown earlier in Figs. 6.26 and 6.27. The AVA gathers created from the unprocessed data show a large amount of noise and strong amplitude fluctuations not present in the processed data gathers. They also contain obvious reflection events.

Figure 6.34 shows the results of stacking the unprocessed AVA gathers over a range of angles of 35–65 degrees. In spite of the complete absence of wavefield processing the upgoing and downgoing stacks look quite similar to those made with processed data shown in Fig. 6.28. Although the stacks are a bit noisier they still show strong, coherent, well-to-well reflections. One negative effect of the wavefield processing on the Fig. 6.28 downgoing stack is readily apparent between 2900 and 3000 ft. Compared to the Fig. 6.34 downgoing stack the processed data stack contains less high (spatial) frequency information. The unprocessed data stack appears sharper and with higher resolution.

The quality of the unprocessed data stacks has several implications. The first is that the ray-theoretic approach is appropriate and effective for crosswell reflection imaging under the conditions present in this experiment. The second implication is that, while the noise removed by the wavefield processing prior to mapping leads to less noise in the final stack, it appears to be at the expense of some high frequency information and resolution. This suggests that improved wavefield processing routines and application procedures should be developed in order to minimize the loss of data and resolution in the final stacks. The final



\* straight ray approximation

Figure 6.32: This figure shows upgoing mapped reflection data in the AVA domain. The gathers represent offsets in the Mc68-02b image located at 25, 75, 125, and 175 ft, "A" through "D" respectively as in Fig. 6.26. The data were not processed at all prior to mapping. Compare to Fig. 6.26.



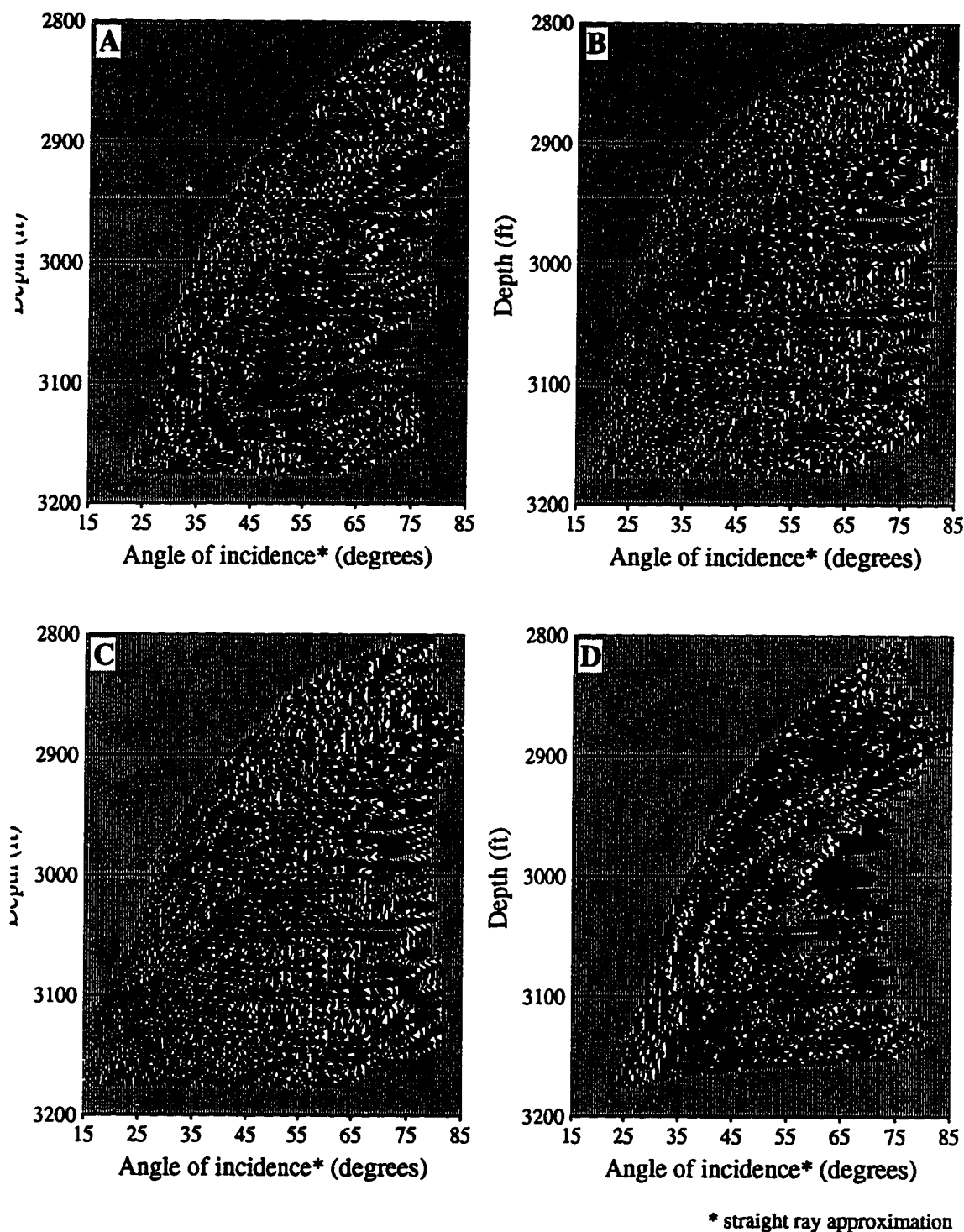


Figure 6.33: This figure shows downgoing mapped reflection data in the AVA domain. The gathers represent offsets in the Mc68-02b image located at 25, 75, 125, and 175 ft, “A” through “D” respectively as in Fig. 6.26. The data were not processed at all prior to mapping. Compare to Fig. 6.27.

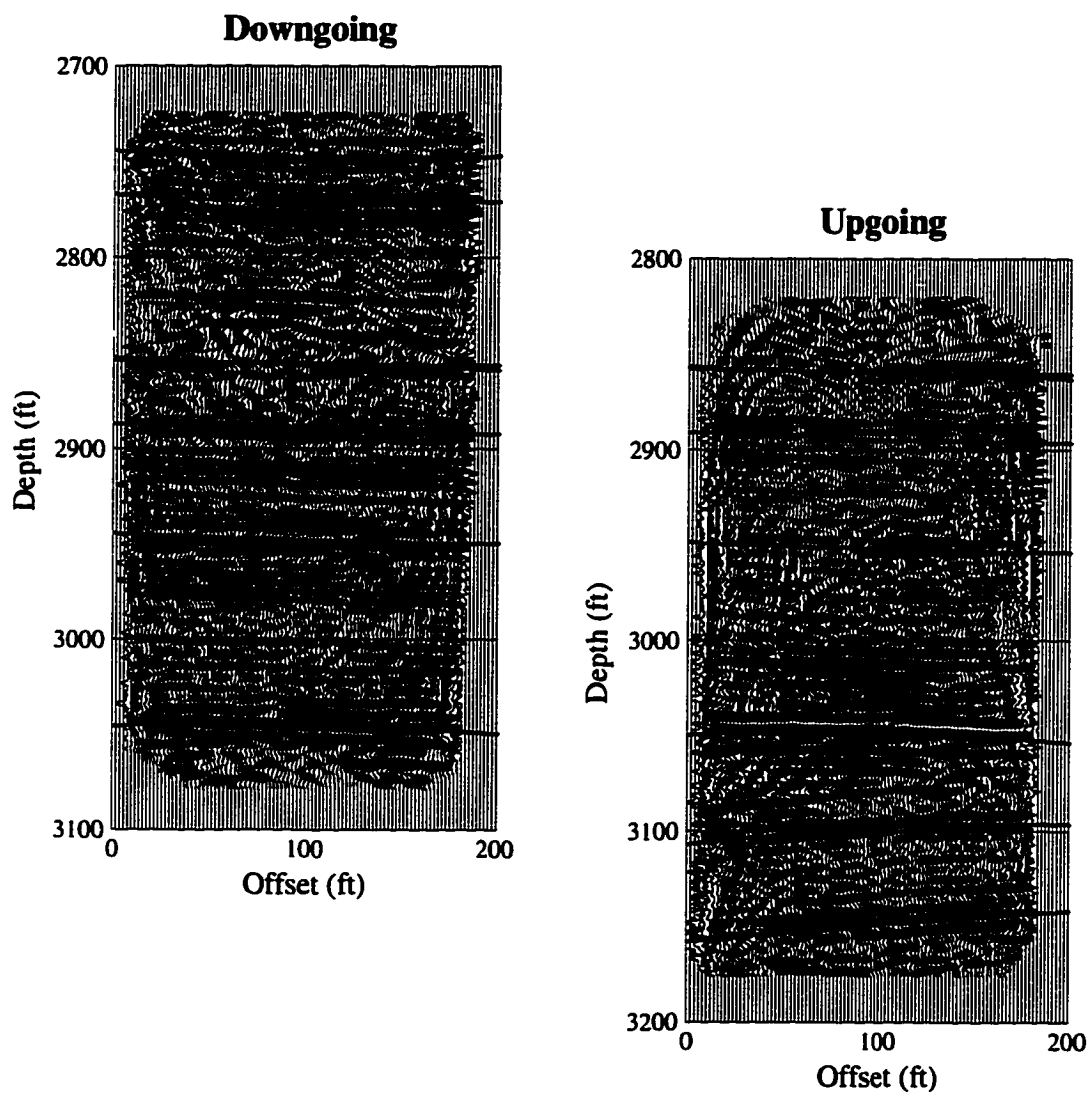


Figure 6.34: These reflection images are limited angle (35–65 degrees) stacks of *unprocessed* seismic data from the Mc68-02b survey mapped using the CDRATT T11 model. Compare these stacks with those shown in Fig. 6.28 created using processed data. Although these stack are slightly noisier they contain more high frequencies as can be easily seen in the downgoing image located on the left-hand-side between the depths of 2900 and 3000 ft.

point made by these images is that stacking can be a powerful tool given an appropriate imaging model to correctly locate events prior to the stacking process.

## 6.6 Conclusions

The simultaneous use of direct and reflected arrival traveltime information from the crosswell wavefield can satisfy two objectives in crosswell imaging: 1) improving the angular coverage within the surveyed area, especially near the top and bottom edges, and hence hopefully resolution and accuracy, and 2) providing an accurate velocity model and the reflector geometry information required for effective reflection imaging. I have achieved both of these objectives using Combined Direct and Reflected Arrival Traveltime Tomography, the basis of the CDRATT velocity estimation method.

I have demonstrated the use of the CDRATT velocity estimation method on field data for obtaining traveltime tomograms with less velocity artifacts and a better correlation with well logs. I have also demonstrated its effectiveness as a velocity estimation tool for obtaining information necessary for effective reflection imaging. In the example shown the largest improvements in imaging take place near the top and bottom edges of the surveyed area. The importance of extending the accuracy of the crosswell imaging techniques to the edges results from the targets in crosswell studies undertaken in the oil field environment so often being near the bottom of the survey. This is true since wells are not often drilled far beyond the reservoir depth.

The important processing tools I developed to implement crosswell reflection velocity estimation are the CDRATT algorithm and a wavefront-based XSP-CDP mapping algorithm designed to use CDRATT models. Just as important, I also developed a methodology for collecting reflection traveltimes from crosswell data. This approach requires effective wavefield processing techniques to enhance reflections. The largest potential stumbling block to easily extending CDRATT velocity estimation to all crosswell reflection imaging problems is the reflection traveltime picking step. This should become less of a problem as wavefield processing methods become more effective. Also, applying new technology, such as 3-D interactive seismic interpretation stations, could make reflection traveltime picking trivial.

It has been demonstrated in previous work that to maintain the same resolution in the crosswell reflection image the required accuracy of the mapping velocity model *increases* as the distances between wells increases. This is coupled with the reality that as the well offsets increase the average angular aperture of the experiment *decreases* making the calculation of accurate velocity models more difficult. The CDRATT velocity estimation

**offers a solution to this dilemma by providing a robust method for making use of a larger proportion of the information available in the crosswell wavefield than was possible before.**

.

## References

- Abdalla, A. A. and Stewart, R. R., 1990, Traveltime inversion and reflection processing of cross-hole seismic data: 60th Ann. Internat. Mtg. of SEG., Expanded Abstracts, 47–50.
- Baker, L. J. and Harris, J. M., 1984, Cross-borehole seismic imaging: 54th Ann. Internat. Mtg. of SEG., Expanded Abstracts, 23–25.
- Beydoun, W. B., Delvaux, J., Mendes, M., Noual, G., and Tarantola, A., 1989, Practical aspects of an elastic migration/inversion of crosshole data for reservoir characterization: A Paris basin example: *Geophysics*, **54**, 1587–1595.
- Bishop, T. N., Bube, K. P., Cutler, R. T., Langan, R. T., Love, P. L., Resnick, J. R., Shuey, R. T., Spindler, D. A., and Wyld, H. W., 1985, Tomographic determination of velocity and depth in laterally varying media: *Geophysics*, **50**, 903–923.
- Born, M. and Wolf, E., 1980, Principle of optics electromagnetic theory of propagation interference and diffraction of light, 6th Edition, Pergamon Press, Inc., 808.
- Bregman, N. D., Hurley, P. A., and West, G. F., 1989, Ghosts in tomography: *Can. J. Expl. Geophys.*, **25**, 7–27.
- Bube, B. P., and Langan, R. T., 1995, Resolution of crosswell tomography with transmitted and reflected traveltimes: STP-6, Paper I.
- Bube, B. P., and Langan, R. T., 1994, A continuation approach to regularization for traveltime tomography: 64th Ann. Internat. Mtg. of SEG., Expanded Abstracts, 980–981.
- Bube, B. P., Langan, R. T., and Resnick, J. R. 1989, Unique determination of reflector depths in seismic reflection tomography: 59th Ann. Internat. Mtg. of SEG., Expanded Abstracts, 918–921.
- Calnan, C., and Schuster, G. T., 1989, Reflection + Transmission Crosswell Tomography: 59th Ann. Internat. Mtg., Soc. Expl. Geophys., Expanded Abstracts, 908–911.
- Carrion, P. M., Sato, H. K., and Buono, A. V. D., 1991, Wavefront sets analysis of limited aperture migration sections: *Geophysics*, **56**, 778–784.
- Cassell, B. R., Alam, M. A., and Millahn, K. O., 1984, Interactive VSP-CDP mapping in complex media: 54th Ann. Internat. Mtg. of SEG., Expanded Abstracts, 23–25.
- Delvaux, J., Nicoletis, L., Noual, G., and Dutzer, J. F., 1987, Acquisition techniques in cross-hole seismic surveys: 62nd Ann. Tech. Conf. and Expos. of SPE., Proc. no. 16785, 23–25.
- Dillon, P. B. and Thomson, R. C., 1984, Offset source VSP surveys and their image reconstruction: *Geophys. Prosp.*, **32**, 790–811.
- Findlay, M. J., Goult, N. R., and Kragh, K. E., 1991, The crosshole seismic reflection

- method in opencast coal exploration: *First Break*, **9**, 509–514.
- Goulty, N. R., Thatcher, J. S., Findlay, M. J., Kragh, J. E., Jackson, P. D., 1990, Experimental investigation of crosshole seismic techniques for shallow coal exploration: *Quarterly Journal of Engineering Geology*, London, **23**, 217–228.
- Harris, J. M., Nolen-Hoeksema, R. C., Rector, J. W., Lazaratos, S. K., and Van Schaack, M. A., 1995, High-resolution crosswell imaging of a west Texas carbonate reservoir: Part 1 — Project summary and interpretation: *Geophysics*, **60**, 667–681.
- Harris, J. M., 1992, Initial value raytracing in smoothly varying heterogeneous media: STP-3, Paper I.
- Harris, P. M. and Walker, S. D., 1988, Atlas of oil and gas fields, McElroy field-U.S.A., Texas, Permian Basin: *Treatise of Petroleum Geology*, AAPG.
- Hu, L.-Z., McMechan, G. A., and Harris, J. M., 1988, Acoustic modeling and migration of stacked cross-hole data: *Geophysics*, **53**, 1015–1023.
- Ivansson, S., 1986, Some remarks concerning seismic reflection tomography and velocity analysis: *Geophys. J. R. Astr. Soc.*, **87**, 539–557.
- Iverson, W. P., 1988, Crosswell logging for acoustic impedance: *J. Pet. Tech.*, **40**, 75–82.
- Justice, J. H., Vassiliou, A. A., Singh, S., Logel, J. D., Hansen, P. A., Hall, B. R., Hutt, P. R., and Solanki, J. J., 1989, Acoustic monitoring for monitoring enhanced oil recovery: *The Leading Edge*, **8**, 12–19.
- Khalil, A. A., Stewart, R. R., and Henley, D. C., 1993, Full-waveform processing and interpretation of kilohertz cross-well seismic data: *Geophysics*, **58**, 1248–1256.
- Langan, R.T., Harris, J. M., Lazaratos, S. K., and Van Schaack, M. A., 1995, Crosswell seismic imaging in the Permian Basin, west Texas, USA: 65th Ann. Internat. Mtg. of SEG., Expanded Abstracts, 81–84.
- Langan, R.T., Lerche, I., and Cutler, R.T., 1985, Tracing of rays through an heterogeneous media: An accurate and efficient procedure: *Geophysics*, **50**, September.
- Lazaratos, S. K., Harris, J. M., Rector, J. W., and Van Schaack, M. A., 1995, High-resolution crosswell imaging of a wet Texas Carbonate reservoir: Part 4 — Reflection imaging: *Geophysics*, **60**, 702–711.
- Lazaratos, S. K., 1993, Cross-well reflection imaging: Ph.D. thesis, Stanford University.
- Lemen, M. A., Burlas, T. C., and Roe, L. M., 1990, Waterflood pattern realignment at the McElroy field — Section 205 case history: *SPE Paper 20120* presented at the 1990 Permian Basin Oil & Gas Recovery Conference, Midland, Texas, March 8–9.
- Lines, L., Tan, H., Treitel, S., Beck, J., Chambers, R., Eager, J., Savage, C., Queen, J., Rizer, W., Buller, P., Cox, D., Sinton, J., Ballard, J., Kokkoross, G., Track, A., Guerendel, P., Harris, J., Lazaratos, S., Van Schaack, M., 1995, Integrated reservoir

- characterization: Beyond tomography: *Geophysics*, **60**, 354–364.
- Marquardt, D. W., 1963, An algorithm for least-squares estimation of non-linear parameters: *Soc. of Industr. Appl. Math.*, **11**, 431–441.
- Mathisen, M. E., Vassiliou, A. A., Cunningham, P. S., Shaw, J., Justice, J. H., and Guinzy, N. J., 1995, Time-lapse crosswell seismic tomogram interpretation: Implications for heavy oil reservoir characterization, thermal recovery process monitoring, and tomographic imaging technology: *Geophysics*, **60**, 631–650.
- Matsuoka, T. and Ezaka, T., 1992, Ray tracing using reciprocity: *Geophysics*, **57**, 326–333.
- Menke, W., 1984, The resolving power of cross-borehole tomography: *Geophys. Res. Letters*, **11**, 105–108.
- Mo, L.-W., 1994, Calculation of direct arrival traveltimes by the eikonal equation: *STP-5*, Paper K.
- Mo, L.-W. and Harris, J. M., 1993, Migration of crosswell seismic data: field data case: *STP-4*, Paper L.
- Moser, T. J., 1989, Efficient seismic ray tracing using graph theory: 59th Ann. Internat. Mtg. of SEG., Expanded Abstracts, 1106–1108.
- Paulsson, B. N. P., Meredith, J. A., Wang, Z., and Fairborn, J. W., 1994, The Steepbanks crosswell seismic project: Reservoir definition and evaluation of steamflood technology in Alberta tar sands: *The Leading Edge*, **8**, 737–747.
- Paulsson, B. N. P., Cook, N. G. W., and McEvilly, T. V., 1985, Elastic-wave velocities and attenuation in an underground repository for nuclear waste: *Geophysics*, **50**, 551–570.
- Qin, F. and Schuster, G. T., 1993, Constrained Kirchhoff migration of cross-well seismic data: 63rd Ann. Internat. Mtg. of SEG., Expanded Abstracts, 99–102.
- Radon, J., 1917, Über die Bestimmung von Funktionen durch ihre Integralwerte langs gesisser Mannigfaltigkeiten: *Ber., Verh. Sachs. Akad.*, **69**, 262–277.
- Rector, J. W., Lazaratos, S. K., Harris, J. M., and Van Schaack, M. A., 1995, High-resolution crosswell imaging of a west Texas carbonate reservoir: Part 3 — Wavefield separation of reflections: *Geophysics*, **60**, 692–701.
- Rector, J. W. and Washbourne, J. K., 1994, Characterization of resolution and uniqueness in crosswell direct-arrival traveltome tomography: *Geophysics*, **59**, 1642–1649.
- Rector, J. W., Lazaratos, S. K., Harris, J. M., and Van Schaack, M. A., 1994, Multi-domain analysis and wavefield separation of cross-well seismic data: *Geophysics*, **59**, 10–20.
- Rowbotham, P. S. and Goulty, N. R., 1994, Wavefield separation by 3-D filtering in crosshole seismic reflection processing: *Geophysics*, **59**, 1065–1071.
- Rowbotham, P. S. and Goulty, N. R., 1993, Imaging capability of cross-hole seismic reflection surveys: *Geophys. Prosp.*, **41**, 927–941.

- Saito, H., 1989, Traveltimes and raypaths of first arrival seismic waves: Computation method based on Huygen's principle: 59th Ann. Internat. Mtg. of SEG., Expanded Abstracts, 244–247
- Smalley, N., 1994, Crosswell reflection depth and velocity analysis: STP-5, Paper F.
- Smalley, N., 1993, Crosswell reflection velocity analysis: STP-4, Paper G.
- Smalley, N. and Harris, J. M., 1992, CDP stacking and imaging of cross-well reflectors: 62nd Ann. Internat. Mtg. of SEG., Expanded Abstracts, 87–90.
- Stork, C., 1992a, Reflection tomography in the postmigrated domain: *Geophysics*, **57**, 680–692.
- Stork, C., 1992b, Singular value decomposition of the velocity-reflector depth tradeoff, Part 2: High-resolution analysis of a generic model: *Geophysics*, **57**, 933–943.
- Stork, C., 1988, Ray trace tomographic velocity analysis of surface seismic reflection data: Ph.D. thesis, California Institute of Technology.
- Taner, M. T. and Koehler, F., 1969, Velocity spectra — digital computer derivation and applications of velocity functions: *Geophysics*, **39**, 859–881.
- Tura, M. A. C., Greaves, R. J., and Beydoun, W. B., 1994, Crosswell seismic reflection/diffraction tomography: A reservoir characterization application: *Geophysics*, **59**, 351–361.
- Van Schaack, M. A., Harris, J. M., Rector, J. W., and Lazaratos, S. K., 1995, High-resolution crosswell imaging of a west Texas carbonate reservoir: Part 2 — Wavefield modeling and analysis: *Geophysics*, **60**, 682–691.
- Van Schaack, M. A., 1994, Integrated crosswell imaging: Reflection tomography — Synthetic examples: STP-5, Paper A.
- Van Schaack, M. A. and Lazaratos, S. K., 1993, An approach to interval velocity analysis for crosswell reflection imaging using reflection traveltimes: STP-4, Paper F.
- Van Trier, J. and Symes, W. W., 1991, Upwind finite-difference calculation of traveltimes: *Geophysics*, **56**, 812–821.
- Vidale, J. E., 1988, Finite-difference calculation of traveltimes: *Bull. Seis. Soc. Am.*, **78**, 2062–2076.
- Walker, S. D. and Harris, P. M., 1986, McElroy Field — Development of a dolomite reservoir, Permian Basin of west Texas: Permian Basin/SEPM Publication, **86-26**, 127–132.
- Wiggins, W., Ng, P., and Manzur, A., 1986, The relation between the VSP-CDP transformation and VSP migration: 56th Ann. Internat. Mtg. of SEG., Expanded Abstracts, 565–568.
- Williamson, P. R. and Worthington, M. H., 1993, Resolution limits in ray tomography due



- to wave behavior: Numerical experiments: *Geophysics*, **58**, 727–735.
- Wong, J., Hurley, P., and West, G. F., 1983, Crosshole seismology and seismic imaging in crystalline rocks: *Geophys. Res. Letters*, **10**, 686–689.
- Wyatt, K. D. and Wyatt, S. B., 1981, Determination of subsurface structural information using the vertical seismic profile: 51st Ann. Internat. Mtg. of SEG., Expanded Abstracts, 55–56.
- Zhang, L., 1993, Imaging by the wavefront propagation method, Ph.D. Thesis, Stanford University.
- Zhou, C., Cai, W., Luo, Y., Schuster, G. T., and Hassanzadeh, S., 1995, Acoustic wave-equation travelttime and waveform inversion of crosshole seismic data: *Geophysics*, **60**, 765–773.
- Zhu, X. and McMechan, G. A., 1988, Acoustic modeling and migration of stacked cross-hole data: *Geophysics*, **53**, 492–500.